

Kütahya Dumlupınar University Institute of Graduate Studies



Journal of Scientific Reports-A E-ISSN: 2687-6167

Number 62, September 2025

Owner

On Behalf of Kütahya Dumlupınar University Prof. Dr. Süleyman KIZILTOPRAK (Rector), On Behalf of Institute of Graduate Studies Assoc. Prof. Dr. Eray ACAR (Director)

Editorial Board

Önder UYSALKütahya Dumlupınar UniversityFatih ŞENKütahya Dumlupınar UniversityOktay ŞAHBAZKütahya Dumlupınar UniversityNevzat BEYAZITOndokuz Mayıs UniversityOnur KARAMANAkdeniz University

Cafer ÖZKUL Kütahya Dumlupınar University

Levent URTEKİN Ahi Evran University

Ümran ERÇETİN Kütahya Dumlupınar University

Ceren KARAMAN Akdeniz University

Durmuş ÖZDEMİR
Kütahya Dumlupınar University
Fatih Yavuz ILGIN
Güray KAYA
Relin Çağım TOKAT BİRGİN
Özlem KAYA
Kütahya Dumlupınar University
Kütahya Dumlupınar University
Sivas Cumhuriyet University

Özlem KAYA Sivas Cumhuriyet University
Tayfun ŞENGÜL Kütahya Dumlupınar University
Saadet ÇELİKÖZÜ Kütahya Dumlupınar University
Mehmet Selçuk ERDOĞAN Kütahya Dumlupınar University

Nataliia BALYTSKA Zhytomyr State Technological University

Natalia ZUIEVSKA National Technical University of Ukraine 'Igor Sikorsky

Kyiv Polytechnic Institute'

Oksana VOVK National Technical University of Ukraine 'Igor Sikorsky

Kyiv Polytechnic Institute'

Nodor SULASHVILI The University of Georgia

Csoknyai TAMAS

Budapest University of Technology and Economics

Budapest University of Technology and Economics

Budapest University of Technology and Economics

Kütahya Dumlupınar University

Kütahya Dumlupınar University Mehmet Selçuk ERDOĞAN Kütahya Dumlupınar University Sait ALTUN Sevgi KARACA Kütahya Dumlupınar University Kütahya Dumlupınar University Ramazan BAYAT Muhammed BEKMEZCİ Kütahya Dumlupınar University Kütahya Dumlupınar University Ayşenur AYGÜN Safa DÖRTERLER Kütahya Dumlupınar University Seyfullah ARSLAN Kütahya Dumlupınar University Büşra TUTUMLU Kütahya Dumlupınar University Merve ARSLAN Kütahya Dumlupınar University Bahadır YÖRÜR Kütahya Dumlupınar University



Journal of Scientific Reports-A, Number 62, September 2025

Sinem MAVİLER Kütahya Dumlupınar University Cemile Nur HEPGÜNEŞ Kütahya Dumlupınar University Anıl Orhan GÜRSOY Kütahya Dumlupınar University Nihal Yiğit ERTAŞ Kütahya Dumlupınar University Merve PAKSOY Kütahya Dumlupınar University Merve AKIN Kütahya Dumlupınar University Alper ÖZENGÜL Kütahya Dumlupınar University Ebru HALVACI Kütahya Dumlupınar University Damla İKBALLİ Kütahya Dumlupınar University

Journal of Scientific Reports-A started its publication life in 2000 as name of Journal of Science and Technology of Dumlupinar University and is a national peer-reviewed journal published regularly four times a year in March, June, September and December. The language of the journal is English. Articles submitted to the journal are evaluated by at least two referees who are experts in the subject and selected by the editorial board. All articles submitted to the journal are evaluated by the double-blind method. Articles submitted to our journal for review should not be previously published, accepted for publication and in the process of being evaluated for publication in another journal. All responsibility for the articles published in the journal belongs to the author(s).

The journal aims to share scientific studies carried out in the fields of science and engineering at national and international level with scientists and the public. Original research articles, review articles and short notes in science and engineering disciplines are accepted for the journal. Original research articles are expected to contain theoretical and experimental results and should not be published in other journals. In the review articles, it is expected that scientific, technological and current developments on a specific subject are reflected by using an extensive bibliography and made a satisfying evaluation of these. Short notes should be brief writings prepared to announce the first findings of an original study.

Editorial Policy

The journal is open access and the article evaluation period is between 1-2 months.

Correspondence Address: Kütahya Dumlupınar Üniversitesi Evliya Çelebi Yerleşkesi Fen Bilimleri Enstitüsü

43270 KÜTAHYA

E-mail: <u>joursra@gmail.com</u> **Phone:** 0 274 443 19 42 **Webpage:** gsjsra.com **Fax:** 0 274 265 20 60



Section Editors

Civil Engineering

Prof. Dr. M. Çağatay KARABÖRK Kütahya Dumlupınar University

Mechanical Engineering

Prof. Dr. Ramazan KÖSE Kütahya Dumlupınar University

Electrical-Electronics Engineering

Assoc. Prof. Kadir VARDAR Kütahya Dumlupınar University

Computer Engineering

Assoc. Prof. Doğan AYDIN Kütahya Dumlupınar University

Industrial Engineering

Assist. Prof. Üyesi Kerem CİDDİ Kütahya Dumlupınar University

Mining Engineering

Assist. Prof. Uğur DEMİR Kütahya Dumlupınar University

Geology Engineering

Assist. Prof. Muzaffer ÖZBURAN Kütahya Dumlupınar University

Metallurgical and Materials Engineering

Prof. Dr. İskender IŞIK Kütahya Dumlupınar University

Food Engineering

Prof. Dr. Muhammet DÖNMEZ Kütahya Dumlupınar University

Environmental Engineering

Prof. Dr. Nevzat BEYAZIT Ondokuz Mayıs University

Mathematics

Assist. Prof. Cansu KESKİN Kütahya Dumlupınar University

Physics

Prof. Dr. Huriye Sanem AYDOĞU Kütahya Dumlupınar University

Chemistry

Prof. Dr. Bülent ZEYBEK Kütahya Dumlupınar University

Biology

Assist. Prof. Nüket Akalın BİNGÖL Kütahya Dumlupınar University

Biochemistry

Assoc. Prof. Derya KOYUNCU ZEYBEK Kütahya Dumlupınar University

Occupational Health and Safety

Prof. Dr. Cem ŞENSÖĞÜT Kütahya Dumlupınar University

Software Engineering

Assist. Prof. Şerif Ali SADIK Kütahya Dumlupınar University



Advisory Board

Şükrü ASLAN Sivas Cumhuriyet University/ Turkey Erdal ÇELİK Ankara Yıldırım Beyazıt University/ Turkey

Cemal PARLAK Ege University/ Turkey

Muhammet DÖNMEZ Kütahya Dumlupınar University/ Turkey Konya Technical University/ Turkey İhsan ÖZKAN

Ercan ARPAZ Kocaeli University/ Turkey Yavuz GÜL Sivas Cumhuriyet University/ Turkey

Ataç BAŞÇETİN İstanbul Technical University/ Turkey Taner ERDOĞAN Kocaeli University/ Turkey

Derek ABBOTT University of Adeliaide/ Australia Kristian ALMSTRUP Copenhagen University Hospital/ Denmark

University of Birmingham/ UK Josette Camilleri Fudan University/ China Yan-Ru LOU

Ken HAENEN Hasselt University/ Belgium

Fanming JIN Shanghai Jiao Tong University/ China Suneel KODAMBAKA Florida International University/ USA Hvovoung LEE Sungkyunkwan University/Republic of Korea

Vinod TIWARI Banaras Hindu University/ India

Sabine WURMEHL Leibniz Institute/ Germany

Kai XIAO Oak Ridge National Laboratory/ USA Shahid ADEEL Government College University/ Pakistan

Arizona State University/ USA J. Marty ANDERIES University of Ghana/ Ghana Ayaga BAWAH University of Georgia/ USA Lilong CHAI Idiano D'ADAMO Sapienza University of Rome/ Italy Sanjit DEB Texas Tech University/ USA

Caroline HACHEM-VERMETTE University of Calgary/ Canada

Marlia Mohd HANAFIAH The National University of Malaysia/ Malaysia

Nick HOLDEN University College Dublin/ Ireland

Chang-Wei HU Sichuan University/ China Masashi KATO Nagoya University/ Japan

Tafadzwanashe MABHAUDHI University of KwaZulu-Natal/ South Africa Universiti Teknologi Brunei/ Brunei Mubarak MUJAWAR

United Nations University CRIS/ Belgium Nidhi NAGABHATLA Gunnar SEIDE Maastricht University/ Netherlands

Jonathan Wong Hong Kong Baptist University/ Hong Kong Yenchun Jim WU National Waiwan Normal University/ Taiwan

Jie ZHUANG

University of Tennessee/ USA



JOURNAL OF SCIENTIFIC REPORTS-A E-ISSN: 2687-6167

CONTENTS

RESEARCH ARTICLES

Investigation of the Antimicrobial Effects of Niclosamide, Furosemide and Nifedipine Drugs Released from A Modified Hydrogel Structure Mukaddes KESKİNATEŞ*, Bahar YILMAZ, Mevlüt BAYRAKÇI	1-11
Prediction of the Earthquake Magnitudes with A New Estimator via Sub-Sampling Method Ceren ÜNAL*, Gamze ÖZEL	12-28
Tuning the Magnetization by Preserving Half-Metallicity of Fecl ₂ via Embedding Transition Metal Atoms: A DFT Study Ali Emre GENÇ*	29-39
Crustal Melting During Exhumation of the Menderes Core Complex: Insights from the Mineral Chemistry of the Güneşli Granite (Western Türkiye) Ömer KAMACI*	40-60
Study of Geometric Texture on Tensile Properties of PLA Polymer Parts Produced by FDM Faik YILAN*, İbrahim M.M. AlZRAIQI, Levent URTEKİN	61-70
An Energy Efficient Cluster Head Selection in Priority Region Aware Wireless Sensor Networks Using Metaheuristic Algorithms Osman GÖKALP*, Doğan AYDIN, Aybars UĞUR	71-89
A Deformation Structure and Origin of Metamorphic Sole Rocks Beneath the Eldivan and Ahlat Ophiolites (Çankırı), Northern Anatolia. Tijen ÜNER*, Üner ÇAKIR	90-110
Betaine Induces Apoptosis via ROS-Independent Mechanisms in U87 Glioblastoma Cells: A Potential Metabolic Anticancer Strategy Neslihan MERİÇ*, Ezgir KAR, Fatih KAR	111-124



Journal of Scientific Reports-A, Number 62, September 2025

MCST-Based Finite Element Solution for Short-Fiber-Reinforced Microbeam Vibration with the Effects of Rotary Inertia and Pasternak Medium Büşra UZUN*	125-147
Exploring Matrix Applications Across Interdisciplinary Domains: Insights from Business, Geology and Robotics Khadeejah James AUDU*, Mahmud Adeiza LAWAL, Oloruntobi Olalekan BALOGUN, Abraham Ajeolu OLUWASEGUN, Stephen Udugbai EGBE	148-159
Investigation of Physicochemical and Filtration Performances of Ag-Doped PVDF-Cellulose Composites Prepared by Different Precipitation Methods Hüseyin GÜMÜŞ*	160-170
Deep Learning-Based Automated Garbage Image Classification Using Light-Weight Models Gözde YOLCU ÖZTEL*	171-181
Prioritization of Renewable Energy Resources Using Intuitionistic Fuzzy AHP and VIKOR Methods: TR33 Region Example Bahadır YÖRÜR*, Emir AY, Nutiye ŞENTÜRK, Hilem ORMAN, Simge Hilal İVACIK	182-199
REVIEW ARTICLE	
A-to-I Editing Technologies: Unlocking New Avenues in Cancer Therapy Hasret TÜRKMEN*, Nefise DEMİR, Mustafa ŞEN, Mustafa CAN	200-216



Contents lists available at Dergipark

Journal of Scientific Reports-A

journal homepage: https://dergipark.org.tr/tr/pub/jsr-a



E-ISSN: 2687-6167 Number 62, September 2025

RESEARCH ARTICLE

Investigation of the antimicrobial effects of niclosamide, furosemide and nifedipine drugs released from a modified hydrogel structure

Mukaddes Keskinates^{a*}, Bahar Yılmaz^b, Mevlüt Bayrakcı^c

- ^aKaramanoglu Mehmetbey University, Kazım Karabekir Vocational School, Department of Environmental Protection Technologies, Karaman 70100, Türkiye, ORCID: 000-0002-1799-7180
- ^bKaramanoglu Mehmetbey University, Faculty of Engineering, Department of Bioengineering, Karaman, 70100, Türkiye, ORCID: 000-0002-6315-3018
- ^cKaramanoglu Mehmetbey University, Faculty of Engineering, Department of Bioengineering, Karaman, 70100, Türkiye, ORCID: 000-0002-1416-2870

Abstract

HEMA-based hydrogels were also developed and they were characterized for a few drugs including nifedipine, furosemide and niclosamide. The HEMA hydrogels were synthesized by functionalizing with methacrylated β -cyclodextrin monomer and then were tested in drug release studies. Antimicrobial study against bacteria: The pathogen was studied using disc diffusion and microdilution methods for the drug released from HEMA-based hydrogels. The hydrogel synthesized was found to have a very high capacity for absorption of water and it was also found that depending on this, the potential of drug absorption was also very high. In vitro, cumulative drug release studies on nifedipine, furosemide and niclosamide were carried out using hydrogel under various time and pH conditions. The released drug was adjustable as we obtained data on drug release profiles. Nifedipine, furosemide and niclosamide release percentages were $68.9\pm3.8\%$, $75.2\pm3.6\%$ and $58.7\pm4.2\%$, respectively. Additionally, all three drugs exhibited marked activity against bacteria. These findings indicate that the synthesized hydrogels are a promising basis for bio-medical applications.

© 2023 DPU All rights reserved.

Keywords: Methacrylated β-Cyclodextrin; Niclosamide; Furosemide; Nifedipine; Antimicrobial activity

1. Introduction

Recently, the field of biomaterials has been drawing more and more attention in the research community. This process has been followed by an increase in research activities concerning drug delivery systems which are a successful method in the application of biomedical drugs [1, 2]. Drug delivery means that the active substance is released from the system in a controlled manner, at a desired time, with a certain velocity and a certain amount [3]. There are two main components in drug delivery: the active substance and the polymeric support material. Support

material controls the release of active substances. When a polymer (either natural or synthetic) is used in drug delivery, the active substance is released as planned [4,5]. Typically, in drug delivery systems, three-dimensional, network-structured, and cross-linked hydrogels are used [6]. Hydrogels are highly hydrophilic polymers that can swell significantly in water without dissolving, and they are flexible with high mechanical stability [7]. The degree of hydrophilicity of hydrogels depends on the presence of polar groups in their structure, and due to the advantages, they provide, they show excellent biocompatibility [8, 9]. Hydrogels are three-dimensional hydrophilic structures with the ability to adsorb large amounts of water. Because of their variable network structure, high water content, and soft texture, they are used not only in drug delivery systems but also as biomaterials [10]. These structures, in their hydrated form, have mechanical properties and water content similar to those of soft tissues, which is why they exhibit high biocompatibility. Hydrogels also exhibit swelling behavior depending on the external environment [11, 12].

Antimicrobial studies play a crucial role in drug delivery systems. These studies are essential in the fight against various infectious diseases. However, there are challenges such as bacterial resistance and some side effects with current treatment options [13,14]. In the treatment of such pathologies, the choice and application of drugs with various mechanisms of action become crucial in developing effective options [15, 16]. Niclosamide, nifedipine, and furosemide have the most pronounced and positive action in this respect [17, 18].

The current study focused on the encapsulation, protection, and release of such drugs using HEMA-based hydrogels [19,20]. It also provided an in-depth discussion on the release patterns of these antimicrobial agents. Nifedipine, niclosamide and furosemide are broad-spectrum drugs. These drugs are widely used in the treatment of bacterial and antimicrobial infections [21, 22]. HEMA-based hydrogels improved the effectiveness of these drugs, controlled the release, and ensured more reliable and successful treatments. [23, 24] Antimicrobial effectiveness of these drugs was fully investigated in this study to determine their effectiveness [25]. Results obtained will be helpful in supporting the future clinical application of these drug molecules.

2. Experimental

2.1. Materials

All chemical utilized in the research was acquired from Sigma-Aldrich and Merck. In the trials, purchased substances were utilized as such.

2.2. Synthesis process for preparing HEMA-based hydrogels with GMA-bound β-cyclodextrin monomer

HEMA was mixed with the prepared monomer and subjected to polymerisation to form gels. Two hydrogels were prepared for each drug. Then, two more hydrogels were prepared to provide negative and positive control groups. GMA-bound β-cyclodextrin was dissolved in 5 mL of pure water and mixed with HEMA polymer. MBAAm crosslinker was dissolved in 10 mL of pure water in another beaker. The two solutions obtained were mixed and the mixture was placed in an ice bath for 10 minutes and transferred to the mixer. APS was then added to the mixture in the ice bath to act as a radical initiator. TEMED was added to this mixture to accelerate polymerization. The resulting mixture was then transferred to empty containers, making sure that no air bubbles remained. The empty containers were placed in the freezer to remain in this bath. These containers were placed in a freezer at -20°C and kept there for 24 hours. After 24 hours, it was removed from -20 °C. It was left at room conditions for approximately 2 hours to replace the ice crystals in the voids in the hydrogel with empty compartments. The resulting hydrogel was washed with pure water to ensure the adhesion of the drugs to be immobilized [26].

2.3. FT-IR analysis

FT-IR spectroscopy was used to investigate the structure of drug-doped HEMA hydrogels and pure 2-hydroxyethyl

methacrylate (HEMA). The Fourier transform infrared spectra were measured between 4000 and 400 cm⁻¹ using a Bruker Vertex 70 ATR-FTIR spectrophotometer [17, 27].

2.4. Morphological studies

The structural nature of the GMA-bound β -CD doped HEMA hydrogel was examined using scanning electron microscopy and the results are presented. The SEM images of the GMA-bonded β -CD doped HEMA hydrogel samples coated with 5 nm gold (Au) were examined at approximately 1 μ m [27].

2.5. Swelling measurement

Free hydrogels' equilibrium swelling (ES) was determined in distilled water and different buffer solutions. The maximum swelling of HEMA hydrogels was used to calculate the ES ratio. For this, they were put in 50 mL of the solution prepared at 25 °C for 20 hours. The equilibrium swelling percentage was computed using the following formula, as shown in Equation (1).

$$ES = W2 - W1/W1 \otimes 100 \tag{1}$$

According to this formula, W1 is the initial weight of the prepared hydrogels after drying, and W2 is the weight of the prepared hydrogels after swelling for 20 h. The swelling capacities of all prepared hydrogels were obtained using different pH buffers. The pH values of these buffers were calculated as 2, 4, 7, 9 and 12. Three or four repetitions of each experiment were performed [27].

2.6. Antimicrobial activity test method

2.6.1. MIC dilution

The broth microdilution method determined the antibacterial activity of the drugs used in the study. In the antibacterial test, different concentrations of these drugs (0.1-10 mg/ml) were used to determine the minimum inhibitory concentration (MIC) values on *Staphylococcus aureus* and *Pseudomonas aeruginosa* bacteria. In this investigation, buffer solution was used to replace the negative control, and chloramphenicol was used to replace the positive control. The lowest drug concentration that inhibited bacterial growth was calculated and reported as the MIC [28].

2.6.2. DISC diffusion

In this study, an agar diffusion test was conducted to test the antimicrobial activity of the drug-loaded hydrogel disks. During the test, 1-1.5 mm-thick hydrogel samples for each group were positioned on agar plates, to which 0.1 ml cultures of *Staphylococcus aureus* ATCC 25923 and *Pseudomonas aeruginosa* ATCC 10145 bacteria were added. This subject was focused on because drug-loaded hydrogel systems play a very important role in developing effective antimicrobial agents. The present study was performed to investigate the antimicrobial efficacy of 2-hydroxyethyl methacrylate (HEMA) hydrogel discs eluted by different drug solutions. The incubation of the tests was performed at 37 °C after 24 hours, and then measurements were taken around each specimen on the created areas of inhibition. Therein obtaining the numerical quantitative values of such activity. The prepared hydrogel disks were loaded with drug solution concentrations of 6, 12, 18, 30 and 50 mg/g HEMA hydrogel disk structure, respectively. In such a way that the influence of different drug loading could be investigated on the antimicrobial activities of the prepared drugloaded discs. Drug-free hydrogel discs were used as a control, which exhibited no inhibition, proving the inhibition

by the drug effect alone. To enhance the reliability of the experiments, all the tests were repeated three times, and their average results were statistically accurate. It is a very strict method that gives scientific validity to the obtained results and reproducibility. These results demonstrated that the antimicrobial properties of HEMA-based drug delivery systems can be improved and were a very important step towards improving the usability of the systems discussed in clinical applications, including the treatment of wound healing and infections. This research provides an important basis for improving drug delivery formulations [29].

3. Results and discussion

3.1. Nuclear Magnetic Resonance Spectroscopy analysis

Figure 1 shows the proton from the methacrylate group, a part of GMA, around 6.2 ppm. This signal is due to the vinyl protons of the methacrylate group of GMA. The chemical shift at approximately 6.2 ppm is characteristic for protons attached to a carbon-carbon double bond, confirming the presence of the methacrylate functionality in the GMA- β -CD complex. Methyl protons-CH₃ are detected at about 1.8 ppm. This signal points to protons on a methyl group, which is part of the GMA structure. A chemical shift value of about 1.8 ppm may be indicative of a methyl substitution in a relatively electron-rich environment, such as that linked to the methacrylate part of GMA. It has been proved from the 1H-NMR spectra that GMA- β -CD forms with its molecular structure, one GMA molecule covalently attached to the β -CD through a methacrylate group. The complexation so formed will further confirm the hypothesis on successful synthesis that could be further characterized or used for various applications involving drug delivery or material science [30, 31].

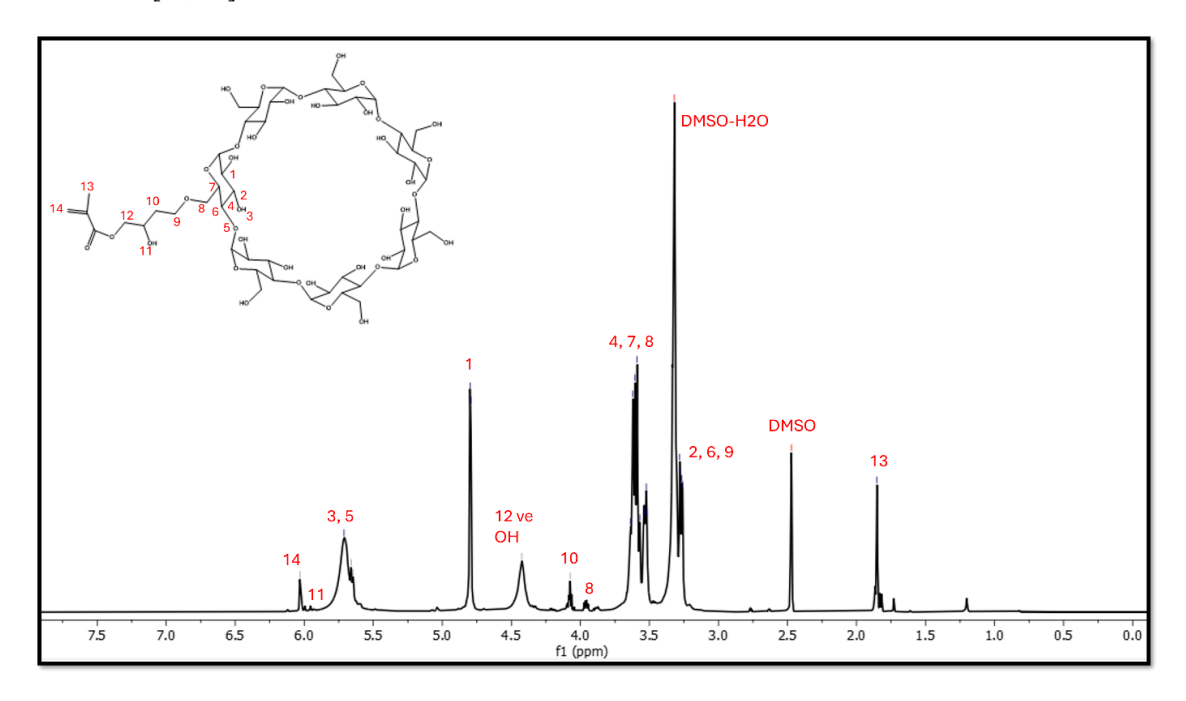


Fig. 1. NMR Graph of the synthesized GMA+ β -CD monomer

3.2. Fourier-transform infrared spectroscopy analysis

The distinctive spectra of the β-CD monomer attached to GMA were visible in the acquired FTIR spectrum. Figure 2 shows that the stretching vibrations of the carbonyl group (C=O) and the double bond C=C of the methacrylate structures are observed in the HEMA spectrum at about 1716 cm-1 and 1633 cm-1, respectively. In the β-CD spectrum, the vibrations of C-O-C (ether group) and -OH (hydroxyl group) were found between 1000-1200 cm⁻¹ and 3300-3500 cm⁻¹. The interactions between β-CD and HEMA, which indicate cross-linking, appeared as changes in the 1100-1300 cm⁻¹ range. This suggests that HEMA and β-CD have successfully bonded to form a network structure. The FTIR spectra of the drugs also showed characteristic peaks for functional groups. For nifedipine, peaks for C=O and -NO₂ groups appeared at about 1740 cm⁻¹ and 1320 cm⁻¹, respectively. Niclosamide exhibited peaks for amide groups and aromatic rings at approximately 1630 cm⁻¹ and 1650 cm⁻¹, while furosemide had peaks for carbonyl groups and sulfonamide at about 1300 cm⁻¹ and 1650 cm⁻¹. The shifting, broadening, or disappearance of some peaks in the FTIR spectra of the drugs indicates the interaction between the drugs and the HEMA-β-CD hydrogel network. Of importance are changes in the -OH peaks, which may indicate interactions between the drugs and the hydroxyl groups in the network. These results show that the pharmaceuticals under investigation have been successfully added to the β-CD-HEMA and GMA-β-CD-HEMA hydrogels and that the drug release properties of the hydrogel may be influenced by these copolymer structures. The effective preparation of HEMA-based hydrogels made with GMAcoupled β-CD interacting with the drugs under study was confirmed by the resulting FTIR spectra. Drugs are absorbed into the network, as indicated by changes in their FTIR peaks, which may impact regulated release. The study constitutes an important step in designing drug delivery systems and in understanding the interaction of drugs with hydrogel matrices [5, 17].

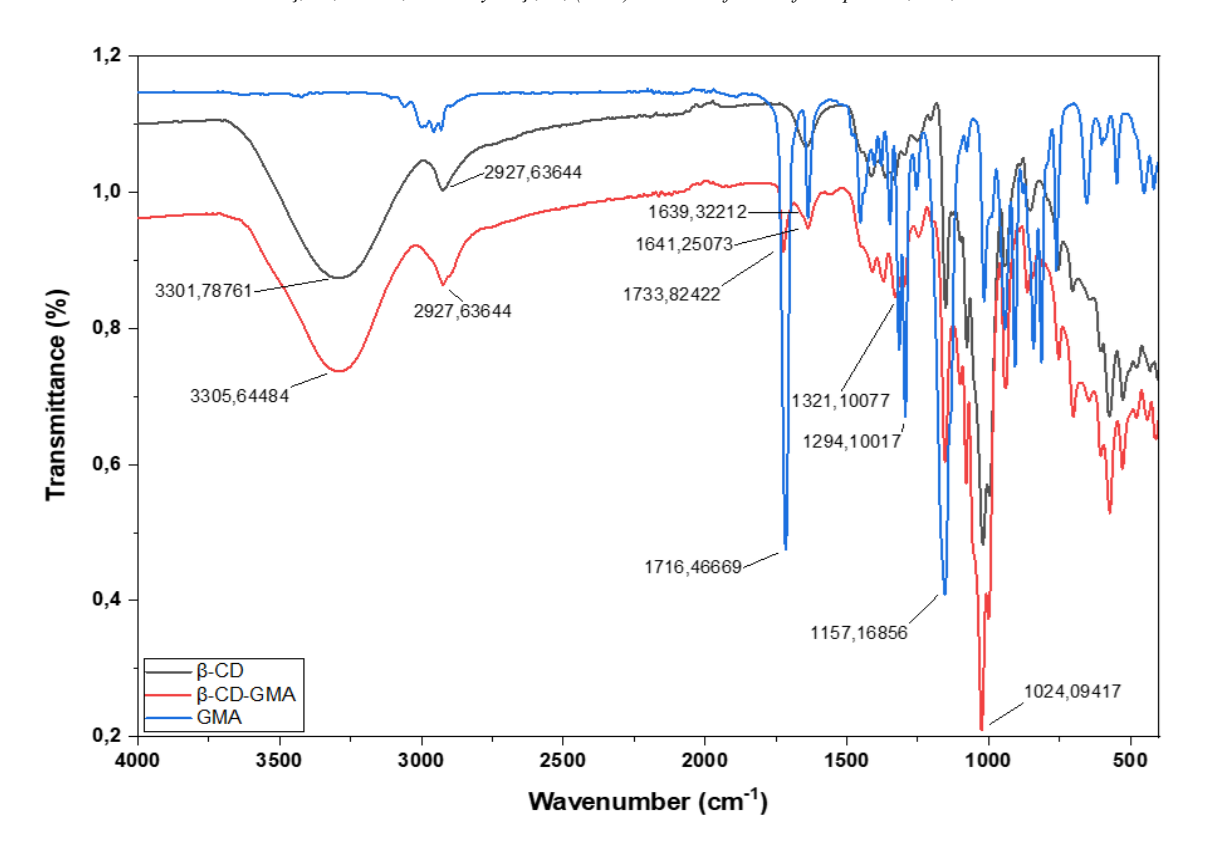


Fig. 2. FTIR spectra of the obtained HEMA+GMA+β-CD hydrogel

3.3. Scanning electron microscope analysis

Figure 3 shows SEM images of the surface, pore structure, and network in HEMA hydrogels modified with methacrylated GMA+ β -CD monomer. The homogenous and consistent nature of the pores is critical for drug transport to be supported, as is their controlled release in these hydrogels. The images show that the methacrylate samples exhibit a sharply curved structure. At the same time, the pronounced hollow structure helps the medicines to be transported easily. The smooth surface and continuous network structure may help improve hydrogel efficacy and stability for biomedical applications. The SEM images show that the HEMA hydrogels made of copolymer with GMA-bonded β -CD were effectively created and have the appropriate properties [17].

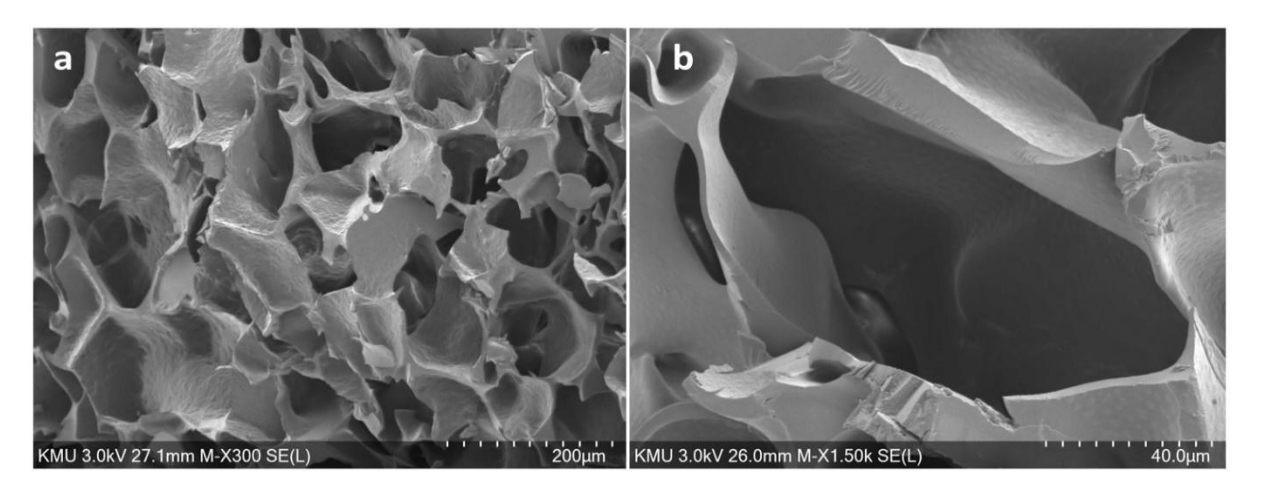


Fig. 3. SEM images of produced GMA-bound β-CD HEMA hydrogel (a) 200 μm (b) 40.0 μm size

3.4. Hydrogel's swelling and cumulative release

The swelling behaviour of HEMA hydrogels copolymerized with GMA-bound β -CD was studied in different buffers with pH values of 2, 4, 7, 9, and 12, and the results are shown in Figure 4. The hydrogel absorbed the most water at pH 7. The swelling of the hydrogel depends on the pH of the surrounding solution, with higher pH values generally leading to more swelling. However, when the pH went above 7, the swelling ratio of the HEMA hydrogel decreased. This is because the hydrogen bonds between the oxygen atoms in the ether groups and the carboxylic acid groups of MBA were broken, causing MBA's carboxyl groups to ionize. Since the ideal pH for the hydrogel is around 7, it does not cause any issues for its biological properties. Drug release from hydrogel was achieved using the homogeneous matrices technique in Diffusion-Based Matrix Systems. The release of drugs was rapid in the first hours, then slowed down over the next 10 hours and finally stabilized (Figure 4). After 10 hours, the release percentages of nifedipine, furosemide and niclosamide were $68.9 \pm 3.8\%$, $75.2 \pm 3.6\%$ and $58.7 \pm 4.2\%$, respectively [27].

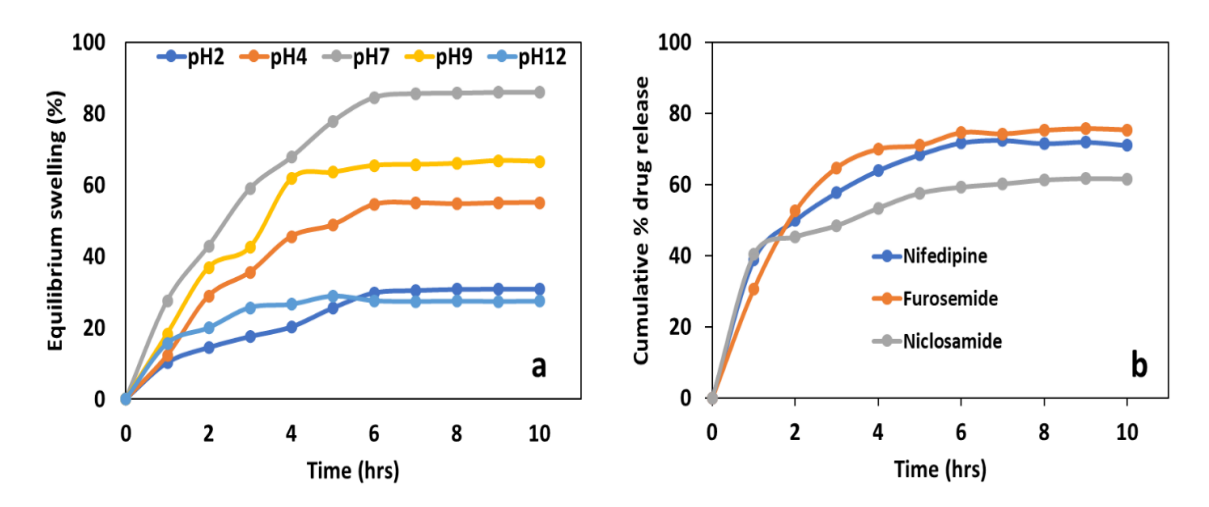


Fig. 4. As time depends, (a) Equilibrium swelling behaviour of hydrogels at different pHs (b) Total drug release from HEMA hydrogel

3.5. Results of antimicrobial tests

3.5.1. Minimum inhibitory concentration dilution

MIC dilution test was used to determine the smallest concentration of drugs needed to stop bacterial growth. The findings indicate that GMA-linked β -CD monomer-based hydrogels based on HEMA can be a useful material for antimicrobial drug testing (Figure 5). The low MIC values obtained from niclosamide among the tested drugs indicate that it is a potent antimicrobial agent. It thus infers that the drug has retained its effectiveness even upon loading into the hydrogel. Niclosamide maintains its antimicrobial property during effective transport and release by the hydrogels. It provides evidence that HEMA hydrogels are to be exploited in drug release applications as well as in assessing the effectiveness of anti-microbial drugs. Therefore, such information leads to the use of the hydrogel system towards assessing other varieties of drugs besides drug delivery mechanisms and methodologies improvement.

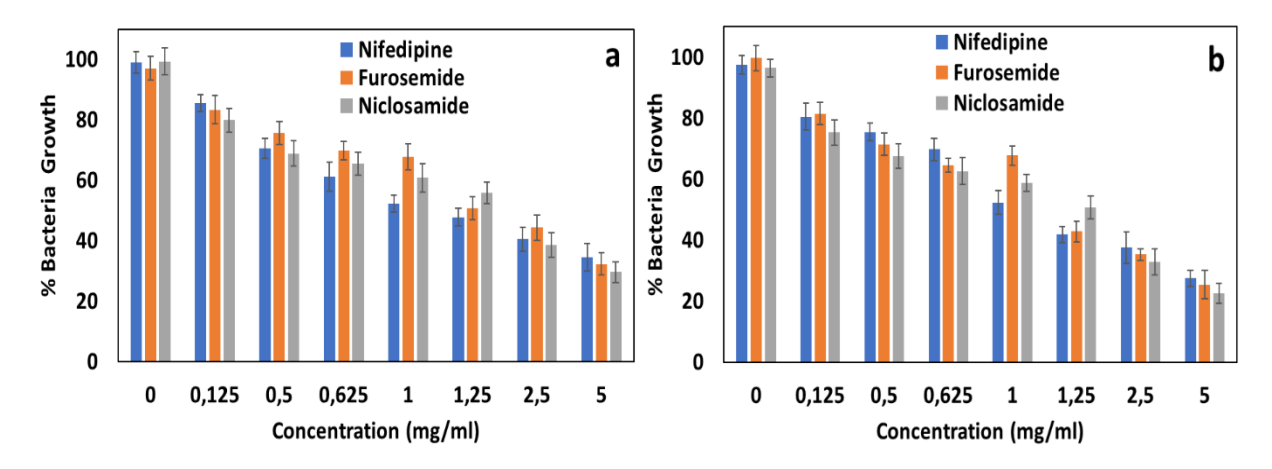


Fig. 5. The lowest amount of drug that inhibits bacterial cultures when removed from the HEMA hydrogel and administered to bacteria of (a)

*Pseudomonas aeruginosa (P A) and (b) Staphylococcus aureus (S A)

3.5.2. Disc diffusion

Antimicrobial activity testing of drug-loaded hydrogel samples was done using a disk diffusion method. To this end, hydrogels at five different drug concentrations, such as 6, 12, 18, 30, and 50 mg/g polymer, were prepared. The measured diameter of the inhibition zone in Figure 6 has been presented. After incubation for 24 hours, the drug-loaded hydrogels showed clear antimicrobial effects. Figure 5 shows the lowest amounts of drug that inhibited the growth of Pseudomonas aeruginosa and Staphylococcus aureus bacterial cultures upon release in the hydrogels. Activity was concentration-dependent and depended on the type of microorganism. In particular, the inhibition zones were larger for the Gram-negative *P. aeruginosa* compared to the Gram-positive *S. aureus*. Niclosamide was found to exhibit enhanced antimicrobial activity when released from a HEMA hydrogel matrix containing methacrylated β -CD. The diameters of the inhibition zones emphasize that niclosamide is active against both bacteria. Interestingly, hydrogel molds with drug concentrations of 30-50 mg showed similar results to hydrogels with drug concentrations of 6-18 mg. Larger inhibition zones were the outcome of lower medication concentrations.

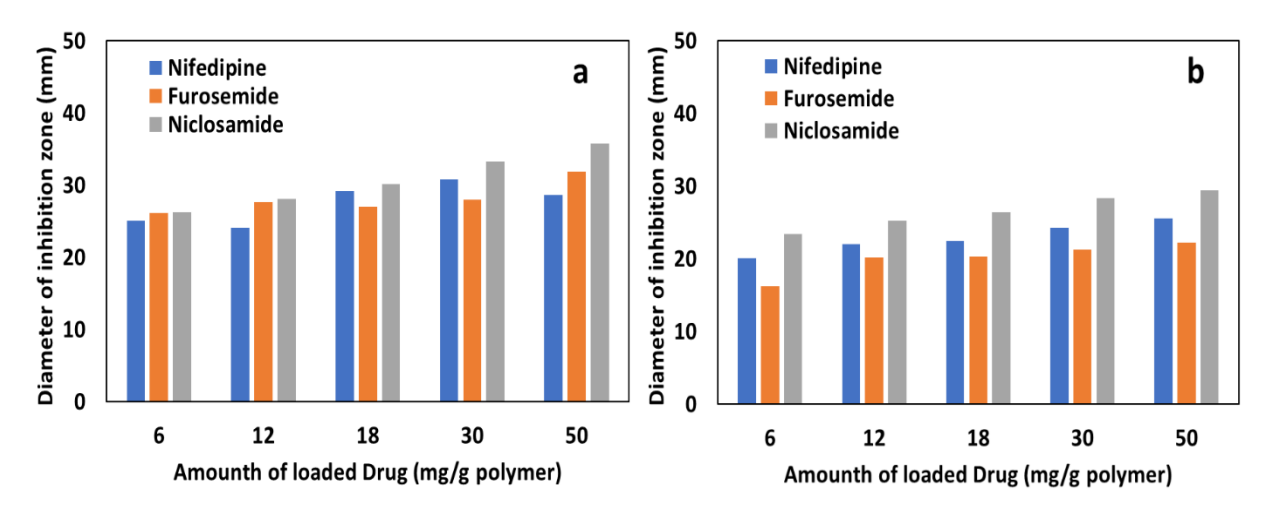


Fig. 6. pHEMA hydrogel disks' inhibition zone diameters with bacterial cultures (37°C, 24 hours) (a) *Staphylococcus aureus* (S A) and (b) *Pseudomonas aeruginosa* (P A)

4. Conclusion

In this study, HEMA-based hydrogels were prepared and the hydrogels were functionalized with GMA-linked βcyclodextrin monomer. The drug release profiles of the developed hydrogels were assessed for drugs like nifedipine, niclosamide and furosemide and the outcomes were stated. The potency of the drug molecules that are released was assessed on the antibacterial activity against the Gram-positive and Gram-negative bacteria by the disk diffusion and microdilution methods. The findings show that they will provide significant benefits for such studies. From these data, it is also seen that these hydrogels will be highly useful as drug delivery systems. Especially, it has been observed that these hydrogels have high drug carrying capacity and hence are effective in infection therapy. The research also found that the hydrogels that were prepared from the combination of HEMA and β-CD effectively controlled the drug release and produced favourable results. The drug release profiles of nifedipine, niclosamide, and furosemide from the gels also presented pH and time-dependent release profiles. This indicates that the embedding of GAM-linked β-CD into the HEMA network is capable of delivering the drug in a controlled and specific manner. Thus, the drug release can be constant and extended during the whole period of treatment. This may enable better control of the dosage. The assay of the antimicrobial test has revealed that the drug molecules have an excellent antibacterial effect against the indicated bacterial strains, especially niclosamide shows high antibacterial activity against the Gram-negative bacteria. It has been noticed that the HEMA-based hydrogels synthesized in the present work with methacrylated β-CD have high potential and offer strong evidence for their use in various biomedical applications. In addition, these hydrogels can be applied in various fields with their remarkable ability to absorb water and release drugs. Future studies will examine the interactions of these hydrogels with different drugs and biological systems and create new opportunities for clinical research.

Appendix A.

This study is presented as a part of Mukaddes Keskinates' doctoral thesis. Conflict of Interest The authors declare that they have no conflict of interest.

Acknowlegde

The author is very grateful to Karamanoglu Mehmetbey University for their support during the data collection for this current work.

Author Contribution

All authors contributed to the conceptualization and design of the study. Material preparation, method research and implementation, data collection and analysis were carried out by Mukaddes Keskinates. Bahar Yılmaz played an important role in research, methodology, data editing, writing the original draft and verification. Mevlüt Bayrakcı contributed as a supervisor to research, methodology, data editing, writing the original draft and verification. All authors read and approved the final draft.

References

- [1] M. Berthet and J. Durand, "Controlled release of drugs from hydrogels: A review of recent developments and applications", *J. Control. Release*, 284, 1-14. 2018, doi: 10.1016/j.jconrel.2018.06.005
- [2] H. Santos and F. Azevedo, "Development and evaluation of novel HEMA-based hydrogels for controlled drug delivery", *Mater. Sci. Eng. C*, 104, 109974. 2019, doi: 10.1016/j.msec.2019.109974
- [3] M. Alsenani, M. Ali, and N. A. Alwabel, "Antibacterial activities of marine macroalgae extracts using the broth microdilution method", *J. Appl. Phycol.*, 32(4), 2291-2300. 2020, doi: 10.1007/s10811-020-02194-0
- [4] L. Cheng and J. Liu, "Development and characterization of HEMA-based hydrogels for controlled drug delivery applications", *J. Biomed. Mater. Res. Part A*, 109 5 800-812 2021, doi: 10.1002/jbm.a.36987
- [5] B. Y. Altınok, M. Keskinateş, and M. Bayrakci, "Metal chelate for protein adsorption studies pHEMA-GMA column filling materials including groups preparation", Niğde Ö. H. Univ. J. Eng. Sci., 13 2 1-1 2024, doi: 10.28948-ngumuh.1382364-3501433
- [6] Furosemide, "In The Merck Index Online", Merck Index Online, 2022, Retrieved from https://www.rsc.org/Merck-Index
- [7] R. Kumar and A. Arora, "Evaluation of the antimicrobial efficacy of nifedipine and its potential therapeutic uses", *J. Antimicrob. Chemother.*, 72 5 1326-1331 2017, doi: 10.1093/jac/dkx020
- [8] N. Mahmood and R. Raza, "Controlled release and antimicrobial efficacy of furosemide in HEMA-based hydrogels", Int. J. Pharm., 552 1-2 1-
- 10 2018, doi: 10.1016/j.ijpharm.2018.09.031 [9] A. Alvarez-Lueje and S. Scheel, "Synthesis and characterization of methacrylated β-cyclodextrin for drug delivery applications", *Eur. J. Pharm.*
- Biopharm., 142 311-319 2019, doi:10.1016/j.ejpb.2019.07.017 [10] Y. Feng and H. Wang, "Release kinetics and antimicrobial properties of nifedipine-loaded hydrogels", Eur. J. Pharm. Sci., 137 104967 2019, doi:10.1016/j.ejps.2019.104967
- [11] E. Armagan, M. Keskinates, N. E. Gumus, Z. Aydin, B. Yilmaz, and M. Bayrakci, "Macroalgal (Ulva compressa) Silver Nanoparticles: Their Characterization, Cytotoxicity, and Antibacterial Applications", *Turk. J. Fish. Aquat. Sci.*, 24 9 2024, doi: 10.4194/TRJFAS25612
- [12] S. Lu and K. S. Anseth, "Photopolymerization of multilaminated poly (HEMA) hydrogels for controlled release", *J. Control. Release*, 57 3 291-300 1999, doi:10.1016/S0168-3659(98)00125-4
- [13] H. Yuan and Q. Zhang, "Antimicrobial activity of drug-loaded hydrogels: A review of current research", J. Control. Release, 270 15-28 2018, doi:10.1016/j.iconrel.2018.01.019
- [14] Niclosamide, "In Drug Information Portal", U.S. Natl. Libr. Med., 2021, Retrieved from
- [15] R. Santos and A. Oliveira, "Antimicrobial activity of hydrogels containing β-cyclodextrin and its applications in controlled drug delivery", J. Drug Deliv. Sci., Technol. 56 101431 2020, doi:10.1016/j.jddst.2020.101431
- [16] T. Nguyen and P. Tran, "Synthesis and evaluation of methacrylated β -cyclodextrin for use in hydrogels and drug delivery systems", *Mater. Sci. Eng. C*, 101 154-165 2019, doi:10.1016/j.msec.2019.04.067
- [17] M. Bayrakci, M. Keskinates, and B. Yilmaz, "Antibacterial, thermal decomposition and in vitro time release studies of chloramphenicol from novel PLA and PVA nanofiber mats", *Mater. Sci. Eng. C*, 122 111895 2021, doi:10.1016/j.msec.2021.111895
- [18] P. Patel and R. Patel, "Pharmacokinetics and release characteristics of furosemide from polymer-based hydrogels", *J. Drug Deliv. Sci. Technol.*, 36 58-64 2016, doi:10.1016/j.jddst.2016.08.005
- [19] K. Ozturk and S. Kan, "Antimicrobial activity of methacrylated β-cyclodextrin and its applications in drug delivery systems", *Int. J. Pharm.*, 587 119682 2020, doi:10.1016/j.ijpharm.2020.119682
- [20] N. Eczacioglu, B. Yilmaz, Y. Ulusu, and M. Bayrakci, "Recovery and reusability of apounag fluorescence protein from the unconjugated bilirubin complex structure", *J. Fluoresc.*, 30(3) 497-503 2020, doi:10.1007/s10895-020-02519-w
- [21] B. Yilmaz, N. Aydin, and M. Bayrakci, "Pesticide binding and urea-induced controlled release applications with calixarene naphthalimide molecules by host–guest complexation", *J. Environ. Sci. Health*, Part B 53(10) 669-676 2018, doi:10.1080/03601234.2018.1474557
- [22] H. B. Keskinkaya, E. Deveci, B. Y. Altınok, N. E. Gümüş, E. Ş. O. Aslan, C. Akköz, and S. Karakurt, "HPLC-UV analysis of phenolic compounds and biological activities of Padina pavonica and Zanardinia typus marine macroalgae species", *Turk. J. Bot.*, 47(3) 231-243 2023,

- doi:10.55730/1300-008X.2761
- [23] N. A. Peppas, P. Bures, W. S. Leobandung, and H. Ichikawa, "Hydrogels in pharmaceutical formulations", *Eur. J. Pharm. Biopharm.*, 50(1) 27-46 2000, doi:10.1016/S0939-6411(00)00090-4
- [24] C. Miller and M. Martin, "The role of β -cyclodextrin in modifying drug release profiles from hydrogels", *Adv. Drug Deliv. Rev.*, 174 77-88 2022, doi:10.1016/j.addr.2021.12.003
- [25] X. Zhao and X. Zhang, "Antibacterial properties of drug-loaded hydrogels: A review", Adv. Drug Deliv. Rev., 127 32-49 2018, doi:10.1016/j.addr.2018.05.001
- [26] P. Kumar and S. Sharma, "Antimicrobial activity of niklosamide and its implications for drug delivery systems", *J. Antimicrob. Chemother.*, 75(8) 2155-2161 2020, doi:10.1093/jac/dkaa215
- [27] B. Yilmaz, "Release of nifedipine, furosemide, and niclosamide drugs from the biocompatible poly (HEMA) hydrogel structures", *Turk. J. Chem.*, 46(5) 1710-1722 2022, doi:10.55730/1300-0527.3474
- [28] R. Bayat, M. Akin, B. Yilmaz, M. Bekmezci, M. Bayrakci, and F. Sen, "Biogenic platinum based nanoparticles: Synthesis, characterization and their applications for cell cytotoxic, antibacterial effect, and direct alcohol fuel cells", *Chem. Eng. J. Adv.*, 14 100471 2023, doi:10.1016/j.ceja.2023.100471
- [29] F. Ayhan and S. Özkan, "Gentamicin release from photopolymerized PEG diacrylate and pHEMA hydrogel discs and their in vitro antimicrobial activities", *Drug Deliv.*, 14(7) 433-439 2007, doi:10.1080/10717540701202911
- [30] H. Ahmadi, M. Javanbakht, B. Akbari-Adergani, and M. Shabanian, "Photo-grafting of β-cyclodextrin onto the polyethersulfone microfiltration-membrane: Fast surface hydrophilicity improvement and continuous phthalate ester removal", *J. Appl. Polym. Sci.*, 136(24) 47632 2019, doi:10.1002/app.47632
- [31] Y. Liu, Z. Fan, H. Y. Zhang, Y. W. Yang, F. Ding, S. X. Liu, ... and Y. Inoue, "Supramolecular self-assemblies of β-cyclodextrins with aromatic tethers: factors governing the helical columnar versus linear channel superstructures", *J. Org. Chem.*, 68(22) 8345-8352 2003, doi:10.1021/jo034632q
- [32] C. P. Okoli, G. O. Adewuyi, Q. Zhang, P. N. Diagboya, and Q. Guo, "Mechanism of dialkyl phthalates removal from aqueous solution using γ-cyclodextrin and starch based polyurethane polymer adsorbents", *Carbohydr. Polym.*, 2014, 114 440-449
- [33] Y. C. Chung and C. Y. Chen, "Competitive adsorption of a phthalate esters mixture by chitosan bead and α-cyclodextrin-linked chitosan bead", *Environ. Technol.*, 30(13) 1343-1350 2009, doi:10.1080/09593330902858914



Contents lists available at Dergipark

Journal of Scientific Reports-A

journal homepage: https://dergipark.org.tr/tr/pub/jsr-a



E-ISSN: 2687-6167

Number 62, September 2025

RESEARCH ARTICLE

Receive Date: 30.04.2025 Accepted Date: 11.09.2025

Prediction of the earthquake magnitudes with A new estimator via sub-sampling method

Ceren Ünala*, Gamze Özelb

^aHacettepe University Department of Statistics, , 06800, Ankara, Türkiye, ORCID: 0000-0002-9357-1771 ^bHacettepe University, Department of Statistics, 06800, Ankara, Türkiye, ORCID: 0000-0003-3886-3074

Abstract

Türkiye is situated on active fault lines, where significant tectonic movements occur, resulting in earthquakes, and is located in one of the world's most active earthquake zones, the Alpine-Himalayan seismic belt. We propose an estimator to examine the population mean of the earthquake magnitude using the information of the largest aftershocks among aftershocks via the subsampling method under the non-response scheme. The proposed estimator is obtained and the expressions for the bias, mean square error (MSE) and minimum mean square error are also derived to the first order of approximation. We evaluate earthquakes in the Aegean Region of Türkiye between the years 1900 - 2021mbased on different scenarios within the dataset. The results show that the estimation of the population mean is the perfect fit for the real earthquake magnitude population mean via the proposed estimator. By analyzing earthquake data from Türkiye, we successfully highlighted the practical significance and applicability of our proposed estimator in a real-world scenario.

© 2023 DPU All rights reserved.

Keywords: Aftershock; Earthquake; Sub-sampling Method; Population Mean Estimator.

1. Introduction

Earthquakes are natural disasters that can cause sudden and extensive devastation, having a detrimental impact on the lives and property of thousands of people in Türkiye and around the world. Türkiye is located in one of the world's most active earthquake zones, the Alpine-Himalayan seismic belt. Approximately 42% of its land area falls within the first-degree earthquake hazard. Most of Türkiye sits on the Anatolian tectonic plate, which is located between the Eurasian and African plates, as well as the Arabian plate [1,2, Fig. 1]. Consequently, Türkiye lies on multiple fault lines. Examining Türkiye's earthquake history reveals that numerous destructive earthquakes have taken place over time [3]. Türkiye's western provinces, particularly the Marmara Region, are highly prone to earthquakes. The North Anatolian Fault Zone (NAFZ), which runs alongside the Marmara Sea (Fig. 1), is an active fault line capable of

generating major earthquakes [4]. Western Türkiye's commercial areas encompass large cities and industrial centres with dense populations and significant economic importance. Cities such as Istanbul, Bursa, İzmir, and Ankara are major trade hubs. These areas experience intense tourism, commercial, and industrial activities. However, it is important to analyse these areas in terms of earthquake risk because earthquakes can affect commercial activities. A large-scale earthquake could damage infrastructure and buildings thereby negatively impacting trade and the economy [5].

On 17 August 1999, a magnitude 7.4 earthquake struck the Marmara Region, resulting in an estimated death toll of over 17,000 people [6, 7]. Cities like Istanbul, Sakarya, and Gölcük suffered significant damage, with thousands of buildings collapsing or sustaining severe damage. On 12 November 1999, a 7.2-magnitude earthquake occurred in Düzce, causing around 900 deaths and 3000 injuries [8]. Many buildings collapsed or sustained damage in Düzce, Sakarya, Bolu, and the surrounding areas. On 18 March 1953, a 7.4-magnitude earthquake occurred in the Yenice-Gönen region of Balıkesir, causing an estimated death toll of approximately 9670 buildings were heavily damaged and 265 people [9, 10]. On 28 March 1970, the Gediz earthquake occurred on the Erdoğmuş fault in the Gediz district of Kütahya in Western Anatolia, causing around 1086 deaths. [11]. According to the Disaster and Emergency Management Authority (AFAD) [12] in Türkiye, it is crucial to estimate the occurrence of strong earthquakes in the western Türkiye and take the necessary precautions due to the risk of destructive earthquakes [12, 13].

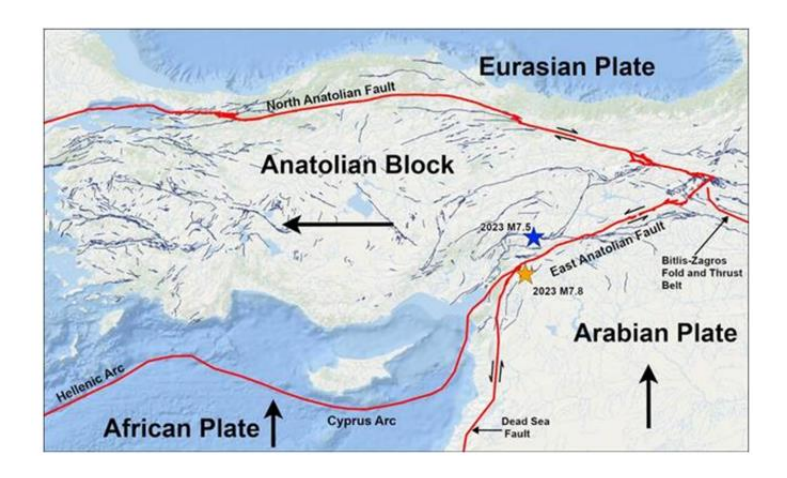


Fig. 1. Geographical location of the study area in the Aegean Region of Türkiye [1, 2].

Earthquakes are one of the most significant natural hazards, particularly in seismically active regions such as Türkiye. The ability to estimate earthquake magnitudes accurately is crucial for hazard assessment and mitigation strategies. There are many studies in the literature based on the statistical models for the earthquake hazard analysis due to the Türkiye's high seismicity. Various statistical models, including Markov chains, Poisson models, and regression-based approaches, have been employed in earthquake forecasting [14]. These approaches can be listed as Markov chains [14, 15] linear models [16], probabilistic assessment of earthquake insurance rates [17], statistical distributions [18, 19, 20, 21] and Poisson approaches [22, 23]. In recent years, estimation methods in sampling theory have become popular for the prediction of earthquake parameters. Earthquake magnitude prediction with sampling involves using a subset of earthquake data to estimate or predict the magnitudes of future earthquakes. The choice of sampling strategy and the specific modelling techniques used can vary depending on the research context and objectives. Different methods such as stratified sampling, simple random sampling, or systematic sampling can be employed to select the subset of earthquakes for prediction purposes [23, 24, 25]. Özel [23] found that the generalized estimators for the earthquake frequency were found suitable to the earthquake catalogues using simple random

sampling design. Sharma et al. [24] and Khare et al. [25] mentioned that the ratio type estimators give us information about the number of aftershocks in a specified region in stratified random sampling. Khare et al. [25] concludes that the proposed estimator performs better as compared to other estimators in the case of earthquake data.

A sampling strategy is devised to select a subset of earthquakes from the catalogue. The sampling strategy can be based on various criteria, such as period, geographic region, magnitude range, or other factors. The goal is to obtain a representative sample that captures the variability of earthquake magnitudes. Estimating the average magnitude helps analyze the overall level of seismic activity in a specific region during the given time period. It provides a summary measure that can be used to assess the typical size or strength of earthquakes occurring within that timeframe. Besides, by estimating the average magnitude, seismic activity across different regions or periods can be compared. This allows for the identification of relative differences in seismicity levels and helps discern any trends or changes in the average magnitude over time. By this way, a comparison and trend identification are done. Furthermore, while the maximum magnitude is crucial for assessing the potential hazard posed by earthquakes, the average magnitude provides additional information about the typical seismic activity in a given region. This information can contribute to probabilistic seismic hazard assessment studies, which consider various factors, including the average magnitude, to estimate the likelihood and impact of future earthquakes. Cataloguing historical data is very important to access earthquake information easily. However, catalogue studies on historical earthquakes in Türkiye are limited. The missing data is a persistent issue in earthquake catalogues due to undetected or unreported seismic events. In the context of earthquake catalogue, there are also many events having no magnitude [26]. For this reason, the nonresponse rate refers to the proportion of earthquakes that are not recorded or reported in the catalogue.

Traditional methods for handling missing data, such as multiple imputations have been widely used [27]. However, these methods often rely on assumptions that may not hold in earthquake data. In contrast, the sub-sampling method, originally introduced by Hansen and Hurwitz [28], provides a practical approach by leveraging auxiliary information to estimate missing values. In this study, we extend the sub-sampling method by introducing a new estimator tailored to non-response schemes in earthquake data. The study aims to address the issue of missing data or non-response in earthquake-related studies and propose a method to estimate the population mean considering this limitation. By utilizing information on earthquake magnitudes and their aftershocks, the researchers seek to provide a new approach for predicting the unknown population mean. Sub-sampling is a statistical method that involves selecting a subset of data from a larger dataset for analysis. It is commonly used when dealing with large datasets or when computational limitations exist. In the context of earthquake magnitude prediction, sub-sampling can be employed to estimate the magnitudes of earthquakes in a specific region or time period. The sub-sampling method typically involves randomly selecting a representative subset of earthquakes from the available dataset. This subset is then used to develop a statistical model or estimator to predict the magnitudes of the entire population of earthquakes. The advantage of subsampling is that it allows for efficient analysis and prediction by reducing the computational burden and focusing on a representative subset of data. However, it is important to note that the accuracy and reliability of the predictions depend on the representativeness of the sub-sample and the quality of the statistical model used. While there may not be a specific study on earthquake magnitude prediction in Türkiye using the sub-sampling method, the general concept of sub-sampling can be applied to various studies in earthquake seismology and statistical analysis. Researchers often employ sub-sampling techniques to study earthquake catalogues, assess seismic hazard, or analyze specific earthquake sequences.

Earthquake catalogues are databases that compile information about earthquakes, including their location, magnitude, depth, and other relevant parameters. The non-response scheme in an earthquake catalogue can arise due to various factors. One common reason is that small or minor earthquakes may go undetected or unnoticed by the monitoring systems. These earthquakes may occur in remote areas with limited or no seismic instrumentation, or they may have magnitudes that are below the detection threshold of the monitoring equipment. Another reason for non-response in earthquake catalogues is incomplete reporting. While seismic monitoring networks strive to capture and report all significant earthquakes, there can be cases where earthquakes are not reported due to technical issues, human error, or delays in data processing and verification. Some earthquakes may be detected by the monitoring system but

not included in the catalogue if they do not meet certain criteria set by the catalogue compilers (e.g., minimum magnitude threshold).

The purpose of the present study is to predict the population mean via a new proposed estimator using information of the earthquake magnitude and their aftershocks under non-response scheme. The outline of this article is organized as follows: In Section 2, motivated by Hansen and Hurwitz [28], we introduce a new ratio type estimator with the exponential function using the information of auxiliary variable (x) under non-response scheme. In Section 3, the study area is defined in detail. After that, the data set is explained in Section 4. In Section 5, using proposed estimator, the estimation of earthquake magnitudes is obtained, and this proposed estimator is compared with main estimators numerically and visually. We conclude the article in Section 6.

2. Methodology

Population parameters such as variance, proportion, and mean can be estimated using samples because populations can be challenging to study directly. Therefore, it is crucial to select an appropriate sampling method to determine the sample. Different types of estimators, including unbiased, exponential, In-type, ratio, product, and regression estimators, have been used to estimate various unknown population parameters [29, 30, 31, 32]. Ratio type estimators are suitable when there is a positive correlation between variables and are often used in agricultural and educational applications [32, 33, 34, 35, 36, 37]. On the other hand, if there is negative correlation, product type estimators are more appropriate for sampling design. Selecting an appropriate sampling method and estimator is crucial for accurately estimating population parameters [38]. Ratio and product type estimators are commonly used, depending on the correlation between variables. The efficiency of an estimator is often assessed using the mean square error (MSE). There are various methods described in the literature to increase efficiency with one of the most common being the utilization of auxiliary variables (x) [31]. In this context, the study variable (y) could be the number of building damage counts in seismology, while the auxiliary variables (x) could be the depth and magnitude of earthquakes, among others. However, it is important to note that in earthquake catalogues, it may not always be possible to have all the necessary information for the variables [39].

Many estimators have been developed assuming that all required information is available in sampling studies. However, in situations where necessary information is missing, non-response rate occurs in the data. In sampling methodology, the non-response rate refers to the proportion of selected individuals or units who do not participate or provide a response to a survey or study. The non-response can occur for various reasons, such as refusal to participate, inability to be reached, or simply not providing a response. In the context of earthquake catalogues, a non-response scheme refers to the methods and strategies used to address and account for the earthquakes that are not detected or recorded by the seismic monitoring network. These schemes are designed to mitigate potential biases and improve the completeness and accuracy of the earthquake catalogue. If the non-response is related to the variables being studied in the earthquake catalogues, it may result in a biased sample that does not accurately represent the target population.

Hansen and Hurwitz [28] introduced a method called sub-sampling. This method addresses the non-response scheme and has led to the development of new estimators to deal with such scenarios. Here, population (N) is composed of response and non-response units. Therefore, this situation is the same for sample (n) as well. At this point, r units, $(r = \frac{n_2}{z}, z > 1)$ information is obtained from non-response units with extra effort in the sample and $(n_1 + r)$ units can be used for estimating the unknown population substituted for sample size n. The appropriateness of the proposed estimator for all combinations can be demonstrated here by obtaining the r units differently using various z values. According to the Hansen and Hurwitz [28] method, the design of non-response scheme is given in Fig. 2.

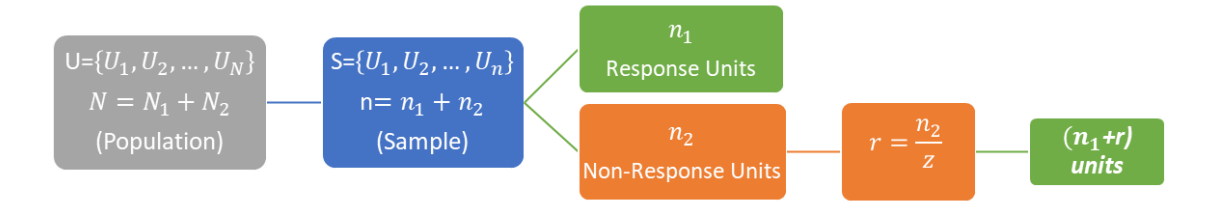


Fig. 2. Non-response scheme design [28].

Hansen and Hurwitz [28] introduced unbiased estimator to estimate the unknown population mean and the estimator is unbiased, the variance of t_{HH} are given as

$$t_{HH} = w_1 \bar{y}_1 + w_2 \bar{y}_{2(r)}, \tag{1}$$

$$V(t_{HH}) = \overline{Y}^{2} \left(\lambda C_{y}^{2} + \frac{W_{2}(z-1)}{n} C_{y(2)}^{2} \right).$$
 (2)

Here, $w_1 = \frac{n_1}{n}$ is the response proportion in the sample. $W_2 = \frac{N_2}{N}$ and $w_2 = \frac{n_2}{n}$ are non-response proportions in the population and sample, respectively. In the context of earthquake sampling, the response unit refers to the unit of main shocks in a sample that are successfully detected, recorded, and included in the earthquake catalogue. The non-response unit in the population refers to the unit of all earthquakes that occur in a given region or time period but are not recorded or detected by the seismic monitoring network. In Eq. (2), \overline{y}_1 and $\overline{y}_{2(r)}$ are the sample means of the auxiliary variable (y) based on response and r units, respectively. The ratio of the size of the sample to that of the population, is called the sampling fraction and is denoted by f and equal to $f = \frac{n}{N}$. $\lambda = \frac{(1-f)}{n}$ is defined as the abbreviation expression. $C_y^2 = \frac{S_y^2}{\bar{Y}_2}$ and $C_{y(2)}^2 = \frac{S_{y(2)}^2}{\bar{Y}_2}$ are the squares of the coefficients of variation based on response and non-response units, respectively, of y_i in the population in case \bar{Y} represents the population mean of y as well [40].

In sub-sampling method, we examine in case non-response exists on both x and y as well and the population mean of x is known. The study variable (y) and the auxiliary variable (x) are symbolized as (y^*) and (x^*) , respectively, in the presence of non-response scheme. Motivated from Hansen and Hurwitz [28], several studies have been done under the non-response scheme. Cochran [40] introduced ratio and regression type estimator under non-response scheme. Singh et al. [41] introduced a new type of estimator using exponential function for estimating the population mean as follows:

$$t_{\exp}^{**} = \overline{y}^* \exp\left(\frac{\overline{X} - \overline{x}^*}{\overline{X} + \overline{x}^*}\right) \tag{3}$$

whose mean square error (MSE) of this estimator is given as

$$MSE\left(t_{\exp}^{**}\right) = \overline{Y}^{2} \left(\lambda C_{y}^{2} + \lambda \frac{C_{x}^{2}}{4} - \lambda C_{yx} + \frac{W_{2}(z-1)}{n} \left(C_{y(2)}^{2} + \frac{C_{x(2)}^{2}}{4} - C_{yx(2)}\right)\right). \tag{4}$$

In Eq. (3), \overline{y}^* and \overline{x}^* refer the sample mean of y and x under the non-response scheme, respectively. \overline{X} is the population means of x. In Eq. (4), $C_{yx} = \rho_{xy}C_yC_x$ and $C_{yx(2)} = \rho_{xy(2)}C_{y(2)}C_{x(2)}$ are relative covariance for response and non-response units, respectively. Here, ρ_{xy} and $\rho_{xy(2)}$ are the correlation coefficients between y and x of the whole population and non-response class [42]. $C_x^2 = \frac{S_x^2}{\bar{X}^2}$ and $C_{x(2)}^2 = \frac{S_{x(2)}^2}{\bar{X}^2}$ are the squares of the coefficients of variation based on response and non-response units, respectively, of x_i in the population in case \bar{X} represents the population mean of x as well [40].

Now, we propose a new estimator by taking the advantage of the exponential function to develop an efficient estimator under the non-response scheme. The proposed estimator, t_{CC2}^* , is given as

$$t_{CC2}^{**} = \overline{y}^* \frac{\overline{X}}{\overline{x}^*} \exp\left[\frac{\overline{X}}{\psi_2 \overline{x}^* + (1 - \psi_2) \overline{X}} - 1\right]$$
 (5)

where ψ_2 represents the chosen constant that makes MSE minimum. To obtain the bias and MSE of t_{CC2}^{**} , $B(t_{CC2}^{**})$, and $MSE(t_{CC2}^{**})$, we can write the formulations, respectively, as

$$B(t_{CC2}^*) = E[t_{CC2}^* - \overline{Y}],$$

$$MSE(t_{CC2}^*) = E[t_{CC2}^* - \overline{Y}]^2.$$

In some cases, an alternative method can be used instead of Taylor series for the theoretical inferences of the estimators since the derivative of the estimator can hardly to computed or may be non-differentiable [31]. Some notations can be defined for this alternative method as

$$e_x^* = \frac{\overline{x}^* - \overline{X}}{\overline{X}}, e_y^* = \frac{\overline{y}^* - \overline{Y}}{\overline{Y}} \ .$$

Using these notations, we define $\overline{x}^* = (\overline{X} + \overline{X}e_x^*)$, $\overline{y}^* = (\overline{Y} + \overline{Y}e_y^*)$. It is clear that

$$E(e_x^*) = 0$$
, $E(e_y^*) = 0$, $E(e_x^2) = \lambda C_x^2$,

$$E\left(e_{x}^{*^{2}}\right) = \lambda C_{x}^{2} + \frac{W_{2}(z-1)}{n}C_{x(2)}^{2}, E\left(e_{y}^{*^{2}}\right) = \lambda C_{y}^{2} + \frac{W_{2}(z-1)}{n}C_{y(2)}^{2},$$

$$E(e_{y}^{*}e_{x}) = \lambda \rho_{xy}C_{y}C_{x}, \quad E(e_{y}^{*}e_{x}^{*}) = \lambda \rho_{xy}C_{y}C_{x} + \frac{W_{2}(z-1)}{n}\rho_{xy(2)}C_{y(2)}C_{x(2)}.$$

Using these equations, the bias $B(t_{CC2}^{**})$ and the MSE of t_{CC2}^{**} , $MSE(t_{CC2}^{**})$, are obtained as

$$B(t_{CC2}^{**}) = \overline{Y}\left(\left(\frac{3\psi_{2}^{2}}{2} + \psi_{2} + 1\right)\left(\lambda C_{x}^{2} + \frac{W_{2}(z-1)}{n}C_{x(2)}^{2}\right) - \left(\lambda C_{yx} + \frac{W_{2}(z-1)}{n}C_{yx(2)}\right)(\psi_{2} + 1)\right),$$
(6)

$$MSE(t_{CC2}^{**}) = \overline{Y}^{2} \left(\lambda \left(C_{y}^{2} + C_{x}^{2} \left(\psi_{2} + 1 \right)^{2} - 2C_{yx} \left(\psi_{2} + 1 \right) \right) + \frac{W_{2}(z-1)}{n} \left(C_{y(2)}^{2} + \left(\psi_{2} + 1 \right)^{2} C_{x(2)}^{2} \right) - \frac{W_{2}(z-1)}{n} \left(2(\psi_{2} + 1)C_{yx(2)} \right).$$

$$(7)$$

For the minimum $MSE\left(t_{CC2}^{**}\right)$, the optimal $\psi_2\left(\psi_2^*\right)$ is obtained by taking the derivative with respect to ψ_2 . The ψ_2^* value is substituted for ψ_2 in Eq. (7) and the minimum of $MSE\left(t_{CC2}^{**}\right)$ is finally obtained by

$$MSE_{\min}\left(t_{CC2}^{**}\right) = \overline{Y}^{2} \left(\lambda C_{y}^{2} + \frac{W_{2}(z-1)}{n} C_{y(2)}^{2}\right) - \frac{\left(\lambda C_{yx} + \frac{W_{2}(z-1)}{n} C_{yx(2)}\right)^{2}}{\left(\lambda C_{x}^{2} + \frac{W_{2}(z-1)}{n} C_{x(2)}^{2}\right)}\right). \tag{8}$$

In Equation (7), we derive the second derivative of the MSE with respect to confirm that a minimum exists. The second derivative is given by:

$$\frac{d^2MSE\left(t_{CC2}^{**}\right)}{d\psi_2^2} > 0$$

which ensures that the function reaches a minimum. Furthermore, we analyse the asymptotic properties of our estimator and demonstrate that it is unbiased and consistent as the sample size increases. This guarantees that the estimator converges to the true population mean, providing reliable long-term predictions. The second derivative of the MSE function with respect to is:

$$\frac{d^2MSE(t_{CC2}^{**})}{d\psi_2^2} = 2 + e^{-\psi_2}.$$

Since e^{-w_2} is always positive, the second derivative is always greater than zero. This confirms that the MSE function is convex and has a minimum.

3. Study area

Türkiye is largely in Western Asia and a part of Eurasia. It is between the 36-42 0N latitudes and 26- 450E longitudes and seismically active area within the complex zone of collision between the Eurasian Plate and both the Arabian and African Plates [1, 2, Fig. 1]. Türkiye is influenced by various active fault lines where tectonic movements occur, leading to earthquakes. It is important to analyse each plates separately in Türkiye because they are located on different tectonic structures and fault lines, which can result in variations in earthquake risks and magnitudes. The NAFZ stretches from the Karlıova triple junction, which is the junction point with the East Anatolian Fault Zone (EAFZ) in the east, and extends to the Aegean Sea in the west. On the other hand, the eastern part of Türkiye lies on the East Anatolian Fault Zone [43, 44, Fig. 1]. The East Anatolian Fault Zone (EAFZ), stretching from the Karlıova triple junction to the Mediterranean Sea, is a significant element of indentation and escape tectonics in the eastern Mediterranean region [45]. Two strong earthquakes have been occurred in the eastern part of Türkiye in 2023. However, the western part of the country is affected by the southward migration of the Hellenic arc, which is causing earthquakes [43, 44, 46, 47]. For this reason, we focus on the west part of Türkiye in this study.

In recent years, 20 March 2019-Acıpayam (Denizli) (Mw-5.5), 08 August 2019-Bozkurt (Denizli) (Mw-6.0), 21 July 2017 (Mw-6.6)-Bodrum (Mugla), 26 June 2020-Manisa (Mw-5.5), 30 October 2020-Samos (Greece) (Mw-7.0) earthquakes indicate that seismicity of region should be investigated [10]. The focus of the study is the Aegean Region

and the 200 km surrounding buffer zone as given in Figure 3 [1, 2]. This region is characterised by a complex tectonic structure and numerous independent fault lines [48, 49].



Fig. 3. Location map of the study area [1, 2].

4. Data

The data set is obtained within the scope of The Scientific and Technological Research Council of Türkiye (TUBITAK 1002) Scientific and Technological Research Projects Funding Program - 1002 Project which is numbered 124F059 and titled as "Earthquake Magnitude Prediction with Bidirectional Deep Learning Methods for Western Anatolia Region" [2]. In this study, it is aimed to obtain as complete and reliable earthquake catalogue. The catalogue created for the study area was compiled by reviewing three earthquake catalogues covering the study area, as shown in Fig. 3. The first of these earthquake catalogues is the Disaster and Emergency Management Presidency, Earthquake Department catalogue (AFAD-DDA) catalogue, which is considered as the basic catalogue. As the other two earthquake catalogues, Kandilli Observatory Earthquake Catalogue (KOERI) and Tan [48] earthquake catalogues were considered. In the AFAD-DDA catalogue, the number of earthquakes that occurred within the boundaries of the study area between 1900-2021 is 202,080. In this catalogue, which is not homogeneous in terms of earthquake magnitude, the smallest earthquake magnitude is ML 0.5. It has been determined in the KOERI catalogue that 13,950 earthquakes occurred between 1900-2021 were within the study area. Although the KOERI earthquake catalogue is not homogeneous in terms of earthquake magnitude, earthquakes of M 3.5 and above are considered. In the Tan [48], another source considered in the creation of the study catalogue, earthquakes between 1905 and 2018 were present, and it was seen that 252,594 of the 337,429 earthquakes in the catalogue were located within the earthquake study area.

To control the parameters of earthquakes in the AFAD-DDA catalogue, it is primarily aimed to detect common earthquakes between AFAD-DDA and KOERI and AFAD-DDA and Tan [48] catalogues. The following criteria were taken into consideration for the determination of common earthquakes: Time difference between earthquakes ≤ 3 minutes, position difference: (Longitude 1-Longitude $2 \leq 0.5$ degrees, Latitude 1-Latitude $2 \leq 0.5$ degrees). Using these criteria, earthquake parameters were compared for the earthquakes that matched both in the AFAD-DDA catalogue and in the other two catalogues, and it was determined whether there was a discrepancy in the data series in terms of earthquake magnitudes in the AFAD-DDA catalogue. The results show that there is a good correlation

between AFAD-DDA and Tan [48] catalogues in terms of earthquake magnitudes, especially for earthquakes of magnitude 3.0 and above. The fact that the comparisons between the two earthquake catalogues are based on a total of 153,533 earthquakes indicate that the AFAD-DDA catalogue is reliable. Based on this, it was concluded that the differences in earthquake magnitudes observed in the comparisons of AFAD-DDA and KOERI catalogues may be due to the KOERI earthquake catalogue, and it has been determined that there is no harm in using the AFAD-DDA catalogue as the basic catalogue in compiling the study catalogue.

As the next step in the compilation of the study catalogue, the earthquake catalogues used were combined and the parameter corrections of the matching earthquakes and the detection of possible missing earthquakes in the AFAD-DDA catalogue were started. For this purpose, an earthquake number is given for the earthquakes included in the catalogues, together with the catalogue prefix it belongs to, and all earthquakes are listed according to time. Subsequently, each earthquake was examined one by one, and repeated earthquakes were deleted from the catalogue, parameter corrections were made for the matching earthquakes, and a common catalogue was produced by adding earthquakes that were not included in the AFAD-DDA catalogue. The earthquakes not included in the AFAD-DDA catalogue were rechecked, and the final decision was made by checking whether these earthquakes are in the ISC and ISC_EHB catalogues. In the next step, the study catalogue was homogenized via earthquake magnitude and all earthquakes were converted to Mw earthquake scale. Various empirical relations have been used to convert earthquake magnitudes. For this aim, Kadirioğlu and Kartal [49] and Scordilis [52] magnitude transformation relations were considered. The most important factor in the selection of these relations is that they are produced from earthquake catalogues [50, 51] and that they are transformation relations that are frequently used for earthquakes in the region [52].

Finally, Gardner and Knopoff [53] declustering method was chosen as the catalogue declustering approach. It is one of the standard time-space window methods. The project catalogue was cleared of foreshocks and aftershocks using the ZMAP program, using Gardner and Knopoff [53] delustering algorithm. The decoupled catalogue obtained contains 16,503 earthquakes. Totally, 5284 clusters were identified in the decoupling analysis and 30,107 earthquakes were removed from the catalogue.

Estimating the average magnitude of earthquakes in a short time period for specific regions serves as a useful metric for understanding seismic activity within that timeframe. While the maximum magnitude is indeed important for hazard assessment, the average magnitude provides additional insights into the seismicity of a region. Here, we define the study variable (y) is the magnitude of a main shock and the auxiliary variable (x) is the magnitude of the largest aftershock of this main shock. The descriptive statistics of the population are given in Table 1.

Table 1. Descriptive	statistics	of the	population.
----------------------	------------	--------	-------------

=			
Population Size	1276	Sampling Fraction (f)	0.241
Sample Size	300	$\lambda = 1 - f / n$	0.0025
Mean of the Auxiliary Variable	4.559	Population coefficients of variation of the auxiliary variable	0.105
Mean of the Study Variable	4.858	Population coefficients of variation of the study variable	0.122
Correlation Coefficient	0.855	Kurtosis	4.157

Table 1 indicates that the population size is 1276 in this period. The sample size is determined as 300. The relationship between magnitude of a main shock and magnitude of the largest aftershock has a positive correlation since the value is 0.855. Therefore, if the magnitude of a main shock decreases, magnitude of the largest aftershock also decreases, and if the magnitude of a main shock increases, so do the magnitude of the largest aftershock. The kurtosis value is calculated as 4.157 and this means that a distribution is peaked and possesses thick tails. Leptokurtic distributions have positive kurtosis values and has a higher peak and taller tails than a normal distribution. A scatter plot for the magnitude of main shocks and boxplot of the magnitude of main shocks are presented in Fig. 4 and Fig. 5, respectively. In Fig. 4, the outliers of the magnitude (Mw) are also indicated by each year.

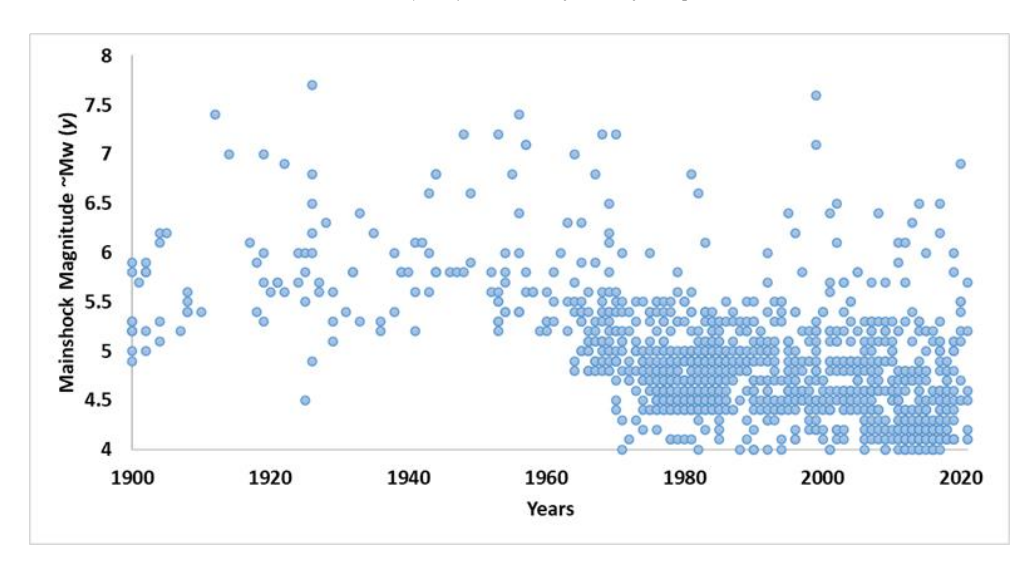


Fig. 4. The scatter plot for the magnitude of main shocks (y) between the years 1900-2021.

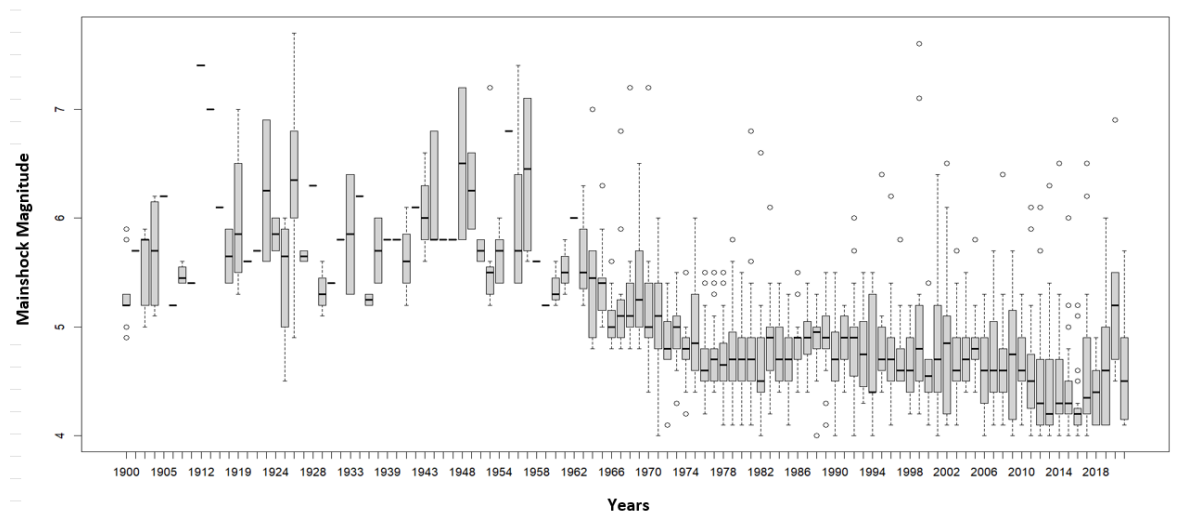


Fig. 5. The boxplots for the magnitude of main shocks (y) between the years 1900-2021.

As seen in Figs. 4 and 5, earthquake records before 1970 in Turkish earthquake catalogues may be more limited and sometimes incomplete, considering the data collection methods and technological capabilities of that period. Therefore, there may be some question marks about the reliability of these records [26]. Hence, we assume that this period contains a non-responses scheme, and the main shocks can be estimated by sub-sampling method. Fig. 6 show that there is relation between the magnitude of a main shock and the magnitude of its largest aftershock. As seen in Fig. 6, all the magnitude of a main shock is greater than the magnitude of the largest aftershock of this main shock.

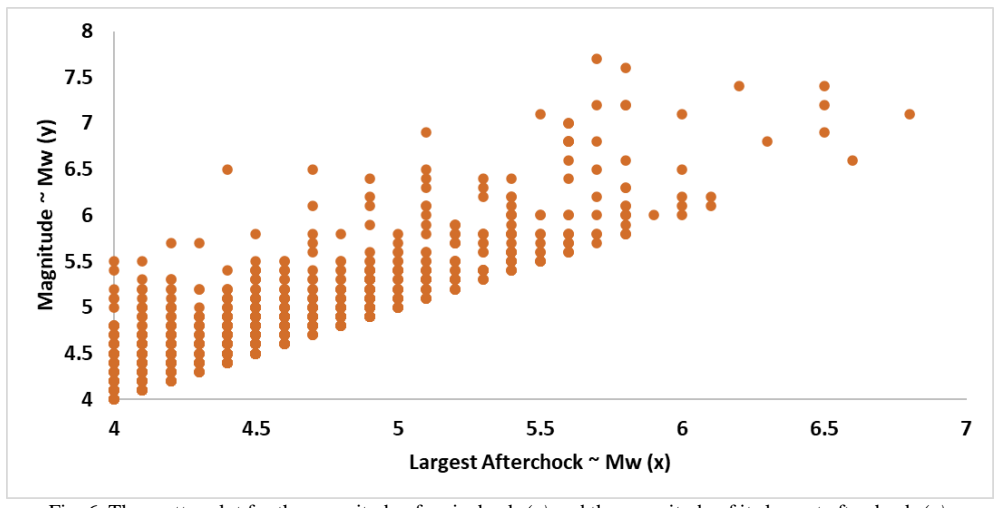


Fig. 6. The scatter plot for the magnitude of mainshock (y) and the magnitude of its largest aftershock (x).

5. Results and Discussion

In this section, the main aim is to estimate the population mean of the magnitude of the main shock using information of the largest aftershock of the main shock using the proposed estimator t_{CC2}^{***} in Section 2. For this aim, we analyse the various non-response rates in the case of non-response, in sub-sampling design. The non-response can be thought for the earthquake data. The non-response rate in the population is considered 20%, 10%, and 5% ($W_2 = 0.20, 0.10, 0.05$). The values of the population parameters are based on the non-responding parts, which are taken as the last 20%, 10%, and 5% units of the population, respectively. Here, the catalogue includes 1276 different main shocks specified and the last 20%, 10%, and 5% of units, respectively, are determined as the non-response units. The scenarios for different combinations are given in Fig. 7.

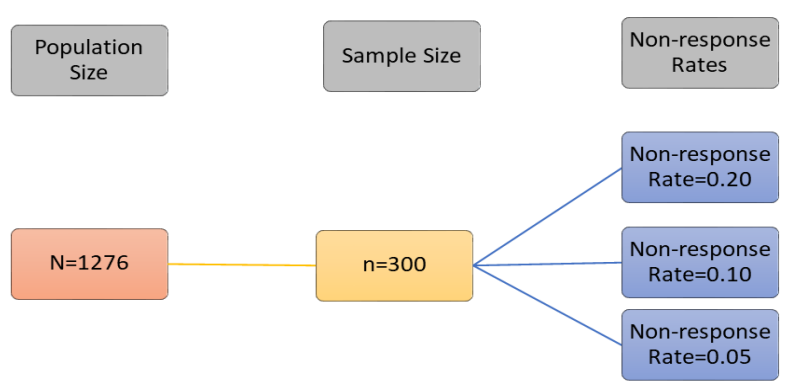


Fig. 7. Scenarios for the earthquake catalogue.

Here, different z-values are used to show the suitability of the proposed estimator for all combinations. To demonstrate this, we selected z-values of 3, 5, 7, and 9 to observe their impact on the estimator. According to the specified values of z (3, 5, 7, 9) and several non-response rates (0.20, 0.10, 0.05), the percentage relative efficiencies

(PRE) of the proposed and compared estimators are computed and presented in Table 2. The formula for PRE-values is given by

$$PRE = \frac{V(t_{HH})}{MSE(t^{**})}.$$
(9)

Here, t^{**} denotes t_{exp}^{**} and t_{CC2}^{**} estimators, respectively. Using the MSE values, the PRE-values are given in Table 2.

Table 2. The PRE-values under several scenarios.

Non-Response Rate = 0.20

352.471

100.000

219.164

362.856

Non-Response Rate = 0.05 z=3

 t_{CC2}^{**}

 t_{HH}

 t_{CC2}^{**}

	z=3	z=5	z=7	z=9
t_{HH}	100.000	100.000	100.000	100.000
t_{exp}^{**}	204.527	196.173	191.138	187.785
t_{CC2}^{**}	332.624	316.985	308.312	302.902
Non-Response $Rate = 0.10$				
	z=3	z=5	z=7	z=9
$t_{H\!H}$	100.000	100.000	100.000	100.000
t_{exp}^{**}	213.649	207.925	203.919	200.936

341.406

100.000

216.359

356.454

z=5

334.04

z=7

100.000

214.103

351.401

328.776

100.000

212.227

347.264

z=9

According to the different values of non-response rates, the PRE-values of t_{CC2}^{**} decrease with the increased z values for all non-response rates. When the non-response rate decreases, the PRE-values are increasing for all z values (3, 5, 7, and 9). Besides, the highest PRE-values are always seen in cases where the non-response rate was 0.05 for each z values. The minimum PRE-value (302.902) is seen in the case of the non-response rate=0.20 and z=9. The maximum PRE-value (362.856) is also seen in case of the non-response rate=0.05 and z=3. These results are visualized in Fig. 8.

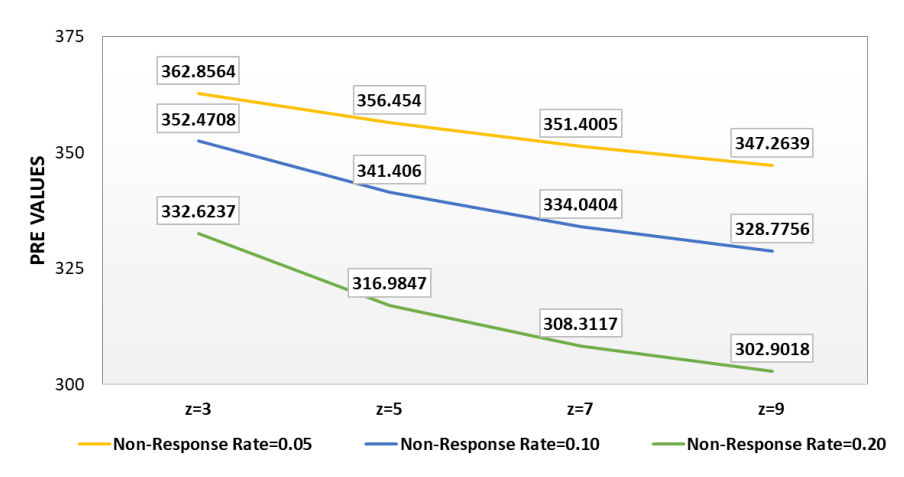


Fig. 8. The MSE values of t_{CC2}^{**} for the various non-response rates.

As seen in Table 2, the estimator t_{CC2}^{**} has the maximum PRE-value among others in the case of determining different z and non-response rates. This estimator is followed by t_{\exp}^{**} estimator with the largest PRE. These comparison results are visualized in Fig. 9 – 11.

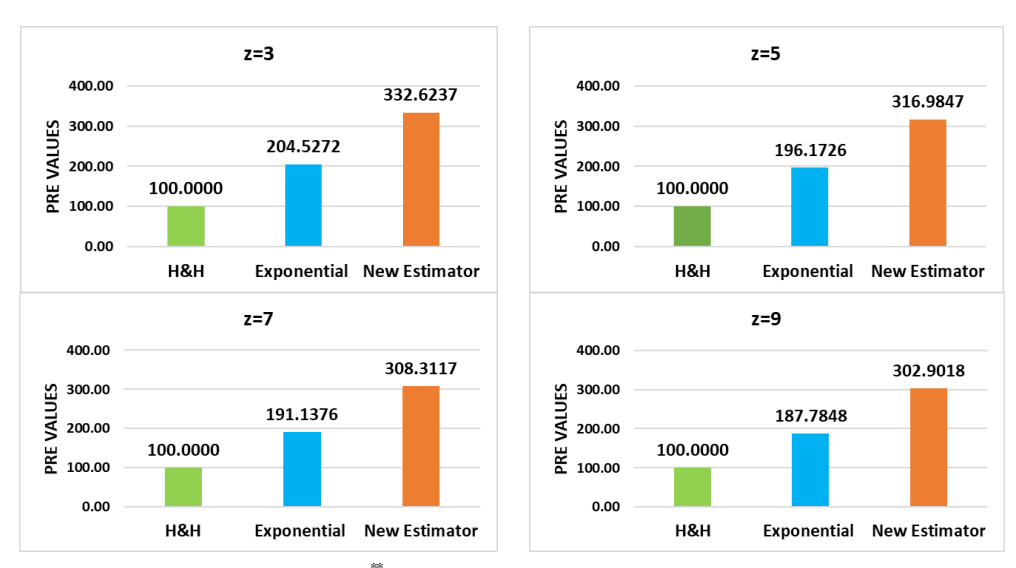


Fig. 9. The MSE values of t_{CC2}^{***} and compared estimators for the non-response rates 0.20.

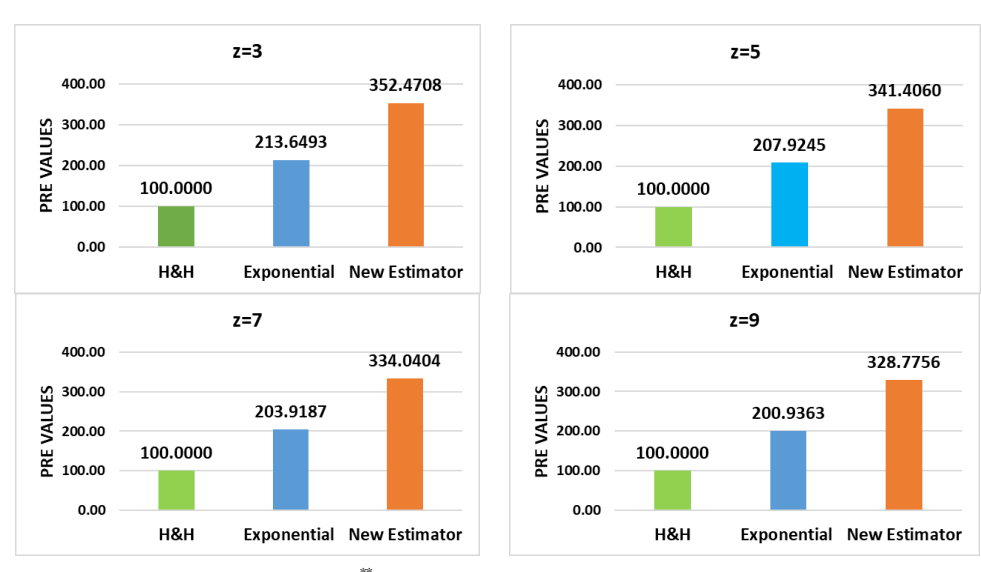


Fig. 10. The MSE values of t_{CC2}^{***} and compared estimators for the non-response rates=0.10.

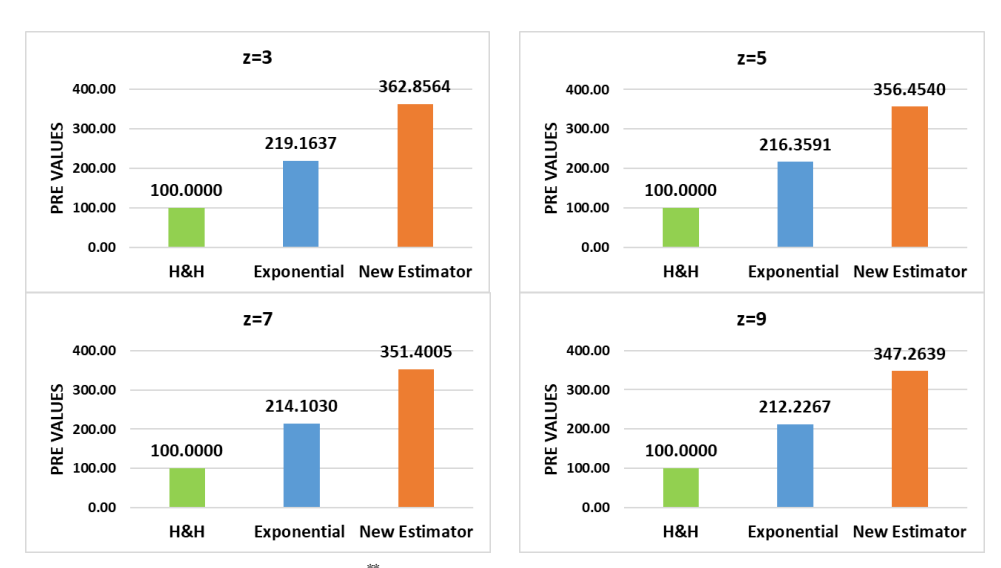


Fig. 11. The MSE values of t_{CC2}^{**} and compared estimators for the non-response rates=0.05.

In line with the study's primary purpose, the population mean of the study variable \overline{Y} are obtained by using the new proposed estimator and the results are given in Table 3.

Table 3. The results for the estimation of the population mean.

Non-Response Rate = 0.20				
	z=3	z=5	z=7	z=9
$\widehat{\bar{Y}}$	4.858342	4.858222	4.857375	4.857963
Non-Response $Rate = 0.10$				
	z=3	z=5	z=7	z=9

Ünal, C. & Özel, G., (2025) / Journal of Scientific Reports-A, 062, 12-28

$\widehat{\bar{Y}}$	4.857633	4.857474	4.858392	4.857619	
Non-Response $Rate = 0.05$					
	z=3	z=5	z=7	z=9	
$\widehat{\bar{Y}}$	4.858247	4.857718	4.857135	4.858119	

The results in Table 3 indicate that the estimations of the population mean for the different z and non-response rate values are fit perfectly to the real population mean of the study variable ($\bar{Y} = 4.8578$) for each combination via the new proposed estimator. It is also seen that the population means value estimation is obtained very close to the population mean in the case of the rate of non-response = 0.05 and z = 5 ($\hat{Y} = 4.857718$). It can be said that the closest estimate of the population means is given when the non-response rate is the minimum.

As we compared our results with previous studies, we found similar conclusions. Same earthquake catalogue was analysed by Markov chains in Ünal et al. [14] and the findings support this study. Ünal et al. [14] found that the probability of an earthquake varies between the magnitudes 4.5 and 4.9 in same region is 42%. We also found that the magnitude mean is approximately 4.6. Furthermore, the results of this study are also similar to the results of Ünal and Çelebioğlu [54] and Ünal et al. [15]. They found that it will take about two months for an earthquake in the range of Mw = 4.5 to Mw = 4.9 to occur. Additionally, compared with the previous studies of Özel [23], Sharma et al. [24] and Khare et al. [25] on the estimators for the population mean using Poisson distribution, the present study by proposing a new exponential type of estimator yields more reliable results since the MSEs are the smaller than the existing studies.

6. Conclusion

Türkiye, positioned at the crossroads of the African, Arabian, and Eurasian tectonic plates, stands as one of the most active regions in the Mediterranean in terms of seismic activity. The continuous movement and interaction of these major plates contribute significantly to the tectonic dynamics of the area [55]. Consequently, the Anatolian Plate, which encompasses a significant portion of Türkiye, bears substantial seismic hazard.

Sampling plays a crucial role in earthquake magnitude prediction as it helps in capturing the diversity and variability of earthquake events. By estimating the average magnitude, it is possible to infer certain characteristics of seismicity, such as the seismic energy release and the relative frequency of different magnitude events. The average magnitude is used for the assessment of seismic activity by providing a summary measure and aiding in trend identification and comparison across regions in a short time period complement. While it is influenced by the parameters of the G-R law, it serves as a valuable metric for understanding the typical size and strength of earthquakes within a specific timeframe and region. The non-response rate in an earthquake catalogue is important to consider when analyzing and interpreting seismic data. It can introduce bias and affect the accuracy of statistical analyses, such as estimating the frequency or recurrence of earthquakes in a particular region. Researchers and seismologists often acknowledge the potential limitations and uncertainties associated with the non-response rate in earthquake catalogs and take them into account when drawing conclusions or making inferences based on the data. Efforts are continuously made to improve earthquake monitoring systems and catalogue completeness. Advances in technology, increased instrumentation coverage, and enhanced reporting mechanisms contribute to reducing the non-response rate and improving the overall accuracy and reliability of earthquake catalogs.

This article proposes a new exponential type of estimator for obtaining earthquake magnitude mean of main shocks. The proposed estimator is examined under the non-response scheme. The non-response proportion in the population refers to the proportion of all earthquakes that occur in a given region or time period but are not recorded or detected by the seismic monitoring network. This scheme is explained in detail. We obtain that the proposed estimator, t_{CC2}^* , can be applied in the earthquake for the estimation of the population mean. The new approach for the estimation of completeness intervals of earthquake catalogues can be considered as an auxiliary tool for completeness analysis though further sensitivity analyses are required to check its validity and accuracy.

Acknowledgements

We like to thank to the support by The Scientific and Technological Research Council of Türkiye (TUBITAK) ARDEB 1002 [Project number: 124F059] program. The authors also thank Asst. Prof. Dr. Tuba Eroğlu Azak for her valuable advice.

Author Contribution

C.U., Methodology, data analysis, writing – original draft. G.O., Conceptualization, Supervision, validation, writing – review & editing. Both authors read and approved the final version of the manuscript.

References

- [1] H. N. Karakavak and C. Kadılar, "INAR(1) and ARIMA models to predict the number of mainshocks and their aftershocks in Turkey," *J Seismol.*, 2025, doi:10.1007/s10950-025-10302-2.
- [2] TÜBİTAK 1002, "Earthquake Magnitude Prediction with Bidirectional Deep Learning Methods for Western Anatolia Region", Project No. 124F059, 2024.
- [3] T. Y. Duman et al., "Türkiye sismotektonik haritası ölçek 1:1.250.000," Maden Tetkik ve Arama Genel Müdürlüğü Özel Yayın Serisi, vol. 34, Ankara, 2017.
- [4] KOERI, "06 Şubat 2023 ML7.5 Ekinözü Kahramanmaraş depremi," [Online]. Available: http://www.koeri.boun.edu.tr/sismo/2/06-subat-2023-ml7-5-ekinozu-kahramanmaras-depremi/. Accessed: Feb. 2023.
- [5] A. Öcal, "Natural disasters in Türkiye: Social and economic perspective," Int J Disaster Risk Manag, vol. 1, no. 1, pp. 51–61, 2019.
- [6] S. McClusky *et al.*, "Global Positioning System constraints on plate kinematics and dynamics in the eastern Mediterranean and Caucasus," *J. Geophys. Res.: Solid Earth*, vol. 105, no. B3, pp. 5695–5719, Mar. 2000.
- [7] M. Erdik, "Report on 1999 Kocaeli and Düzce (Türkiye) earthquakes," in Struct. Control Civ. Infrastruct. Eng., pp. 149-186, 2001.
- [8] B. Ugurhan and A. Askan, "Stochastic strong ground motion simulation of the 12 November 1999 Düzce (Türkiye) earthquake using a dynamic corner frequency approach," *Bull. Seismol. Soc. Am.*, vol. 100, no. 4, pp. 1498–1512, 2010.
- [9] N. Pınar, "Preliminary note on the earthquake of Yenice-G, Türkiye, March 18, 1953," Bull. Seismol. Soc. Am., vol. 43, no. 4, pp. 307–310, 1953.
- [10] İ. H. Çağatay, "Experimental evaluation of buildings damaged in recent earthquakes in Türkiye," Eng. Fail. Anal., vol. 12, no. 3, pp. 440–442, 2005.
- [11] Mitchell, W. A. (1976). Reconstruction after disaster: The Gediz earthquake of 1970. Geographical Review, 296-313.
- [12] AFAD Earthquake Department, "30 October 2020 Aegean Sea, Seferihisar (Izmir) offshore (17.26 km) preliminary evaluation report on Mw 6.6 earthquake," 2020.
- [13] A. Karadaş and E. Öner, "Effects of the alluvial geomorphology on the damage of the Sisam earthquake in the Bornova plain," *J. Geogr.*, vol. 42, pp. 139–153, 2021.
- [14] C. Ünal, G. Özel, and T. Eroğlu Azak, "Markov chain approach for earthquake sequencing in the Aegean Graben system of Türkiye," *Earth Sci. Inf.*, vol. 16, no. 2, pp. 1227–1239, Apr. 2023.
- [15] S. Ünal, S. Çelebioğlu, and B. Özmen, "Seismic hazard assessment of Türkiye by statistical approaches," *Turk. J. Earth Sci.*, vol. 23, pp. 350–360, 2014.
- [16] E. K. Kara and K. Durukan, "The statistical analysis of the earthquake hazard for Türkiye by generalized linear models," *Gazi Univ. J. Sci.*, vol. 30, no. 4, pp. 584–597, 2017.
- [17] M. S. Yücemen, "Probabilistic assessment of earthquake insurance rates for Türkiye," Nat. Hazards, vol. 35, pp. 291-313, 2005.
- [18] E. Firuzan, "Statistical earthquake frequency analysis for western Anatolia," Turk. J. Earth Sci., vol. 17, no. 4, pp. 741-762, 2008.
- [19] Y. Bayrak *et al.*, "Regional variation of the ω-upper bound magnitude of GIII distribution in and around Türkiye: Tectonic implications for earthquake hazards," *Pure Appl. Geophys.*, vol. 165, no. 7, pp. 1367–1390, Jul. 2008.
- [20] Y. Bayrak et al., "Seismicity assessment for different regions in and around Türkiye based on instrumental data: Gumbel first asymptotic distribution and Gutenberg-Richter cumulative frequency law," Nat. Hazards Earth Syst. Sci., vol. 8, pp. 109–122, 2008.
- [21] T. M. Tsapanos *et al.*, "Analysis of largest earthquakes in Türkiye and its vicinity by application of the Gumbel III distribution," *Acta Geophys.*, vol. 62, pp. 59–82, 2014.
- [22] G. Özel, "A bivariate compound Poisson model for the occurrence of foreshock and aftershock sequences in Türkiye," *Environmetrics*, vol. 22, no. 7, pp. 847–856, 2011.
- [23] G. Özel, "Ratio estimators using characteristics of Poisson distribution with application to earthquake data," in Proc. 7th Int. Days Stat. Econ., Prague, Sep. 2013.

- [24] P. Sharma, H. K. Verma, N. K. Adichwal, and R. Singh, "Generalized estimators using characteristics of Poisson distribution," *Int. J. Appl. Comput. Math.*, vol. 3, pp. 745–755, 2017.
- [25] S. Khare, R. Singh, and P. Sharma, "Estimation of population mean for logarithmic observation under Poisson distributed study and auxiliary variates." *Electron. J. Appl. Stat. Anal.*, vol. 13, no. 2, pp. 580–593, 2020.
- [26] O. Tan, M. C. Tapırdamaz, and A. Yörük, "The earthquake catalogues for Türkiye," Turk. J. Earth Sci., vol. 17, no. 2, pp. 405-428, 2008.
- [27] R. J. Little and D. B. Rubin, "Maximum likelihood for general patterns of missing data: introduction and theory with ignorable nonresponse," in Statistical Analysis with Missing Data, pp. 164–189, 2002.
- [28] M. H. Hansen and W. N. Hurwitz, "The problem of non-response in sample surveys," J. Am. Stat. Assoc., vol. 41, no. 236, pp. 517–529, 1946.
- [29] H. O. Cekim and C. Kadilar, "In-type estimators for the population variance in stratified random sampling," *Commun. Stat. Simul. Comput.*, vol. 49, no. 7, pp. 1665–1677, 2020.
- [30] H. O. Cekim and C. Kadilar, "Ln-type variance estimators in simple random sampling," Pak. J. Stat. Oper. Res., vol. 16, no. 4, pp. 689–700, 2020.
- [31] H. Cingi and C. Kadilar, Advances in Sampling Theory: Ratio Method of Estimation, Bentham Science Publishers, 2009.
- [32] R. S. Solanki, H. P. Singh, and A. Rathour, "An alternative estimator for estimating the finite population mean using auxiliary information in sample surveys," *Int. Scholarly Res. Not.*, pp. 1–14, 2012.
- [33] Z. Yan and B. Tian, "Ratio method to the mean estimation using coefficient of skewness of auxiliary variable," in International Conference on Information Computing and Applications, Berlin, Heidelberg: Springer, 2010.
- [34] M. Irfan, M. Javed, and Z. Lin, "Efficient ratio-type estimators of finite population mean based on correlation coefficient," Sci. Iran., vol. 25, no. 4, pp. 2361–2372, 2018.
- [35] A. A. Sifawa and M. Z. Shehu, "Modified ratio-cum-product type estimator for population mean in simple random sampling scheme," *Him. J. Appl. Med. Sci. Res.*, vol. 2, no. 5, pp. 1–5, 2021.
- [36] A. Gupta and R. Tailor, "Ratio in ratio type exponential strategy for the estimation of population mean," *J. Reliab. Stat. Stud.*, vol. 14, no. 2, pp. 551–564, 2021.
- [37] R. K. Gangele, G. K. Vishwakarma, and S. K. Choubey, "An efficient class on linear combination of ratio type estimators for estimating the population mean," *Thail. Stat.*, vol. 20, no. 2, pp. 284–292, 2022.
- [38] J. J. Cai, P. Wan, and G. Özel, "Parametric and non-parametric estimation of extreme earthquake event: the joint tail inference for mainshocks and aftershocks," *Extremes*, vol. 24, pp. 199–214, 2021.
- [39] A. M. Chandler, N. Lam, J. Wilson, and G. L. Hutchinson, "Response spectrum modelling for regions lacking earthquake records," *Electron. J. Struct. Eng.*, vol. 1, no. 1, pp. 60–73, 2001.
- [40] W. G. Cochran, Sampling Techniques, 3rd ed., New York: John Wiley & Sons, 1977.
- [41] R. Singh, M. Kumar, M. K. Chaudhary, and F. Smarandache, "Estimation of mean in presence of non-response using exponential estimator," arXiv preprint, arXiv:0906.2462, 2009.
- [42] G. N. Singh and M. Usman, "Ratio-to-product exponential-type estimators under non-response," *Jordan J. Math. Stat.*, vol. 12, no. 4, pp. 593–616, 2019.
- [43] D. Kalafat and E. Görgün, "An example of triggered earthquakes in western Türkiye: 2000–2015 Afyon-Akşehir Graben earthquake sequences," *J. Asian Earth Sci.*, vol. 146, pp. 103–113, 2017.
- [44] S. Turkan and G. Özel, "Modeling destructive earthquake casualties based on a comparative study for Türkiye," *Nat. Hazards*, vol. 72, no. 2, pp. 1093–1110, 2014.
- [45] E. Akgun and M. İnceöz, "Tectonic evolution of the central part of the East Anatolian Fault Zone, Eastern Turkey," *Turk. J. Earth Sci.*, vol. 30, no. 7, pp. 928-947, 2021.
- [46] F. Flerit, R. Armijo, G. King, and B. Meyer, "The mechanical interaction between the propagating North Anatolian Fault and the back-arc extension in the Aegean," *Earth Planet. Sci. Lett.*, vol. 224, no. 3–4, pp. 347–362, 2004.
- [47] M. Bohnhoff, H. P. Harjes, and T. Meier, "Deformation and stress regimes in the Hellenic subduction zone from focal mechanisms," *J. Seismol.*, vol. 9, no. 3, pp. 341–364, 2005.
- [48] O. Tan, "Turkish Homogenized Earthquake Catalogue (TURHEC)," Nat. Hazards Earth Syst. Sci., Zenodo, 2021. [Online]. Available:
- [49] F. T. Kadirioglu and R. F. Kartal, "The new empirical magnitude conversion relations using an improved earthquake catalogue for Türkiye and its near vicinity (1900–2012)," *Turk. J. Earth Sci.*, vol. 25, no. 4, pp. 300–310, 2016.
- [50] A. M. C. Şengör, "The North Anatolian transform fault: its age, offset and tectonic significance," J. Geol. Soc., vol. 136, pp. 269–282, 1979.
- [51] A. M. C. Şengör, "Mid-Mesozoic closure of Permo-Triassic Tethys and its implications," Nature, vol. 279, pp. 590-593, 1979.
- [52] E. M. Scordilis, "Empirical global relations converting MS and mb to moment magnitude," J. Seismol., vol. 10, pp. 225–236, 2006.
- [53] J. K. Gardner and L. Knopoff, "Is the sequence of earthquakes in Southern California with aftershocks removed, Poissonian?" *Bull. Seismol. Soc. Am.*, vol. 64, no. 5, pp. 1363–1377, 1974.
- [54] S. Ünal and S. Çelebioğlu, "A Markov chain modelling of the earthquakes occurring in Türkiye," *Gazi Univ. J. Sci.*, vol. 24, pp. 263–274, 2011.
- [55] H. A. Cohen, C. J. Dart, H. S. Akyüz, and A. Barka, "Syn-rift sedimentation and structural development of the Gediz and Büyük Menderes graben, western Türkiye," *J. Geol. Soc.*, vol. 152, no. 4, pp. 629–642, 1995.



Contents lists available at Dergipark

Journal of Scientific Reports-A

journal homepage: https://dergipark.org.tr/tr/pub/jsr-a



E-ISSN: 2687-6167 Number 62, September 2025

RESEARCH ARTICLE

Tuning the magnetization by preserving half-metallicity of FeCl₂ via embedding transition metal atoms: a DFT study

Ali Emre GENÇa*

^aGazi University, Department of Physics, 06500, Teknikokullar/Ankara, ORCID: 0000-0001-9567-2018

Abstract

In this article, the varying magnetization of the modified FeCl₂ two-dimensional (2D) layers have been investigated through Density Functional Theory calculations with and without DFT+U method.. Following the optimizations and post-processing electronic analyses regarding the FeCl₂ bulk, the two-dimensional layer was created, and the 3d group of transition metal (TM) atoms (from Sc to Ni) were embedded into the defective Cl position in line with the experimental works. The calculations show that while each Fe atom in FeCl₂ has $4.00 \mu_B$ magnetization in the pure layer, after embedding transition metal atoms, this value varies in a broad range between 8 to 19 μ_B in completely FM (ferromagnetic) ground state based on only DFT calculations. Between these TMembedded layers, Ti embedded FeCl2 layer showed half-metallicity in one of two spin channels with and without DFT+U calculations, a prerequisite for spintronic applications. The Projected Density of States (PDOS) of Ti embedded layer, t2g orbitals (d_{xy}, d_{xz}, and d_{yz}) of the neighboring Fe atoms are responsible for the conductivity in the spin-down channel based on DFT calculations. The hubbard parameters completely changes the picture where the non-neighboring atom contribution to the conductive electronic states are dominant. These findings are supported by band gap curves. The bond type identification has been elucidated by ICOHP (integrated crystal orbital Hamiltonian population) and ICOBI (integrated crystal orbital bond index) parameters. PDOS (partial density of states) and pCOHP (partial crystal orbital Hamiltonian) plots were used to identify which bonding-antibonding orbitals were populated. Finally, embedding Ti into Cl defect positions can induce different magnetization levels by preserving half metallicity while the other layers do not provide half-metallicity. © 2023 DPU All rights reserved.

Keywords: Density functional theory; spintronics; 2D materials; transition metal embedding; FeCl₂; transition metal dihalides.

^{*} Corresponding author. Tel.: +0-000-000-0000 ; fax: +0-000-000-0000 . *E-mail address: aegenc@gazi.edu.tr*

1. Introduction

Materials with valuable properties for spintronic applications have been explored due to offering offer advantages over conventional electronics regarding data transfer and storage [1]. Prerequisites of smaller-than-expected gadgets roused the specialists to plan two-layered materials offering multifunctional qualities, particularly by preserving the data in the type of twist quantum values instead of electrical charge [2]. In this context, spintronic appeared as a new field where half-metallicity plays a vital role presenting plenty of prospects that may be utilized in diverse applications like fast data storage and data processing, etc[3]. Since the invention of Graphene, which led the way for the creation of other similar materials, many 2-D counterparts have been investigated for their spintronic applications, such as g- G_3N_4 nanosheets, BN and AlN monolayers, and N-doped graphene [4-7]. Apart from these single-layer 2-D materials, magnetic Van der Waals materials exhibit easily exfoliated bulk structures and tunable magnetic anisotropy, making these materials promising candidates for spintronic applications [8-10].

Among these materials, TMCl₂-type (TM= transition metal) dihalides, FeCl₂ shows easiness of exfoliation experimentally and magnetization and half-metallicity 2-D [10, 11]. In one of the studies of Torun and co-workers, the 1T-FeCl₂ layer is predicted as more stable via Phonon calculations than 1H-FeCl₂ (hegzagonal) with a half-metallic behavior accompanied by 17 K Curie temperature [12]. According to the experiment in which the 2-D FeCl₂ has been synthesized, 2-D FeCl₂ moieties are observed on Au(111) single-crystal surfaces through MBE (Molecular Beam Epitaxy Method). Another exciting feature of this synthesis is that the FeCl₂ monolayer has Fe and Cl point defects that do not affect the material's structural order [11]. So far, different degrees of magnetization have been obtained over a wide range of materials [8].

In this article, FeCl₂ monolayer is used as a benchmark to reveal magnetic properties after embedding a 3d group of transition metals with DFT and DFT+U computations. As known, embedding or doping foreign atoms in the place of the surface defects is a widely used technique for magnetic adjustment [8, 13]. In the FeCl₂ 2-D monolayer, since the Cl atoms enclose Fe atoms, Cl defects are more likely to possess a more controllable structure. They are easily doped with foreign atoms without having a more complex potential energy surface. As shown in the subsequent chapters, embedding TM atoms will induce different magnetic moments by mostly destroying the half-metallicity except Ti embedded FeCl₂ layer, which is indispensable for spintronic applications. According to our results, even if some of the TM atoms induce different amounts of magnetism concerning the bare and Fe-embedded FeCl₂, half metallicity is lost. For the other layers, the electronic behavior is changed depending upon the Hubbard parameter usage mostly from metallic to semiconductive or vice versa. To our knowledge, embedding the single TM atom for adjusting the magnetic properties of the FeCl₂ monolayer has yet to be investigated in the literature. Our findings are original and might be used to create the desired spintronic devices.

2. Computational Methods

Periodic density functional theory (DFT) calculations were examined through the Quantum Espresso simulation package [14-16]. Electron-ion interactions were softened via PAW-type pseudopotentials, while the exchange-correlation effect was treated by PBE functional [17-19]. The values of 80 Ry for cut-off and 800 Ry for kinetic energy cut-off have been considered adequate for extending plane waves over the Brillouin zone. The Gaussian smearing for Brillouin Zone integration has been used as 0.01 Ry degauss value has been used. The Monkhorst-Pack k-point set has been used as 4x4x1, 6x6x1, and 8x8x1 for FeCl₂ bulk, FeCl₂ monolayer, and elaborate electronic analyses, respectively(i.e., band structure calculations, partial density of states (PDOS), and Crystal Orbital Hamilton Population (COHP) analysis) [20-23]. A vacuum length has been taken as 32 Å to complete the elimination of the unwanted interactions along the z-direction. Grimme-D3 dispersion (Van der Waals) correction has been considered to obtain better geometries and energies, especially for FeCl₂ bulk calculations. The structural relaxations for surface-molecule interactions ceased after reaching the convergence thresholds for ionic minimizations, self-consistency, and atomic forces of 10⁻⁶Ry, 10⁻⁶Ry, and 10⁻⁶ Ry/Bohr, respectively. In all cases, different initial magnetic orders, such as FM, AFM1 and AFM2 have been taken into consideration to have better ground state descriptions, which will

be given and discussed in subsequent chapters. Following the FeCl₂ bulk calculations, one of the Cl-Fe-Cl parts of FeCl₂ has been separated for further analyses and expanded into a 2x2 supercell. Formation energies have been calculated to verify whether these TM-embedded structures can be synthesized experimentally based on Equation (1).

$$E_f = E_{system} + E_{cl} - E_{TM-atom} - E_{TM-FeCl}$$
 (1)

In Equation (1), the 1st term represents the total energy of the bare monolayer, and the 2nd, 3rd, and 4th terms are the total chemical potentials of the Cl atom, TM atoms, and the TM embedded FeCl₂. Adsorption energies were calculated according to Equation (2),

$$E_{ads} = E_{TM-FeCl_2} - (E_{FeCl_2} + E_{TM}) \tag{2}$$

In Equation (2), the 1^{st} , 2^{nd} , and 3^{rd} terms are the total energies of the interacted system, FeCl₂ monolayer, and single atom energies of the transition metals.

Charge Density Differences (CDD) were calculated by subtracting the individual charge densities of the adsorbates and of the functionalized graphene layer from the interacted system:

$$\Delta \rho_{ads} = \rho_{system} - \rho_{adsorbates} - \rho_{MnN_x O_y} \tag{3}$$

Chemical bonding information, mainly focused on elucidating the bonding nature in layers, has been acquired by applying the Crystal Orbital Hamilton Population (COHP) method. This method utilizes electronic wave functions to generate bonding information, as documented in references [24-29]. The Crystal Orbital Bond Index (ICOBI) is a novel metric that characterizes the bonds based on the Wiberg and Mayer bond index adapted for crystals [30-32]. Analyzing chemical bonding information involves considering Integrated Crystal Orbital Hamilton Population (ICOHP) and Integrated Crystal Orbital Bond Index (ICOBI) values. In the case of ICOHP, increasingly negative values indicate a higher covalent character and a stronger bond, while less negative values signify more ionic character. For ICOBI, a value close to one represents a nearly perfect covalent bond, whereas a value close to zero indicates an almost perfect ionic bond. Additionally, both ICOHP and ICOBI allow for examining orbital-projected contributions to overall quantities. Crystal Orbital Hamilton Populations (COHP) plots were employed to scrutinize electron densities over bonding and antibonding orbitals parallel to a Partial Density of States (PDOS). The calculations for COHP in this study were conducted using the Lobster code version 4.0.0[33], and the total ICOHP value for each bond was obtained by summing spin-up and spin-down components. Figures were generated using the Material Studio 6.0 interface [34].

3. Results and Discussion

The structural relaxation of the FeCl₂ bulk structure with various magnetic ordering can be seen in Fig. 1a. According to the literature, since the arrangement 1T (such as TaS_2 , VS_2 , $HfSe_2$) phase is more stable than 1H, 1 T structure has been taken as a basis can be seen in Fig. 1[12]. In this step, the same and different spin configurations for Fe and Cl atoms to break spin symmetry have been given as input in FM (Fe \uparrow , Cl \uparrow) and AFM (Fe \uparrow , Cl \downarrow) configurations.

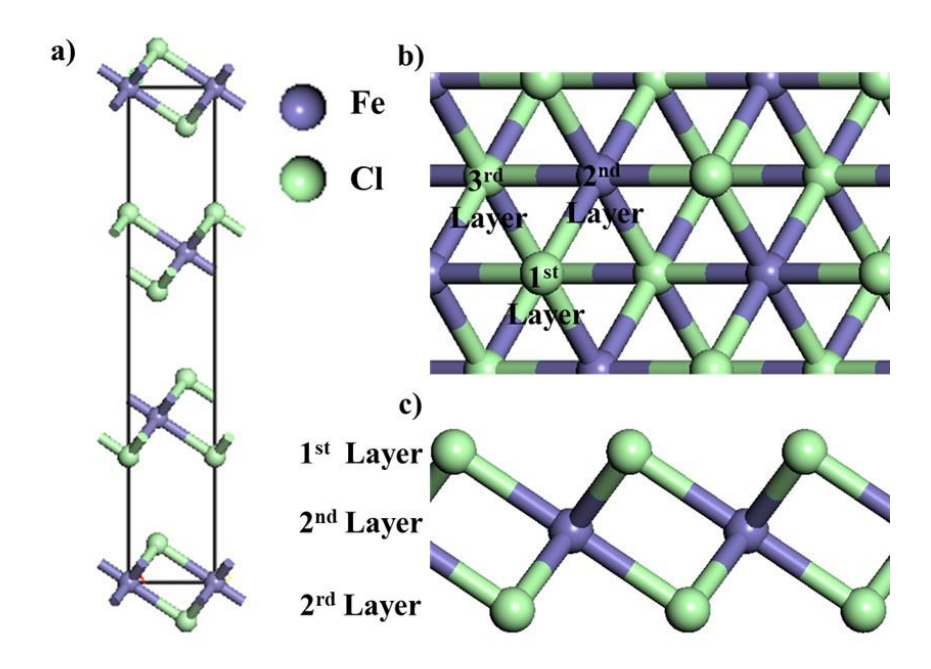


Fig. 1. (a) bulk FeCl₂ (b) top and (c) side view of the FeCl₂ crystal. Purple and light green balls represent Iron and Chlorine atoms, respectively.

Calculations based on FM and AFM spin orders gave similar energies with a difference of 10.3 meV, whereas the AFM order has lower energy, which is consistent with the literature[8]. Some structural parameters are listed in Table 1. d* is the distance between Cl atoms in the interface of the adjacent FeCl2 layer in z-direction. The atomic charges on Fe atoms are donated to Cl atoms, which make these interactions ionic.

Table 1. Calculated parameters of FeCl₂ bulk structure. ΔE_{total} is the total energy difference based on the AFM order total energy. d and d* distances show the Cl-Cl distance in a single layer and interface

FeCl ₂ -Magnetic Phases	$\begin{array}{c} \Delta E_{total} \\ \text{(meV)} \end{array}$	Lattice Parameters (a=b)	d _{Fe-} Cl(Å)	d _{CI} - CI(Å)	d* _{CI} - cı(Å)	Q(Fe)/Q(Cl) (e)
FM	+10.3	3.54	2.47	3.43	3.73	1.10/-0.55
AFM	0	3.54	2.47	3.43	3.73	1.10/-0.55

In the subsequent step, a bare 2D FeCl₂ monolayer was created by isolating the layer already included in the bulk material. Because the lateral interactions might have affected the embedded single TM atom behavior in the layer, the 2x2 supercell was created in Fig. 1b and c. Before embedding TM atoms, some fundamental properties of the pure FeCl₂ layer were investigated to establish our calculations' reliability. First, the FeCl₂ layer was relaxed, and then, electronic properties were studied. Chemical bonding analyses have also been used to show the new bonding

environment of the TM with its environment. Table 2 shows some physical and chemical parameters of the isolated and pure $FeCl_2$ layer.

Table 2. Calculated parameters of free-standing FeCl₂ layer. ICOHP and ICOBI quantities are based on any Cl atom at facet and summed over its 3 Fe neighbors, d is the distance between atoms, Q is the atomic charge and μ_B is the magnetic moment

FeCl ₂ (2x2)	Lattice Parameters (a=b)	d _{Fe-} cı(Å)	d _{Cl} . cl(Å)	Q(Fe)/Q(Cl) (e)	ICOHP (eV)	ICOBI	μ _B (cell) μ _B (f.u.)	μ _B (Fe)	μ _B (Cl)
Super Cell	7.08	2.47	3.45	-1.11/0.55	-4.02	0.07	16.00 4.00	3.50	0.15

Upon relaxation of the pure FeCl₂ layer, the values related to atomic charges and distances between Fe-Cl and Cl-Cl bonds remain unchanged. When the chemical bond strengths and bond types are considered between Fe-Cl bonds, one can see that Fe-Cl bonds are mainly ionic based on 0.07 ICOBI value with a minute non-ionic contribution[30]. Moreover, the ICOHP value is -4.02 eV for the Fe and three Cl neighbors as a total, which implies that there is mostly an ionic bond type. However, this value should be compared to understand its meaningful variations depending on different TM embedding processes. Finally, the magnetic moment of the 2x2 supercell is measured to have 16.00 µB, which shows FM behavior [35]. In line with the literature, the spin-up channel has a semiconducting behavior, while the spin-down channel has a conductive based on the spin-projected Total Density of States (TDOS), which can be seen in Figure 2a. As clearly understood from Figure 2a, the bare FeCl₂ monolayer has a half-metallic behavior in which the conduction takes place on one of the spin channels. Based on the band structure plots in Fig. S1, there is no electron conductance in the spin-up channel, while spin-down electrons provide conductivity for pure FeCl₂ monolayer[12]. Band gap for pure FeCl₂ layer has been calculated to be 4.46 eV which is slightly higher than previously calculated value 4.40 eV [12]. As opposed to our finding, Yang et al found the ground state as insulator and band gap with 3.45 eV with Spin-Orbit Coupling effect [36]. From the TDOS and PDOS curves drawn by summing the contributions of all atoms in the lattice, conductive behavior at around the Fermi level is brought mainly by the Fe atoms, and there is a minute Cl contribution to half metallicity around the Fermi level. Moreover, it is pretty clear that Fe-Cl interactions are negligible and non-bonding characters at the Fermi level from Fig. 2a and 2b. Below the fermi level, a peak around 1.75 eV shows strong antibonding interactions between Fe-Cl atoms on a spin-up channel based on the -pCOHP curve in Fig. 2b. When low-lying electronic states are considered because of the different peak heights between Fe and Cl atoms, one can conclude that the interactions are mainly ionic. Around -3 eV, Cl-Fe interactions are antibonding because of the peak at ~-2.5 eV on the -pCOHP curve. In line with Table 2, spin density is mainly observed on Fe atoms on the monolayer, even if only a tiny part is accumulated on Cl atoms, as shown in Figure 2c.

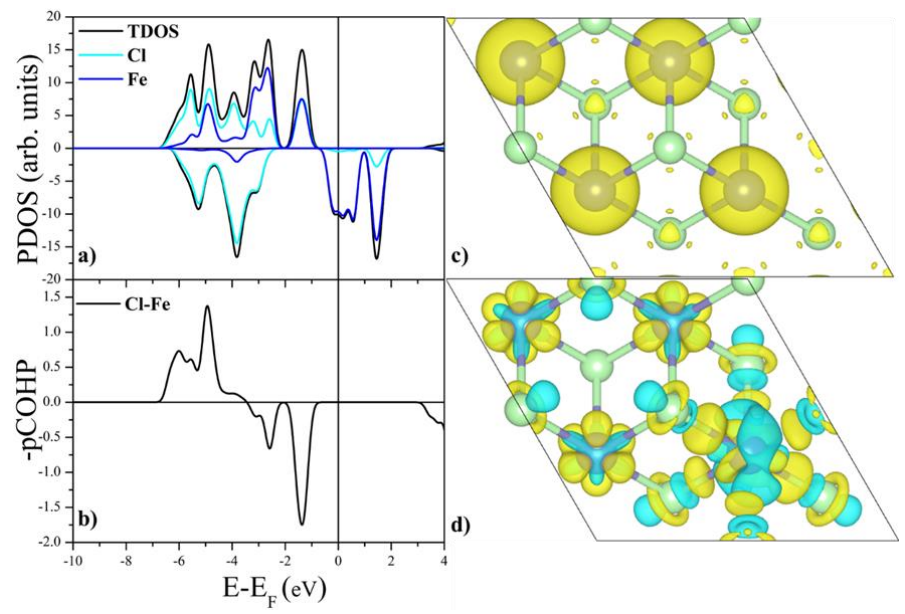


Fig. 2. (a) total density of states (TDOS) and partial density of states (PDOS) over the whole Cl (2p) and Fe (3d) atoms. (b) –pCOHP (Partial Crystal Orbital Hamilton Populations) curve belonging to the surface 1 Cl and its 3 Fe neighbors. (c) spin density and (d) charge density differences (CDD) plot of the pure FeCl₂ layer. Yellow and cyan colors represent the electron accumulation and depletion in space, respectively. Isosurface values are 0.011 *e/Bohr*⁻³ for spin density and 0.0018 *e/Bohr*⁻³ for charge density differences (CDD), respectively. In the PDOS plot, while black lines show TDOS, cyan, and blue curves correspond to the Cl and Fe atoms, respectively.

Figure 2d gives valuable information regarding electron transfer direction between atomic components. As seen, electron transfer is bidirectional since electron accumulation and depletion are observed for both atomic species. Therefore, this phenomenon is explained by the electron donation-back donation rule[37, 38]. Before embedding transition metal into the Cl defects, proven with experimental studies, it will be helpful to visualize the 2x2 supercell model and interactions in Figure 3.

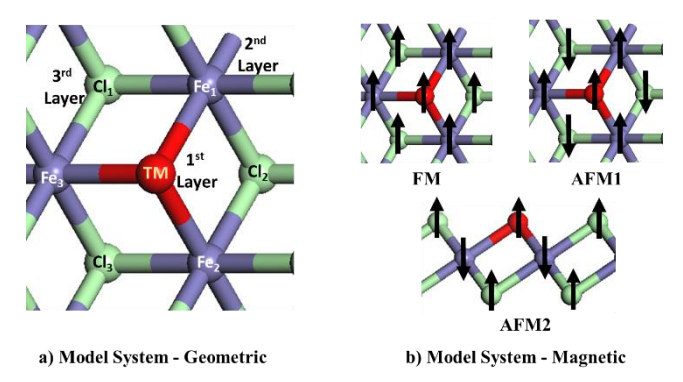


Fig. 3. (a) geometric model and (b) initial magnetic order for pure FeCl₂ and TM embedded FeCl₂ (TM-FeCl₂).

In this step, the Cl atom on the facet is replaced with whole TM atoms from Sc to Ni, respectively. In the geometric model, one of the Cl atoms on the top of the layer is substituted with TM atoms at the first layer, and its interactions with its neighbors will be explored. The magnetic model considers two different spin orders at initial configurations. For the FM order, all starting spins are given in the up direction for all atoms. In AFM1 order, all Fe atoms are shown in an up direction while spin-down directions have been considered for the Cl atoms seen in Figure 3b. In the AFM2 model, while the Cl atoms including embedded TM have up spins, the sandwiched Fe atoms have down spins in the starting configurations.

Table 3. Calculated parameters of free-standing TM embedded FeCl₂ layer. ICOHP and ICOBI quantites are averaged over the bonds with nearest neighbors.

Transition Metals	Ground Magnetic State	Form. Energies (eV)	E _{ads} (eV)	d _{TM-Cl} (Å) (Av)	μ_{Bcell}	μ_{BTM} ,	Q(TM) (e)	ICOHP (TM-3Fe) (eV)	ICOBI (TM-3Fe) (eV)
Sc	FM	-12.08	-2.25	2.53	12.12	-0.70	1.15	-2.55	0.29
Ti	FM	-12.64	-2.80	2.42	11.00	-1.09	1.19	-3.26	0.30
V	FM	-11.84	-2.01	2.32	10.00	-2.24	0.78	-3.26	0.36
Cr	FM	-10.67	-0.84	2.32	9.00	-3.55	0.61	-1.53	0.15
Mn	FM	-10.10	-0.26	2.55	19.00	3.87	0.40	-1.43	0.09
Fe	FM	-11.70	-1.86	2.36	18.00	2.98	0.21	-1.53	0.07
Co	FM	-12.00	-2.16	2.32	17.00	2.04	-0.04	-2.18	0.10
Ni	FM	-11.51	-1.67	2.32	15.55	1.02	-0.04	-1.68	0.10

First, formation energies have been calculated to provide a qualitative interpretation of their experimental synthesizability based on FM and AFM-based ground states. According to Table 3, the formation energies of all structures in magnetic orders that give the lowest energy show that all TM-embedded might be synthesized experimentally. The values related to the distances, ICOHP and ICOBI, are averaged over the number of the neighbors. $\mu_B(TM)$, $\mu_B(Fe)$ (Avg) quantities are given for geometries of the most stable magnetic order. For all layers, FM state has been found as the magnetic ground state based on the geometric optimizations. Transition metals refers to the transition metal embedded FeCl₂ layers. Formation Energies stand for the formation energies. While E_{ads} correspond to the adsorption energies, ΔE_{total} refers to the total energy differences corresponding magnetic structures. Among the reported quantities in Table 3, the adsorption energy is the crucial quantity for the chemical stabilization of embedded transition metals. The largest adsorption energies except Mn are within the chemisorption range, which is generally taken as above 0.6 eV [39]. Therefore, the Mn embedded FeCl₂ layer is not appropriate because of low adsorption energy, which is closer to the lower boundary of the Van der Waals limit. It is important to note that TM-FeCl₂ layers have 4 Fe, 1 TM, and 7 Cl atoms. The total magnetization of all cells is mainly shared by Fe and TM atoms, depending on their magnetic orders. It is found that all of the Fe atoms in the layer have nearly 3 μ B magnetization, which shows they are simultaneously aligned in the same direction. On the contrary, embedded TM atoms have highly varying

magnetization values from -3.55 to 3.87 μ B, which states the usefulness of this strategy in tuning magnetic properties. Considering the bare layers such as TMCl₂ (TM: transition metal), magnetization range is wide in our results [8]. Based on the Bader charges, embedded transition metals donate more electrons to the surrounding Fe atoms from Sc to Ni. This trend nearly follows the Pauling Scale of Electronegativity [40].

Investigating the effect of transition metal embedding on chemical bonding is also very important for practical applications. When looking at the change of the ICOHP parameter between TM and its neighborhoods, it is seen that there is a rough relationship between it and the adsorption energy. For example, the ICOHP value for Fe and Mn atoms is -1.43 eV and -1.53 eV, respectively. When compared with the ICOBI quantity values of 0.09 and 0.07 for the same bonds, it is concluded that the ionic character of the bonds these atoms make with the surrounding Fe atoms is dominant. ICOHP quantities for other metals also comply with ICOBI quantities as expected. This article's primary purpose is to observe electronic behavior by embedding transition metal into Cl defects on the FeCl₂ layer. To reach this aim, spin-dependent PDOS and Band structure curves are crucial to understand. The most critical point in spintronic applications is that regardless of the changes in the structure, conductivity is provided through only a single spin channel.

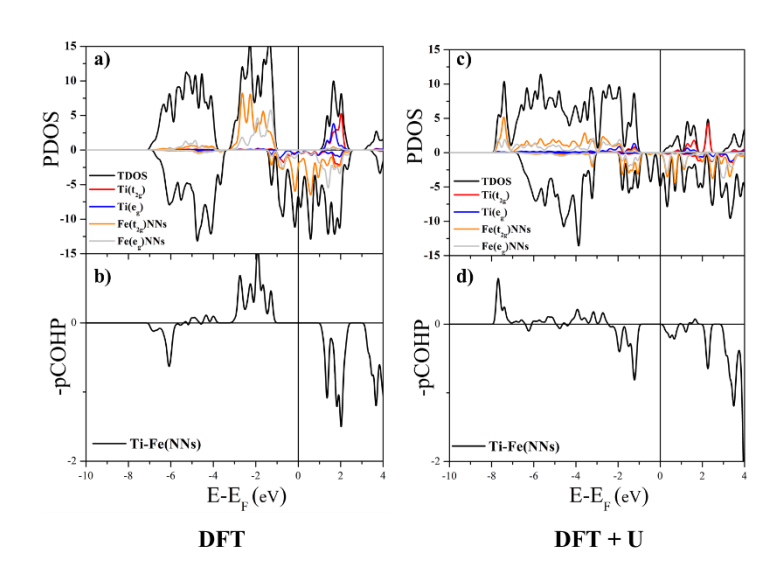


Fig. 4. Projected Density of States and Crystal Orbital Hamiltonian Population curves for (a) Ti-FeCl₂ without U parameter and (b) Ti-FeCl₂ without U parameter. Black, red, blue, orange and green curves correspond to the Total DOS, Ti e_g, Ti t_{2g} orbitals, t_{2g} and eg orbitals of the nearest neighbor Fe to Ti, respectively.

The strong influence of electron correlation on the electronic and magnetic behavior of 2D transition metal (TM) halides arises mainly from the presence of narrow t_{2g} or e_g states near the Fermi level. This complex interplay means that standard density functional theory (DFT) methods, such as LSDA or GGA, often fail to accurately predict their physical properties. As a result, advanced theoretical frameworks like DFT+U are indispensable for a proper description [41]. Hubbard parameters have been taken from the Reference [42]. Because of this reason, the efficient determination of the electronic structures of the TM-FeCl₂ layers have been investigated through the inclusion of the Hubbard U parameters. It is very well known that the crystal field of the neighboring Fe atoms to the embedded transition metal atom undergoes a crystal field splitting [43]. The half-metallicity of the Ti based layer originated from the 3 Fe atoms neighboring the embedded atom. According to Figure 4a, triply degenerate t_{2g} states (d_{xy} , d_{yz} , d_{xz}) and

the doubly degenerate, e.g., states (d_{x2-y2} , d_{z2}) of neighboring Fe atoms are nearly responsible for all electronic states around the Fermi level where there is a minute contribution from Ti atoms. In Fig. 4a, the 3d orbitals of the Ti atom embedded in Cl position show clear interactions with its surrounding Fe atoms at around -1 and -2 eV in spin-up channels. In this regime, the interactions have bonding nature according to the Fig. 4b. It is quite apparent that the conductive behavior of the structure is wholly driven through a spin down channel, which is a half-metallic behavior prerequisite for spintronic applications. Simultaneously, there is a noticeable gap at the spin-up channel. Cl atoms contribute to filling electronic states from -4 eV to the deeper states because TM and Fe contributions are minute. After the inclusion of the Hubbard parameters, the half-metallicity is preserved. The electron conductance is provided through spin-down channel in Fig. 4c, while there is a clear gap at the spin-up channel. According to the pCOHP plots in Fig. 4d, between -1 and -2 eV, the interactions are mainly antibonding. To better understanding the half-metallicity, the picture can be more clear from the band gap plots.

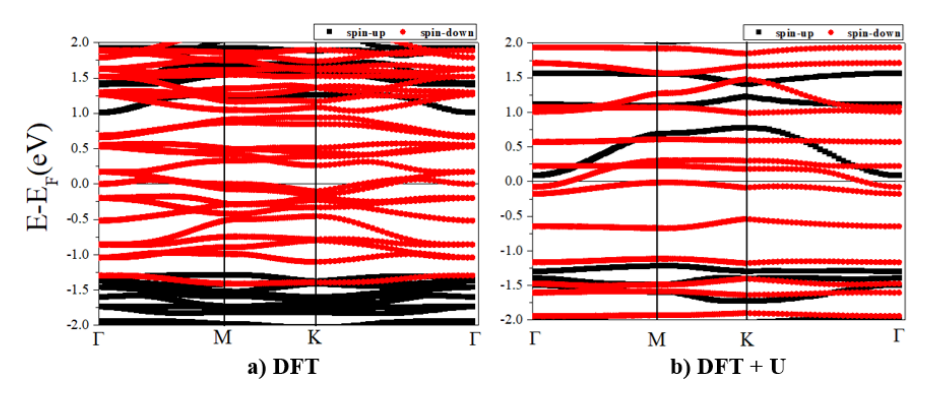


Fig. 5. The calculated band structure plots for the Ti-FeCl₂ layer (a) with DFT and (b) DFT+U. Black and red curves correspond to the bands in spin-up and down channels, respectively.

In Figure 5, spin-polarized electronic band structure figures over the high symmetry points in the Brillouin zones of Ti-FeCl₂ can be seen. In Fig. 5a, where the Hubbard parameters are not included, the conductivity is provided over the spin-down channel which is coherent with the PDOS figures in Fig. 4. Here, the electronic band gap is around 2.5 eV. In Fig. 4b, Ti-FeCl₂ still preserves the half-metallicity although the electronic structure has been dramatically influenced by the U correction. Especially the inclusion of the U parameter into the calculations considerably increases the plausibility of the calculations. The electronic band structure plots for the other layers can be seen between Figs. S2 and S7. From these plots for the other layers, the electronic behavior change is completely between metallicity and semiconductivity.

Conclusions

This article investigated the effect of embedding various transition metals on Cl defects in FeCl₂ material. First, transition metal embedding has been shown to cause a wide range of magnetization values. At this stage, it was determined that Ti-FeCl₂ layers showed half-metallic behavior. The same electronic behavior was observed after the inclusion of the Hubbard U parameter where the Band structure and PDOS plots support each other. Our computations have clarified that the other transition metal embeddings do not provide half-metallicity and electronic behavior swings between metallicity and semiconductivity. Finally, it is suggested that the transition metal embedding strategy in FeCl₂ layers has serious potential for spintronic applications due to the properties as mentioned above.

Acknowledgment

The numerical calculations reported in this paper were completely performed at TUBITAK ULAKBIM, High

Performance and Grid Computing Center (TRUBA resources).

References

- [1] L. Shi and X. Luo, "A first-principles investigation of spintronics of nitrophosphorene doped with 3d transition metals," J. Appl. Phys., vol. 125, no. 23, 2019, doi: 10.1063/1.5089903.
- [2] M. N. Baibich, et al., "Giant magnetoresistance of (001) Fe/(001) Cr magnetic superlattices," Phys. Rev. Lett., vol. 61, no. 21, p. 2472, 1988, doi: 10.1103/PhysRevLett.61.2472.
- [3] I. Khan Muhammad, K. Swera, and M. Abdul, "Computational study of 4d transition metals doped bismuthene for spintronics," Physica E Low-Dimens. Syst. Nanostruct., vol. 126, p. 114464, 2021, doi: 10.1016/j.physe.2020.114464.
- [4] D. Gao, et al., "Defect-related ferromagnetism in ultrathin metal-free gC₃N₄ nanosheets," Nanoscale, vol. 6, no. 5, pp. 2577–2581, 2014, doi: 10.1039/c3nr04743a.
- [5] M. Luo, H. Yin, and Y. Shen, "Magnetic and electronic properties of BN nanosheets with different nonmagnetic metal dopants: A first-principles study," J. Supercond. Nov. Magn., vol. 31, pp. 2211–2216, 2018, doi: 10.1007/s10948-018-4589-8.
- [6] E.-J. Kan, et al., "Half-metallicity in hybrid BCN nanoribbons," J. Chem. Phys., vol. 129, no. 8, 2008, doi: 10.1063/1.2971187.
- [7] K. Li, et al., "First-principles study on ferromagnetism in C-doped AlN," Phys. Lett. A, vol. 374, no. 35, pp. 3671–3675, 2010, doi: 10.1016/j.physleta.2010.07.011.
- [8] A. S. Botana and M. R. Norman, "Electronic structure and magnetism of transition metal dihalides: bulk to monolayer," Phys. Rev. Mater., vol. 3, no. 4, p. 044001, 2019, doi: 10.1103/PhysRevMaterials.3.044001.
- [9] M. Ashton, et al., "Two-dimensional intrinsic half-metals with large spin gaps," Nano Lett., vol. 17, no. 9, pp. 5251–5257, 2017, doi: 10.1021/acs.nanolett.7b01367.
- [10] M. A. McGuire, "Crystal and magnetic structures in layered, transition metal dihalides and trihalides," Crystals, vol. 7, no. 5, p. 121, 2017, doi: 10.3390/cryst7050121.
- [11] X. Zhou, et al., "Atomically thin 1T-FeCl₂ grown by molecular-beam epitaxy," J. Phys. Chem. C, vol. 124, no. 17, pp. 9416–9423, 2020, doi: 10.1021/acs.jpcc.0c03050.
- [12] E. Torun, et al., "Stable half-metallic monolayers of FeCl₂," Appl. Phys. Lett., vol. 106, no. 19, 2015, doi: 10.1063/1.4921096.
- [13] C. Sun and X. Luo, "Tuning the magnetic and electronic properties of monolayer VI₃ by 3d transition metal doping: A first-principles study," Appl. Surf. Sci., vol. 571, p. 151208, 2022, doi: 10.1016/j.apsusc.2021.151208.
- [14] P. Giannozzi, et al., "Advanced capabilities for materials modelling with Quantum ESPRESSO," J. Phys. Condens. Matter, vol. 29, no. 46, p. 465901, 2017, doi: 10.1088/1361-648X/aa8f79.
- [15] P. Giannozzi, et al., "QUANTUM ESPRESSO: a modular and open-source software project for quantum simulations of materials," J. Phys. Condens. Matter, vol. 21, no. 39, p. 395502, 2009, doi: 10.1088/0953-8984/21/39/395502.
- [16] X. Liao, et al., "Density functional theory for electrocatalysis," Energy Environ. Mater., vol. 5, no. 1, pp. 157–185, 2022, doi: 10.1002/eem2.12204.
- [17] P. E. Blöchl, "Projector augmented-wave method," Phys. Rev. B, vol. 50, no. 24, p. 17953, 1994, doi: 10.1103/PhysRevB.50.17953.
- [18] G. Kresse and D. Joubert, "From ultrasoft pseudopotentials to the projector augmented-wave method," Phys. Rev. B, vol. 59, no. 3, p. 1758, 1999, doi: 10.1103/PhysRevB.59.1758.
- [19] J. P. Perdew, K. Burke, and M. Ernzerhof, "Generalized gradient approximation made simple," Phys. Rev. Lett., vol. 77, no. 18, p. 3865, 1996, doi: 10.1103/PhysRevLett.77.3865.
- [20] H. J. Monkhorst and J. D. Pack, "Special points for Brillouin-zone integrations," Phys. Rev. B, vol. 13, no. 12, p. 5188, 1976, doi: 10.1103/PhysRevB.13.5188.
- [21] G. Henkelman, A. Arnaldsson, and H. Jónsson, "A fast and robust algorithm for Bader decomposition of charge density," Comput. Mater. Sci., vol. 36, no. 3, pp. 354–360, 2006, doi: 10.1016/j.commatsci.2005.04.010.
- [22] E. Sanville, et al., "Improved grid based algorithm for Bader charge allocation," J. Comput. Chem., vol. 28, no. 5, pp. 899 908, 2007, doi: 10.1002/jcc.20575.
- [23] W. Tang, E. Sanville, and G. Henkelman, "A grid-based Bader analysis algorithm without lattice bias," J. Phys. Condens. Matter, vol. 21, no. 8, p. 084204, 2009, doi: 10.1088/0953-8984/21/8/084204.
- [24] V. L. Deringer, A. L. Tchougréeff, and R. Dronskowski, "Crystal orbital Hamilton population (COHP) analysis as projected from plane-wave basis sets," J. Phys. Chem. A, vol. 115, no. 21, pp. 5461–5466, 2011, doi: 10.1021/jp202489s.
- [25] R. Dronskowski and P. E. Bloechl, "Crystal orbital Hamilton populations (COHP): energy-resolved visualization of chemical bonding in solids based on density-functional calculations," J. Phys. Chem., vol. 97, no. 33, pp. 8617–8624, 1993, doi: 10.1021/j100135a014.
- [26] R. Y. Rohling, et al., "Electronic structure analysis of the Diels-Alder cycloaddition catalyzed by alkali-exchanged faujasites," J. Phys. Chem. C, vol. 122, no. 26, pp. 14733–14743, 2018, doi: 10.1021/acs.jpcc.8b04409.
- [27] R. Y. Rohling, et al., "Correlations between density-based bond orders and orbital-based bond energies for chemical bonding analysis," J. Phys. Chem. C, vol. 123, no. 5, pp. 2843–2854, 2019, doi: 10.1021/acs.jpcc.8b08934.
- [28] R. Van Santen and I. Tranca, "How molecular is the chemisorptive bond?" Phys. Chem. Chem. Phys., vol. 18, no. 31, pp. 20868–20894, 2016, doi: 10.1039/C6CP01394E.
- [29] R. A. van Santen, I. Tranca, and E. J. Hensen, "Theory of surface chemistry and reactivity of reducible oxides," Catal. Today, vol. 244, pp. 63–84, 2015, doi: 10.1016/j.cattod.2014.07.009.
- [30] P. C. Müller, et al., "Crystal orbital bond index: covalent bond orders in solids," J. Phys. Chem. C, vol. 125, no. 14, pp. 7959–7970, 2021, doi: 10.1021/acs.jpcc.1c00718.

- [31] K. B. Wiberg, "Application of the Pople-Santry-Segal CNDO method to the cyclopropylcarbinyl and cyclobutyl cation and to bicyclobutane," Tetrahedron, vol. 24, no. 3, pp. 1083–1096, 1968, doi: 10.1016/0040-4020(68)88057-3.
- [32] I. Mayer, "Charge, bond order and valence in the AB initio SCF theory," Chem. Phys. Lett., vol. 97, no. 3, pp. 270-274, 1983, doi: 10.1016/0009-2614(83)80005-0.
- [33] S. Maintz, et al., "LOBSTER: A tool to extract chemical bonding from plane wave based DFT," J. Comput. Chem., 2016, doi: 10.1002/jcc.24300.
- [34] S. J. Clark, et al., "First principles methods using CASTEP," Z. Kristallogr., vol. 220, no. 5-6, pp. 567-570, 2005, doi: 10.1524/zkri.220.5.567.65075.
- [35] R. K. Ghosh, A. Jose, and G. Kumari, "Intrinsic spin-dynamical properties of two-dimensional half-metallic FeX₂ (X = Cl, Br, I) ferromagnets: Insight from density functional theory calculations," Phys. Rev. B, vol. 103, no. 5, p. 054409, 2021, doi: 10.1103/PhysRevB.103.054409.
- [36] Yang, Y., et al., "An insulating and easy magnetization-plane magnet: The DFT+ U and constrained electron population study of 1 T-FeCl₂," Computational Materials Science, vol. 233, p. 112752, 2024. https://doi.org/10.1016/j.commatsci.2023.112752
- [37] D. V. Yandulov and R. R. Schrock, "Catalytic reduction of dinitrogen to ammonia at a single molybdenum center," Science, vol. 301, no. 5629, pp. 76–78, 2003, doi: 10.1126/science.1085326.
- [38] E. Dražević and E. Skúlason, "Are there any overlooked catalysts for electrochemical NH₃ synthesis—new insights from analysis of thermochemical data," iScience, vol. 23, no. 12, p. 101803, 2020, doi: 10.1016/j.isci.2020.101803.
- [39] V. Orazi, et al., "DFT study of the hydrogen adsorption and storage on Ni₄ cluster embedded in multivacancy graphene," Int. J. Hydrogen Energy, vol. 45, no. 55, pp. 30805–30817, 2020, doi: 10.1016/j.ijhydene.2020.08.106.
- [40] L. Pauling, "The nature of the chemical bond. IV. The energy of single bonds and the relative electronegativity of atoms," J. Am. Chem. Soc., vol. 54, no. 9, pp. 3570–3582, 1932, doi: 10.1021/ja01348a011.
- [41] Wang, H., V. Eyert, and U. Schwingenschlögl, "Electronic structure and magnetic ordering of the semiconducting chromium trihalides CrCl3, CrBr3, and Crl3". Journal of Physics: Condensed Matter, Vol. 23, no. 11, p. 116003. 2011.doi: 10.1088/0953-8984/23/11/116003
- [42] Yekta, Y., et al., "Strength of effective Coulomb interaction in two-dimensional transition-metal halides MX 2 and MX 3 (M= Ti, V, Cr, Mn, Fe, Co, Ni; X= Cl, Br, I)". Physical Review Materials, Vol. 5, no. 3: p. 034001, 2021. doi: https://doi.org/10.1103/PhysRevMaterials.5.034001
- [43] Y. Feng, et al., "Robust half-metallicities and perfect spin transport properties in 2D transition metal dichlorides," J. Mater. Chem. C, vol. 6, no. 15, pp. 4087–4094, 2018, doi: 10.1039/C8TC00443A.



Contents lists available at Dergipark

Journal of Scientific Reports-A

journal homepage: https://dergipark.org.tr/tr/pub/jsr-a



E-ISSN: 2687-6167

Number 62, September 2025

RESEARCH ARTICLE

Crustal melting during exhumation of the Menderes Core Complex: Insights from the mineral chemistry of the Güneşli granite (Western Türkiye)

Ömer Kamacı^a*

^aIstanbul Technical University. Eurasia Institute of Earth Sciences. Sartyer. Istanbul. 34469. Türkiye, ORCID: 0000-0002-6893-2985

Abstract

The Güneşli Granite, located in the Gördes Submassif within the northern part of the Menderes Massif, represents one of the Early Miocene intrusions in the region. This high-K calc-alkaline, slightly peraluminous two-mica granite comprises two compositional members: granite and granodiorite, with some exhibiting adaktic signatures. This study investigates the intrusion's plagioclase, biotite, and muscovite chemistry. Plagioclases in the Güneşli granite predominantly consist of oligoclase, while the granodiorite exhibits anorthite contents ranging from An₁₄ to An₃₀, indicating oligoclase and occasionally andesine compositions. Black micas are classified as biotite, characterized by high Fe numbers and convergence toward annite composition due to low A1^{IV} content. White micas are classified as muscovite based on their low Si and ferromagnesian content. Both mica types are of magmatic origin and show no evidence of post-magmatic alteration. Measured minerals are generally similar in adakitic and non-adakitic samples; however, adaktic rocks exhibit higher OH⁻ compositions. The source rocks are predominantly crustal and closely resemble the peraluminous biotites found in S-type granites. The intrusion's oxygen fugacity (fO2), determined from biotite chemistry, indicates a slightly oxidizing state at FMQ+0.1 to +0.8 buffer. Thermobarometric calculations based on machine learning applied to biotite chemistry suggest that the magma crystallized at depths between 5.8 and 10.5 kbar, deeper than previously expected, with temperatures ranging from 723 to 779 °C. The integration of regional geology, field studies, and mineral chemistry indicates that the Güneşli granites originated from deep-crustal sections and were emplaced at mid-crustal depths within the Menderes Massif. These crustal-derived granites evolved through assimilation-fractional crystallization, indicating a crustal reworking during the development of the Gördes Dome in the Early Miocene.

© 2023 DPU All rights reserved.

Keywords: Menderes Massif, Güneşli granite, mineral chemistry, thermobarometry,

* Corresponding author. Tel.: 0 212 2857361 *E-mail address:* kamaciom@itu.edu.tr

1. Introduction

The Aegean region is a key example of extensional tectonics (Fig. 1a) [1]. Within this framework, Western Anatolia, located in the back-arc region of the Hellenic arc, has been subjected to intense extensional tectonics since the Oligocene, driven primarily by slab rollback of the Hellenic subduction zone [2; and references therein]. This extensional regime has resulted in the formation of extensional sedimentary basins, syn-extensional granitoids, and the exhumation of metamorphic core complexes, such as the Uludağ, Kazdağ, Çataldağ, and Menderes complexes [3-19].

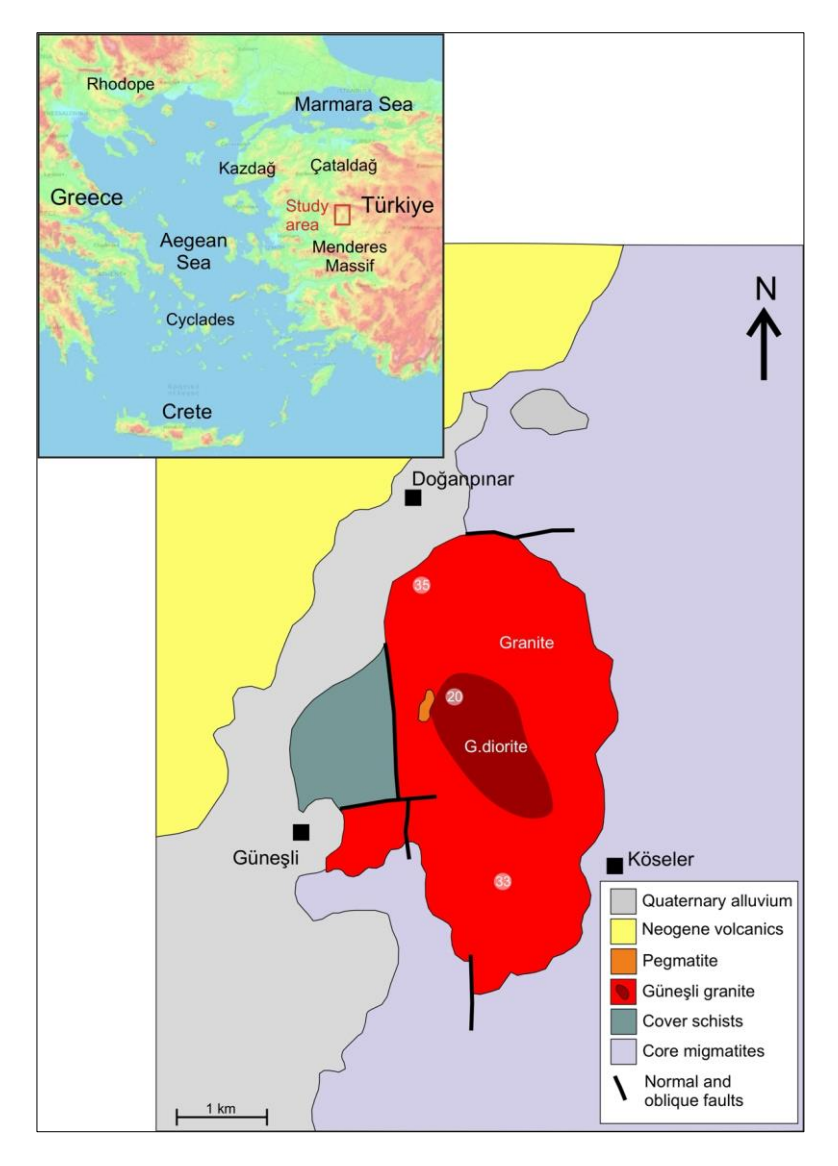


Fig. 1. Digital image of the Aegean Region and Western Anatolia (ESRI) (a) and geological map of Güneşli granite (after Kamacı, 2025) (b). Metamorphic massifs and core complexes: Rhodope, Menderes, Kazdağ, Çataldağ, Cyclades. Numbers show analytic samples.

The tectonic and magmatic evolution of Western Anatolia is linked to the collision of the Sakarya Continent in the north and the Anatolide-Tauride Platform (Menderes-Taurus block) in the south along the İzmir-Ankara-Erzincan Suture Zone (IAESZ), which occurred before the Eocene [20, 21, 22]. Following this collision, long-lived magmatism developed, characterized by distinct phases from the Eocene [14-33], Eo-Oligocene [16, 34, 35] and Early-Middle Miocene [36-50], with a broad spatial distribution from the Marmara Region to the Bodrum Peninsula.

The Menderes Massif, located south of the İzmir-Ankara-Erzincan suture zone within the Anatolide-Tauride block (Fig. 1), represents an elliptical-shaped core complex with NE-SW orientation, divided by E-W trending grabens [52]. Based on the Alaşehir (Gediz) and Büyük Menderes grabens, the massif is subdivided into three regions: the Northern submassif (Gördes), the Central submassif, and the Southern submassif (Çine) [53].

The Menderes Massif consists of Precambrian-aged augen gneisses, metagranites, high-grade schists, and metagabbros, and Palaeozoic-Cenozoic-aged schists and metamorphosed carbonates [54-59]. The massif exhibits multiple metamorphic phases, with its primary metamorphism attributed to the Palaeocene–Early Oligocene, linked to the emplacement of the Lycian nappes and ophiolitic thrust sheets [60, 61, 62]. Late-stage migmatization in the Gördes submassif is associated with this deformation phase.

The subsequent exhumation of the massif and deformation leading to syn-tectonic granite emplacement is widely dated to the Late Oligocene–Early Miocene [63, 4, 64, 65]. Northward-directed motion along detachment faults facilitated the massif's exhumation as a core complex, driven by the Oligo-Miocene activity of the Simav, Büyük Menderes, and Alaşehir detachment faults [4, 64, 66, 67, 3, 68, 69, 70]. The syn-extensional granitoids, such as the Eğrigöz, Koyunoba, Alaçamdağ and Turgutlu-Salihli granodiorites, crystallized during the Early to Middle Miocene (21–15 Ma), documenting the interaction of crustal and mantle-derived magmas during extension. These granitoids, along with the Early Miocene Eğrigöz Pluton, exhibit high-K calc-alkaline signatures and were emplaced during the exhumation phases of the Menderes Metamorphic core complex [71, 67, 72, 12, 11, 73].

The Güneşli granite (Fig. 1b) is located in the northern Menderes "Gördes" Massif, which includes the Gördes structural dome. This dome consists of core migmatites that are part of the Menderes Massif [74, 75, 76]. The Güneşli granite intrudes these migmatitic rocks as dykes and sills [74, 77, 51]. Cooling ages determined by K-Ar dating of biotite and muscovite are 19.4 and 28.8 Ma, respectively [78] and while U-Pb zircon ages are 22.3 ± 1.2 Ma [51]. The Güneşli granite exhibits granodiorite to granite compositions (Fig. 2a). Granodiorite is characterized by 45–40% plagioclase. 35–30% quartz. 17–14% K-feldspar. 8–5% biotite. and 5–3% muscovite. Granite (monzogranite) contains 35–30% plagioclase. 35–30% quartz. 28–20% K-feldspar. 8–5% biotite. and 5–3% muscovite. with a notably higher proportion of K-feldspar [51]. Both lithologies commonly exhibit a holocrystalline granular texture (Figs 2b and 2c). Secondary phases include opaque minerals. sericite. and muscovite. while zircon occurs as an accessory phase.

They are high-K calc-alkaline, slightly peraluminous, and show a crustal signature based on Sr-Nd isotopes [51]. Initially categorized as crustal-derived S-type granites [79], later studies by [77] and [51] suggested that they are two-mica I-type granites. Notably, the Güneşli samples display a unique adaktic signature among the Miocene granites of the Menderes Massif, characterized by high Sr/Y and $La_{N/}Yb_{N}$ ratios [51].

Mineral chemistry also provides an understanding of source rocks. This study will present plagioclase, biotite and muscovite mineral chemistry of Güneşli granite to estimate magmatic processes such as crystallization temperature, magma chamber depth, oxygen fugacity and water contents. Combining with regional geology magma chamber parameters helps us to understand crustal processes in Menderes Massif during the exhumation period in the Early Miocene.



Fig. 2. Güneşli granite in the field (a) and under polarizing microscope. cross-polarized (b) and plane-polarized (c).

2. Analytical Methods – EPMA

EPMA was installed at the Earth Sciences Application and Research Centre (YEBIM) of Ankara University. Point and line analyses were carried out on polished thin sections using a JEOL JXA-8230 instrument which is equipped with 5m wavelengths—dispersive spectrometers. Operating conditions were 20 kV accelerating voltage and 20 nA beam current. Natural oxide and mineral reference materials were used for calibration and measurements. The following standards were used: Mg (diopside), Na (albite), Si (orthoclase), F (fluorite), Mn (rhodonite), Al (orthoclase), Fe (olivine), K (orthoclase), Ti (titanium oxide), Ba (barite) and Ca (diopside). Detection limits of standards for each element are 150 ppm for Mg, 188 ppm for Na, 242 ppm for Si, 1087 ppm for F, 94 ppm for Mn,

85 ppm for Al, 104 ppm for Fe, 27 ppm for K, 69 ppm for Ti, 176 ppm for Ba and 39 ppm for Ca. The standard deviation of standard samples for all elements is 0.18% for Mg, 0.30% for Na, 0.08% for Si, 0.26% for F, 0.11% for Mn, 0.12% for Al, 0.21% for Fe, 0.08% for K, 0.07% for Ti, Ba and Ca. Matrix effects were corrected with the ZAF software provided by JEOL which made corrections for atomic number effects (Z), absorption (A) and fluorescence (F). Carbon coating was made using Quorum Q150T ES machine.

3. Results

3.1. Plagioclase

The plagioclases within the Güneşli granite predominantly exhibit euhedral prismatic crystals and oligoclase compositions (Figs 2 and 3). The plagioclase chemistry of Güneşli granite is shown in Table 1. In granodiorite (G-20), the anorthite content ranges from An₁₄ to An₃₀, corresponding to oligoclase and, less commonly, andesine compositions. Measurements taken from the core to the rim indicate an evolutionary trend, starting with andesine and ending with oligoclase. At the outermost rim, there is a sharp decrease in the anorthite content (Fig. 3).

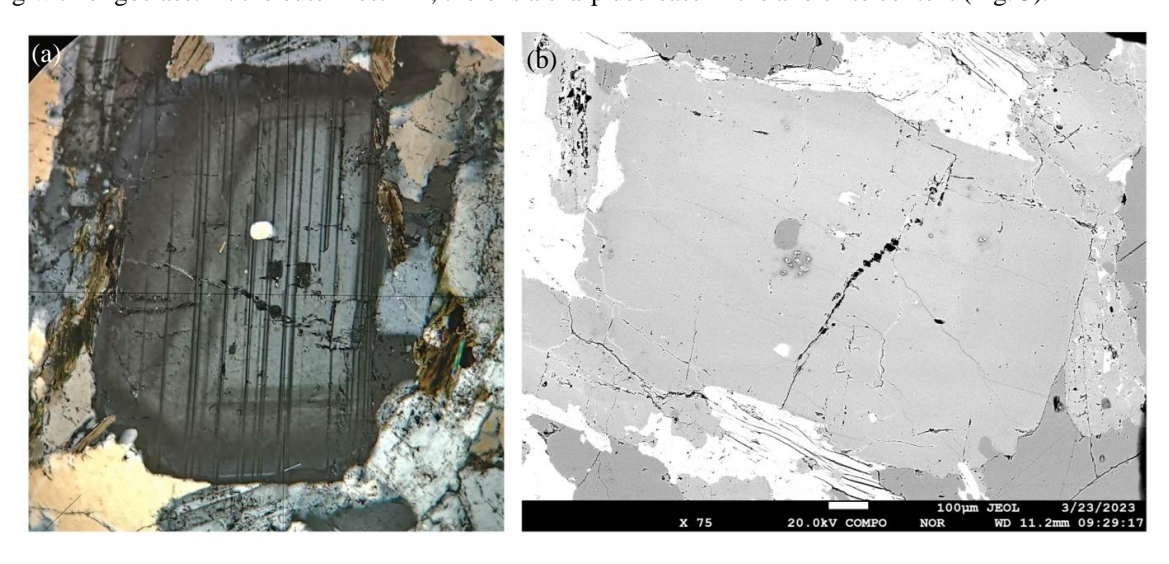


Fig. 3. Cross-polarized light microscope image (a) and backscattered electron image (BSE) of a zoned plagioclase crystal (b) from the G-35 granite sample.

Table 1. Composition (wt % oxides) and Ab-An-Or proportion for plagioclase.

Sample	Spot	Na ₂ O	SiO_2	Al_2O_3	K_2O	FeO	TiO_2	CaO	Total	Anorthite	Albite	Sanidine
	G-35-a6	8.73	68.80	19.5	0.37	0.02	0	1.61	99.1	15	82	3
G-35)	G-35-a5	8.46	68.36	19.5	0.43	0.02	0	1.67	98.5	16	80	4
ple C	G-35-a4	8.44	68.08	20.2	0.44	0.00	0	1.81	98.9	17	79	4
(Sample	G-35-a3	8.21	68.41	20.1	0.44	0.01	0	1.91	99.1	18	78	4
Granite	G-35-a2	8.18	67.92	20.8	0.40	0.02	0.001	1.97	99.3	19	78	4
Gra	G-35-a1	8.27	68.31	20.3	0.40	0.00	0.019	1.88	99.2	18	78	4
-	G-35-b4	8.46	68.19	19.9	0.31	0.06	0.01	1.70	98.6	16	81	3

Kamacı, Ö., (2025) / Journal of Scientific Reports-A, 062, 40-60

	G-35-b3	7.89	68.59	20.2	0.35	0.00	0	1.99	99.1	19	77	3
	G-35-b2	8.20	68.37	20.5	0.37	0.01	0	2.00	99.4	19	78	3
	G-35-b1	7.76	68.55	21.0	0.38	0.00	0.003	2.28	100.0	22	74	4
	G-20-a6	8.03	67.24	20.8	0.45	0.02	0	1.88	98.4	18	78	4
	G-20-a5	6.84	66.20	22.3	0.43	0.01	0.011	2.72	98.5	27	68	4
	G-20-a4	7.24	66.81	22.3	0.44	0.02	0.011	2.52	99.3	25	71	4
	G-20-a3	6.67	65.49	23.1	0.35	0.01	0	2.93	98.5	29	67	3
(0)	G-20-a2	6.59	65.91	23.0	0.35	0.01	0	3.08	99.0	31	66	3
6-5-5	G-20-a1	6.85	66.72	23.2	0.33	0.00	0.009	2.79	99.8	28	69	3
Granodiorite (Sample G-20)	G-20-b2	6.88	66.88	23.0	0.34	0.00	0.006	2.79	99.9	28	69	3
te (S	G-20-b1	6.90	65.96	22.9	0.26	0.00	0.013	2.96	99.1	29	68	3
diori	G-20-c6	8.29	66.10	22.4	0.29	0.04	0.006	1.59	98.8	16	82	3
rano	G-20-c5	8.44	66.92	22.8	0.38	0.05	0.001	1.46	100.0	14	82	4
9	G-20-c4	6.59	64.16	23.6	0.29	0.01	0	2.92	97.5	30	67	3
	G-20-c3	7.06	63.80	23.5	0.38	0.00	0.007	2.68	97.4	27	70	4
	G-20-c2	6.91	63.98	23.3	0.36	0.01	0	2.74	97.3	27	69	4
	G-20-c1	7.40	64.39	22.7	0.35	0.02	0	2.26	97.1	23	74	3
	G-20-c7	7.52	65.08	22.6	0.36	0.01	0.015	2.17	97.8	22	75	4
	G-33-a4	8.20	69.19	18.6	0.32	0.03	0	1.43	97.8	14	82	3
	G-33-a3	7.99	69.56	20.6	0.39	0.01	0	1.85	100.3	18	78	4
	G-33-a2	7.87	68.48	21.3	0.42	0.03	0.003	1.86	100.0	18	78	4
33)	G-33-a1	7.53	67.60	21.4	0.36	0.03	0	2.19	99.1	22	75	4
Granite (Sample G-33)	G-33-b1	7.90	69.74	20.9	0.40	0.03	0	1.62	100.6	16	80	4
ampl	G-33-c7	8.53	67.96	19.8	0.28	0.05	0	1.53	98.2	15	83	3
te (S	G-33-c6	8.58	68.74	20.3	0.38	0.02	0.008	1.57	99.6	15	82	4
Grani	G-33-c5	8.09	68.53	20.6	0.41	0.01	0	1.71	99.3	17	79	4
O	G-33-c4	7.91	68.13	19.9	0.39	0.02	0	1.96	98.3	19	77	4
	G-33-c3	7.91	68.52	20.1	0.36	0.02	0.01	2.08	99.0	20	76	3
	G-33-c2	8.45	68.83	19.4	0.37	0.06	0.008	1.62	98.8	16	81	4
	G-33-c1	7.47	68.18	20.9	0.34	0.01	0.004	2.38	99.3	23	73	3

The plagicclases in sample G-35 from the granite are oligoclase in composition, with an anorthite range of An_{15} to An_{22} . In zoned crystals, the transition from the core to the rim is characterized by decreased anorthite content. However, this transition is not particularly pronounced (Fig. 4). Similarly, in the other granite sample, G-33, the composition is oligoclase (An_{14} - An_{23}) and exhibits characteristics similar to those of sample G-35.

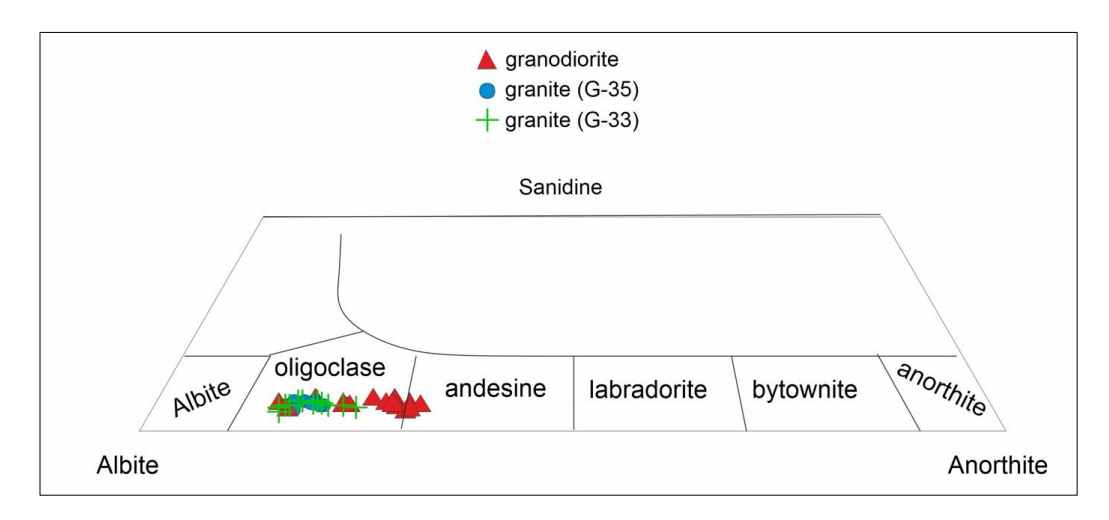


Fig. 4. Plagioclase classification of the Güneşli granite.

3.2. Biotite

The black micas in the Güneşli granite are in subhedral form and classified as biotite due to their high Fe numbers and exhibit a convergence toward annite composition, as indicated by their low Al^{IV} contents (Fig. 5 and Table 2). In the ternary diagram proposed by [80], the biotites are classified as primary magmatic biotites.

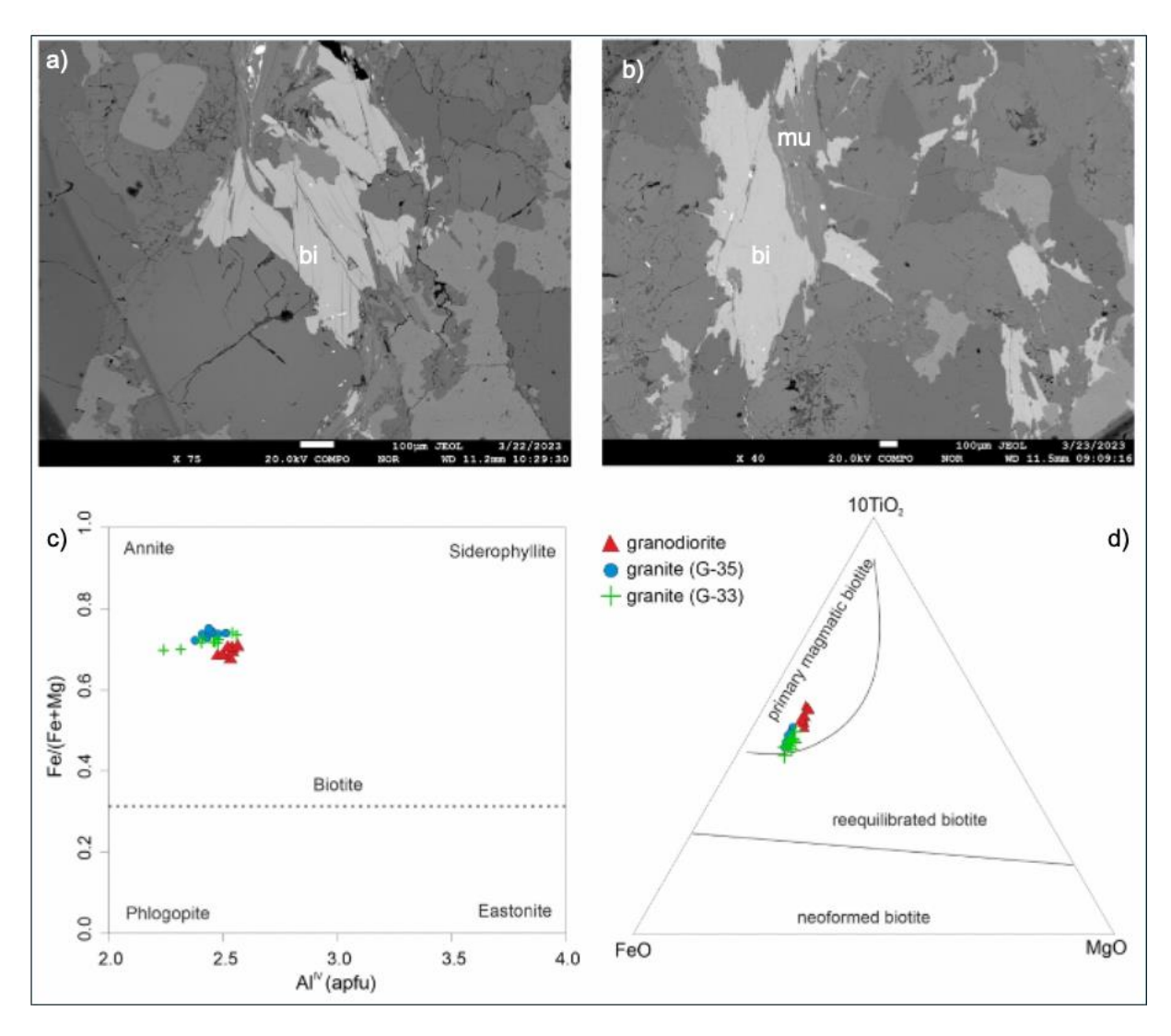


Fig. 5. BSE images of biotites from the Güneşli granite (a and b) and classification diagrams (c and d). bi: biotite. mu: muscovite.

Table 2. Biotite major oxide and F-Cl chemistry of Güneşli granite. Oxides are shown as wt% and elements as atoms per formula unit (apfu).

Sample					G-35	(Granite)				
Spot	G-35a-1	G-35a-2	G-35b-1	G-35b-2	G-35c-1	G-35c-2	G-35d-1	G-35d-2	G-35e-1	G-35e-2
Na_2O	0.2	0.2	0.1	0.2	0.2	0.1	0.1	0.2	0.2	0.2
MgO	4.4	4.6	4.9	4.5	4.6	4.7	4.5	4.5	4.5	4.4
SiO_2	35.5	36.0	36.2	34.9	36.4	36.3	36.1	36.4	36.0	35.7
F	0.3	0.3	0.5	0.5	0.4	0.4	0.5	0.4	0.5	0.2
Al_2O_3	18.9	18.7	18.3	19.1	18.9	18.6	18.9	19.5	18.9	18.2
K_2O	10.7	10.4	8.7	8.8	8.8	8.8	8.7	8.8	8.9	9.0
FeO	22.0	21.8	22.6	23.0	22.9	24.1	22.9	22.5	23.4	23.6
TiO_2	2.5	2.4	2.3	2.4	2.4	2.3	2.7	2.5	2.4	2.6
Cr_2O_3	0.021	0.002	0.009	0	0	0.023	0.006	0.006	0.001	0.005
Cl	0.05	0.05	0.057	0.054	0.051	0.064	0.046	0.059	0.064	0.057
CaO	0	0.011	0.013	0.014	0.018	0.022	0.01	0.052	0.045	0.028
Total	94.55	94.41	93.67	93.54	94.51	95.38	94.65	94.81	94.83	93.94
Li ₂ O*	0.64	0.78	0.85	0.48	0.90	0.86	0.82	0.90	0.78	0.68
H_2O^*	3.72	3.73	3.62	3.59	3.72	3.71	3.65	3.75	3.64	3.72
Subtotal	98.90	98.91	98.14	97.60	99.13	99.96	99.12	99.45	99.26	98.34
Si	5.52	5.57	5.62	5.49	5.59	5.56	5.56	5.56	5.55	5.56
$Al^{\mathrm{i}\nu}$	2.48	2.43	2.38	2.51	2.41	2.44	2.44	2.44	2.45	2.44
Al^{vi}	0.98	0.99	0.97	1.03	1.01	0.92	0.99	1.07	0.98	0.92
Ti	0.30	0.28	0.26	0.28	0.27	0.27	0.32	0.29	0.28	0.30
Fe	2.86	2.82	2.94	3.02	2.93	3.09	2.94	2.86	3.01	3.08
Mg	1.02	1.06	1.13	1.06	1.05	1.07	1.03	1.01	1.04	1.03
Li*	0.40	0.48	0.53	0.30	0.55	0.53	0.51	0.55	0.48	0.43
Na	0.05	0.05	0.04	0.06	0.05	0.03	0.04	0.06	0.07	0.05
K	2.13	2.06	1.71	1.77	1.72	1.71	1.71	1.71	1.75	1.78
ОН*	3.86	3.85	3.75	3.76	3.81	3.79	3.74	3.81	3.75	3.87
Temperature**	759	759	739	734	730	736	738	730	740	738
Pressure**	10.46	10.13	6.76	6.89	6.83	6.84	6.73	6.93	6.98	6.82

Sample				anodiorite)	e)					
Spot	G-20a-2	G-20a-1	G-20b-1	G-20b-2	G-20c-1	G-20c-2	G-20d-1	G-20d-2	G-20e-1	G-20e-2
Na_2O	0.2	0.2	0.2	0.2	0.1	0.2	0.1	0.2	0.2	0.2
MgO	5.8	5.6	5.3	5.4	5.2	5.3	5.6	5.6	5.2	5.2
SiO_2	35.5	36.0	35.1	35.1	35.0	35.3	35.6	35.8	34.8	35.3
F	0.2	0.3	0.2	0.1	0.4	0.1	0.3	0.1	0.1	0.3

Al_2O_3	19.4	19.2	19.1	19.1	18.7	19.0	18.1	18.6	18.8	18.8
K2O	8.8	8.7	8.6	8.7	8.7	8.7	8.9	8.7	8.9	8.9
FeO	21.4	21.7	22.0	21.9	22.2	22.1	21.9	21.8	22.7	22.3
TiO_2	2.7	2.8	2.9	3.0	3.3	3.0	3.2	3.2	2.9	2.9
Cr_2O_3	0	0	0.006	0.015	0	0	0.004	0	0.008	0.01
Cl	0.074	0.071	0.077	0.083	0.089	0.084	0.082	0.078	0.079	0.083
CaO	0.01	0	0.01	0.015	0.013	0.013	0.015	0.006	0.018	0.004
Total	93.97	94.61	93.41	93.60	93.78	93.73	93.87	93.99	93.72	94.19
Li ₂ O*	0.65	0.78	0.51	0.53	0.49	0.57	0.68	0.71	0.43	0.59
H_2O*	3.81	3.79	3.71	3.77	3.62	3.80	3.71	3.82	3.76	3.69
Subtotal	98.42	99.18	97.63	97.90	97.88	98.11	98.26	98.52	97.91	98.47
Si	5.47	5.50	5.46	5.46	5.46	5.47	5.52	5.50	5.43	5.48
Al iv	2.53	2.50	2.54	2.54	2.54	2.53	2.48	2.50	2.57	2.52
Al vi	0.98	0.96	0.97	0.95	0.89	0.95	0.82	0.87	0.91	0.92
Ti	0.31	0.32	0.34	0.35	0.39	0.35	0.38	0.37	0.34	0.34
Fe	2.75	2.77	2.86	2.84	2.90	2.86	2.84	2.81	2.97	2.90
Mg	1.32	1.28	1.24	1.24	1.22	1.22	1.30	1.29	1.22	1.21
Li*	0.40	0.48	0.32	0.33	0.30	0.35	0.42	0.44	0.27	0.37
Na	0.06	0.07	0.05	0.06	0.04	0.05	0.03	0.05	0.05	0.05
K	1.72	1.70	1.71	1.73	1.74	1.73	1.76	1.70	1.76	1.76
OH*	3.91	3.86	3.86	3.91	3.77	3.93	3.84	3.92	3.92	3.81
Temperature**	726	732	733	728	746	723	743	729	728	735
Pressure**	6.23	6.42	6.5	6.31	6.48	5.82	6.45	6.01	6.11	6.35

Sample					G-33 (Granite)				
Spot	G-33a-1	G-33a-2	G-33b-1	G-33b-2	G-33c-1	G-33c-2	G-33d-1	G-33d-2	G-33e-1	G-33e-2
Na ₂ O	0.2	0.2	0.2	0.1	0.2	0.2	0.2	0.2	0.2	0.2
MgO	4.6	4.7	4.9	4.8	5.0	5.0	5.0	4.9	5.2	5.2
SiO_2	35.1	34.9	35.4	35.8	35.0	35.5	35.6	35.1	37.2	37.0
F	0.3	0.4	0.2	0.2	0.4	0.3	0.3	0.1	0.3	0.3
Al_2O_3	18.7	18.9	18.3	17.6	17.8	18.1	18.5	18.3	17.5	18.4
K2O	10.8	10.8	10.8	10.7	10.4	10.5	8.6	8.3	8.1	8.2
FeO	23.5	23.1	22.9	22.9	22.4	22.5	22.9	21.8	21.4	21.7
TiO_2	2.3	2.4	2.1	2.3	2.6	2.4	2.5	2.3	2.3	2.1
Cr_2O_3	0.003	0	0	0	0.01	0	0.011	0	0.014	0.035
Cl	0.077	0.07	0.074	0.096	0.09	0.063	0.058	0.085	0.095	0.094
CaO	0.001	0	0.002	0.008	0.002	0.006	0.001	0.013	0.002	0.004

Kamacı, Ö., (2025) / Journal of Scientific Reports-A, 062, 40-60

Total	95.66	95.32	94.92	94.52	93.79	94.68	93.76	91.11	92.16	93.23
Li ₂ O*	0.52	0.45	0.61	0.72	0.48	0.65	0.67	0.53	1.11	1.06
H_2O^*	3.69	3.65	3.74	3.72	3.57	3.71	3.69	3.67	3.71	3.72
Subtotal	99.87	99.43	99.27	98.95	97.84	99.04	98.12	95.31	96.98	98.00
Si	5.46	5.44	5.52	5.59	5.52	5.53	5.54	5.59	5.76	5.68
Al iv	2.54	2.56	2.48	2.41	2.48	2.47	2.46	2.41	2.24	2.32
Al vi	0.89	0.91	0.88	0.83	0.84	0.86	0.94	1.04	0.96	1.01
Ti	0.27	0.28	0.24	0.27	0.31	0.29	0.29	0.27	0.26	0.25
Fe	3.06	3.01	2.99	2.99	2.96	2.93	2.98	2.90	2.77	2.79
Mg	1.07	1.09	1.14	1.12	1.18	1.16	1.17	1.16	1.20	1.20
Li*	0.32	0.28	0.38	0.45	0.30	0.41	0.42	0.34	0.69	0.65
Na	0.05	0.05	0.06	0.04	0.05	0.06	0.07	0.07	0.05	0.05
K	2.15	2.15	2.15	2.13	2.09	2.08	1.70	1.68	1.59	1.61
OH*	3.83	3.80	3.89	3.87	3.77	3.86	3.83	3.90	3.84	3.81
Temperature**	760	763	759	776	777	768	737	731	740	730
Pressure**	10.49	10.43	10.34	10.54	10.07	10.01	6.6	6.59	6.82	6.56

^{*}Calculated by the machine learning approach of Li et al., 2020

3.3. Muscovite

All white micas observed in the Güneşli granites are classified as muscovite according to the classification by [81], characterized by low Si and ferromagnesian contents (Fig. 6 and Table 3). To test whether the muscovites formed through post-magmatic processes from biotite, the Güneşli samples were evaluated using the classification by [82]. Based on their high Na and low Mg contents, they are identified as primary magmatic muscovites (Fig. 6).

^{**}Calculated by the machine learning approach of Li and Zhang, 2022

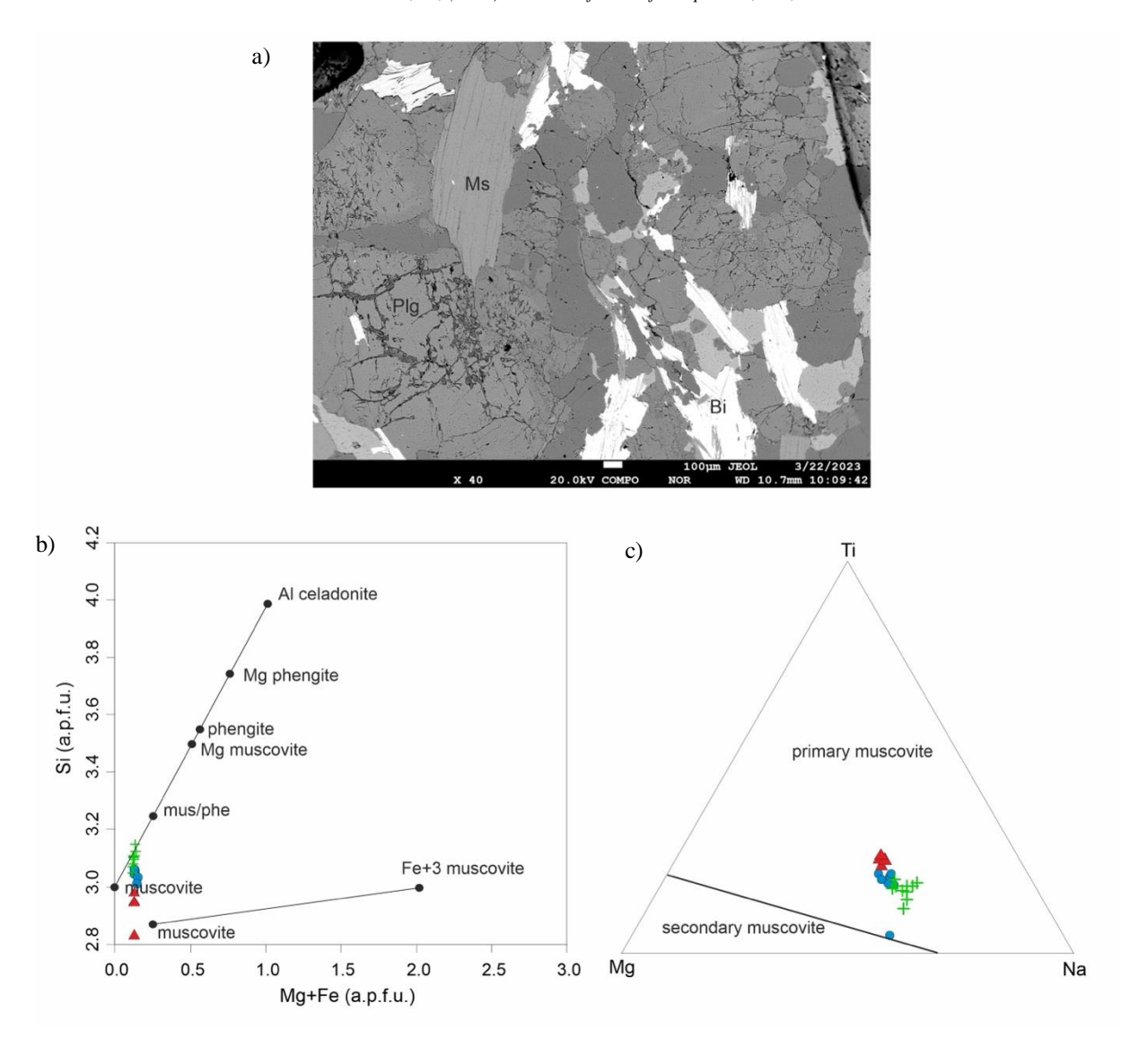


Fig. 6. BSE image of muscovite (a) and classification diagrams (b and c). Ms: muscovite. Bi: biotite. Plg: plagioclase.

Table 3. Muscovite major oxide chemistry of Güneşli granite. Oxides are shown as wt% and elements as atoms per formula unit (apfu).

	Spt	Na ₂ O	MgO	SiO_2	Al_2O_3	K_2O	FeO	TiO ₂	CaO	Total	Si	Ti	Al	Fe	Mg	Na	K
	a1	0.6	0.5	44.6	35.5	9.6	1.4	0.48	0.01	92.7	3	0.03	2.9	0.08	0.05	0.08	0.83
anite)	a2	0.6	0.5	44.8	35.2	9.2	1.4	0.57	0.01	92.5	3	0.03	2.8	0.08	0.05	0.08	0.81
Gr.	a3	0.6	0.5	44.5	34.9	9.3	1.5	0.56	0.00	91.9	3	0.03	2.8	0.09	0.05	0.08	0.81
G-35	b1	0.6	0.5	44.6	35.1	9.4	1.4	0.52	0.01	92.3	3	0.03	2.8	0.08	0.05	0.08	0.82
	b2	0.6	0.5	45.0	35.0	9.5	1.3	0.58	0.00	92.7	3	0.03	2.8	0.08	0.05	0.08	0.82

	b3	0.6	0.5	44.9	35.2	9.7	1.3	0.48	0.00	92.7	3	0.02	2.8	0.08	0.05	0.08	0.84
	c1	0.6	0.5	44.6	35.8	9.5	1.7	0.16	0.02	93.1	3	0.01	2.9	0.10	0.05	0.08	0.83
	c2	0.6	0.5	43.6	35.4	9.4	1.5	0.52	0.02	91.7	3	0.03	2.9	0.09	0.05	0.08	0.83
	a2	0.6	0.5	42.4	35.0	10.0	1.27	0.73	0.00	90.4	3	0.04	2.9	0.07	0.05	0.08	0.89
G-20	a1	0.6	0.5	42.4	35.9	10.0	1.33	0.77	0.01	91.6	3	0.04	2.9	0.08	0.05	0.08	0.88
ؿ	b1	0.6	0.5	41.0	38.0	10.0	1.32	0.80	0.02	92.5	3	0.04	3.1	0.08	0.05	0.08	0.88
	b2	0.6	0.5	42.9	36.5	9.7	1.35	0.83	0.02	92.3	3	0.04	3.0	0.08	0.05	0.08	0.85
	a-1	0.7	0.5	45.5	34.6	8.7	1.31	0.53	0.01	92.0	3	0.03	2.8	0.07	0.05	0.09	0.76
	a-2	0.6	0.4	44.8	34.2	8.7	1.37	0.51	0.02	90.9	3	0.03	2.8	0.08	0.04	0.09	0.77
	b1	0.6	0.4	45.2	35.0	9.3	1.34	0.50	0.02	92.7	3	0.03	2.8	0.08	0.05	0.08	0.81
ite)	b2	0.6	0.5	45.6	34.6	9.4	1.40	0.56	0.01	92.7	3	0.03	2.8	0.08	0.05	0.08	0.82
Gran	c1	0.6	0.4	44.9	35.1	9.4	1.33	0.50	0.01	92.5	3	0.03	2.8	0.08	0.04	0.08	0.82
G-33 (Granite)	c2	0.7	0.4	44.5	35.3	9.3	1.33	0.56	0.01	92.1	3	0.03	2.9	0.08	0.04	0.09	0.81
9	d1	0.7	0.5	45.2	34.6	9.3	1.44	0.43	0.01	92.1	3	0.02	2.8	0.08	0.05	0.09	0.81
	d2	0.6	0.5	45.9	34.7	9.2	1.46	0.51	0.01	93.1	3	0.03	2.8	0.08	0.05	0.08	0.80
	e1	0.7	0.5	45.2	33.7	9.3	1.46	0.37	0.02	91.2	3	0.02	2.7	0.08	0.05	0.10	0.82
	e2	0.7	0.5	45.4	33.1	9.3	1.47	0.51	0.01	90.9	3	0.03	2.7	0.08	0.05	0.09	0.82

4. Magma Chamber Conditions

The Güneşli granite's pressure-temperature conditions were calculated using the Ti-in-biotite thermometer [83] and the biotite thermobarometer based on a machine-learning approach [84]. The Ti-in-biotite thermometer by [83] is highly sensitive to Ti content and is valid within a pressure range of 4-6 kbar. According to this method, the crystallization temperature of the granite ranges from 570 to 620 °C, while the granodiorite exhibits higher temperatures, ranging from 610 to 650 °C (Fig. 7a). These temperature estimates are notably cooler than the typical crystallization temperature of biotite.

The machine learning approach of [84] provides a more reliable temperature estimate for biotite crystallization, ranging from 723 to 777 $^{\circ}$ C across all samples (Fig. 7b). No significant temperature difference was observed between the granite and granodiorite samples. The K_2 O-sensitive approach estimates a wide range of pressures for the granites, ranging from 6.2 to 10.5 kbar, while the granodiorite is associated with shallower conditions, with pressures ranging from 5.8 to 6.5 kbar.

A pressure of 10 kbar is unlikely to represent a reliable crystallization environment for the studied samples, as the potential source rocks are not derived from the deepest sections of the Menderes crust (51). Instead, the source rocks are expected to be more felsic and emplaced at shallower depths than 10 kbar. Consequently, a pressure of around 6 kbar is considered a more plausible estimate for the magma chamber depth of the Güneşli two-mica granites (please see the following section for the source discussion).

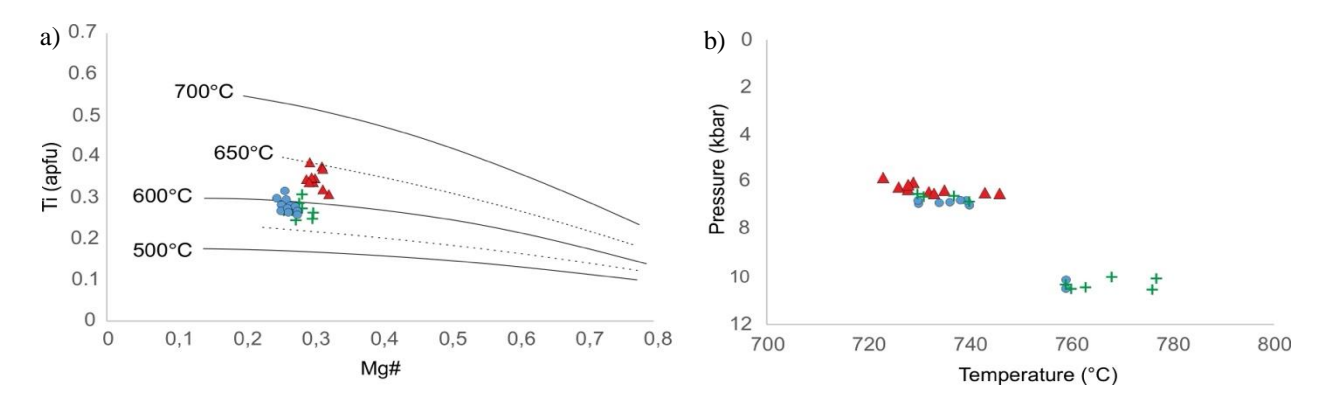


Fig. 7. Ti-in-biotite thermometry results (a) and Machine-learning thermobarometry estimations (b) for biotites of Güneşli granite.

The oxygen fugacity (fO_2) calculations, attributed to [85], indicate intermediate oxidation states for granite and granodiorite, with values falling between +0.1 and +0.8 relative to the FMQ buffer, reflecting an oxidizing environment (Fig. 8). Among these, the adakitic granodiorite exhibits the highest fO_2 values, while the non-adakitic granite shows the lowest. This aligns with the expectation that adakitic melts typically form under higher oxidizing conditions

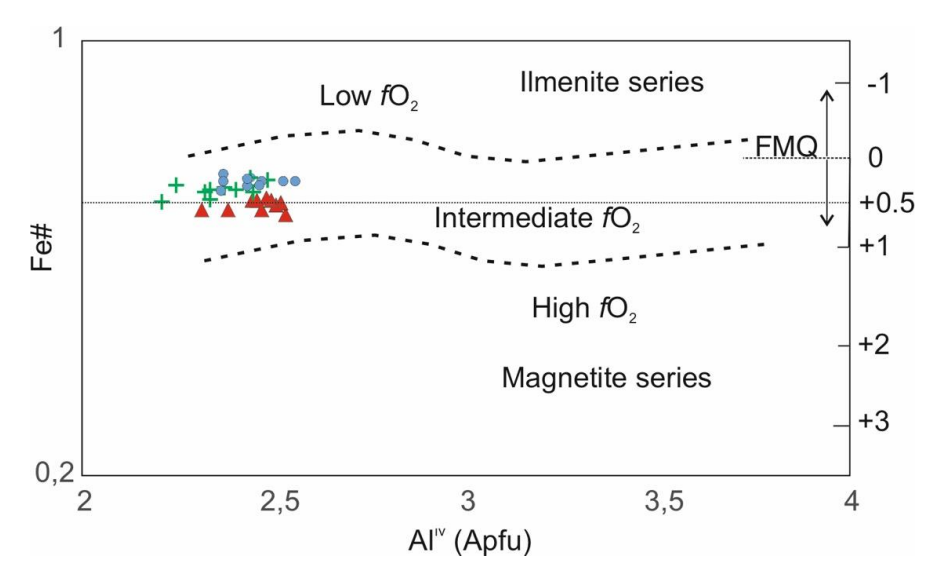


Fig. 8. Oxygen fugacity estimations of biotites in Güneşli granite.

In summary, empirical approaches suggest that the emplacement conditions of the Güneşli granites were characterized by temperatures ranging from 723 to 777 °C, pressures around 6 kbar, corresponding to mid-crustal depths, and slightly oxidizing conditions.

5. Source Rock and Evolution

The high SiO₂ content (>71.6 wt.%), elevated ASI (Alumina Saturation Index = 1.0–1.1), high initial Sr isotopic ratios (0.709275 to 0.712199), and low εNd values (from -10.6 to -7.3) of the Güneşli Granite (GG) are distinct indicators of its crustal sources (51). The presence of muscovite and its primary magmatic character supports the hypothesis that the Güneşli granite is a product of crustal-derived magma (Fig. 6c).

The biotites also give some clues about crustal sources. They plot within the S-type peraluminous field, according to [86] (Fig. 9a). Similarly, in the classification by [87], they fall within the field of S-type granites, characterized by a high aluminium saturation index (Fig. 9b). In the source rock affinity diagram [88], similar results are observed, with the biotites plotting in the crustal-derived biotite field due to their high Fe numbers (Fig. 9c). Low anorthite compositions of plagioclases also support a felsic rock, which is a possible member of Menderes crust.

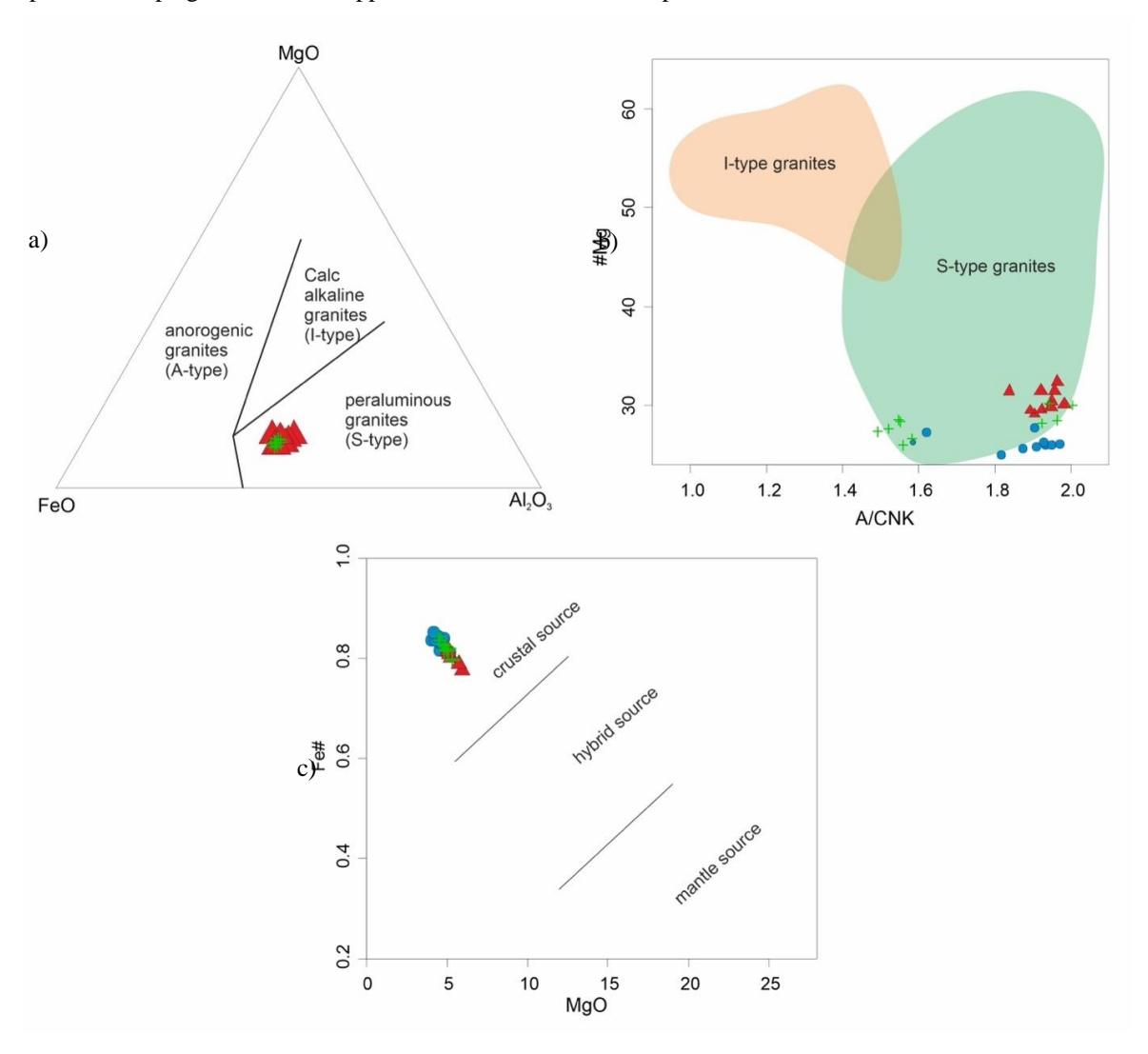


Fig. 9. Tectonic discrimination (a and b) and source rock (c) of biotites in Güneşli granite. The references are cited within the text.

Interestingly, the whole-rock classification of the Güneşli granite (GG) identifies it as a peraluminous I-type granite with an aluminium saturation index (ASI) below 1.1 [51]. However, the biotites within GG show characteristics typical of S-type plutons. This discrepancy may result from the assimilation of high K_2O -bearing rocks during open-system differentiation. Incorporating K_2O increases the proportion of alkali components, reducing the ASI (Al $_2O_3$ / (CaO + Na $_2O$ + K_2O)) and leading to the classification of GG as an I-type granite.

Another important observation is the adakitic signatures of the Güneşli granites. These signatures become more pronounced in some samples but are absent in others [51]. Although the adakitic signature is not associated with slab melting, its primary formation mechanism is water-present melting in the lower crust. Consequently, the OH-composition of biotite plays a key role in influencing adakitic signatures. Additionally, the F/Cl ratio of biotites is significant, as it reflects high water activity during biotite crystallization. This effect is evident in the diagram, where biotites from adakitic rocks display high OH- content and low F/Cl ratios (Fig. 10).

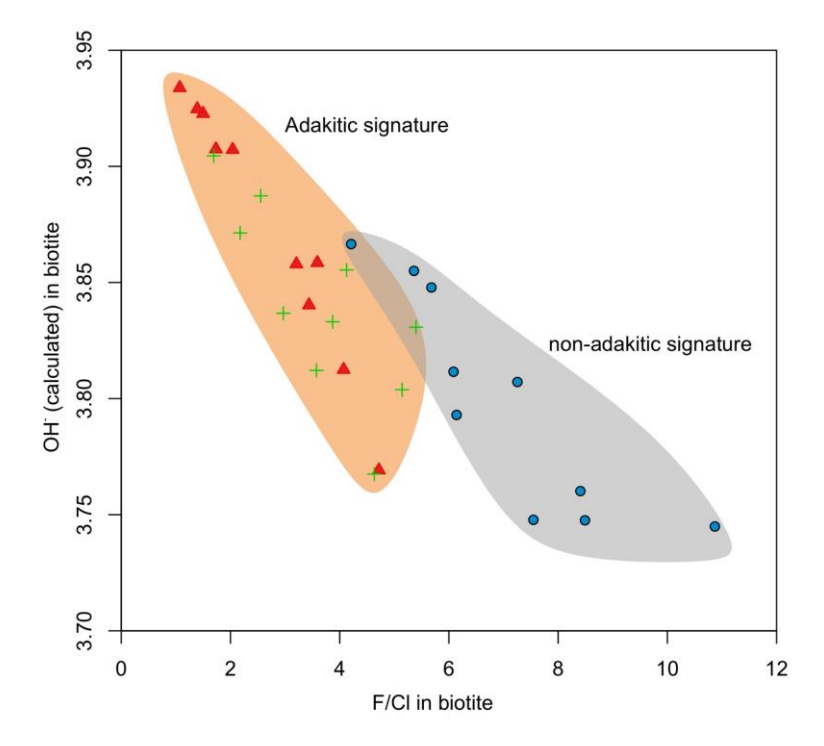


Fig. 10. OH- vs F/Cl in biotites of Güneşli granite. OH- values are calculated by [89].

Magmatic evolution within the mid-crustal magma chamber of the Güneşli Granite (GG) samples reveals open system effects [51]. Anorthite compositions in plagioclase decrease from core to rim, suggesting a reduction in anorthite content during magmatic evolution. While this trend could result from fractional crystallization in a closed system, the evolved members, such as the Güneşli granites, exhibit initial isotope data that dynamically reflect open-system evolution. This is consistent with assimilation and fractional crystallization (AFC) processes involving enriched crustal materials. This effect is evident even in the granodioritic sample, where the anorthite content decreases from An₃₀ to An₁₈ in the rim (Fig. 11). A similar evolutionary trend is observed in the biotite chemistry of

the granodiorite sample (G-20), where the calculated crystallization temperatures decrease from core to rim, ranging from 746 °C to 723 °C (Fig. 12).

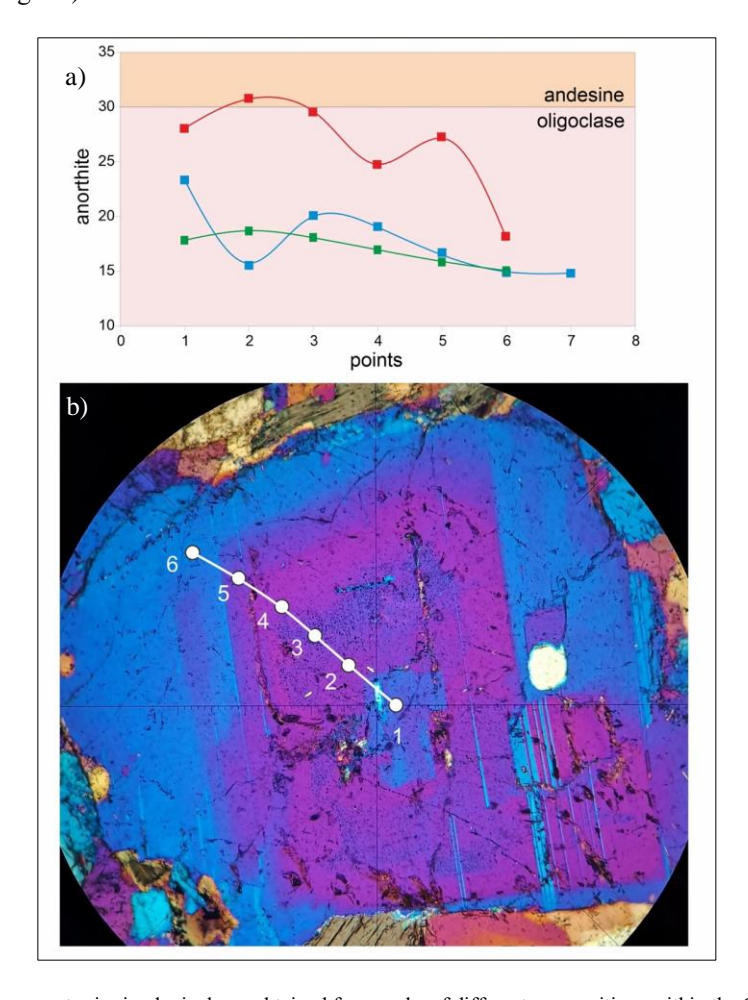


Fig. 11. Anorthite variation from core to rim in plagioclases obtained from rocks of different compositions within the Güneşli granite (a); analysis points of zoned plagioclase in granodiorite (granodiorite sample – red symbol). In crossed polar with quartz plate. Magnification: 4x.

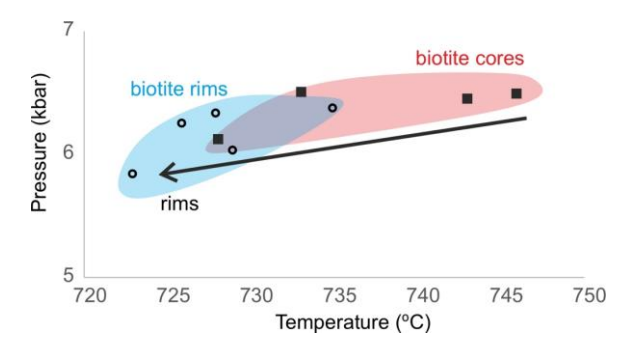


Fig. 12. Temperature changes from cores and rims of biotites in Güneşli granite

In summary, the Güneşli Granite (GG) samples evolved, likely following an open-system trend involving crustal assimilation in a mid-crustal magma chamber. No evidence of new hot magma batches intruding during the magmatic evolution exists.

6. Conclusions

This study on the mineral chemistry of the Güneşli granite provides critical insights into its petrogenesis and emplacement. The findings suggest that the Güneşli granite was derived from crustal source(s) and intruded into the mid-crustal levels of the Menderes Massif during the Early Miocene. Adakitic signatures are evident in the higher OH values and lower F/Cl ratios observed in biotites. Temperature profiles reveal a decrease through the rim zones of plagioclase and biotite, accompanied by a decline in oxygen fugacity from granodiorite to granite compositions.

All analytical data indicate that the magmatic evolution of the Güneşli granite occurred in an open system characterized by increasing crustal assimilation over time. These findings are significant for understanding crustal reworking processes during the exhumation of the Menderes Massif as a metamorphic core complex, which occurred amidst the intense extensional tectonics of Western Anatolia in the Early Miocene.

Acknowledgement

This study was supported by Istanbul Technical University (Scientific Research Projects - BAP Project 43563). I extend my thanks to T. Arık for his assistance during the fieldwork and K. Deniz for their support with the EPMA in YEBİM. I am also deeply grateful to S. Altunkaynak, A. Ünal and A. T. Ünlüer for their insightful scientific discussions regarding the study area. Special appreciation goes to M. A. Oral for his meticulous work in preparing the thin sections for this research. The editors and reviewers provided valuable feedback that enhanced the quality of the manuscript.

References

- [1] Jolivet, L., & Faccenna, C., 2000. Mediterranean extension and the Africa-Eurasia collision. Tectonics, 19(6), 1095-1106. https://doi.org/10.1029/2000TC900018
- [2] Jolivet, L., Faccenna, C., Huet, B., Labrousse, L., Le Pourhiet, L., Lacombe, O., & Driussi, O., 2013. Aegean tectonics: Strain localisation, slab tearing and trench retreat. Tectonophysics, 597, 1-33.
- [3] Gessner, K., Ring, U., Johnson, C., Hetzel, R., Passchier, C. W., & Güngör, T., 2001. An active bivergent rolling-hinge detachment system: Central Menderes metamorphic core complex in western Turkey. Geology, 29(7), 611-614.
- [4] Işık, V., Seyitoğlu, G., & Çemen, İ., 2003. Ductile-brittle transition along the Alaşehir detachment fault and its structural relationship with the Simav detachment fault, Menderes massif, western Turkey. Tectonophysics, 374(1), 1-18. https://doi.org/10.1016/S0040-1951(03)00275-0
- [5] Çemen, I., Catlos, E. J., Göğüş, O., & Özerdem, C., 2006. Postcollisional extensional tectonics and exhumation of the Menderes massif in the Western Anatolia extended terrane, Turkey. In: Dilek, Y., Pavlides, S. (Eds.), Postcollisional Tectonics and Magmatism in the Mediterranean Region and Asia. Geological Society of America, pp. 279-312.
- [6] Dilek, Y., Altunkaynak, Ş., Öner, Z., 2009. Syn-extensional granitoids in the Menderes core complex and the late Cenozoic extensional tectonics of the Aegean province. In: Ring, U., et al. (Eds.), Extensional Tectonics of the Western Mediterranean Region. Geological Society, London, Special Publications, 321, 197-223. https://doi.org/10.1144/SP321.10
- [7] Catlos, E. J., Baker, C., Sorensen, S. S., Çemen, I., & Hançer, M., 2010. Geochemistry, geochronology, and cathodoluminescence imagery of the Salihli and Turgutlu granites (central Menderes Massif, western Turkey): Implications for Aegean tectonics. Tectonophysics, 488(1-4), 110-130.
- [8] Catlos, E., Jacob, L., Oyman, T., & Sorensen, S., 2012. Long-term exhumation of an Aegean metamorphic core complex granitoids in the Northern Menderes Massif, western Turkey. American Journal of Science, 312(5), 534-571.
- [9] Hasözbek, A., Akay, E., Erdoğan, B., Satır, M., & Siebel, W., 2010. Early Miocene granite formation by detachment tectonics or not? A case study from the northern Menderes Massif (Western Turkey). Journal of Geodynamics, 50(2), 67-80.
- [10] Öner, Z., & Dilek, Y., 2011. Supradetachment basin evolution during continental extension: The Aegean province of Western Anatolia, Turkey. Geological Society of America Bulletin.
- [11] Erkül, S. T., & Erkül, F., 2012. Magma interaction processes in syn-extensional granitoids: The Tertiary Menderes Metamorphic Core Complex, western Turkey. Lithos, 142-143, 16-33. https://doi.org/10.1016/j.lithos.2012.02.008

- [12] Altunkaynak, Ş., Dilek, Y., Genç, C.Ş., Sunal, G., Gertisser, R., Furnes, H., Foland, K.A., Yang, J., 2012a. Spatial, temporal and geochemical evolution of Oligo–Miocene granitoid magmatism in western Anatolia, Turkey. Gondwana Research, 21, 961–986. https://doi.org/10.1016/j.gr.2011.10.010
- [13] Erkül, F., Erkül, S. T., Manap, H. S., & Çolak, C., 2017. An extensional and transfersional origin of elongated magmatic domes and localised transfer faults in the northern Menderes metamorphic core complex, western Turkey. Geodinamica Acta, 29(1), 139-159.
- [14] Okay, A. I., & Satir, M., 2000. Coeval plutonism and metamorphism in a latest Oligocene metamorphic core complex in northwest Turkey. Geological Magazine, 137(5), 495-516. https://doi.org/10.1017/S0016756800004532
- [15] Genç, Ş. C., & Altunkaynak, Ş., 2007. Eybek graniti (Biga yarımadası, KB Anadolu) üzerine: Yeni jeokimya verileri ışığında yeni bir değerlendirme. Yerbilimleri, 28(2), 75-98.
- [16] Okay, A. I., Satir, M., Zattin, M., Cavazza, W., & Topuz, G., 2008. An Oligocene ductile strike-slip shear zone: The Uludağ Massif, northwest Turkey—Implications for the westward translation of Anatolia. Geological Society of America Bulletin, 120(7-8), 893-911.
- [17] Black, K. N., Catlos, E. J., Oyman, T., & Demirbilek, M., 2013. Timing Aegean extension: evidence from in situ U-Pb geochronology and cathodoluminescence imaging of granitoids from NW Turkey. Lithos. 180, 92-108.
- [18] Kamacı, Ö., & Altunkaynak, Ş., 2019a. Cooling and deformation history of the Çataldağ Metamorphic Core Complex (NW Turkey). Journal of Asian Earth Sciences, 172, 279-291. https://doi.org/10.1016/j.jseaes.2018.09.012
- [19] Altunkaynak, Ş., Ünal, A., Sunal, G., Kamacı, Ö., Dunkl, I., 2021. Miocene uplift and exhumation history of northwestern Anatolia (Turkey): Implications from apatite (U-Th)/He thermochronology of syn-extensional plutons. Journal of Asian Earth Sciences, 213, 104770.
- [20] Şengör, A. M. C., & Yılmaz, Y., 1981. Tethyan evolution of Turkey: A plate tectonic approach. Tectonophysics, 75(3-4), 181-241. https://doi.org/10.1016/0040-1951(81)90275-4
- [21] Okay, A. I., & Tüysüz, O., 1999. Tethyan sutures of northern Turkey. In: Durand, B., et al. (Eds.), The Mediterranean Basins: Tertiary Extension Within the Alpine Orogen. Geological Society, London, Special Publications, 156, 475-515. https://doi.org/10.1144/GSL.SP.1999.156.01.22
- [22] Şengör, A. M. C., Lom, N., Sunal, G., Zabcı, C., & Sancar, T., 2019. The phanerozoic palaeotectonics of Turkey. Part I: an inventory. Mediterranean Geoscience Reviews, 1, 91-161.
- [23] Genç, S., & Yilmaz, Y. (1997). An example of post-collisional magmatism in northwestern Anatolia: the Kızderbent volcanics (Armutlu peninsula, Turkey). Turkish Journal of Earth Sciences. 6(1), 33-42.
- [24] Okay, A. I., & Satir, M., 2006. Geochronology of Eocene plutonism and metamorphism in northwest Turkey. Geodinamica Acta, 19(5), 251-266.
- [25] Karacık, Z., Yılmaz, Y., Pearce, J. A., & Ece, Ö. I., 2008. Petrochemistry of the south Marmara granitoids, northwest Anatolia, Turkey. International Journal of Earth Sciences, 97(6), 1181-1200.
- [26] Ustaömer, P. A., Ustaömer, T., Collins, A. S., & Reischpeitsch, J., 2009. Lutetian arc-type magmatism along the southern Eurasian margin: new U-Pb LA-ICPMS and whole-rock geochemical data from Marmara Island, NW Turkey. Mineralogy and Petrology, 96(1-2), 177-196.
- [27] Gülmez, F., Genç, Ş. C., Keskin, M., & Tüysüz, O., 2013. A post-collision slab-breakoff model for the origin of the Middle Eocene magmatic rocks of the Armutlu–Almacık belt, NW Turkey and its regional implications. Geological Society, London, Special Publications, 372(1), 107-139. [28] Altunkaynak, Ş., Sunal, G., Aldanmaz, E., Genç, C.Ş., Dilek, Y., Furnes, H., Foland, K.A., Yang, J., Yıldız, M., 2012b. Eocene Granitic Magmatism in NW Anatolia (Turkey) revisited: New implications from comparative zircon SHRIMP U–Pb and 40Ar–39Ar geochronology and isotope geochemistry on magma genesis and emplacement. Lithos, 155, 289–309. https://doi.org/10.1016/j.lithos.2012.09.008
- [29] Güraslan, I. N., & Altunkaynak, Ş., 2019. Role of mantle and lower continental crust in the genesis of Eocene post-collisional granitoids: Insights from the Topuk pluton (NW Turkey). Journal of Asian Earth Sciences, 179, 365-384. https://doi.org/10.1016/j.jseaes.2019.05.012
- [30] Özyurt, M., & Altunkaynak, Ş., 2020. Origin of Eocene adakitic magmatism in northwest Turkey. Journal of Asian Earth Sciences, 190, 104147.
- [31] Ersoy, E. Y., Akal, C., Palmer, M. R., & Mertz-Kraus, R., 2023. U-Pb dating of arc to post-collisional magmatic events in northwestern Anatolia: The Eocene Granitoids in NW Anatolia revisited. Journal of Asian Earth Sciences: X, 9, 100148.
- [32] Kocatürk, H., Kumral, M., Creaser, R. A., DuFrane, S. A., Ünlüer, A. T., Sendir, H., Abdelnasser, A., 2024. Magma nature and tectonomagmatic context of the Eocene Uludağ granitoids (NW-Türkiye): Insights into the Cenozoic geodynamics of the Tethyan Orogenic Belt. Geochemistry, 126170.
- [33] Arık, T., Ünal, A., Altunkaynak, Ş. (2025). An Eocene transtensional shear zone driven by the strain localization along slab break-off: Implications from the sheared syn-kinematic northern Kapıdağ Pluton (NW Anatolia, Turkey). Journal of Asian Earth Sciences, 279, 106444. https://doi.org/10.1016/j.jseaes.2024.106444
- [34] Topuz, G., & Okay, A. I., 2017. Late Eocene–Early Oligocene two-mica granites in NW Turkey (the Uludağ Massif): Water-fluxed melting products of a mafic metagreywacke. Lithos, 268-271, 334-350. https://doi.org/10.1016/j.lithos.2016.11.010
- [35] Kamacı, Ö., & Altunkaynak, Ş., 2020. The role of accreted continental crust in the formation of granites within the Alpine style continental collision zone: Geochemical and geochronological constrains from leucogranites in the Çataldağ Metamorphic Core Complex (NW Turkey). Lithos, 354-355, 105347. https://doi.org/10.1016/j.lithos.2019.105347
- [36] Aldanmaz, E., Pearce, J. A., Thirlwall, M. F., & Mitchell, J. G., 2000. Petrogenetic evolution of late Cenozoic, post-collision volcanism in western Anatolia, Turkey. Journal of Volcanology and Geothermal Research.
- [37] Altunkaynak, Ş., 2007. Collision-driven slab breakoff magmatism in northwestern Anatolia, Turkey. The Journal of Geology, 115(1), 63-82. [38] Altunkaynak, Ş., & Yilmaz, Y., 1998. The Mount Kozak magmatic complex, Western Anatolia. Journal of Volcanology and Geothermal
- [39] Genç, Ş. C., 1998. Evolution of the Bayramiç magmatic complex, northwestern Anatolia. Journal of volcanology and geothermal research, 85(1-4), 233-249.

- [40] Karacık, Z., & Yılmaz, Y., 1998. Geology of the ignimbrites and the associated volcano-plutonic complex of the Ezine area, northwestern Anatolia. Journal of Volcanology and Geothermal Research, 85(1-4), 251-264.
- [41] Aysal, N., 2015. Mineral chemistry, crystallization conditions and geodynamic implications of the Oligo–Miocene granitoids in the Biga Peninsula, Northwest Turkey. Journal of Asian Earth Sciences, 105, 68-84.
- [42] Kamacı, Ö., & Altunkaynak, Ş., 2019b. Magma chamber processes and dynamics beneath northwestern Anatolia: Insights from mineral chemistry and crystal size distributions (CSDs) of the Kepsut volcanic complex (NW Turkey). Journal of Asian Earth Sciences, 181, 103889. https://doi.org/10.1016/j.jseaes.2019.103889
- [43] Kamacı, Ö., & Altunkaynak, Ş., 2024. Petrological insights into connections between the S-and I-type magmatic associations in metamorphic core complexes: A case study of the Cataldag metamorphic core complex (NW Turkey). Lithos, 464, 107433.
- [44] Ünal, A., & Altunkaynak, Ş., 2018. Nature and genesis of potassic high Ba-Sr granitoids associated with syn-convergent extension in NW Turkey. Lithos, 316, 261-277.
- [45] Ünal, A., Altunkaynak, Ş., 2019. Interplay between volcanic and plutonic systems: A case study of the early Miocene Solarya Volcano-plutonic Complex in NW Anatolia (Turkey). Journal of Asian Earth Sciences, 179, 319–336. https://doi.org/10.1016/j.jseaes.2019.03.013.
- [46] Ünal, A., Altunkaynak, Ş., Kamacı, Ö., Dunkl, I., & Benowitz, J. A., 2019. The emplacement history of granitic intrusions into the upper crust: Forceful to passive emplacement of the early Miocene Solarya Pluton (NW Turkey) as a case study. Journal of Asian Earth Sciences, 183, 103979. https://doi.org/10.1016/j.jseaes.2019.103979
- [47] Yücel-Öztürk, Y., Akal, C., Ersoy, E. Y., Sevim, S., & Mertz-Kraus, R., 2023. Geochronology and geochemistry of the Miocene Kadıkalesi monzonite (Bodrum Peninsula, western Anatolia): Implications for its relation with the South Aegean Volcanic Arc. Geochemistry, 83(3), 125982. [48] Doner, Z., Unluer, A.T., Özdamar, Ş., Sarıkaya, O., Roden, M.F., Kaya, M., Kocaturk, H., Kumral, M., Esenli, F. (2024). The origin of alkali granites and Th-U±REE enrichments in Kestanbol Magmatic Complex (NW Anatolia) revisited: Evidences from bulk-rock geochemistry and isotopic data, zircon U-Pb, biotite Ar/Ar and apatite (U-Th)/He geochronology. Lithos, 484, 107751. https://doi.org/10.1016/j.lithos.2024.107751 [49] Özdamar, Ş., Zou, H., Billor, M. Z., Hames, W., Roden, M. F., Sarıkaya, O., Georgiev, S., 2024. Petrogenesis, geochronology and thermochronology of Oligocene to Miocene Western Anatolia granitoid plutons in Turkey. Lithos, 464, 107430.
- [50] Ünluer, A.T., Doner, Z., Ünal, A., Kamaci, O., Kaya, M., Ozturk, S., Kumral, M. (2024). The first finding of a highly evolved Mg-rich carbonatite intrusion in NW Anatolia (Arıklı-Çanakkale). Geochemistry, 84(4), 126124. https://doi.org/10.1016/j.chemer.2024.126124 [51] Kamacı, inpress
- [52] Bozkurt, E., & Park, R. G., 1994. Southern Menderes Massif: an incipient metamorphic core complex in western Anatolia, Turkey. Journal of the Geological Society, 151(3), 545-554.
- [53] Işık, V., Tekeli, O., Seyitoğlu, G., 2004. The 40 Ar/39 Ar age of extensional ductile deformation and granitoid intrusion in the northern Menderes core complex: implications for the initiation of extensional tectonics in western Turkey. Journal of Asian Earth Sciences, 23(4), 555-566.
- [54] Akdeniz, N., & Konak, N., 1979. Menderes Masifinin Simav dolayındaki kaya birimleri ve metabazik, meta ultramafik kayaların konumu. Türk Jeoloji Kurumu Bülteni, 22(2), 175-183.
- [55] Loos, S., & Reischmann, T., 1999. The evolution of the southern Menderes Massif in SW Turkey as revealed by zircon dating. Journal of the Geological Society, 156(5), 1021-1030.
- [56] Candan, O., Dora, O., Oberhänsli, R., Çetinkaplan, M., Partzsch, J., Warkus, F., & Dürr, S., 2001. Pan-African high-pressure metamorphism in the Precambrian basement of the Menderes Massif, western Anatolia, Turkey. International Journal of Earth Sciences, 89, 793-811.
- [57] Bozkurt, E., & Oberhänsli, R., 2001. Menderes Massif (western Turkey): structural, metamorphic and magmatic evolution—a synthesis. International Journal of Earth Sciences, 89(4), 679-708.
- [58] Rimmelé, G., Oberhänsli, R., Goffé, B., Jolivet, L., Candan, O., & Çetinkaplan, M., 2003. First evidence of high-pressure metamorphism in the "Cover Series" of the southern Menderes Massif. Tectonic and metamorphic implications for the evolution of SW Turkey. Lithos, 71(1-2), 19-46.
- [59] Gülmez, F., Damcı, E., Ülgen, U.B., Okay, A., 2019. Deep structure of Central Menderes Massif: Data from deep geothermal wells. Turkish Journal of Earth Sciences, 28(4), Article 3. https://doi.org/10.3906/yer-1903-16.
- [60] Şengör, A. M. C., Satir, M., & Akkök, R., 1984. Timing of tectonic events in the Menderes Massif, western Turkey: Implications for tectonic evolution and evidence for Pan-African basement in Turkey. Tectonics, 3(7), 693-707.
- [61] Özer, S., Sözbilir, H., Özkar, İ., Toker, V., & Sari, B., 2001. Stratigraphy of Upper Cretaceous—Palaeogene sequences in the southern and eastern Menderes Massif (western Turkey). International Journal of Earth Sciences, 89(5), 852-866.
- [62] Candan, O., Çetinkaplan, M., Oberhänsli, R., Rimmelé, G., & Akal, C., 2005. Alpine high-P/low-T metamorphism of the Afyon Zone and implications for the metamorphic evolution of Western Anatolia, Turkey. Lithos, 84(1-2), 102-124.
- [63] Bozkurt, E., & Satir, M., 2000. The southern Menderes Massif (western Turkey): geochronology and exhumation history. Geological Journal, 35(3-4), 285-296.
- [64] Ring, U., & Collins, A. S., 2005. U-Pb SIMS dating of synkinematic granites: Timing of core-complex formation in the northern Anatolide belt of western Turkey. Journal of the Geological Society, 162(4), 523-531.
- [65] Thomson, S. N., & Ring, U., 2006. Thermochronologic evaluation of postcollision extension in the Anatolide orogen, western Turkey. Tectonics, 25(3).
- [66] Catlos, E. J., & Cemen, I., 2005. Monazite ages and the evolution of the Menderes Massif, western Turkey. International Journal of Earth Sciences, 94, 204-217.
- [67] Erkül, F., 2010. Tectonic significance of synextensional ductile shear zones within the Early Miocene Alaçamdağ granites, northwestern Turkey. Geological Magazine, 147(4), 611-637.
- [68] Seyitoğlu, G., & Işık, V., 2015. Late Cenozoic extensional tectonics in western Anatolia: Exhumation of the Menderes core complex and formation of related basins. Bulletin of the Mineral Research and Exploration, 151(151), 47-106.

- [69] Cenki-Tok, B., Expert, M., Işık, V., et al., 2016. Complete Alpine reworking of the northern Menderes Massif, western Turkey. International Journal of Earth Sciences, 105, 1507-1524.
- [70] Etzel, T. M., Catlos, E. J., Cemen, I., Ozerdem, C., Oyman, T., & Miggins, D., 2020. Documenting exhumation in the Central and Northern Menderes Massif (Western Turkey): New insights from garnet-based PT estimates and K-feldspar 40Ar/39Ar geochronology. Lithosphere, 2020(1), 8818289.
- [71] Özgenc, I., & Ilbeyli, N., 2008. Petrogenesis of the Late Cenozoic Egrigöz pluton in western Anatolia, Turkey: implications for magma genesis and crustal processes. International Geology Review, 50(4), 375-391.
- [72] Öner, Z., Dilek, Y., & Kadioglu, Y. K., 2010. Geology and geochemistry of the synextensional Salihli granitoid in the Menderes core complex, western Anatolia, Turkey. International Geology Review, 52(2-3), 336-368.
- [73] Erkül, F., Tatar Erkül, S., Manap, H. S., & Çolak, C., 2017. An extensional and transtensional origin of elongated magmatic domes and localised transfer faults in the northern Menderes metamorphic core complex, western Turkey. Geodinamica acta, 29(1), 139-159.
- [74] Ayan, M., 1973. Migmatites in the Gördes area. Bulletin of the Mineral Research and Exploration, 81, 6.
- [75] Buğdaycıoğlu, Ç., 2004. Tectono-metamorphic evolution of the northern Menderes Massif: evidence from the horst between Gördes and Demirci Basins (West Anatolia, Turkey). MSc Thesis, Middle East Technical University.
- [76] Bozkurt, E., Satır, M., & Buğdaycıoğlu, Ç., 2010. Timing of post-orogenic extension in the Gördes migmatite dome, Western Turkey: insights from U–Pb and Rb-Sr chronology. In: Tectonic Crossroads: Evolving Orogens of Eurasia-Africa-Arabia, Ankara, Turkey.
- [77] Kuşcu, R., 2010. Güneşli granitoyidinin (Gördes/Manisa) petroloji ve jeolojisi. MSc Thesis, Ankara Universitesi, Turkey.
- [78] Delaloye, M., & Bingol, E., 2000. Granitoids from western and northwestern Anatolia: geochemistry and modeling of geodynamic evolution. International Geology Review, 42, 241-268.
- [79] Dağ and Asutay, 1994. The petrological properties of Güneşli granite located in gördes migmatites, 47. Türkiye Jeoloji Kurultayi Bildiri Özleri, 137.
- [80] Nachit, H., Ibhi, A., & Ohoud, M. B., 2005. Discrimination between primary magmatic biotites, reequilibrated biotites and neoformed biotites. Comptes Rendus. Géoscience, 337(16), 1415-1420.
- [81] Tischendorf, G., Rieder, M., Förster, H. J., Gottesmann, B., & Guidotti, C. V., 2004. A new graphical presentation and subdivision of potassium micas. Mineralogical Magazine, 68(4), 649-667.
- [82] Miller, C. F., Stoddard, E. F., Bradfish, L. J., & Dollase, W. A., 1981. Composition of plutonic muscovite: genetic implications. Canadian Mineralogist, 19(1), 25-34.
- [83] Henry, D. J., Guidotti, C. V., & Thomson, J. A., 2005. The Ti-saturation surface for low-to-medium pressure metapelitic biotites: Implications for geothermometry and Ti-substitution mechanisms. American mineralogist, 90(2-3), 316-328.
- [84] Li, X., & Zhang, C., 2022. Machine learning thermobarometry for biotite-bearing magmas. Journal of Geophysical Research: Solid Earth, 127, e2022JB024137. https://doi.org/10.1029/2022JB024137
- [85] Anderson, J. L., & Smith, D. R. (1995). The effects of temperature and f O2 on the Al-in-hornblende barometer. American mineralogist, 80(5-6), 549-559.
- [86] Abdel-Rahman, A. F. M., 1994. Nature of biotites from alkaline, calc-alkaline, and peraluminous magmas. Journal of petrology, 35(2), 525-541.
- [87] Gao, P., Zhao, Z. F., & Zheng, Y. F., 2016. Magma mixing in granite petrogenesis: Insights from biotite inclusions in quartz and feldspar of Mesozoic granites from South China. Journal of Asian Earth Sciences, 123, 142-161.
- [88] Zhou, Z. X., 1986. The origin of intrusive mass in Fengshandong, Hubei province. Acta Petrologica Sinica, 2(2), 59-70.
- [89] Li, X., Zhang, C., Behrens, H., & Holtz, F., 2020. Calculating biotite formula from electron microprobe analysis data using a machine learning method based on principal components regression. Lithos, 356, 105371.



Contents lists available at Dergipark

Journal of Scientific Reports-A

journal homepage: https://dergipark.org.tr/tr/pub/jsr-a



E-ISSN: 2687-6167 Number 62, September 2025

RESEARCH ARTICLE

Study of geometric texture on tensile properties of PLA polymer parts produced by FDM

Faik Yılan^a*, Ibrahim M. M. Alzraıqı^b, and Levent Urtekin^c

- ^a Kırşehir Ahi Evran University, Faculty of Engineering and Architecture, Department of Mechanical Engineering, Kırşehir 40100 Turkey, ORCID: 0000-0001-7166-8604
- ^b Kırşehir Ahi Evran University, Faculty of Engineering and Architecture, Department of Mechanical Engineering, Kırşehir 40100 Turkey, ORCID: 0009-0002-9630-0587
- ^c Kırşehir Ahi Evran University, Faculty of Engineering and Architecture, Department of Mechanical Engineering, Kırşehir 40100 Turkey, ORCID: 0000-0003-4348-4749

Abstract

In this study, it is aimed to analyse the effects of texture geometries on mechanical response of polylactic acid (PLA) parts manufactured through fused deposition modeling (FDM). Experimental mechanical analyses of PLA samples with hexagonal, circular, square, full, triangle and ellipse geometries were carried out and their tensile responses were examined. Result show that the full geometry exhibited that the full geometry exhibited the highest tensile strength (36 MPa) and deformation capacity (3.1%), making it ideal for applications requiring maximum load-bearing capacity. However, the elliptical geometry demonstrated strength (28 MPa) and deformation capacities close to the full structure, offering a practical balance between mechanical performance, material savings, and production efficiency. Other geometries, such as hexagonal, circular, and square, provided moderate performance suitable for lightweight designs. X-ray tomography was used to analyse internal structures, manufacturing quality, further supporting the correlation between geometric design and mechanical properties. These findings highlight the potential for optimizing material usage and production time without significantly compromising mechanical performance in 3D-printed PLA components.

© 2023 DPU All rights reserved.

* Corresponding author. Tel.: +90 386 280 2326 E-mail address: faik.yilan@ahievran.edu.tr

1. Introduction

Additive manufacturing (AM) is a production method that has become widespread in the industry with the development of technology. This technique is essentially the process of completing the production by adding the materials layer by layer to a surface called the production plate using three-dimensional (3D) geometric data [1], [2]. We can list the production types of AM technique for processing different materials as the following:

- Stereolithography (SLA).
- Selective laser sintering (SLS).
- Fused deposition modeling (FDM) [3].

This technique was discovered in 1980s. Since these discovered process were not very efficient at that time, they started to be widely used only in the 2000s. This production method, which has been further developed day by day, has now become very popular in mass production.

In the FDM technique, thermoplastic materials Acrylonitrile Butadiene Styrene (ABS), Polyurethane (TPU) and Poly Lactic Acid (PLA) that are wound on a reel are used as production raw materials [4], [5]. These printer devices operate by controlling several drive elements. A drive unit connected to the reel during production separates the material from the reel as needed. The separated material comes to the feeder of the heater nozzle and is melted there. The molten plastic passing through the fine-tipped channels in the extrusion head is plastered to the production surface as a thin layer and layers are formed. As soon as the plastering process is done, the molten material solidifies. After the first layer, the building layer goes down as much as the layer size and the new step is started. The machine ends the production by renewing this process at each step [6], [7], [8].

Solid models that are planned to be produced often cannot be sent directly to the fabrication device. As a preprocess, the 3D solid model is converted to a file with the STL extension, which is the additive manufacturing standard interface [9]. This STL file makes some adjustments such as error checking, placing support elements where necessary, determining the direction of construction and selecting some device parameters through the intermediate applications suggested by the machine to be produced. This intermediate application then slices the solid model into equal segments, breaking it into two-dimensional (2D) layers. The device that will make the production performs the production process by using the data of these 2D layers [10], [11], [12].

Different texture-patterned geometries produced by the FDM process affect the mechanical properties of the parts [13], [14]. One of early studies was researched by Tonsilav Galeta et al. [15] and they designed the internal structures of the samples as full, honeycombs, drills and stripes and observed the highest tensile strength in the honeycomb model. LR Lopez et al. [16] was 3D printed with smooth and zebra pattern border interface transitions using PLA, TPU and PET filaments. In this case, they revealed that zebra patterned samples showed a decrease in tensile strength and modulus of elasticity. In a different comparative study, S. Batai and M.H. Ali [17] designed honeycomb, pentagonal, square and drill model ABS and PLA specimens with the same volume ratio and optimized their mechanical analysis in the finite element method (FEM). Also, in another study is that changing their geometric structure affects the yield strength of printed parts. Therefore, it was concluded that the hexagonal pattern showed better mechanical properties than the other patterns [18].

The demands for the evaluation and inspection of complex addictive manufacturing parts using X-ray technology has gained much importance in recent years [19], [20], [21]. Since X-ray tomography method is a non-destructive scanning, it can be used for analysis in different fields such as industrial and academic [22], [23], [24]. Thanks to X-ray CT, the dimensional evaluation, roughness analysis, density measurement and defect detection of the parts produced with 3D printing technology can be characterized. Thus, X-ray CT offers many advantages such as energy,

material and time savings [25].

As mentioned above, different geometries designs are highly influence on the mechanical properties in 3D printing. In this context, this study aimed to determine the influences of geometries textures (circular, square, elliptical, hexagonal and triangular) with 3D printer parameters on the mechanical properties of PLA filament material. X-ray tomography device was used to check the dimensions, pores and defects of the printed parts.

2. Materials and methods

2.1. Manufacturing of Specimens and Printing Parameters

In this study specimens were fabricated using a 3D FDM device that was designed and manufactured in-house [14]. Table 1 shows the mechanical properties of PLA (esun3d-Ø1,75 mm). It is considered to analyze PLA filament material that used be commonly used for 3D printing. Table 2 shows the parameter values that are used in 3D printing.

Table 1. Mechanical properties of PLA.

Density (g/cm³)	Tensile Ultimate Strength (MPa)	Tensile Yield Strength (MPa)	Young's Modulus (MPa)
1.24	59	70	3500

Table 2. Setup parameters for each sample used in this study.

Parameters	Values	
Layer height (mm)	0.2	
Extruder temperature (°C)	205	
Bed temperature (°C)	45	
Print speed (mm/s)	35	
Infill density (%)	100	
Infill pattern	Line	
Print core (nuzzle) size (mm)	AA 0.4	

There is a specific standard focusing on the tensile testing of polymer materials. Therefore, the dimensions of the specimens were prepared separately in accordance with the ASTM D638 IV standards [26]. Therefore, the specimens with different surface patterns were designed with SolidWorks 2020 software. Holes in different shapes, such as circular, square, ellipse, hexagonal and triangular, were drilled corresponding to the regions of the specimens that were expected to rupture. In order to find out the effect on tensile strength of patterns shape, all specimens have the same number of textures, same area density, and same area of a pattern, as it can be seen Table 3.

Table 3. An example of a table. Design parameters of tensile test specimens.

•	- 1	•		
Pattern geometry	Area density (%)	Number of patterns	Distance of patterns (mm)	Area of a dimple (mm ²)
Full	100	-	-	-
Circle	80	8	4	4.9
000				

Yılan, F., Alzraıqı, M. M. I. and Urtekin, L., (2025)/ Journal of Scientific Reports-A, 062, 61-70

Square	80	8	4	4.9
Ellipse	80	8	4	4.9
000				
Hexagon	80	8	4	4.9
$\bigcirc\bigcirc\bigcirc\bigcirc$				
Triangle	80	8	4	4.9
$\triangle\triangle\triangle$				

2.2. Tensile Tests

Tensile tests were conducted by using a universal testing machine (WDM-100E Model/Japan). The maximum load capacity of the machine was 100 kN. The specimens were carefully clamped in the holders and tensile tests were performed (Fig. 1). Deformation and load data were automatically recorded in a computer system. The test speed was kept as 1 mm/min for all the specimens as suggested by the test standard. Each test was repeated at least five times and tensile strengths of the polymer materials were obtained from the average strengths.



Fig. 1. Overview of the tensile test machine (KAEU-Mechanical Engineering Mechanics Lab.).

2.3. X-Ray Tomography

A laboratory scale, an X-CT system generally includes an X-ray source that converts electrical power into X-rays, a rotating stage where the specimen is positioned for scanning, and a detector, as depicted in Fig. 2 (a-b). The main principle of the X-Ray tomography system is related to irradiating the X-ray beam onto the sample and mathematically measuring the images with the help of a detector [27]. YXIon X-Ray tomography unit was used to examine dimensions, pores and defects of the printed samples. The image analysis was performed using at 85 kW and 0.05 A.

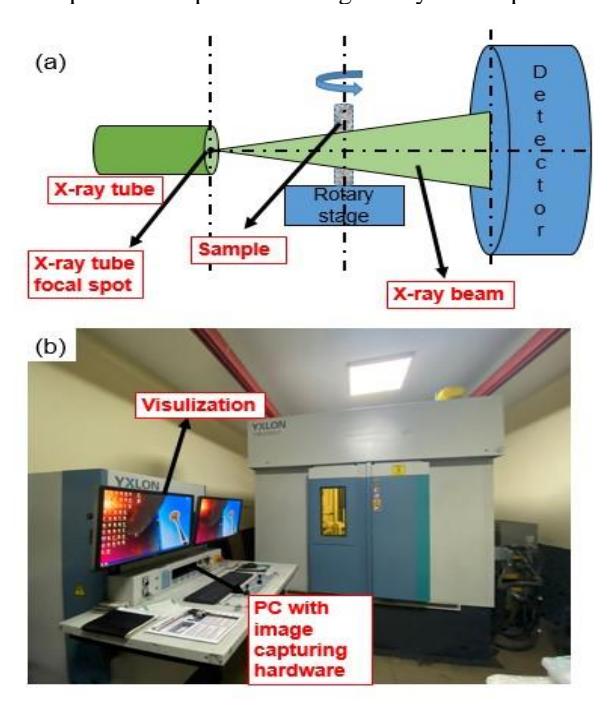


Fig. 2. (a) CT working principle; (b) X-ray computed tomography device.

3. Results and Discussion

The Fig. 3 shows a comprehensive analysis of the mechanical performance and stress-strain curves of the PLA material produced from the 3D printer in different geometric textures. The Full structure stands out with the highest tensile strength (36 MPa) and the largest deformation capacity (3.1%) among all geometries. This structure was provided a design where the load-carrying capacity is maximized throughout the entire structure thanks to its continuous and homogeneous internal structure. The Full structure, which exhibits the best performance in terms of strength and deformation, is ideal for applications where heavy loads need to be carried and durability is critical. However, high material usage and weight may make this structure disadvantageous in lightened design requirements. The Ellipse structure draws attention with its strength values (28 MPa) and deformation capacities close to the Full structure (3.1% strain). Although the concave form of the ellipse cannot increase the strength to the Full level, it stands out as a structure that offers sufficient strength and material savings together. Hexagon offers a medium-class mechanical performance with a tensile strength of approximately 25 MPa and a strain capacity of 2.66%. However, the interrupted areas and internal geometric gaps in this structure cause the strength to be lower compared to Full or

Ellipse. Hexagon can be used in medium-load capacity applications where a lightweight structure is required. Circle and Hexagon textures are similar to each other in terms of strength (25 MPa) and deformation capacity (2.75%) and perform at the same limits as the Square structure. Circle has a slight advantage over Hexagon in terms of deformation (3.2% strain) thanks to the uniform distribution of stress. However, both structures exhibit less strength compared to Full and Ellipse textures. These two structures can be preferred in applications where lightness is required and medium load carrying capacity is needed. Triangle offers the lowest strength (22 MPa) and deformation capacity (1.75% strain) among all textures. The sharp angles and corners of the triangular form cause the stress concentration to accumulate in certain areas, accelerating the fracture. Therefore, the Triangle texture is only suitable for designs with low load-carrying requirements and where lightness and aesthetic requirements are more important than durability. Its use is not recommended in areas where strength and durability are priorities.

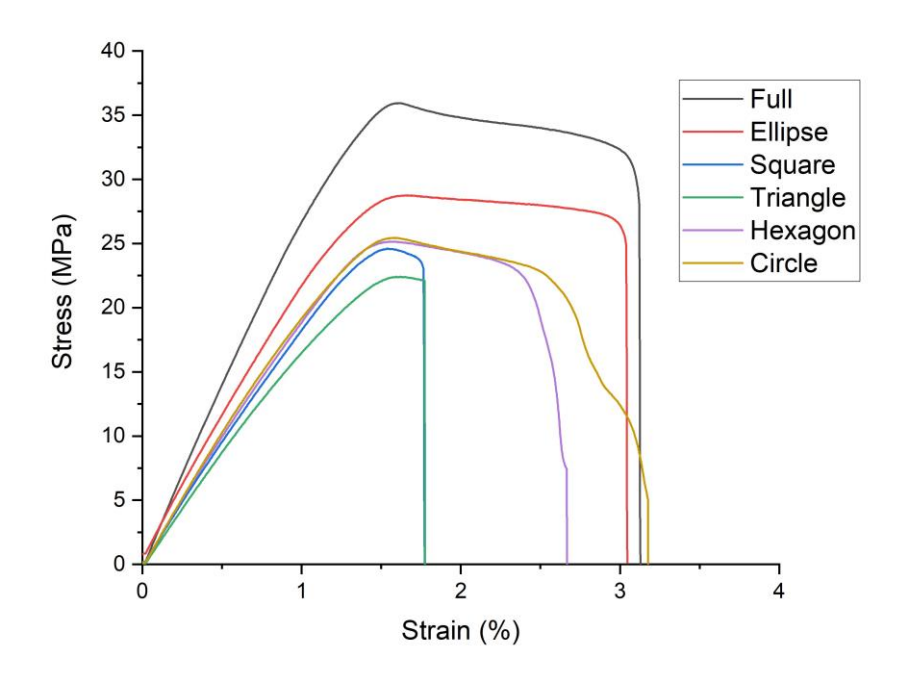


Fig. 3. Tensile stress-strain curve of PLA parts.

In Fig. 4, the tensile strength results show that there is a strong correlation between the design geometry and material performance under tensile stress. The full cross-section, having no stress-concentrating edges or interruptions, understandably achieves the highest tensile strength (36 MPa). This makes it the most reliable structure for applications requiring maximum load-bearing capabilities. On the other hand, shapes with angular edges, such as the square (24 MPa) and triangle (22 MPa), show the lowest tensile strength. This weakness is attributed to stress concentrations at the sharp corners, which reduce their ability to handle uniform tensile forces. Rounded geometries, such as the circle (25 MPa) and ellipse (28 MPa), perform significantly better because they distribute stress more evenly. The hexagon (25 MPa) also achieves decent performance, reflecting its relatively uniform design, though it does not match the strength of smoother, curved shapes.

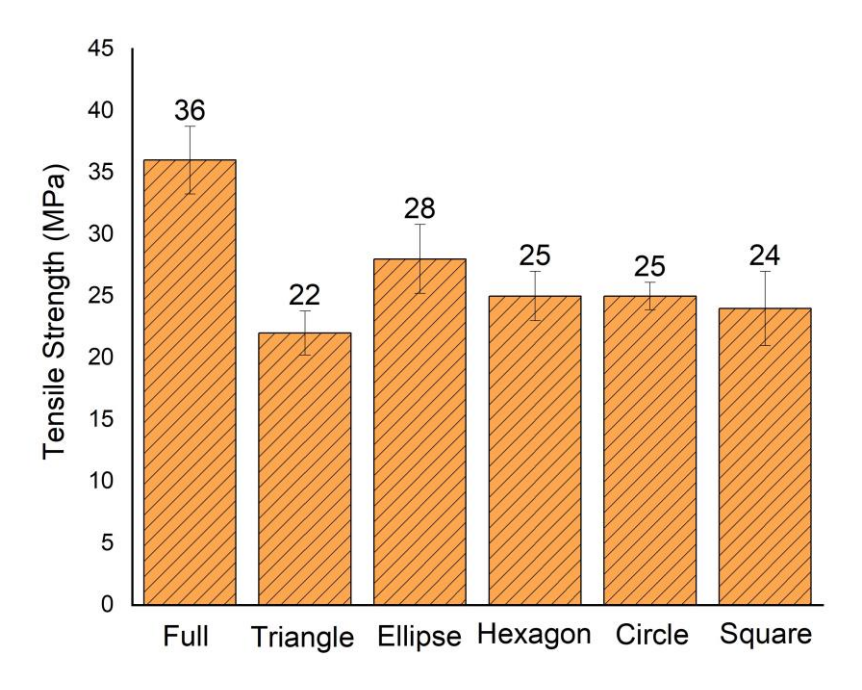


Fig. 4. Results of tensile strength tests.

This X-ray analysis reveals the fundamental differences in the internal structures of different geometric textures produced with PLA material, and these differences allow us to understand the mechanical performance of each structure. The Fig. 5 shows the void shapes, fullness ratios and regularities of the textures, which are critical elements that determine how stress is distributed throughout the material and how it affects behaviors such as fracture or deformation. The full structure has a completely full and homogeneous internal structure. Since there is no void inside, this structure can distribute stress evenly throughout the material and stands out as the most resistant geometry against external effects. This makes the full structure the most robust design, but it also makes it unsuitable for applications that require lightness. The full structure minimizes the risk of sudden breakage thanks to the absence of voids and offers a highly durable integrity. The interior of the ellipse structure is designed with regular and soft oval voids. The elliptical shape enables more uniform stress distribution evenly and reduces the risk of cracking not having any corners or sharp edges. The ellipse design is a balanced option that optimizes weight instead of fullness, while still offering a highly robust performance. A special advantage of this structure is that it offers a balance between lightness and strength. While the Hexagon structure consists of regular hexagonal spaces, the sharp edges of these spaces attract attention. Sharp edges cause stress to accumulate in certain focuses during loading, making the material vulnerable to damage earlier than other regular structures. However, the hexagonal geometry is advantageous in terms of providing lightness and optimizing the fullness ratio. However, this design cannot fully maximize durability and remains at a certain limit. Circle and Square structures generally exhibit similar structural characteristics. While the circular structure can distribute the stress more evenly thanks to its soft edges, the square structure has sharp corners and this increases the risk of breakage. While the circular design provides more balanced strength, the square structure is more

disadvantageous due to sharper geometric focuses. Both structures are suitable for applications that target a mid-range performance between lightness and strength. The triangle structure has the most sharp edges and irregular stress distribution among the analyzed geometries. The sharp edges and corners created by triangles cause stress to concentrate at specific points, resulting in premature fractures. The complexity and discontinuity of its internal structure proves that the triangular design is poor in terms of durability. Although it can be used for light and aesthetic designs, it is not a suitable structure for applications requiring load carrying. This X-ray analysis clearly shows the influence of the internal layouts of geometric structures on the performance of the material. Fully-filled structures offer the highest durability, while structures with regular gaps optimize lightness and minimize weaknesses. While stress is distributed more appropriately in oval and circular structures, weak points occur due to stress accumulation in designs with angular and sharp lines (Triangle and Square).

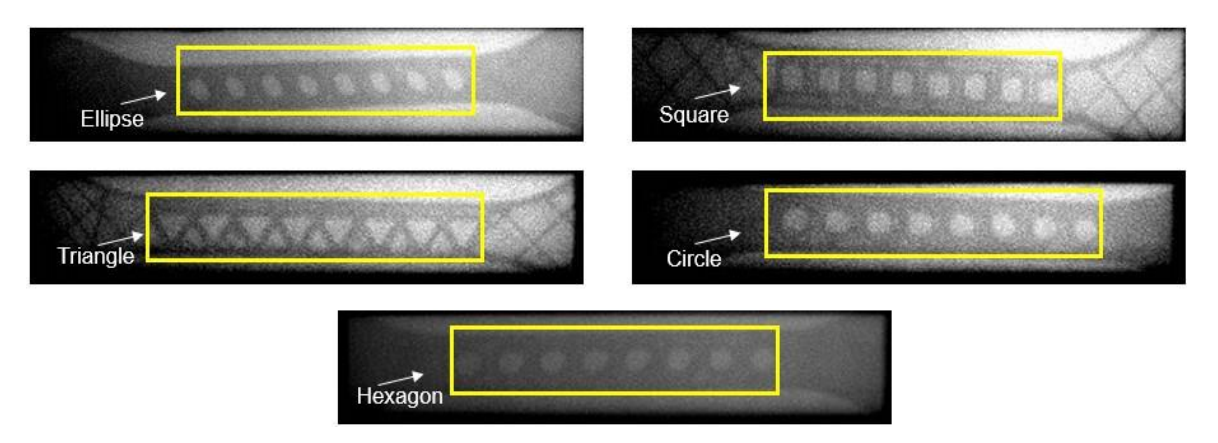


Fig. 5. X-ray images of the PLA parts.

4. Conclusions

This study analyzed the effects of geometric textures on the tensile properties of PLA parts produced using fused deposition modeling (FDM). The results demonstrated that the "Full" geometry exhibited the highest tensile strength (36 MPa) and deformation capacity (3.1%), making it the most suitable design for applications requiring maximum load-bearing capacity and durability. Its continuous and homogeneous internal structure ensures even stress distribution and minimizes weak points, resulting in superior mechanical performance. The elliptical geometry, with strength values (28 MPa) and deformation capacities close to the full structure, offers a balanced solution for applications prioritizing both material savings and mechanical performance. Geometries such as hexagonal, circular, and square exhibited moderate tensile strength and strain capacities, making them suitable for lightweight designs with medium load requirements. The triangular geometry, with the lowest tensile strength (22 MPa), is limited to aesthetic or low-load applications due to stress concentrations at sharp corners. X-ray tomography analysis provided critical insights into the internal structures, dimensions, and defects of the printed samples, highlighting the correlation between geometric design and mechanical properties. These findings emphasize the importance of texture geometry in optimizing the mechanical performance of 3D-printed PLA components.

Future studies could explore the effects of different materials, printing parameters, and more complex geometric patterns to further enhance the mechanical performance and broaden the application scope of FDM technology.

Acknowledgements

This study was supported by the TUBITAK 2209-A National Undergraduate Student Research Projects Support Programme (Project no: 1919B012319180).

Author Contributions

F.Y. and I.A. organized and performed all the analyses and wrote the manuscript. L.U. determined the main idea of the study and carried out paper revisions.

References

- [1] N. Babacan, and H. Şeremet, "Investigation of the Load-Bearing Capacity of Co-Cr Lattice Structures Fabricated by Selective Laser Melting," *Int. J. 3D Print. Technol. Digit. Ind.*, vol. 6, no. 2, pp. 286–291, 2022, doi: 10.46519/ij3dptdi.1139802.
- [2] F. Yilan, R. Ekici, and L. Urtekin, "Recent advances in the AlSi10Mg materials fabrication by selective laser melting: process parameters, optimization, low-velocity and ballistic impact responses," *Prog. Addit. Manuf.*, no. 0123456789, 2024, doi: 10.1007/s40964-024-00856-x.
- [3] T. C. Yang and C. H. Yeh, "Morphology and mechanical properties of 3D printed wood fiber/polylactic acid composite parts using Fused Deposition Modeling (FDM): The effects of printing speed," *Polymers (Basel).*, vol. 12, no. 6, p. 1334, 2020, doi: 10.3390/POLYM12061334.
- [4] M. Samykano, S. K. Selvamani, K. Kadirgama, W. K. Ngui, G. Kanagaraj, and K. Sudhakar, "Mechanical property of FDM printed ABS: influence of printing parameters," *Int. J. Adv. Manuf. Technol.*, vol. 102, no. 9–12, pp. 2779–2796, 2019, doi: 10.1007/s00170-019-03313-0.
- [5] M. Srivastava, S. Rathee, V. Patel, A. Kumar, and P. G. Koppad, "A review of various materials for additive manufacturing: Recent trends and processing issues," *J. Mater. Res. Technol.*, vol. 21, pp. 2612–2641, 2022, doi: 10.1016/j.jmrt.2022.10.015.
- [6] F. Yilan, İ. B. Şahin, F. Koç, and L. Urtekin, "The Effects of Different Process Parameters of PLA+ on Tensile Strengths in 3D Printer Produced by Fused Deposition Modeling," *El-Cezeri J. Sci. Eng.*, vol. 10, no. 1, pp. 160–173, 2023, doi: 10.31202/ecjse.1179492.

 [7] U. L. Yılan F, Şahin İ. B, "3d Printing Design and Manufacturing: Dual-Extrusion System," in *New Trends in Engineering Sciences*, New
- [7] U. L. Yılan F, Şahin İ. B, "3d Printing Design and Manufacturing: Dual-Extrusion System," in *New Trends in Engineering Sciences*, New Trends in Engineering Sciences, 2022, pp. 151–161. [Online]. Available: https://www.dosyaupload.com/3sNvc?pt=VTFKS2VqWlZObTh6TkRSelRXSnNZa0p0VHpaeVFUMDlPc29yeTVtaHZQd0YyUkNxMmJNWT Y4TT0%3D
- [8] S. A. M. Tofail, E. P. Koumoulos, A. Bandyopadhyay, S. Bose, L. O'Donoghue, and C. Charitidis, "Additive manufacturing: scientific and technological challenges, market uptake and opportunities," *Mater. Today*, vol. 21, no. 1, pp. 22–37, 2018, doi: 10.1016/j.mattod.2017.07.001.
- [9] P. Cătălin Iancu, E. Daniela Iancu, and D. Alin Stăncioiu, "From CAD Model To 3D Print Via 'STL' File Format," Fiability Durab., no. 1, pp. 73–80, 2010
- [10] A. Çelebi, and M. M. İmanç, "Evaluation of Mechanical Properties of PLA Auxetic Structures Produced by Additive Manufacturing," *J. Mater. Mechatronics A*, vol. 4, no. 2, pp. 384–396, 2023, doi: 10.55546/jmm.1309858.
- [11] A. Çelebi, A. Korkmaz, T. Yılmaz, and H. Tosun, "3 Boyutlu Yazıcı ile 6 Eksenli Robot Kol Tasarım Ve İmalatı," *Int. J. 3D Print. Technol. Digit. Ind.*, vol. 3, no. 3, pp. 269–278, 2019.
- [12] A. Çelebi and A. Tosun, "Application And Comparison Of Topology Optimization For Additive Manufacturing And Machining Methods," *Int. J. 3D Print. Tech. Dig. Ind*, vol. 5, no. 3, pp. 676–691, 2021, doi: 10.46519/ij3dptdi.
- [13] P. Zhang and A. C. To, "Transversely isotropic hyperelastic-viscoplastic model for glassy polymers with application to additive manufactured photopolymers," *Int. J. Plast.*, vol. 80, pp. 56–74, 2016, doi: 10.1016/j.ijplas.2015.12.012.
- [14] Y. Kim, Y. Kim, T. I. Lee, T. S. Kim, and S. Ryu, "An extended analytic model for the elastic properties of platelet-staggered composites and its application to 3D printed structures," *Compos. Struct.*, vol. 189, no. January, pp. 27–36, 2018, doi: 10.1016/j.compstruct.2018.01.038.
- [15] T. Galeta, P. Raos, J. Stojšíć, and I. Pakši, "Influence of structure on mechanical properties of 3D printed objects," *Procedia Eng.*, vol. 149, no. June, pp. 100–104, 2016, doi: 10.1016/j.proeng.2016.06.644.
- [16] L. R. Lopes, A. F. Silva, and O. S. Carneiro, "Multi-material 3D printing: The relevance of materials affinity on the boundary interface performance," *Addit. Manuf.*, vol. 23, no. June, pp. 45–52, 2018, doi: 10.1016/j.addma.2018.06.027.
- [17] M. H. A. Shaheidula Batai, "Mechanical Performance Optimization of 3D Printing Material," in *Advances in Materials and Manufacturing Engineering*, 2020, pp. 257–263. doi: 10.1007/978-981-15-1307-7_28.
- [18] S. Ganeshkumar *et al.*, "Investigation of Tensile Properties of Different Infill Pattern Structures of 3D-Printed PLA Polymers: Analysis and Validation Using Finite Element Analysis in ANSYS," *Materials (Basel).*, vol. 15, no. 15, 2022, doi: 10.3390/ma15155142.
- [19] A. Du Plessis, I. Yadroitsev, I. Yadroitseva, and S. G. Le Roux, "X-Ray Microcomputed Tomography in Additive Manufacturing: A Review of the Current Technology and Applications," 3D Print. Addit. Manuf., vol. 5, no. 3, pp. 227–247, 2018, doi: 10.1089/3dp.2018.0060.
- [20] H. Villarraga-g and N. Carolina, "Role of X-ray / CT Technologies in the "3D Printing Revolution"," no. June, 2017.
- [21] A. du Plessis, "X-ray tomography for the advancement of laser powder bed fusion additive manufacturing," *J. Microsc.*, vol. 285, no. 3, pp. 121–130, 2022, doi: 10.1111/jmi.12930.
- [22] A. du Plessis, S. G. le Roux, and M. Tshibalanganda, "Advancing X-ray micro computed tomography in Africa: Going far, together," *Sci. African*, vol. 3, p. e00061, 2019, doi: 10.1016/j.sciaf.2019.e00061.

- [23] L. Urtekin, F. Bozkurt, and M. Çanli, "Analysis of biomedical titanium implant green parts by X-Ray tomography," J. Mater. Res. Technol., vol. 14, pp. 277–286, 2021, doi: 10.1016/j.jmrt.2021.06.083.
- [24] A. du Plessis, I. Yadroitsava, and I. Yadroitsev, "Effects of defects on mechanical properties in metal additive manufacturing: A review
- focusing on X-ray tomography insights," *Mater. Des.*, vol. 187, p. 108385, 2020, doi: 10.1016/j.matdes.2019.108385.

 [25] M. R. Khosravani and T. Reinicke, "On the Use of X-ray Computed Tomography in Assessment of 3D-Printed Components," *J. Nondestruct. Eval.*, vol. 39, no. 4, 2020, doi: 10.1007/s10921-020-00721-1.
- [26] J. J. Laureto and J. M. Pearce, "Anisotropic mechanical property variance between ASTM D638-14 type i and type iv fused filament fabricated specimens," Polym. Test., vol. 68, no. April, pp. 294-301, 2018, doi: 10.1016/j.polymertesting.2018.04.029.
- [27] F. Dababneh and H. Taheri, "Investigation of the influence of process interruption on mechanical properties of metal additive manufacturing parts," CIRP J. Manuf. Sci. Technol., vol. 38, pp. 706-716, 2022, doi: 10.1016/j.cirpj.2022.06.008.



Contents lists available at Dergipark

Journal of Scientific Reports-A

journal homepage: https://dergipark.org.tr/tr/pub/jsr-a



E-ISSN: 2687-6167 Number 62, September 2025

RESEARCH ARTICLE

An energy efficient cluster head selection in priority region aware wireless sensor networks using metaheuristic algorithms

Osman Gökalp^{a,*}, Doğan Aydın^b, Aybars Uğur^c

"Izmir Institute of Technology, Computer Engineering Department, İzmir, 35430, Türkiye, ORCID: 0000-0002-7604-8647

bIzmir Katip Çelebi University, Computer Engineering Department, İzmir, 35640, Türkiye, ORCID: 0000-0003-2478-4818

c Ege University, Computer Engineering Department, İzmir, 35040, Türkiye, ORCID: 0000-0003-3622-7672

Abstract

The cluster head (CH) selection problem is one of the challenges posed by wireless sensor network (WSN) design, where nodes assume leadership roles. The primary objective of this problem is energy conservation, as becoming a CH requires high energy consumption. Therefore, optimizing the CH selection process is crucial. Despite numerous attempts to solve this problem, existing algorithms do not consider area prioritization, where certain regions such as industrial facilities with hazardous zones and military surveillance areas require special attention. This work first describes the standard CH selection problem in non-priority environments and then introduces priority region-aware WSNs. It then presents how energy-efficient CH selection using metaheuristics, with a priority- and energy-aware fitness function developed in this study, can be performed in such networks for the first time in the literature. The findings from comprehensive simulation-based experiments demonstrate the superior performance of both classical and state-of-the-art metaheuristic-driven approaches compared to the baseline Low-Energy Adaptive Clustering Hierarchy (LEACH) algorithm. Specifically, the Adaptive Differential Evolution with Optional External Archive (JADE) algorithm improves the performance of LEACH by up to 16% in terms of the total priority of transferred packets. Additionally, it can extend the lifetime of nodes in high-priority regions by up to 27% to 44%.

Keywords: Cluster head selection; energy minimization, region priority, wireless sensor networks, metaheuristics

71

^{*} Corresponding author. Tel.: +90-232-750-7844; fax: +90-232-750-7862. E-mail address: osmangokalp@iyte.edu.tr

1. Introduction

Wireless Sensor Networks (WSNs) consist of small, autonomous, and distributed sensors that are used to monitor the area of interest for a specific goal such as forest fire prevention [1], electrocardiogram healthcare monitoring [2], underwater resources monitoring [3], and surveillance of military areas [4].

Various optimization problems can arise when designing WSNs. Optimizing sensor deployment for area or target coverage [5] is a major challenge in WSN design, especially when sensors can be dynamically relocated or strategically placed. However, in most cases, sensors are randomly distributed in the environment and left unattended. Therefore, efficient energy usage from limited batteries becomes a critical concern [6]. Another main optimization problem in WSNs is cluster head (CH) selection, which addresses energy limitations by establishing hierarchical communication between nodes and the base station (BS) [7,8,9].

Several routing protocols are used in WSNs for communication, such as (i) direct communication, where each sensor transmits data directly to the BS; (ii) minimum-transmission-energy (MTE), where sensors relay data through intermediate nodes that minimize energy consumption until reaching the BS; (iii) static two-tier clustering, where CHs are predetermined and collect data from their members to forward to the BS; and (iv) dynamic two-tier clustering, where CHs are rotated after each transmission to achieve more balanced energy usage. However, [10] showed that dynamic clustering approaches, such as the Low-Energy Adaptive Clustering Hierarchy (LEACH), outperform others in terms of energy efficiency and network lifetime. Therefore, this study focuses on dynamic clustering and the optimization of the CH selection process.

In CH-based communication, a subset of active sensors is elected as CHs before each transmission. The remaining active nodes are then assigned to the most suitable CH (e.g., the closest one) to form clusters. Once clusters are formed, each CH collects data from its members, aggregates it, and transmits it to the BS. This hierarchical communication saves significant energy, as normal nodes transmit data to nearby CHs rather than directly to the distant BS. However, serving as a CH demands more energy because it involves receiving data from member nodes and transmitting it to the distant BS. Thus, CHs must be rotated regularly to prevent rapid energy depletion. Selecting the most suitable CHs is a non-trivial task and requires an optimization process. Metaheuristics have been successfully applied to various optimization problems [5,11] and are widely used for CH selection [8,12].

Although efficient algorithms exist for solving classical CH selection problems, real-world applications may impose priority requirements, such as in forested areas with diverse flora, military zones with varying threat levels, disaster-prone regions, and conservation areas along wildlife migration routes. In such cases, the CH selection problem must be extended to consider regional priorities.

This paper aims to address the gap in the literature concerning priority-based CH selection optimization. For this purpose, the priority region-aware CH selection problem is introduced and formulated. Then, several classical and state-of-the-art metaheuristic optimization algorithms using priority-aware fitness functions are designed to solve this problem. Detailed experimental work on different priority scenarios showed that the proposed method is effective for CH selection in WSNs with priority regions.

The main contributions of this paper can be listed as follows:

- Formulates a novel CH selection optimization problem that accounts for regional priorities.
- Proposes a unified, priority-aware fitness function for use in metaheuristic algorithms.
- Conducts a comprehensive experimental study across multiple priority-based scenarios, comparing the baseline priority-unaware decentralized algorithm LEACH with classical metaheuristics (Artificial Bee Colony (ABC) [13], Differential Evolution (DE) [14], and Particle Swarm Optimization (PSO) [15]) and advanced metaheuristics (Covariance Matrix Adaptation Evolution Strategy (CMAES) [16], Adaptive Differential Evolution with Optional External Archive (JADE) [17], and Success-History Based Parameter Adaptation for Differential Evolution (SHADE) [18]).

The remainder of this paper is organized as follows. Section 2 provides background on the CH selection problem and the energy dissipation model in WSN communication. Section 3 reviews related work and positions the proposed method in context. Section 4 introduces and formulates the priority region-aware CH selection problem. Section 5 describes the components of the metaheuristic algorithms, including the priority-aware fitness function, solution representation, discretization, and cluster formation. Section 6 presents experimental results and analysis. Finally, Section 7 concludes the paper by summarizing key findings and suggesting directions for future research.

2. Background

2.1. Clustering based communication in WSNs

Clustering provides an efficient way to organize sensors and is commonly used as a communication protocol in WSNs. Clusters are formed by first selecting CHs and then assigning the remaining sensors to one of them as members. Once clusters are formed, member sensors transmit their data to their respective CHs. Each CH then aggregates the collected data into a single packet and transmits it to the BS, also referred to as the sink. Once a transmission cycle is completed (i.e., the BS has received the data), CH selection, cluster formation, data collection, and transmission are repeated until all nodes have depleted their energy. This process is an example of a two-tier hierarchy as shown in Fig. 1.

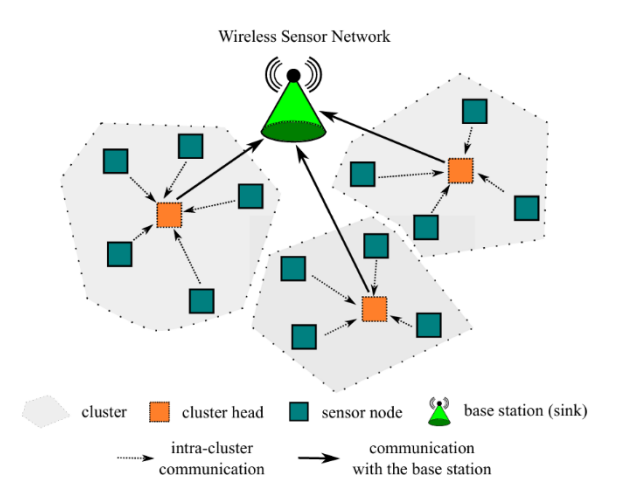


Fig. 1. An example of WSN communication with cluster organization.

Clustering approaches can be divided into two classes: static and dynamic. In static clustering, CHs are selected at the beginning and are not changed until the end of the network lifetime. However, this strategy is ineffective because CH nodes consume more energy than regular nodes, as they collect data from multiple nodes, aggregate it, and transmit it to the distant BS. To prevent CH energy depletion, a dynamic clustering approach can be applied by rotating the CH roles [7,10]. That is, CHs are re-elected at each frame of data transfer, so the overhead of being a CH is distributed among the nodes.

The general outline of the CH selection process is given in Algorithm 1. In the initialization phase, a WSN is set up by randomly deploying sensors and determining the location of the BS. Then, sensors communicate with the BS throughout the network lifetime, e.g., until the last node dies. At each communication step, CHs are first selected from the sensors that are still alive, i.e., those with remaining battery energy. Secondly, clusters are formed by assigning

non-CH nodes to one of the CHs as cluster members. In the final step, called the steady-state phase, two-tier hierarchical communication is carried out as follows. At first, CHs receive all data packets from member nodes according to a Time Division Multiple Access (TDMA) schedule (intra-cluster communication). Once all the data packets have been received by CHs, they are aggregated (using CH's own data as well) and sent to the BS. If a cluster has no members after formation (i.e., only one active node remains in the network), that CH simply sends its own data to the BS. Note that being a CH consumes more energy than being a regular node, as CHs must receive multiple packets and transmit to a distant base station.

Algorithm 1. Outline of the CH Selection-Based Communication

-
CH Selection-Based Communication
1: Deploy sensors randomly on the specified area
2: Determine the position of the BS
3: while network is alive do
4: CH selection phase
5: Cluster formation phase
6: Steady-state phase
7· end

2.2. Energy dissipation model

This paper adopts the energy dissipation model from [7], which is a simplified representation of radio hardware. In this model, both the transmitter and the receiver consume energy to operate the radio electronics. Additionally, the transmitter expends extra energy to power the amplifier.

When a sensor transmits a message, the energy dissipated by that sensor is calculated using (1). The notation $E_{Tx}(l,d)$ represents the energy required to transmit a 1-bit message over a distance d. The terms $E_{Tx-elec}$ and E_{Tx-amp} refer to the energy consumed by the transmitter electronics and the power amplifier, respectively. Note that the calculation depends on the threshold distance d_0 : the free space model (with d^2 power loss and coefficient ϵ_{fs}) is used if the distance is below the threshold, while the multi-path fading model (with d^4 power loss and coefficient ϵ_{mp}) is applied otherwise. This threshold makes long-distance communication inefficient, so transmitting data to nearby nodes is more energy-efficient. E_{elec} denotes the electronics energy, which depends on the WSN design.

$$E_{Tx}(l,d) = E_{Tx-elec}(l) + E_{Tx-amp}(l,d) = \begin{cases} l \times E_{elec} + l \times \epsilon_{fs} \times d^2, d < d_0 \\ l \times E_{elec} + l \times \epsilon_{fmp} \times d^4, d \ge d_0 \end{cases}$$
 (1)

The energy dissipated when receiving a message is calculated using (2). The notation $E_{Rx}(l)$ represents the energy required to receive an 1-bit packet, where the energy consumed per bit by the receiver electronics is denoted by $E_{Rx-elec}$.

$$E_{Rx}(l) = E_{Rx-elec}(l) = l \times E_{elec}$$
(2)

3. Related work

3.1. Heuristic-based CH selection methods

LEACH [10] is the most well-known heuristic-based distributed clustering algorithm in WSNs. It is a protocol based on the random selection of CHs and provides significant energy savings compared to static clustering and the Minimum Transmission Energy (MTE) protocol. However, since it may select low-energy nodes as CHs, overall network performance can degrade. To address this limitation, several variants have been proposed. LEACH-C [7] uses node energy and location awareness for CH selection. E-LEACH [19] avoids low-energy CHs by employing a minimum spanning tree technique. V-LEACH [20] introduces auxiliary nodes that act as backup CHs, improving reliability but potentially leading to inefficient energy use. TL-LEACH [21] uses a two-level clustering scheme to facilitate long-distance broadcasts to the BS, but its scalability for large WSNs is limited. PEGASIS [22], though not hierarchical like LEACH, uses a chain-based data transmission approach built via a greedy algorithm. While it performs better than LEACH in some respects, its latency makes it unsuitable for time-sensitive applications. HEED (Hybrid Energy-Efficient Distributed) [23] enhances clustering by considering residual energy as the primary factor and node degree and distance as secondary factors. Similarly, the Energy-Aware Clustering Method (EACM) [24] has been proposed to improve energy efficiency through heuristic clustering strategies.

3.2. Metaheuristic-based CH selection approaches

In recent years, metaheuristic algorithms have been increasingly adopted for CH selection in WSNs to address the limitations of heuristic methods. [25] introduced a particle swarm optimization (PSO) algorithm to determine optimal CH locations and increase intra-cluster distance. [26] proposed a PSO-based clustering approach that incorporates a modified fitness function accounting for both intra-cluster and penetration distances. [27] further improved PSO by integrating energy-awareness, considering parameters such as average intra-cluster distance and the ratio of total initial energy to the current energy of CHs. [8] introduced an Artificial Bee Colony (ABC) clustering protocol for WSNs. [28] introduced an energy-sensitive PSO approach using a fitness function based on distance, energy, and node density. [29] proposed a PSO algorithm tailored for time-sensitive applications, though fault tolerance was not adequately addressed. [9] incorporated intra-cluster distance, sink distance, and residual energy into the PSO process.

3.3. Priority-aware WSNs

While most research on CH selection focuses on energy efficiency, priority-aware WSNs have also gained attention in recent years. [30] introduced the idea of priority regions in sensor deployment optimization using a genetic algorithm to maximize coverage of high-priority (hot spot) regions. This idea was extended by [31], who incorporated area priority estimation and tested their method on satellite imagery. [32] proposed a WSN-based smart grid system using priority scheduling for traffic management. Their algorithm optimizes system utility through cognitive radio-based channel allocation and priority-aware traffic scheduling. Similarly, [33] developed a packet transmission scheduling framework for cluster-based industrial WSNs with node-level priority awareness. [34] proposed a UAV-based frame selection strategy that adjusts the contention window based on regional priority, thereby improving sensor-to-UAV data transmission.

3.4. Research gap and contribution

Although many studies in the literature have addressed either dynamic CH selection or priority awareness in WSNs, few have attempted to integrate both aspects into a unified solution. As summarized in Table 1, prior works typically

focus on optimizing CH selection without considering priority-based region awareness, or conversely, address priority considerations without dynamic CH optimization.

Table 1. Comparison of main related works showing the research gap in priority-aware dynamic CH selection.

Study	Priority-aware WSN	Dynamic CH selection
Heinzelman et al. [10]	no	yes
Karaboğa et al. [8]	no	yes
Rao et al. [9]	no	yes
Kalaycı and Uğur [30]	yes (region-based)	no
Huang and Soong [33]	yes (node value-based)	no
Say et al. [34]	yes (UAV-based)	no
This study	yes (region-based)	yes

This paper extends the classical CH selection problem by integrating region-based priority awareness for the first time. The proposed method dynamically selects energy-efficient CHs while ensuring that data from high-priority regions is transmitted with appropriate attention, thus addressing a gap in existing literature.

4. CH selection optimization with priority regions

4.1. Standard CH selection in WSNs

The standard CH selection problem is described as follows. Let A = (W, H) denote a 2D Euclidean plane, where W and H represent the width and height of the area, respectively. $S = S_1, S_2, \dots, S_n$ is the set of sensors, where each $S_i = (x_i, y_i)$ represents the coordinates of sensor i, satisfying $0 \le x_i \le W$ and $0 \le y_i \le H$. The base station is denoted by BS, with coordinates (BS_x, BS_y) . Normal sensor nodes transmit data to CHs, which then forward the aggregated data to the BS after receiving all packets from their member nodes. It is assumed that the BS has an unlimited power supply, while each sensor has a non-rechargeable battery with initial energy $E_i = E_0 > 0$. When a sensor runs out of energy, i.e, $E_i = 0$, it is considered dead and can no longer perform any transmission or reception. The energy consumed by each sensor is calculated using the energy dissipation model detailed in Section 2.2, which depends on both distance and packet length. Distances are calculated as the 2D Euclidean distance between any pair of locations.

The goal is to select CHs in every transmission round to ensure energy efficiency, i.e., to distribute the energy load evenly among sensors and prevent premature node failure due to poor cluster design. Achieving this goal provides key benefits, such as extending network lifetime and increasing the number of packets transmitted. This problem is an instance of the k-center problem, where $k \le n$ cluster centers are selected among n points to minimize the maximum distance from any point to its nearest cluster center. Since the k-center problem is NP-hard [35] with exponential time complexity, heuristic-based methods are preferred in practice.

4.2. Priority region aware CH selection in WSNs

This subsection defines the priority-aware extension of the standard CH selection problem introduced earlier (see Section 4.1). In the standard CH selection problem, all sensors are assumed to be located in an area of equal importance. However, this assumption may not hold in real-world scenarios where certain parts of the observation area require more attention.

Fig. 2 illustrates a sample WSN scenario with three different priority values and four defined priority regions. The importance of each priority region is determined by its rank. Each priority rank is associated with a numeric value—the higher the value, the greater the priority assigned to that region. For example, Region 3 with rank 3 (priority value 3.5) has higher priority than Region 1 and 2. Similarly, Region 2 has higher priority than Region 1 and 4, since its priority value is greater (2.5 > 1.5). As in this example, a non-priority region—covering the area outside the defined priority zones—can be assigned rank 0 with a value of 1.0. Thus, two nodes in the non-priority region would have the same total priority value as a single node in Region 2, and decisions should account for this. Note that priority values can be any suitable number greater than 1.0, as long as they realistically reflect the priority requirements of the target environment.

To integrate priority-aware decisions into classical CH selection in WSNs (see 4.1), we explicitly define priority regions as a set $RS = R_1, \dots, R_l$, where l is the number of regions. Considering that the same priority rank can be shared among several regions, ranks are defined as a set $KS = K_0, K_1, \dots, K_m$, where m is the number of ranks. Each rank has a unique priority value denoted by K_i . p_value. Rank 0 (K_0) is reserved for the non-priority region and assigned a priority value of 1.0. Any priority region can now be defined by a pair of values as $R_i = (K_j, boundary_i)$, where $K_j \in KS$ and $j \neq 0$, and $boundary_i$ defines the location and shape of region i. Accordingly, the total priority of a network with operating nodes (i.e., nodes with remaining energy $E_i > 0$) can be calculated using (3).

$$totalOpPriority = \sum_{i:E_i > 0} S_i.region.rank.p_value$$
(3)

The goal of the problem is now to select CHs at every transmission round to ensure energy efficiency while preserving the total priority of operating nodes. Therefore, algorithms designed to solve this new problem should also consider the priority levels of nodes as a design parameter and provide techniques to address this requirement.

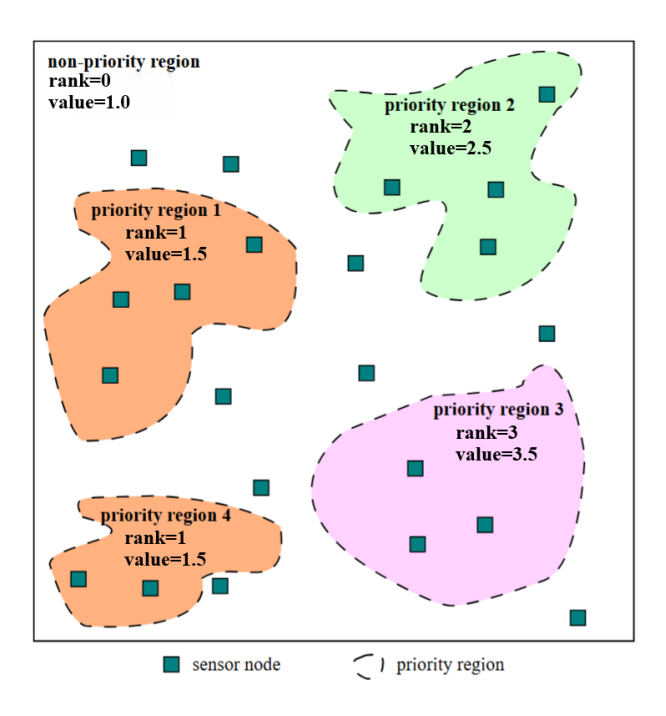


Fig. 2. An example of a WSN with four priority regions at three different priority ranks. The priority rank of the area outside the priority regions (non-priority region) is set to 0, with a value of 1.0.

5. The proposed algorithm and its components

5.1. Solution representation, discretization, and cluster formation

Representation of solutions is an important design step in any optimization algorithm. To solve the CH selection problem using continuous optimization algorithms, each solution is represented as a real-valued vector, as shown in Fig. 3. The size of the solution vector is $k \times 2$, where k is the number of CHs to be elected, and each CH is represented by a pair of coordinates (x, y).

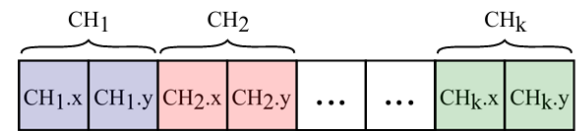


Fig. 3. Representation of solutions in CH selection optimization.

Before evaluating the quality of a solution, it must first be mapped to actual nodes, a process known as discretization. Since the original continuous optimization algorithms operate on real-valued coordinates, these hypothetical positions must be assigned to real, active nodes. In this study, we use a closest-node matching strategy, where each CH position in the solution vector is assigned to the nearest active node in the WSN (see Fig. 4-a). The resulting CH vector, of size k, is then used for subsequent steps such as fitness evaluation and cluster formation. For the cluster formation step, we use a deterministic approach that assigns each active non-CH node to its closest CH (see Fig. 4-b). This simple rule helps keep intra-cluster distances short, thereby reducing the overall communication cost in the network.

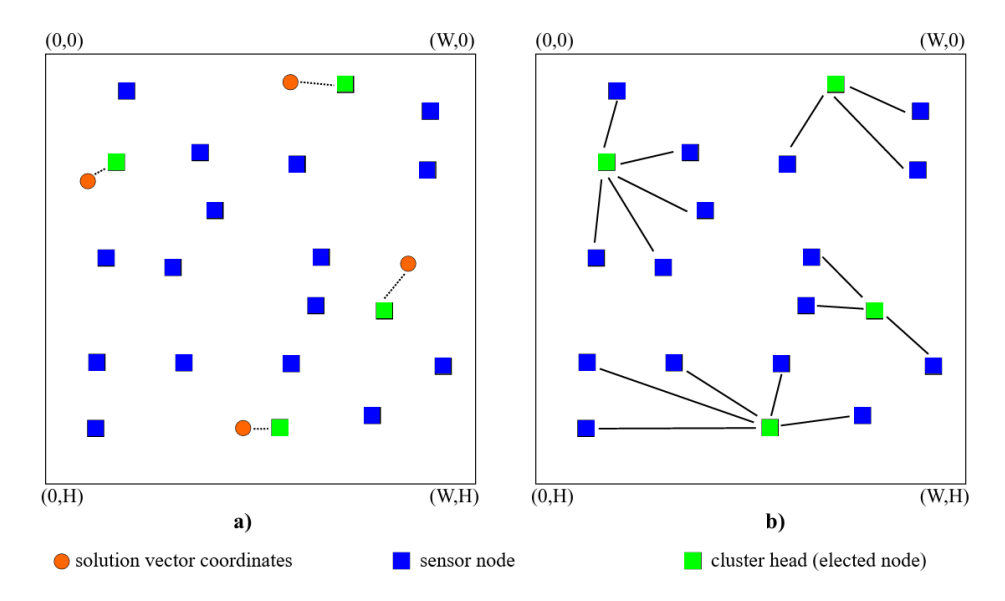


Fig. 4. An illustration of discretization (a), and cluster formation (b) phases of a real-valued solution vector for n=20 and k=4. W is the width, H is the height.

5.2. Design of the fitness function

The fitness function is a crucial component of any metaheuristic optimization algorithm. Since the entire search process relies heavily on it, the fitness function must accurately reflect all the objectives that need to be achieved.

5.2.1. Components of the fitness function

Considering that our primary goal is to ensure energy efficiency in priority-aware environments, three components have been identified for designing the fitness function: fDist, f_CH_Energy , and $f_CH_Priority$, which are explained as follows.

fDist is used to minimize the total distance between nodes. Since energy dissipation is directly related to the distance between the transmitter and receiver, it is efficient to keep both inter-cluster distances and CH-to-BS distances as short as possible. The calculation of fDist sums the total intra-cluster distances and the total distance between the CHs and the BS.

 f_CH_Energy is the second component of the fitness function. It aims to maximize the total energy of the CHs, helping to prevent them from running out of energy and dying. The calculation of f_CH_Energy sums the total energy of the current CHs. Then the summation is multiplied by -1 because f_CH_Energy is maximized, while the overall fitness function is minimized.

 $f_CH_Priority$ is the third component of the fitness function. It is used to minimize the total priority values of the CHs, helping to prevent high-priority nodes from depleting their energy too quickly. The calculation of $f_CH_Priority$ sums the priority values of the regions corresponding to every CHs. It is specifically designed to reduce CH selection in high-priority regions to prevent early node depletion which is a key concern in mission-critical WSN applications.

5.2.2. Unified fitness function

In this section, we define the unified fitness function, which combines the three components described in Section 5.2.1. Rather than using the raw values of these components directly, we normalize them based on insights from preliminary experiments. Specifically, fDistN represents the total distance normalized by the average edge length of the problem area (see (4)), $f_CH_EnergyN$ is the total CH energy normalized by the number of CHs and the initial energy (see (5)), and $f_CH_PriorityN$ is the total CH priority normalized by the number of CHs as in (6).

$$fDistN = \frac{fDist}{(W+H)/2} \tag{4}$$

$$f_CH_EnergyN = \frac{f_CH_Energy}{k \times E_0}$$
 (5)

$$f_CH_PriorityN = \frac{f_CH_Priority}{k}$$
(6)

Using the normalized component values, we define the unified fitness function as shown in (7), where the weighting factors satisfy the constraint $\alpha + \beta + \gamma = 1.0$.

$$f = \alpha \times fDistN + \beta \times f_CH_EnergyN + \gamma \times f_CH_PriorityN$$
 (7)

5.3. Outline of the proposed algorithm

The proposed algorithm in Algorithm 2 specifically addresses the CH selection phase of the generic WSN operation pipeline given in Algorithm 1. This phase is critical, as it directly affects energy efficiency and network lifetime considering priority regions. Our approach employs a metaheuristic (MH)-based optimization strategy to iteratively search for optimal CH role assignments within a constrained, energy-aware, and priority-region-aware simulation environment.

The algorithm accepts several inputs: the metaheuristic algorithm MH, the list of sensor nodes \$sensors\$, the number of CHs k, the population size NP, the maximum number of fitness evaluations MAX_FEs , algorithm-specific parameters alg_params , and problem-specific parameters $prob_params$. The alg_params include hyperparameters of the MH algorithm—such as crossover and mutation rates (depending on the MH used)—and coefficients (e.g., α , β , γ) used in the multi-objective fitness function. The $prob_params$ define static attributes of the environment, such as the regional boundaries and initial energy levels of the sensor nodes.

Each candidate solution encodes the spatial coordinates of k CHs as a real-valued vector of dimension $dim = 2 \times k$, corresponding to 2D positions for each CH. The initial population of NP candidate solutions is randomly generated within the area boundaries specified by $prob_params$.

The most computationally expensive operation in the algorithm is the fitness function evaluation, which simulates the cluster formation and steady-state phases to assess the quality of the proposed CH configurations. These simulations are virtual and do not involve actual network communication. The fitness of each solution is calculated using a priority-aware unified objective function (see (7)), which balances energy efficiency and the extended monitoring of priority regions.

After initializing the population and computing their fitness values, the algorithm enters its main optimization loop, which continues until the total number of function evaluations (FEs) reaches the budget limit MAX_FEs . In each iteration:

- The MH operator generates a new set of candidate solutions (pop_new) based on the current population.
- Each candidate in *pop_new* is evaluated using the same fitness function.
- The best CH configuration found so far is updated if a better solution is discovered.
- A new population for the next iteration is selected using the *solutionAcceptance* strategy, which depends on the specific MH algorithm employed.

When the termination condition is satisfied at the end of the evaluation budget, the algorithm returns the best CH configuration (best CH list) found during the optimization.

Algorithm 2. MH-based Priority-Region-Aware CH Selection Algorithm

```
MH-based Priority-Region-Aware CH Selection

Input: MH, sensors, p, k, NP, MAX_FES, alg_params, prob_params

Output: best_CH_list

1: // Initialization

2: dim \leftarrow k \times 2

3: MH.init(alg_params, prob_params)

4: pop \leftarrow initPopulation(NP, dim, prob_params)

5: FEs \leftarrow 0

6: for i \leftarrow 1 to NP do

7: pop[i].fitness \leftarrow calculate priority-aware fitness of pop[i].CH_list using alg_params, prob_params, and equation (7)

8: FEs \leftarrow FEs + 1

9: end
```

```
10: // main loop: CH selection optimization using MH
11: while FEs < MAX_FEs do</li>
12: pop_new ← MH.generateNewSolutions(pop)
13: for i ← 1 to |pop_new| do
14: pop_new[i]. fitness ← calculate priority-aware fitness of pop_new[i]. CH_list using alg_params, prob_params, and equation (7)
15: FEs ← FEs + 1
16: end
17: best_CH_list ← findBestSolution(pop, pop_new)
18: pop ← solutionAcceptance(pop, pop_new)
19: end
20: return best_CH_list
```

5.4. Computational complexity and scalability considerations

The time complexity of the proposed algorithm is dominated by the evaluation of the fitness function, which simulates cluster formation and steady-state communication behavior in a virtual WSN. Let NP denote the population size and MAX_FEs the maximum number of fitness evaluations. Since each iteration evaluates a set of candidate solutions, the total number of fitness function calls is bounded by MAX_FEs. Therefore, the overall time complexity is approximately $O(MAX_FEs \times T_{pit})$, where T_{pit} represents the time required to evaluate the fitness of a single candidate solution.

The dimensionality of the search space is dim = $2 \times k$, where $k = \rho \times n$ is the number of CHs, n is the number of sensor nodes, and ρ is a user-defined ratio ($0 < \rho < 1$) controlling CH density. As the number of sensor nodes increases, both the problem dimensionality and the computational cost of fitness evaluation grow. This is due to more complex clustering behaviors and energy interactions needing to be simulated.

To maintain performance as the network size scales up, the evaluation budget MAX_FEs may be proportionally increased. However, the algorithm is inherently parallelizable: each candidate solution in the population can be evaluated independently. This allows the algorithm to be efficiently executed in parallel on multi-core processors. Accordingly, the proposed approach is scalable to large-scale WSN scenarios, provided that appropriate computational resources are available.

Together, although the algorithm exhibits linear complexity in terms of the number of fitness evaluations, its high parallelizability ensures that scalability is achievable in practice, making it suitable for real-world deployments involving large sensor networks.

6. Experimental work

In this section, we conduct an experimental study to analyze priority-based scenarios using energy-efficient CH selection algorithms. We include LEACH as a representative decentralized and priority-unaware protocol solely as a reference baseline to provide contextual comparison; it is not intended for direct comparison with our centralized proposed method. For the metaheuristic-based solutions, we select a diverse set of six population-based algorithms. The first group includes classical methods: ABC, PSO, and DE, which are widely used in WSN applications due to their simplicity, adaptability, and proven effectiveness in balancing exploration and exploitation. These methods are well-established in the literature for solving energy-aware CH selection problems. The second group comprises more recent, state-of-the-art algorithms: JADE, SHADE, and CMAES. These advanced optimizers introduce dynamic adaptation strategies such as parameter self-tuning (JADE, SHADE) and covariance matrix learning (CMAES), making them highly effective for navigating complex, multimodal search spaces. This selection allows us to compare

traditional and modern centralized techniques within a unified experimental framework while ensuring strong performance diversity and relevance to WSN clustering.

6.1. Experimental setup

In our experiments, the simulation environment was set up as listed in Table 2, which was adopted from [9]. The number of sensors was fixed at n=400, and the BS was located at the center of the WSN area. The implementation of the LEACH algorithm followed the original description in [10]. The number of CHs at each step was calculated as $k = \lfloor \rho \times numberOfOperatingNodes \rfloor$, with ρ set to 0.1 for all experiments. If k=0 (which may occur towards the end of the simulation) it was set to 1 to ensure at least one CH is selected. The population size (number of candidate solutions) for the optimization algorithms was set to NP=20. To ensure a fair comparison among the metaheuristics, the termination criterion was set to $NP \times 1000$ function evaluations. Due to the stochastic nature of the algorithms, multiple runs were necessary, and each algorithm was executed 5 times with different random seeds; despite this limited number—chosen to manage high computational cost—the low variability among runs supports the reliability of the reported average results.

Simulation parameter	Value
WSN Area (W,H)	200 m, 200 m
E_0	1.0 J
d_0	30 m
1	4000 bits
p (CH ratio)	0.1
$E_{ m elec}$	50 nJ/bit
ϵ_{fs}	10 pJ/bit/m ²
$\epsilon_{ m mp}$	0.0013 pJ/bit/m ⁴

Table 2. Simulation parameters used in experiments.

After preliminary experiments, the parameters for the metaheuristic algorithms were set as follows. The fitness function weights were empirically chosen as $\alpha=0.1$, $\beta=0.1$, and $\gamma=0.8$ after testing both an extreme weighting scheme—assigning 0.8 to one parameter and 0.1 to the others—and a balanced setting (assigning 0.333 to all), with the selected values yielding better performance. For the Artificial Bee Colony (ABC) algorithm, the limit parameter was set to $limit=NP\times D$, where D is the problem dimension. The Particle Swarm Optimization (PSO) parameters—cognitive, social, and inertia weights—were set to 2.0, 2.0, and 0.9, respectively. The Differential Evolution (DE) algorithm used a differential weight (F) of 0.9 and a crossover rate of 0.5. The JADE algorithm parameters p and p were set to 0.1, with the archive enabled (p of 0.9 archive p of 0.5. The SHADE algorithm, we set p of p of 0.9, p of 0.9, p of 0.9, p of 0.9, p of 0.5 algorithm, we employed the implementation from the Apache Commons Math library.

6.2. Problem scenarios

To evaluate the impact of different problem characteristics on the performance of CH selection optimization, we designed three problem scenarios based on four priority regions. The shapes and positions of these regions are

^{*} https://commons.apache.org/proper/commons-math/

illustrated in Fig. 5. Note that the area outside the priority regions is considered a non-priority region with rank 0 and a priority value of 1.0.

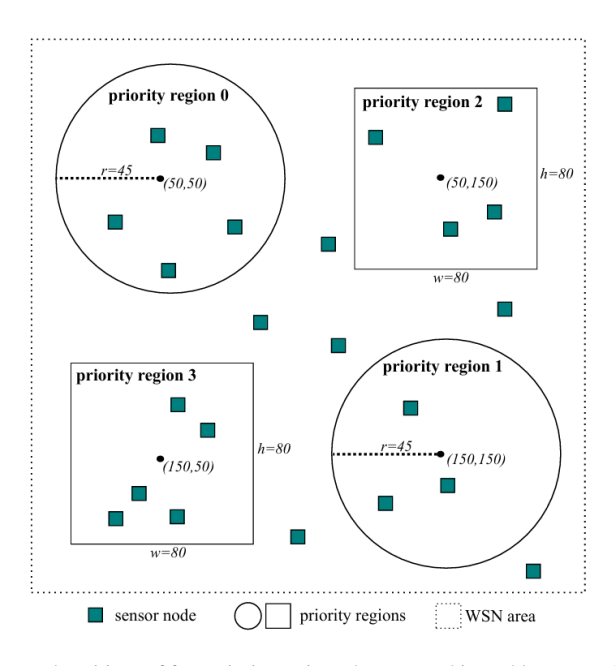


Fig. 5. Demonstration of the shapes and positions of four priority regions that are used in problem scenarios. r denotes the radius of circle shape regions. w and h denote the width and height of the rectangle shape regions. dot denotes the center of the regions.

Table 3 provides detailed information about the three problem scenarios. Each scenario assigns different priority values to the ranks. Scenario 1 represents the non-priority case, where all regions have the same priority value of 1.0. Scenarios 2 and 3 are designed for priority-aware environments. In Scenario 2, the priority values for the ranks are close to each other, such as 1.5 and 2.0, whereas in Scenario 3, the priority values differ significantly, with values like 5.0 and 25.0. Each priority rank corresponds to a numerical priority value that reflects the importance of the respective region—the higher the value, the higher the priority. The algorithm aims to keep nodes in higher priority regions alive for as long as possible. For further details, please refer to Section 4.2.

Table 3. Three scenarios used in the experimental work. Scenario 1: non-priority with equal region values; Scenarios 2 and 3: priority-aware with increasing gaps between priority levels.

Region	Scenario 1	Scenario 2	Scenario 3		
non-priority region	rank=0, p_value=1.0	rank=0, p_value=1.0	rank=0, p_value=1.0		
priority region 0	rank=0, p_value=1.0	rank=1, p_value=1.5	rank=1, p_value=5.0		
priority region 1	rank=0, p_value=1.0	rank=1, p_value=1.5	rank=1, p_value=5.0		
priority region 2	rank=0, p_value=1.0	rank=2, p_value=2.0	rank=2, p_value=25.0		
priority region 3	rank=0, p_value=1.0	rank=2, p_value=2.0	rank=2, p_value=25.0		

6.3. Performance metrics

6.3.1. Total priority of packet transmissions

This performance metric measures the total priority of packets received by the BS over the entire network lifetime. At each transmission step, all active sensors are assumed to transmit one packet to the BS. The total priority of these transmitted packets is then calculated using (8), where t denotes the transmission index, t_{max} the total number of transmissions, and $totalOpPriority_t$ is computed as defined in (3).

$$\sum_{t=1}^{t_{max}} totalOpPriority_t \tag{8}$$

6.3.2. Network lifetime

Network lifetime is measured by the number of transmission cycles completed until the last node in the WSN depletes its energy and dies. In this study, the lifetimes of nodes within different priority ranks are evaluated separately. A longer network lifetime indicates better overall network performance.

6.4. Experimental results

6.4.1. Performance comparison of the algorithms

In this section, we compare the optimization algorithms to determine which performs best for the priority-aware CH selection problem. We begin by analyzing the total priority of transmitted packets under Scenario 2. As shown in Fig. 6, the top three algorithms are ABC, JADE, and SHADE. The baseline algorithm, LEACH, exhibits poor performance due to its decentralized operation and lack of consideration for priority information. Among the tested algorithms, JADE achieved the highest median total priority of transmitted packets, improving it by approximately 16% compared to LEACH.

To further analyze whether the differences between algorithms are significant, we applied the Kruskal-Wallis test to assess the total priority of packets transmitted among the algorithms. The test yielded a p-value of 3.14×10^{-5} , indicating a statistically significant difference. Based on this result, we conducted post-hoc pairwise Mann-Whitney U tests to identify which specific algorithm pairs showed significant performance differences. These non-parametric tests were chosen because each algorithm was run only five times, resulting in a small sample size, and because the performance metrics derived from stochastic metaheuristic algorithms may not follow a normal distribution. As reported in Table 4, the results indicate significant differences (p < 0.05) between most algorithm pairs, except for ABC vs. JADE (p = 0.3095), ABC vs. SHADE (p = 0.3095), DE vs. SHADE (p = 0.0556), and JADE vs. SHADE (p = 0.5476), suggesting that these algorithms exhibit statistically similar performance in terms of total priority packets transmitted. Overall, ABC and JADE are the most successful and distinctive algorithms, showing significant differences from most others. However, JADE was selected for further experimental analysis because it has a higher median value than ABC.

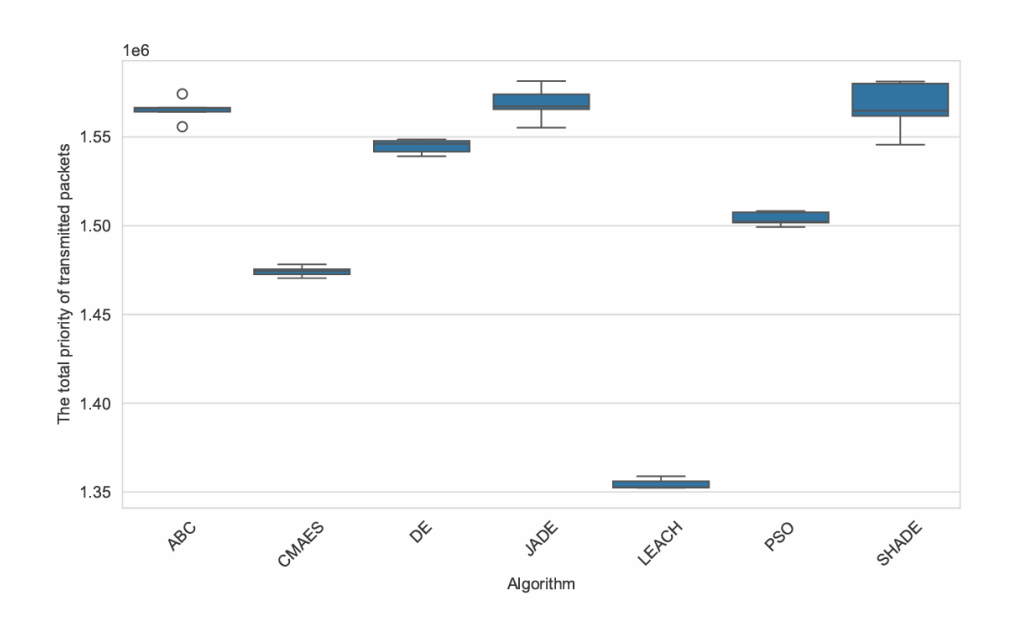


Fig. 6. Box plots of algorithms showing the total priority of transmitted packets in Scenario 2.

Table 4. Pairwise Mann-Whitney U test p-values for the total priority of transmitted packets in Scenario 2. Bold values indicate statistically significant differences at p<0.05.

	ABC	CMAES	DE	JADE	LEACH	PSO	SHADE
ABC	-	0.0079	0.0079	0.6905	0.0079	0.0079	1.0
CMAES	-	-	0.0079	0.0079	0.0079	0.0079	0.0079
DE	-	-	-	0.0079	0.0079	0.0079	0.0556
JADE	-	-	-	-	0.0079	0.0079	0.6905
LEACH	-	-	-	-	-	0.0079	0.0079
PSO	-	-	-	-	-	-	0.0079
SHADE	-	-	-	-	-	-	-

6.4.2. Network lifetime across different scenarios

To analyze the network lifetimes achieved by the JADE metaheuristic, three scenarios were considered, as illustrated in Fig. 7. The LEACH algorithm was used as a baseline for comparison. A total of 400 sensors were randomly distributed, with approximately 133 nodes assigned to each priority level, enabling a clearer evaluation of differences across ranks in priority scenarios. In Scenario 1, which has no priority regions, the centralized JADE algorithm improves network lifetime by approximately 27%. In the priority-based Scenarios 2 and 3, LEACH performs similarly to Scenario 1, with overlapping lifetime curves across priority levels indicating no differentiation. Conversely, the priority-aware JADE algorithm effectively extends the lifetime of higher-priority nodes by initially sacrificing lower-priority ones. Specifically, nodes at the highest priority level survive up to 4,000 transmissions in both scenarios, resulting in a network lifetime improvement of about 44%.

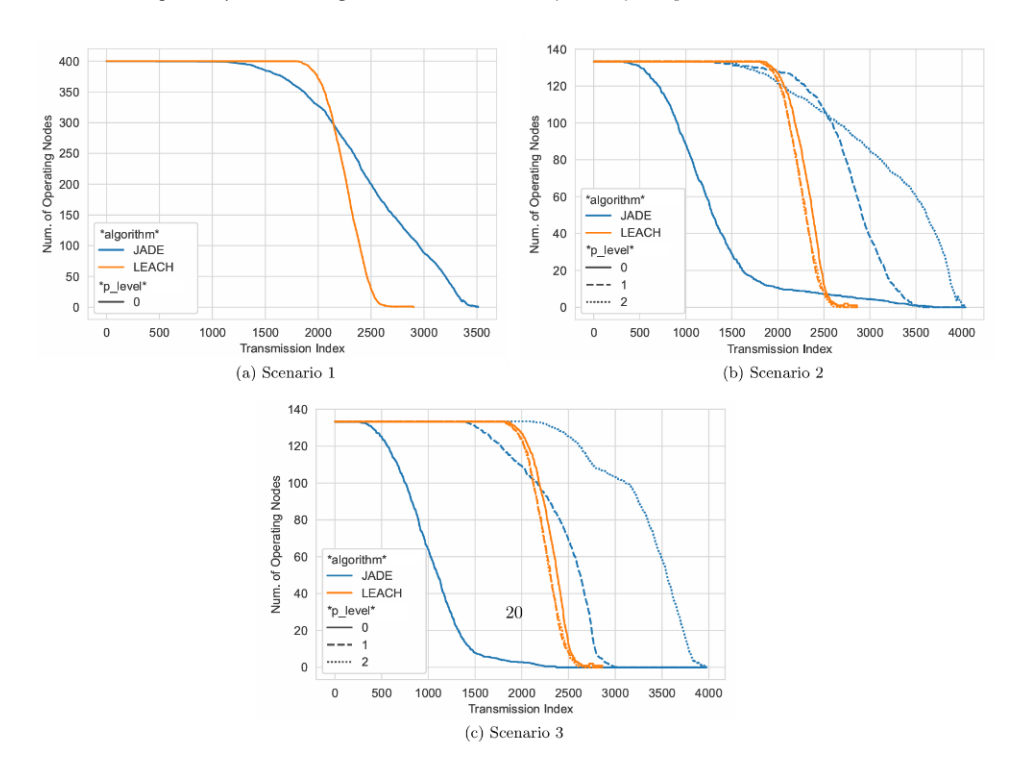


Fig. 7. Comparison of network lifetimes for LEACH and JADE across different scenarios and priority levels. Note that 400 sensors are randomly distributed across different priority levels (~133 each) in scenarios 2 and 3.

6.4.3. Energy dissipation across different scenarios

Fig. 8 shows energy dissipation during the network lifetime for the JADE algorithm. As seen in Fig. 8-a, nodes in priority level 0 (non-priority region) dissipate more energy than others at the beginning of the iterations. This occurs because these nodes are more likely to be selected as CHs. As they begin to deplete over time, the overall energy consumption decreases due to the reduced number of active nodes. At this stage, we observe that energy consumption for nodes in priority regions increases but is spread over a longer duration for high-priority nodes (e.g., the curve for level 2 extends longer than that for level 1). The difference is even more noticeable in Fig. 8-b, where the gap between levels 1 and 2 is significant.

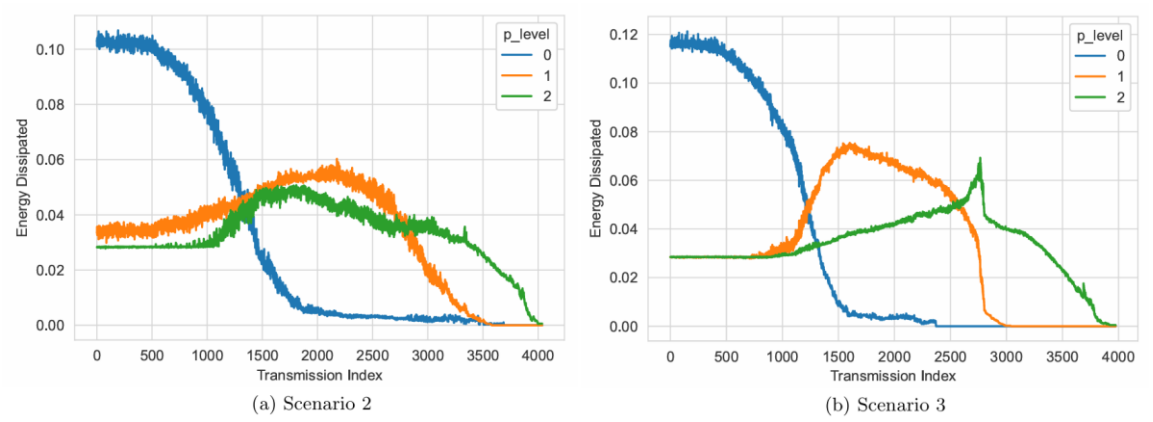


Fig. 8. Energy dissipation based on priority ranks using JADE metaheuristic algorithm for scenario 2 (a) and scenario 3 (b).

7. Conclusion

CH selection is a crucial optimization problem in the design of WSNs. The primary challenge is to prolong the network's lifetime and conserve the energy of individual nodes. Despite numerous attempts to address this issue, to the best of our knowledge, none have considered area prioritization. This problem is relevant in various scenarios, such as industrial facilities with hazardous zones and military surveillance areas, which require special attention. In this study, we formulated a priority-aware CH selection problem and proposed a novel approach that employs metaheuristic algorithms.

To evaluate the performance of the proposed algorithm, three different scenarios were designed. In Scenario 1, all regions have the same level of priority, while in Scenarios 2 and 3, regions may have different priorities. To measure the impact of priority levels, the gap between priority values was set higher in Scenario 3 compared to Scenario 2. A comprehensive experimental study was conducted in a simulation environment based on these scenarios. The results showed that integrating priority-aware CH selection significantly improves energy efficiency and packet transmission in high-priority regions. Compared to the decentralized baseline Low-Energy Adaptive Clustering Hierarchy (LEACH) algorithm, the proposed metaheuristic-driven approach demonstrated superior performance across all scenarios. In particular, the JADE algorithm achieved up to a 16% improvement in the total priority of transferred packets. Furthermore, it extended the lifetime of nodes in high-priority regions by 27% to 44%, ensuring better coverage and prolonged operation in critical areas. These findings highlight the effectiveness of metaheuristic-based centralized CH selection strategies in optimizing both energy conservation and priority-aware packet transmission in WSNs.

The main limitation of this type of problem is the need to run an optimization algorithm at each transmission step. While metaheuristic algorithms are well-suited for solving complex optimization problems, they can require considerable processing time. Future research could explore the development of local search algorithms or enhancements to the fitness function to achieve improved performance within a limited timeframe. Additionally, the use of multi-objective optimization techniques, instead of a unified fitness function, could be investigated. Although the priority objective in our fitness function—which minimizes the total priority value of selected CHs—has proven effective in preserving energy in high-priority regions, alternative formulations or adaptive strategies may be explored to better accommodate specific application needs or mission-critical dynamics.

In terms of scalability, the algorithm exhibits linear time complexity with respect to the number of fitness evaluations and is highly parallelizable, making it suitable for deployment in large-scale WSNs when sufficient computational resources are available. Furthermore, while this study considered fixed priority regions, extending the model to support dynamically changing priority areas remains a limitation and represents a valuable direction for

future work. Since metaheuristic algorithms are capable of adapting to dynamic environments, incorporating such behavior into WSN optimization may lead to more responsive and resilient network designs under evolving operational conditions.

Declaration of interests

The authors declare that they have no conflict of interest.

Acknowledgements

This research did not receive any specific grant from funding agencies in the public, commercial, or not-for-profit sectors.

Author Contributions

Osman Gökalp: Methodology, Software, Investigation, Writing - Original Draft. Doğan Aydın: Methodology, Software, Investigation, Writing- Original Draft. Aybars Uğur: Conceptualization, Methodology, Project Administration, Supervision, Writing - Review & Editing.

References

- [1] M. A. Jan, P. Nanda, X. He, and R. P. Liu, "A Sybil attack detection scheme for a forest wildfire monitoring application", *Future Gener. Comput. Syst.*, vol. 80, pp. 613–626, 2018, doi: 10.1016/j.future.2016.05.034.
- [2] N. Dey et al., "Developing residential wireless sensor networks for ECG healthcare monitoring", *IEEE Trans. Consum. Electron.*, vol. 63, no. 4, pp. 442–449, 2017, doi: 10.1109/TCE.2017.015063.
- [3] S. Li et al., "Survey on high reliability wireless communication for underwater sensor networks", *J. Network Comput. Appl.*, vol. 148, p. 102446, 2019, doi: 10.1016/j.jnca.2019.102446.
- [4] E. Felemban, "Advanced border intrusion detection and surveillance using wireless sensor network technology", *Int. J. Commun., Netw. and Syst. Sci.*, vol. 148, no. 5, pp. 251–259, 2013, doi: 10.4236/ijcns.2013.65028.
- [5] O. Gökalp, "Optimizing Connected Target Coverage in Wireless Sensor Networks Using Self-Adaptive Differential Evolution", *Balkan J. Electr. Comput. Eng.*, vol. 8, no. 4, pp. 325–330, 2020, doi: 10.17694/bajece.624527.
- [6] J. Dai et al., "Cluster head selection method of multiple UAVs under COVID-19 situation", *Comput. Commun.*, vol. 196, pp. 141–147, 2022, doi: 10.1016/j.comcom.2022.09.026.
- [7] W. B. Heinzelman, A. P. Chandrakasan, and H. Balakrishnan, "An application-specific protocol architecture for wireless microsensor networks", *IEEE Trans. Wireless Commun.*, vol. 1, no. 4, pp. 660–670, 2002, doi: 10.1109/TWC.2002.804190.
- [8] D. Karaboga, S. Okdem, and C. Ozturk, "Cluster based wireless sensor network routing using artificial bee colony algorithm", *Wireless Netw.*, vol. 18, no. 7, pp. 847–860, 2012, doi: 10.1007/s11276-012-0438-z.
- [9] P. C. S. Rao, P. K. Jana, and H. Banka, "A particle swarm optimization based energy efficient cluster head selection algorithm for wireless sensor networks", *Wireless Netw.*, vol. 23, no. 7, pp. 2005–2020, 2017, doi: 10.1007/s11276-016-1270-7.
- [10] W. R. Heinzelman, A. Chandrakasan, and H. Balakrishnan, "Energy-efficient communication protocol for wireless microsensor networks", in *Proc. of the 33rd Annu. Hawaii Int. Conf. Syst. Sci.*, 2000, pp. 10–pp, doi: 10.1109/HICSS.2000.926982.
- [11] A. C. Çabuker, M. N. Almalı, and İ. Parlar, "Evaluation of controller parameters on the twin rotor multiple input multiple output system using butterfly-based particle swarm optimization", *JSR-A Trans*, no. 052, pp. 174–189, 2023, doi: 10.59313/jsr-a.1198441.
- [12] P. C. S. Rao and H. Banka, "Novel chemical reaction optimization based unequal clustering and routing algorithms for wireless sensor networks", *Wireless Netw.*, vol. 23, no. 3, pp. 759–778, 2017, doi: 10.1007/s11276-015-1148-0.
- [13] D. Karaboga, "An idea based on honey bee swarm for numerical optimization", Technical report TR06, Erciyes University, Engineering Faculty, Computer Engineering Department, 2005.
- [14] K. V. Price, "Differential evolution", in Handb. Optim.: From Classical to Mod. Approach, Springer, 2013, pp. 187–214, doi: 10.1007/978-3-642-30504-7_8.
- [15] J. Kennedy and R. Eberhart, "Particle swarm optimization", in Proc. ICNN'95 Int. Conf. on Neural Networks, vol. 4, 1995, pp. 1942–1948, doi: 10.1109/ICNN.1995.488968.
- [16] N. Hansen, "The CMA evolution strategy: a comparing review", in Towards a New Evol. Comput.: Adv. Estimation of Distrib. Algorithms, Springer, 2006, pp. 75–102, doi: 10.1007/3-540-32494-1_4.
- [17] J. Zhang and A. C. Sanderson, "JADE: adaptive differential evolution with optional external archive", *IEEE Trans. Evol. Comput.*, vol. 13, no. 5, pp. 945–958, 2009, doi: 10.1109/TEVC.2009.2014613.

- [18] R. Tanabe and A. Fukunaga, "Success-history based parameter adaptation for differential evolution", in 2013 IEEE Congr. on Evol. Comput., 2013, pp. 71–78, doi: 10.1109/CEC.2013.6557555.
- [19] J. Xu et al., "Improvement of LEACH protocol for WSN", in 2012 9th Int. Conf. on Fuzzy Syst. Knowl. Discovery, 2012, pp. 2174–2177, doi: 10.1109/FSKD.2012.6233907.
- [20] M. B. Yassein, Y. Khamayseh, and W. Mardini, "Improvement on LEACH protocol of wireless sensor network (VLEACH)", *J. Digit. Content Technol. its Appl.*, 2009.
- [21] V. Loscri, G. Morabito, and S. Marano, "A two-levels hierarchy for low-energy adaptive clustering hierarchy (TL-LEACH)", in IEEE Veh. Technol. Conf., vol. 62, no. 3, pp. 1809, 2005.
- [22] S. Lindsey and C. S. Raghavendra, "PEGASIS: Power-efficient gathering in sensor information systems", in *Proc., IEEE Aerosp. Conf.*, vol. 3, pp. 3–3, 2002, doi: 10.1109/AERO.2002.1035242.
- [23] O. Younis and S. Fahmy, "HEED: a hybrid, energy-efficient, distributed clustering approach for ad hoc sensor networks", *IEEE Trans. Mob. Comput.*, vol. 3, no. 4, pp. 366–379, 2004, doi: 10.1109/TMC.2004.41.
- [24] E. Alimohammadi, S. Haghzad Klidbary, and M. Javadian, "Energy-aware clustering method for cluster head selection to increasing lifetime in wireless sensor network", *J. Supercomput.*, vol. 81, no. 1, p. 2, 2025, doi: 10.1007/s11227-024-06474-2.
- [25] J. Tillett, R. Rao, and F. Sahin, "Cluster-head identification in ad hoc sensor networks using particle swarm optimization", in 2002 IEEE Int. Conf. on Pers. Wireless Commun., 2002, pp. 201–205, doi: 10.1109/ICPWC.2002.1177277.
- [26] S. M. Guru, S. K. Halgamuge, and S. Fernando, "Particle swarm optimisers for cluster formation in wireless sensor networks", in 2005 Int. Conf. on Intell. Sens., Sensor Networks and Information Processing, 2005, pp. 319–324, doi: 10.1109/ISSNIP.2005.1595599.
- [27] N. M. A. Latiff, C. C. Tsimenidis, and B. S. Sharif, "Energy-aware clustering for wireless sensor networks using particle swarm optimization", in 2007 IEEE 18th Int. Symp. on Pers., Indoor and Mobile Radio Commun., 2007, pp. 1–5, doi: 10.1109/PIMRC.2007.4394521.
- [28] B. Singh and D. K. Lobiyal, "A novel energy-aware cluster head selection based on particle swarm optimization for wireless sensor networks", *Hum.-centric Comput. Inf. Sci.*, vol. 2, no. 1, pp. 1–18, 2012, doi: 10.1186/2192-1962-2-13.
- [29] H. Banka, P. K. Jana et al., "PSO-based multiple-sink placement algorithm for protracting the lifetime of wireless sensor networks", in *Proc. Second Int. Conf. on Comput. Commun. Technol.*, 2016, pp. 605–616, doi: 10.1007/978-81-322-2517-1_58.
- [30] T. E. Kalayci and A. Uğur, "Genetic algorithm-based sensor deployment with area priority", *Cybern. Syst.*, vol. 42, no. 8, pp. 605–620, 2011, doi: 10.1080/01969722.2011.634676.
- [31] E. Ateş, T. E. Kalayci, and A. Uğur, "Area-priority-based sensor deployment optimisation with priority estimation using K-means", *IET Commun.*, vol. 11, no. 7, pp. 1082–1090, 2017, doi: 10.1049/iet-com.2016.1264.
- [32] J. Huang, H. Wang, Y. Qian, and C. Wang, "Priority-based traffic scheduling and utility optimization for cognitive radio communication infrastructure-based smart grid", *IEEE Trans. Smart Grid*, vol. 4, no. 1, pp. 78–86, 2013, doi: 10.1109/TSG.2012.2227282.
- [33] J. Huang and B. H. Soong, "Priority-aware hybrid scheduling for fast, energy-efficient max function computation in single-hop networks", *IET Commun.*, vol. 10, no. 18, pp. 2606–2612, 2016, doi: https://doi.org/10.1049/iet-com.2016.0311.
- [34] S. Say, H. Inata, J. Liu, and S. Shimamoto, "Priority-based data gathering framework in UAV-assisted wireless sensor networks", *IEEE Sens. J.*, vol. 16, no. 14, pp. 5785–5794, 2016, doi: 10.1109/JSEN.2016.2568260.
- [35] P. K. Agarwal and C. M. Procopiuc, "Exact and approximation algorithms for clustering," *Algorithmica*, vol. 33, no. 2, pp. 201–226, 2002, doi: 10.1007/s00453-001-0110-y.



Contents lists available at Dergipark

Journal of Scientific Reports-A

journal homepage: https://dergipark.org.tr/tr/pub/jsr-a



E-ISSN: 2687-6167 Number 62, September 2025

RESEARCH ARTICLE

A deformation structure and origin of metamorphic sole rocks beneath the Eldivan and Ahlat ophiolites (Çankırı), Northern Anatolia.

Tijen ÜNER^{a,*}, Üner ÇAKIR^b

^aVan Yüzüncü Yıl University Geological Engineering, 65100,Tuşba-VAN, ORCID Number: 0000-0001-6059-9148 ^bHacettepe University, Geological Engineering, 06100, Ankara(retired), ORCID Number: 0009-0005-6581-734X

Abstract

Eldivan and Ahlat ophiolitic rocks are located in the central part of the İzmir-Ankara-Erzincan Suture Belt at the northwest of Çankırı (Türkiye). They occurred at the base of the Tethys Ocean in the Jurassic-Cretaceous period and moved on the continent during the closure period of the ocean in the Late Cretaceous. Metamorphic sole rocks in ophiolites are formed by mostly amphibolites and partially quartzite and schist. This study aims to determine the origin, temperature and pressure of metamorphic sole rocks in Eldivan and Ahlat ophiolites.

According to energy-dispersive X-Ray spectroscopy (EDS) analysis of amphibolite samples from Eldivan and Ahlat ophiolites, amphibole minerals take place in edenite (Mg-hornblende)-pargasite range. In contrast, the plagioclase minerals have albite composition. EDS analysis and petrographical investigations show that all relict pyroxene minerals in rock are primary character. The formation temperature range of the rocks is calculated as 501 - 642 °C. As a result of geochemical analysis, the metamorphic sole rocks at Eldivan and Ahlat ophiolites derived from an OIB-like mantle.

© 2023 DPU All rights reserved.

Keywords: İzmir-Ankara-Erzincan Suture Belt; amphibolite; ophiolitic base metamorphic rocks; pressure; temperature

* Corresponding author. Tel.: +90 (432) 444 50 65 E-mail address: tcakici@yyu.edu.tr

1.Introduction

Research on ophiolites provides critical insights into these rock assemblages geological processes, spanning their formation to eventual emplacement on continental crusts. Such studies elucidate the tectonic environment of formation, geodynamic conditions, magma characteristics, and approximate compositions. The origin of the metamorphic rocks found at the base of ophiolites has been a subject of considerable interest among geoscientists [1], [2], [3], [4], [5], [6], [7], [8]. For instance, detailed petrographic and microstructural investigations of the Baër-Bassit Ophiolite in Syria have revealed that the associated metamorphic rocks are derived from basaltic volcanic and sedimentary precursors [9], [10], [11]. Moreover, it has been established that the initial phase of metamorphism occurred within an oceanic setting rather than during continental obduction. This metamorphic transformation has been attributed to equilibration processes within the oceanic lithosphere itself [12], [13], [14]. [15] conducted a study in Kütahya, where they adopted a similar approach regarding the metamorphic sole rocks in the region. In their study, the counter-clockwise P-T-t paths observed in the sub-ophiolite metamorphic rocks were associated with intraoceanic thrusting and reflected subduction processes during the closure of the İzmir-Ankara-Erzincan Ocean. Continued subduction during the Late Cretaceous led to the widespread formation of blueschists within the Tayşanlı Zone. Subsequently, cold thrusting processes emplaced the ophiolites, metamorphic sole rocks, ophiolitic mélanges, and blueschists onto the Anatolian continental margin. These events occurred prior to the final collision between the Anatolide and Pontide continental domains.

The rocks within the metamorphic sole have undergone intense deformation, including folding and faulting. This pronounced deformation is characterized by a gneissic and schistose fabric in contact zones with peridotites, whereas the basal levels exhibit relatively less deformed rocks, such as phyllites and slates [16], [6].

Amphibolites predominantly represent the metamorphic sole. Geochemical studies of the amphibolites observed in contact zones indicate that they were formed through the metamorphism of alkaline and tholeitic mafic rocks (basalt-gabbro) of oceanic crust origin [6]. Metamorphic soles exhibit inverted metamorphic zonation, transitioning from upper amphibolite/granulite facies to greenschist facies. This zonation is particularly evident in contact zones with peridotites, where granulite facies and even anatexis are observed [17], [18], [19], [20], [15], while initial metamorphism is evident at the basal levels.

All these features of ophiolitic metamorphic sole suggest that the initial phase of metamorphism occurred not during continental obduction but earlier in an oceanic setting, during the thrusting of the oceanic lithosphere onto itself [12], [13], [14], [5].

Similar findings have been reported in studies conducted on the Pozanti-Karsanti Ophiolite in Türkiye. For instance, the presence of diabase dikes cutting through the metamorphic rocks [22], [23] and the age relationships between the metamorphic rocks and other units ([24]) indicate that metamorphism occurred earlier than the emplacement of these rocks onto the continent. This further suggests that metamorphism occurred before the obduction and was related to the processes within the same facies as the cumulates above the metamorphic units [18].

This study aims to determine the formation conditions, including temperature and pressure, as well as the protolith characteristics of the metamorphic sole rocks observed at the base of the Eldivan and Ahlat ophiolites located in the central part of the İzmir-Ankara-Erzincan Suture Zone.

2. Regional Geology

A suture refers to a tectonic boundary that separates two continental margin sequences which were deposited on opposite sides of an ancient ocean (e.g., [25]). It marks a significant geological discontinuity and is often linked with accretionary complexes, ophiolitic mélanges, and ophiolites, which provide evidence of the ocean's lifespan, subduction processes, and eventual closure. The İzmir-Ankara suture in Türkiye forms part of the Mesozoic boundary between the southern Laurasia and the northern Gondwana. This suture extends eastward as the Sevan-Akera suture toward the Lesser Caucasus and westward as the Vardar suture, reaching the Hellenides (Fig. 1a).

The Eldivan and Ahlat ophiolites (Fig. 1b, Fig. 1c), situated within the central portion of the İzmir-Ankara-Erzincan Suture Zone, are remnants of the Neotethys Ocean lithosphere. This oceanic lithosphere initiated rifting during the Late Triassic and was subsequently closed between the Late Cretaceous and Early Paleocene [28], [21], [29], [30]. These ophiolites were tectonically emplaced onto the underlying units along faulted contacts ([31]). This tectonic emplacement indicates that a north-south compressional regime prevailed in the region after the Miocene, resulting in the southward thrusting of the block containing the Eldivan and Ahlat ophiolites over its cover units.

Ar-Ar age analyses conducted on amphibolites from the Eldivan Ophiolite indicate an age range of 177.08 ± 0.9 Ma to 166.9 ± 1.1 Ma (Early-Middle Jurassic) [32]. This age range reflects the tectonic regime, regional compression, and ocean closure period associated with the İzmir-Ankara-Erzincan Zone. Additionally, zircon age analysis performed on the cover rocks overlying the Eldivan Ophiolite yielded an age of 105.2 ± 2 Ma [33].

2.1. Eldivan ophiolite

The Eldivan Ophiolite, trending NE-SW around the Eldivan district of Çankırı, presents a complete ophiolitic sequence. Based on the analysis of samples taken from the overlying cover units, the Eldivan Ophiolite was emplaced during the Albian-Aptian interval. The ophiolite is represented by a volcanic-sedimentary series (basalt, radiolarite-chert, mudstone), metamorphic series (amphibolite, epidote, quartzite), tectonites (harzburgite, dunite, chromite), cumulates (dunite, pyroxenite, wehrlite, gabbro, diorite, plagiogranite), and sheeted dikes (Fig. 2). All units, except for the volcanic-sedimentary series, are cut by isolated diabase dikes. Lateral and vertical transitions among the units of the Eldivan Ophiolite are clearly observable.

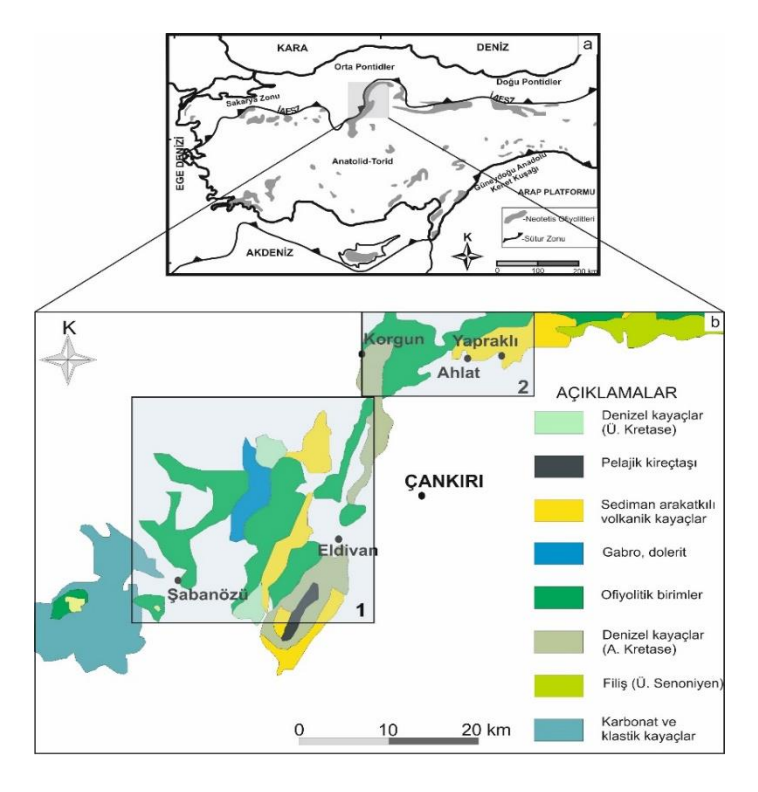


Fig. 1. a) Map of the ophiolitic rocks in Türkiye, and simplified geological map of b) Eldivan c) Ahlat ophiolites and surrounding area (modified from [27]).

The metamorphic sole rocks at the base of the Eldivan Ophiolite are observed as thin slices overlying the volcanic-sedimentary series (Fig. 2). Inverted metamorphism is identified within these metamorphic sole rocks. The unit is predominantly represented by amphibolites, with minor occurrences of quartzites, hornblendites, chlorite-sericite-talc schists, and epidote-garnet schist layers. The metamorphic series, characterized by intense folding and schistosity due to deformation, is crosscut by diabase dikes (Fig. 3a) and quartzite veins (Fig. 3b). The generally east-west trending dikes suggest that a north-south extensional regime was active during their emplacement.

Tectonic interactions between the metamorphic series, harzburgite tectonites, and volcanic-sedimentary sequences are displayed in the study area. These relationships are characterized by faulted contacts, with schistosity planes consistently parallel to the fault boundaries. The folding patterns observed in the unit indicate a complex history of multiple deformation phases.

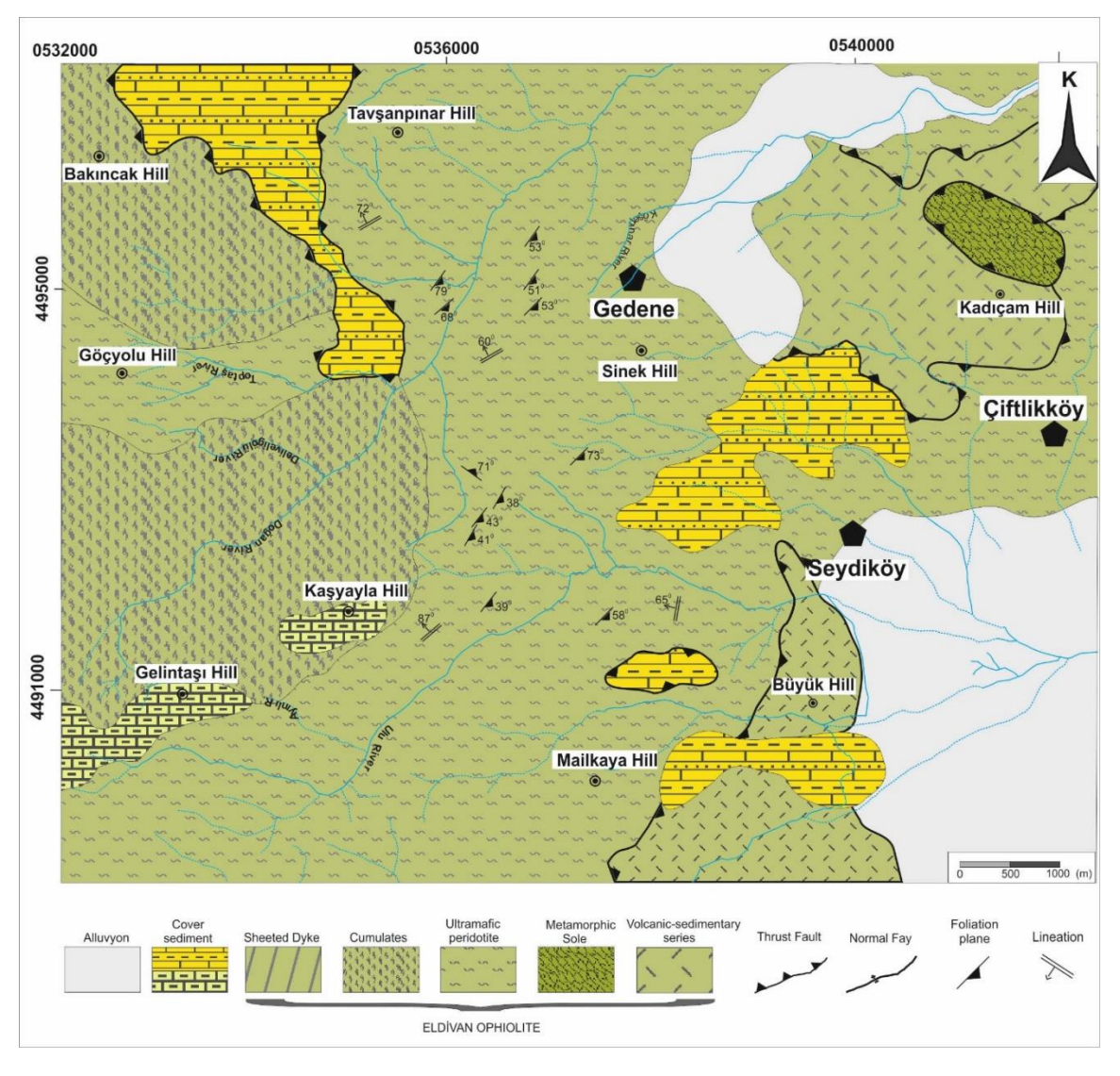


Fig. 2. Geological map showing the Eldivan Ophiolite rocks and surrounding area (modified from [27])

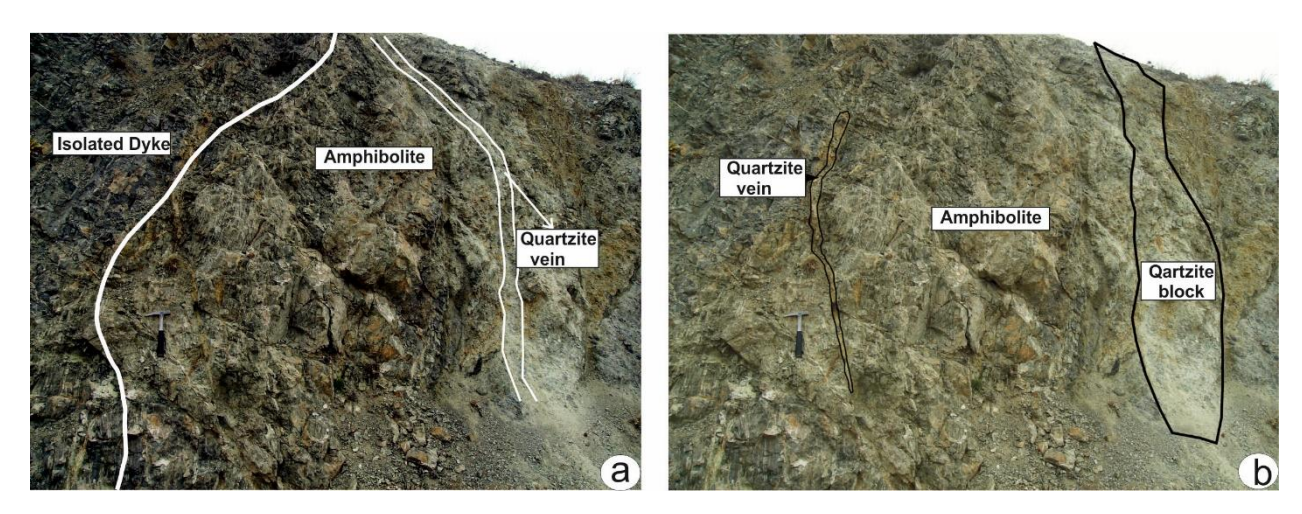


Fig. 3. Structures deformed the amphibolites in Eldivan ophiolite at the north of Akçalı village; a) Diabase dyke, b) Quartzite veins.

2.2. Ahlat ophiolite

The metamorphic sole rocks of the Ahlat Ophiolite exhibit pronounced schistosity and microfolding due to deformation (Fig. 5). The degree of metamorphism is lower compared to the Eldivan Ophiolite. The unit primarily consists of tremolite-actinolite schist, chlorite-sericite-talc schist, and minor amounts of amphibolite. Secondary quartz and calcite veins are observed within the unit.

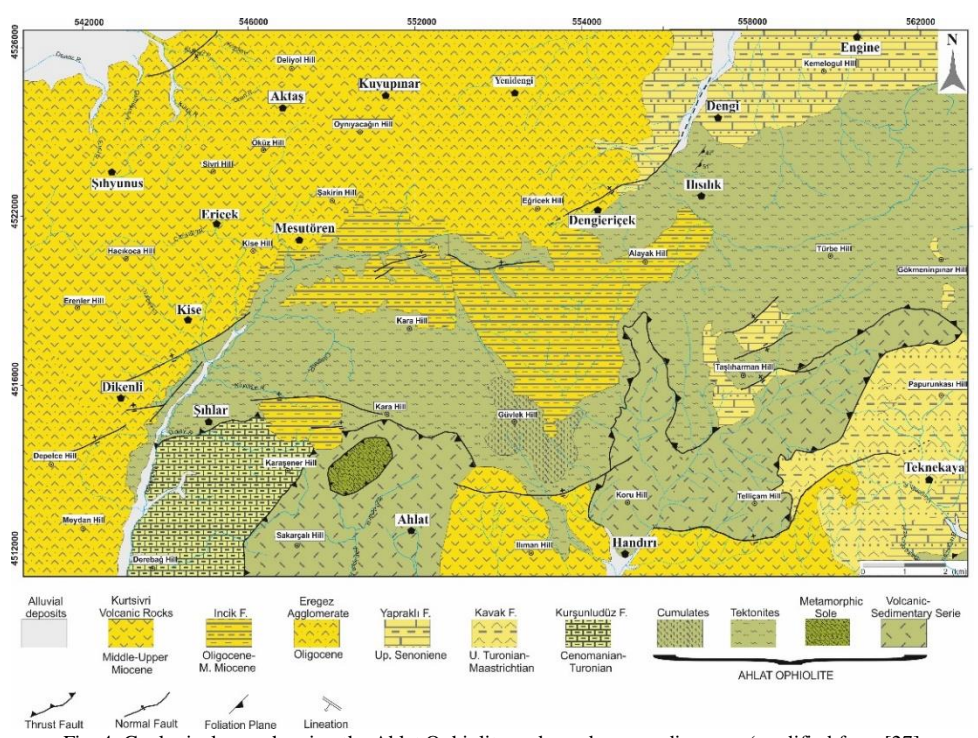


Fig. 4. Geological map showing the Ahlat Ophiolite rocks and surrounding area (modified from [27]

3. Deformation Structures

The metamorphic sole rocks at the Eldivan and Ahlat ophiolites, which occur as discontinuous tectonic slices, exhibit prominent foliation resulting from mineral alignment. The schistosity planes are parallel to the contacts with adjacent rocks. Microfolds within these planes indicate that the rocks have undergone multiple deformation phases. At the base of both ophiolites, the initial deformation phases were synchronous with metamorphism. Additionally, at least two post-metamorphic deformation phases have been identified in the metamorphic sole of the Eldivan Ophiolite. In contrast, at least one post-metamorphic phase is observed in the metamorphics of the Ahlat Ophiolite.

Studies on the amphibolites at the base of the Eldivan and Ahlat ophiolites have revealed distinct deformation structures. These include macroscopic features such as mineral alignments, foliation planes, and folding-faulting structures. Macroscopic analyses highlight the presence of structures contemporaneous with foliation (S_1) and those that developed after foliation (S_2) in the amphibolites (Fig. 6).

In the Eldivan Ophiolite, the first deformation phase (D_1) is synchronous with metamorphism and marks the development of foliation planes. Microfolds are isoclinal, anisotropic, and asymmetrical, with limb separations of less than ~200 μ m. The axial plane is parallel to the limbs. The second deformation phase (D_2) produced microfolds with limb separations ranging from ~200 to 400 μ m. During this phase, schistosity did not develop. Recrystallized quartz minerals are observed locally at crests of folded quartzite bands, indicating deformation and recrystallization.



Fig. 5. General view of metamorphic rocks having schist texture in Ahlat Ophiolite

In the metamorphic sole of the Ahlat Ophiolite, the first deformation phase (S_1) is characterized by microfolds of asymmetric dimensions, with limb separations of ~100–150 μm . These folds are parallel to the primary bedding plane (S_0) . Secondary folds exhibit much larger limb separations, represented by high-amplitude post-tectonic folds. During this phase, minor mineral alignment (S_2) is observed (see Fig. 6). Fracturing is widespread throughout the unit.

4. Petrography

Macroscopically observable S_1 and S_2 structures in amphibolites are also evident during petrographic investigations. These studies reveal two types of deformation structures in metamorphic rocks (Fig. 7). The first type

consists of lineations formed by the parallel alignment of prismatic or platy minerals, resulting from primary deformation and located along tectonic planes (D_1 - S_0 = S_1 structures). The second type of deformation structure comprises minor fold axes, manifesting as small-scale wrinkle lineations on bedding cleavage and schistosity planes (D_2 - S_2 structures) (Fig. 7a). A schematic representation of these structures is provided in Fig. 7b.

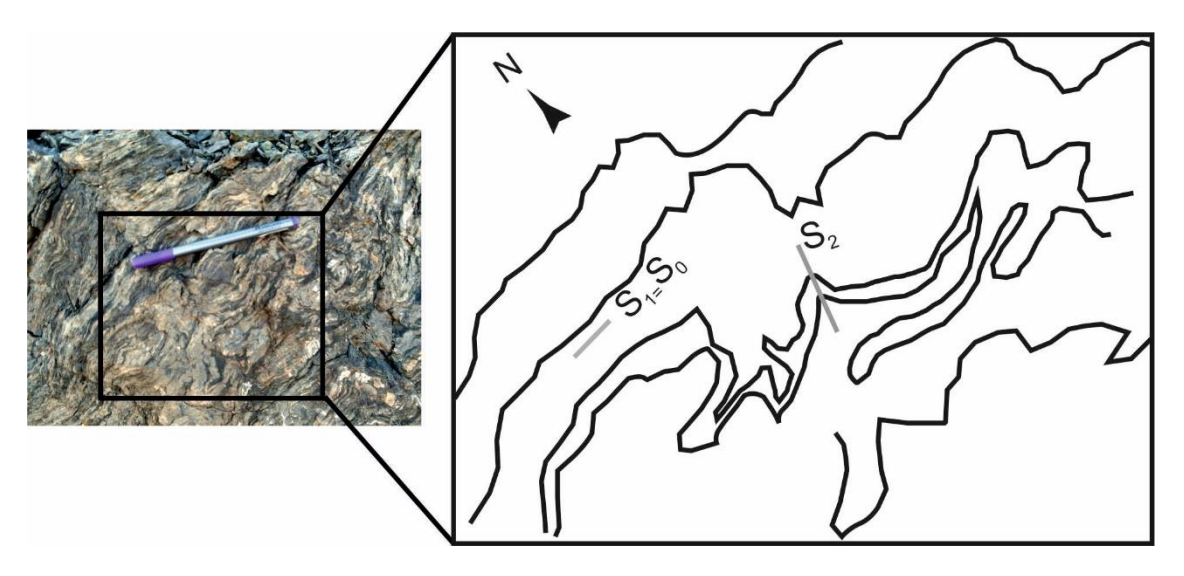


Fig. 6. Structures observed in the metamorphic rocks in Ahlat town $(S_1$: structures formed coevally with foliations, S_2 : later formed from foliations).

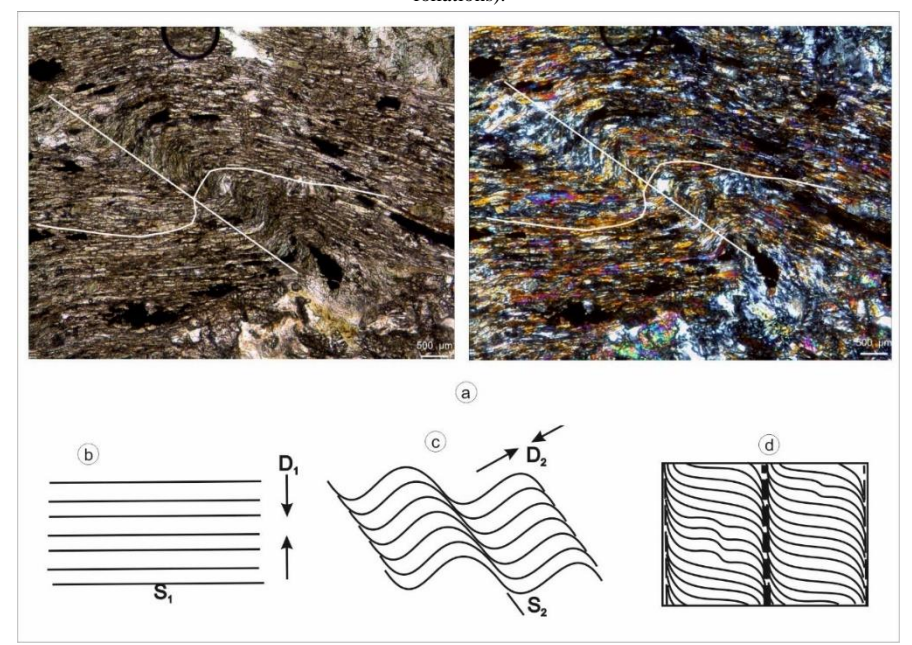


Fig. 7. a) Tectonic deformation and wrinkled cleavage observed in metamorphic rocks (Sn is the dominant texture. Sn+1 is developed in narrowing area of Sn), b) tectonic lineations formed by a vertical compression (Sn), c) wrinkling lineation occured by oblique compression (Sn+1), d) types of wrinkled cleavage depending on deformation intensity and temperature.

Pyroxene minerals, observed as porphyroclasts, display spindle-shaped and microfractured features. These minerals are characteristically elongated in rhomboidal or lens-like forms, indicating alignment and rotation. The strongly oriented spindles align with the tectonic foliation. Sheared and recrystallized pyroxene minerals are also observed, with mineral orientations developing parallel to the tectonic foliation without mantling effects (Fig. 8a). In some samples, porphyroclastic pyroxenes showing flow patterns intersect the simple shear structures (Fig. 8b). Petrographic analysis of the metamorphic rocks indicates the presence of dextral simple shear deformation.

Amphibolites, tremolite-actinolite schist, epidote-garnet schist, and chlorite-sericite-talc schist represent the metamorphic sole rocks of the Eldivan and Ahlat ophiolites.

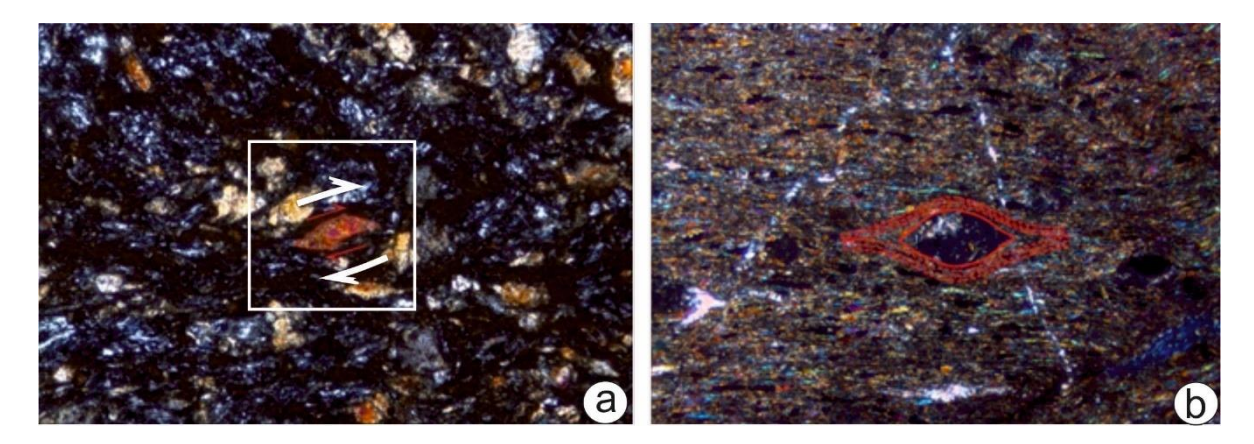


Fig. 8. a) Pyroxene shuttle in the metamorphic rocks. b) Deformed porphyroblastic pyroxene grains.

Amphibolite: Amphibolites are primarily composed of hornblende (40-60%) and plagioclase (10-20%), with minor amounts of quartz (3-5%), epidote (5-10%), and accessory minerals such as titanite and apatite (Fig. 9a-c). The rocks generally exhibit granoblastic (Fig. 9a), nematoblastic (Fig. 9c), and mylonitic textures. Rarely are remnants of ophitic and intersertal textures observed within the amphibolites. Additionally, pyroxene mineral relics are present in the rocks (Fig. 9b). These textural features reflect the pre-metamorphic textures of pillow lavas [4].

<u>Tremolite-Actinolite Schist:</u> Tremolite-actinolite schists predominantly comprise tremolite (55-65%) and actinolite (35-45%). The rocks generally exhibit nematoblastic textures (Fig. 10a). Tremolite is the dominant mineral, appearing as coarse to medium-grained and prismatic crystals. Actinolite minerals are medium-grained, pale green, and exhibit weak pleochroism with high relief. Schistosity is prominently developed in these rocks.

<u>Epidote-Garnet Schist:</u> Epidote-garnet schists primarily consist of epidote (55-70%) and garnet (35-45%), with minor plagioclase (4-6%) (Fig. 10b). The rocks typically exhibit nematoblastic textures. Epidote minerals are lemonyellow, displaying pleochroism, high relief, and high interference colours. They are generally observed as anhedral rod-like aggregates. Garnet minerals are medium to small-sized and occur as subhedral to anhedral grains. They exhibit light to dark brown colour zoning and strong pleochroism. Plagioclase minerals are rarely observed within these rocks.

<u>Chlorite-Sericite-Talc Schist</u>: Chlorite-sericite-talc schists are composed primarily of chlorite (45-55%), sericite (25-35%), and talc (5-10%) (Fig. 10c). The rocks generally exhibit lepidoblastic textures. Chlorite minerals display pale green tones with weak pleochroism and are typically found as anhedral grains. Sericite minerals are colourless and arranged along the (0001) foliation planes, forming flat surfaces. Talc occurs as colourless, fibrous aggregates within the rocks.

5. Analytical Techniques

Energy Dispersive Spectroscopy (EDS) was used to conduct point studies on amphibolite samples from the Eldivan and Ahlat ophiolites. These analyses were conducted at the Turkish Petroleum Corporation (TPAO), Department of Sedimentology and Reservoir Geology, using a JEOL-6490 electron microscope equipped with the SQ analysis program and ZAF correction software.

For amphibole minerals within the amphibolites, cation values were calculated based on 13 cations, with Fe^{+2}/Fe^{+3} ratios determined through PLAG modelling. For plagioclase minerals, calculations were based on O = 8.

Whole-rock analyses were conducted on five amphibolite samples from the Eldivan and Ahlat ophiolites. The analyses were performed at ACME Laboratories, covering major elements using X-ray fluorescence (XRF) methods and trace elements using Inductively Coupled Plasma Mass Spectrometry (ICP-MS).

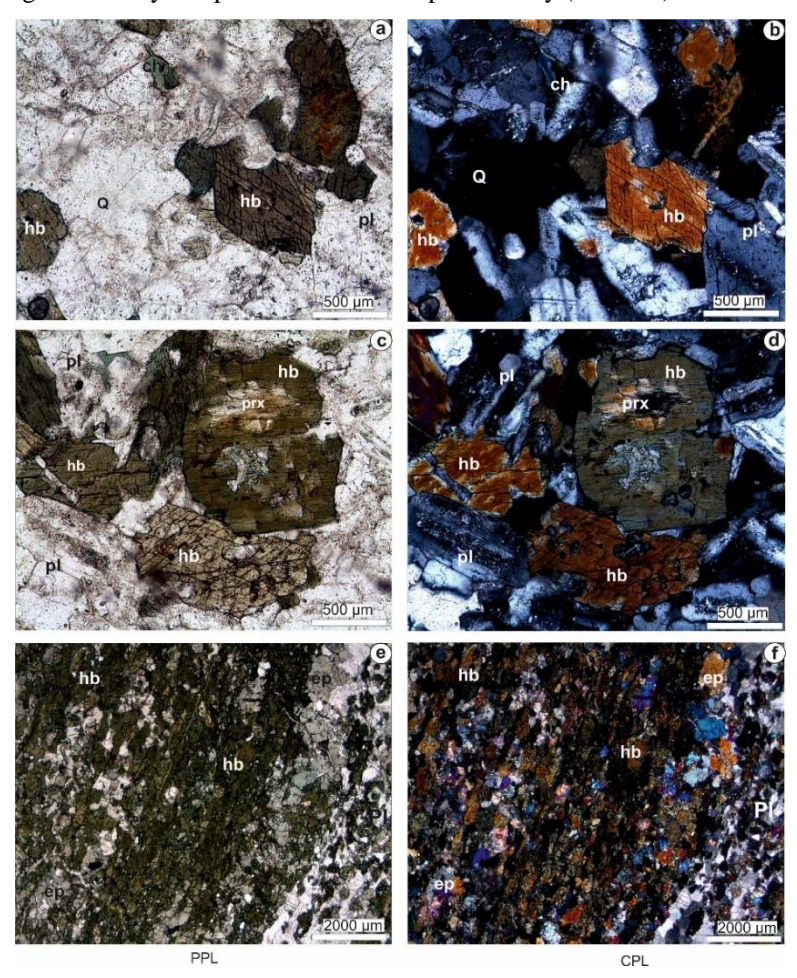


Fig. 9. Thin section view of Amphibolites: a) Granoblastic texture in amphibolites. b) Relict pyroxene minerals and chlorite minerals observed on the edge of hornblend minerals. c) Nematoblasctic texture observed in hornblend, plagioclase, epidote and secondary calcite minerals (Hb:hornblend, Ep:epidote, Pl:plagioclase, Prx:pyroxene, Cl:chlorite, Q:quartz, PPL: plane polarized light image, CPL: cross polarized light image.

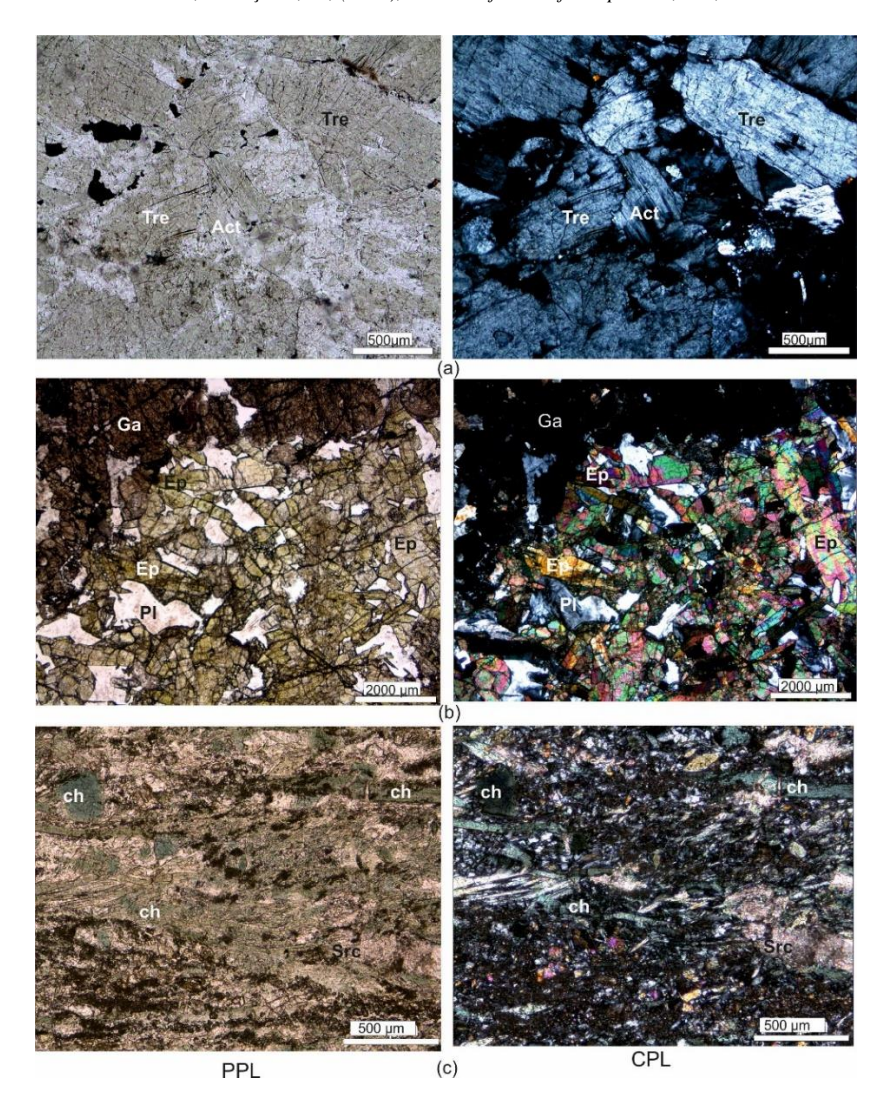


Fig. 10. Thin section view of some rocks observed in the metamorphic basement; a) Tremolite-Actinolite schist, b) Epidote-Garnet schist, c) Chlorite-sericite-talc schist ((Ep:epidote, Ga:garnet, Pl:plagioclase, Tre:tremolite, Act:actinolite, ch:chlorite, Scr:sericite, PPL:plane polarized light image, CPL:cross polarized light image).

6. Mineral Chemistry

Analyses were conducted on amphibole, plagioclase, and pyroxene minerals within the sampled amphibolites. This study aimed to identify the types of amphibole and plagioclase minerals in the rocks and determine their formation temperatures and pressures.

<u>Amphibole:</u> Amphibole minerals were analyzed using EDS, and calculations were based on 23 O ([34], ([35]);. The (Ca+Na) values were calculated (Table 1). Amphibole compositions vary significantly, with $SiO_2 = \%41.7 - 52.34$, $Al_2O_3 = \%3.31-33.57$, FeO = %1.01-15.13, MgO= %0.11-15.60 and $K_2O=\%0.02-1.51$. The samples were plotted on the $Si-Mg/(Mg+Fe^{+2})$ diagram (Fig. 11a) to classify the type of amphiboles. Additionally, to estimate formation temperatures, the samples were plotted on the $Al_2O_3-TiO_2$ diagram (Fig. 11b).

Table 1. Result of analysis and cation values of amphibole minerals in amphibolites belonging to the Eldivan and Ahlat ophiolites (cations=13, Fe^{+2}/Fe^{+3} calculations were made with PLAG modelling).

	AKÇ-4	A					AKÇ-5									
	1_1	1_2	1_3	1_4	3_1	3_4	1_1	1_3	1_4	1_5	1_7	4_3	4_5	6_1	6_5	6_6
SiO ₂	44.98	50.05	52.32	49.76	51.48	51.45	45.97	48.11	51.17	41.29	41.09	41.57	46.65	43.72	33.75	44.64
TiO_2	0.00	0.00	0.00	0.00	0.00	0.00	1.81	1.76	0.98	1.52	2.11	1.99	1.56	0.29	1.91	1.81
Al_2O_3	33.57	7.70	8.69	10.41	10.29	9.89	9.89	8.86	14.76	15.96	15.32	16.07	9.18	3.31	4.45	6.78
Cr_2O_3	0.00	0.00	0.00	0.00	0.00	0.00	0.20	0.20	0.11	0.14	0.27	0.31	0.15	0.37	0.42	0.34
Fe ₂ O ₃	0.00	0.00	0.00	2.57	1.32	0.00	0.00	0.00	0.00	0.59	0.00	1.60	0.00	0.00	0.00	0.00
FeO	1.01	12.72	9.41	8.81	9.44	10.52	8.47	7.74	10.31	13.28	13.94	12.38	8.60	10.34	15.13	9.90
MnO	0.00	0.00	0.00	0.00	0.00	0.00	0.22	0.52	0.23	0.37	0.35	0.48	0.49	0.40	0.77	0.35
MgO	0.11	14.03	15.60	14.64	14.24	14.14	9.71	9.95	6.75	10.61	9.83	10.45	9.43	10.07	6.21	9.44
CaO	19.22	14.38	12.12	12.08	11.50	12.03	22.40	21.42	13.16	12.34	12.86	12.53	22.73	30.66	36.40	25.32
Na ₂ O	1.04	1.10	1.80	1.77	1.65	1.84	1.02	1.17	0.75	2.25	2.46	2.47	1.18	0.80	0.77	1.39
K_2O	0.07	0.02	0.07	0.23	0.22	0.14	0.00	0.03	1.29	1.51	1.46	0.00	0.02	0.04	0.19	0.05
H_2O	1.97	2.09	2.16	2,15	2.16	2.14	1.87	1.89	2.04	2.05	2.02	2.07	1,86	1,66	1,46	1,77
Total	101.9 7	102.09	102.1 7	102.4 2	102.3 0	102.1 5	101.5 6	101.6 5	101.5 5	101.9 1	101,7 1	101.9 2	101.8 5	101.6 6	101.4 6	101.7 9
Si	6.83	7.17	7.26	6.94	7.14	7.19	7.39	7.65	7.54	6.03	6.10	6.02	7.54	7.88	6.93	7.55
Al_T	1.17	0.83	0.74	1.06	0.86	0.81	0.61	0.35	0.46	1.97	1,90	1.98	0.46	0.12	1.07	0.45
su 1	8.00	8.00	8.00	8.00	8.00	8.00	8.00	8.00	8.00	8.00	8.00	8.00	8.00	8.00	8.00	8.00
Гі	0.00	0.00	0.00	0.00	0.00	0.00	0.22	0.21	0.11	0.17	0.24	0.22	0.19	0.04	0.05	0.22
Al_{O}	4.85	0.48	0.68	0.66	0.82	0.82	1.26	1.31	2.10	0.78	0.78	0.76	1.29	0.58	0.00	0.90
Cr	0.00	0.00	0.00	0.00	0.00	0.00	0.02	0.02	0.01	0.02	0.03	0.04	0.02	0.05	0.07	0.05
Fe ³	0.00	0.00	0.00	0.27	0.14	0.00	0.00	0.00	0.00	0.07	0.00	0.17	0.00	0.00	0.00	0.00
Fe ²	0.13	1.52	1.09	1.03	1.09	1.23	1.14	1.03	1.27	1.62	1.73	1.50	1.16	1.56	2.60	1.40
Mn	0.00	0.00	0.00	0.00	0.00	0.00	0.03	0.07	0.03	0.04	0.04	0.06	0.07	0.06	0.13	0.05
Мg	0.02	3.00	3.23	3.04	2.95	2.95	2.33	2.36	1.48	2.30	2.18	2.26	2.27	2.71	2.15	2.38
su2	5.00	5.00	5.00	5.00	5.00	5.00	5.00	5.00	5.00	5.00	5.00	5.01	5.00	5.00	5.00	5.00
Са	3.13	2.21	1.80	1.81	1.71	1.80	3.86	3.65	2.08	1.93	2.05	1.94	3.94	5.92	8.01	4.59
Na	0.31	0.30	0.48	0.48	0.44	0.50	0.32	0.36	0.21	0.64	0.71	0.69	0.37	0.28	0.31	0.45
K	0.01	0.00	0.01	0.04	0.04	0.03	0.00	0.01	0.24	0.28	0.28	0.00	0.00	0.01	0.05	0.01
component																
X_{Tr}	1.56	1,10	0.90	0.90	0.85	0.90	1.93	1.82	1.04	0.97	1.02	0.97	1.97	2.96	4.00	2.29
X_{Ri}	0.00	0.00	0.00	0.07	0.13	0.00	0.00	0.00	0.00	0.03	0.00	0.02	0.00	0.00	0.00	0.00
X_{Si}	0.85	0.90	0.91	0.87	0.89	0.90	0.92	0.96	0.94	0.75	0.76	0.75	0.94	0.98	0.87	0.94
X_{Mg}	0.16	0.66	0.75	0.75	0.73	0.71	0.67	0.68	0.53	0.58	0.55	0.59	0.65	0.63	0.41	0.62

1.00 1.00 1.00 1.00 1.00 1.00 1.00 X_{OH} 1.00 1.00 1.00 1.00 1.00 1.00 1.00 1.00 1.00

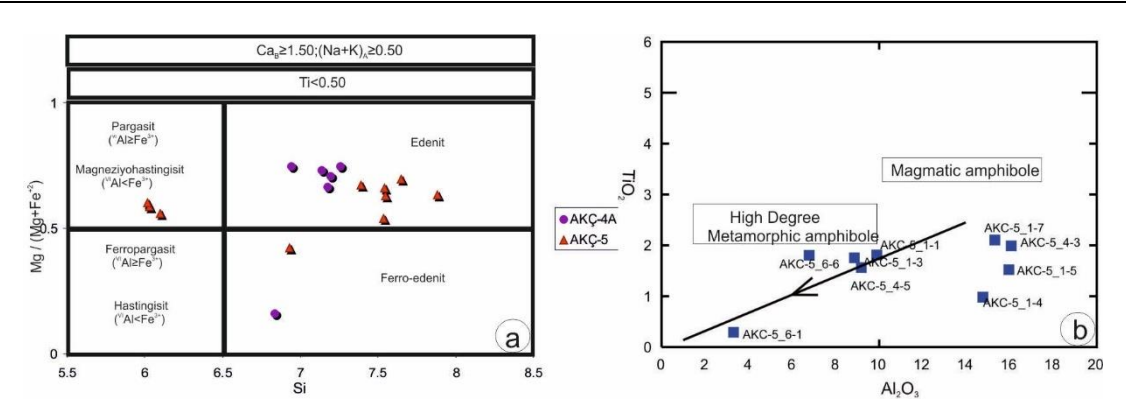


Fig. 11 a) Si-Mg / (Mg+Fe²⁺) diagram of amphibole samples in amphibolites (after [37]), b) Al₂O₃-TiO₂ diagram of amphibole samples.

<u>Plagioclase</u>: Plagioclase, one of the primary minerals in the amphibolites, was analyzed, revealing that these minerals fall within the albite composition range. Their Ab contents vary between 82.85% and 95.1% (Table 2). Except for one sample, all were plotted within the albite field on the Ab-An-Or diagram (Fig. 12a).

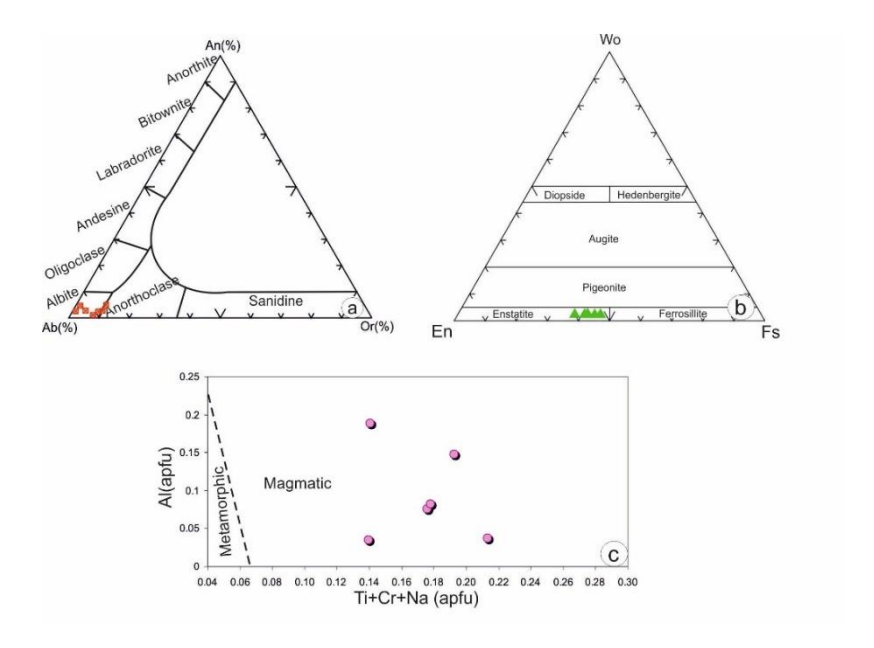


Fig. 12. a) An-Ab-Or plot diagram of plagioclase minerals in amphibolite samples from Eldivan and Ahlat ophiolites, b) En-Wo-Fs plot diagram of pyroxene minerals in amphibolite samples from Eldivan and Ahlat ophiolites, c) Compositional spectrum of pyroxene minerals in amphibolite samples (after, [37]).

<u>Pyroxene</u>: Pyroxene minerals were classified according to [36] and determined to belong to the Mg-Ca-Fe pyroxene group (Table 3). All pyroxene samples were plotted within the clinoenstatite field on the Wo-En-Fs diagram (Fig.

12b). Additionally, to determine the origins of the pyroxenes, the samples were plotted on the Ti + Cr + Na versus Al diagram, where all samples fall within the magmatic field (Fig. 12c)

Table 2. Result of analysis and cation values of plagioclase minerals in amphibolites belonging to the Eldivan and Ahlat ophiolites (Oxygens: 8, for plagioclase mixing model).

	AKÇ - 4	4A	AKÇ -	. 5								
	1_5	3_2	1_6	4_6	4_7	6_7	7_2	7_3	7_4	7_6	8_1	8_4
SiO ₂	67.19	62.20	66.68	48.87	46.90	44.60	65.38	61.91	66.67	66.43	66.84	63.98
TiO_2	0.00	0.00	0.16	0.26	0.16	0.10	0.15	0.15	0.25	0.05	0.13	0.29
Al_2O_3	21.22	22.84	21.20	34.85	26.42	26.29	23.09	26.47	21.13	22.57	21.44	22.03
Cr_2O_3	0.00	0.00	0.22	0.08	0.15	0.20	0.00	0.00	0.00	0.00	0.00	0.00
Fe_2O_3	0.34	0.76	0.34	1.56	5.18	6.85	0.41	0.38	0.32	0.39	0.45	0.37
Mn_2O_3	0.00	0.00	0.03	0.35	0.32	0.20	0.00	0.00	0.00	0.00	0.00	0.21
MgO	0.10	0.78	0.12	1.91	3.89	3.73	0.05	0.10	0.06	0.27	0.06	0.36
CaO	1.13	4.32	0.85	0.40	16.56	21.26	0.69	0.8	0.92	0.70	0.60	1.34
Na_2O	9.87	5.76	10.17	0.25	0.22	0.54	8.93	6.60	10.19	8.20	9.62	9.78
K_2O	0.19	3.74	0.09	12.51	3.24	0.17	1.53	3.78	0.61	1.59	1.09	1.95
Total	100.03	100.40	99.85	101.02	103.04	103.93	100.21	100.20	100.16	100.20	100.23	100.29
Si	2.93	2.77	2.92	2.25	2.17	20.60	2.86	2.74	2.92	2.90	2.92	2.83
Al	1,09	1.20	1.09	1.89	1.44	1.43	1.19	1.38	1.09	1.16	1.10	1.15
Fe ³	0.01	0.03	0.01	0.05	0.18	0.24	0.01	0.01	0.01	0.01	0.01	0.01
Mn^3	0.00	0.00	0.00	0.01	0.01	0.01	0.00	0.00	0.00	0.00	0.00	0.01
Cr	0.00	0.00	0.01	0.00	0.01	0.01	0.00	0.00	0.00	0.00	0.00	0.00
Ti	0.00	0.00	0.01	0.01	0.01	0.00	0.00	0.00	0.01	0.00	0.00	0.01
su_1	4.04	4.05	4.05	4.36	4.08	4.01	4.08	4.14	4.03	4.09	4.05	4.03
Ba	0.00	0.00	0.00	0.00	0.00	0.00	0.00	0.00	0.00	0.00	0.00	0.00
Ca	0.05	0.21	0.04	0.02	0.82	1.05	0.03	0.04	0.04	0.03	0.03	0.06
Na	0.84	0.50	0.86	0.02	0.02	0.05	0.76	0.57	0.86	0.69	0.82	0.84
K	0.01	0.21	0.00	0.70	0.19	0.01	0.09	0.21	0.03	0.09	0.06	0.11
su_2	0.90	0.92	0.91	0.78	1.03	1.11	0.88	0.82	0.94	0.81	0.90	1.01
components												
An(%)	5.80	22.5	4.40	2.50	79.50	94.8	3.70	4.70	4.60	4.02	3.10	6.26
Ab(%)	93.00	54,3	95.10	2.90	1.90	4.30	86.60	69.20	91.80	85.14	90.20	82.85
Or(%)	1.20	23.20	0.50	94.60	18.60	0.90	9.70	26.10	3.60	10.84	6.70	10.89

6.1 Pressure-temperature calculation

The pressure conditions under which the amphibolites formed were estimated based on Al values obtained from EDS analyses of amphiboles. For this purpose, the Al-hornblende barometer calculations proposed by [37], [38], and

[39] were utilized. The calculated values are summarized in Table 4. Based on these results, it can be inferred that the formation of amphibolites occurred under medium to high-pressure conditions.

Table 3. Result of analysis and cation values of pyroxene minerals in amphibolites belonging to the Eldivan and Ahlat ophiolites.

	AKC-5	AKC-5	AKC-5	AKC-5	AKC-5	AKC-5
	4-1	4-2	4-8	7-5	8-3	8-5
SiO ₂	49.78	53.03	51.84	51.77	48.21	53.32
TiO_2	1.37	0.97	0.,87	1.07	1.42	0.40
Al_2O_3	8.25	6.41	5.60	5.80	7.44	4.21
Cr_2O_3	0.22	0.27	0.18	0.00	0.15	0.00
Fe_2O_3	0.01	0.00	0.00	0.00	2.25	0.00
FeO	7.27	6.22	8.44	7.09	6.13	6.02
MnO	0.40	0.25	0.46	0.00	0.26	0.30
MgO	10.18	11.47	10.63	11.12	10.01	12.44
CaO	19.73	17.96	19.83	20.56	22.15	21.02
Na_2O	2.05	2.48	2.03	2.06	1.32	1.80
K2O	0.05	0.00	0.03	0.02	0.06	0.11
Total	99.30	99.08	99.92	99.49	99.38	99.61
Si	1.8525	1.9620	1.9243	1.9178	1.8110	1.9646
Al_T	0.1475	0.0380	0,0757	0.0822	0.1890	0.0354
sum4	2.0000	2.0000	2.0000	2.0000	2.0000	2.0000
Al_{O}	0.2144	0.2417	0.1694	0.1713	0.1403	0.1473
Ti	0.0383	0.0271	0.0244	0.0298	0.0400	0.0110
Cr	0.0065	0.0080	0.0053	0.0000	0.0043	0.0000
Fe^3	0.0001	0.0000	0.0000	0.0001	0.0635	0.0001
Fe^2	0.2262	0.1926	0.2620	0.2197	0.1925	0.1856
Mn	0.0126	0.0079	0.0146	0.0000	0.0082	0.0095
Mg	0.5649	0.6325	0.5880	0.6143	0.5603	0.6831
Ca	0.7869	0.7122	0.7885	0.8161	0.8916	0.8296
Na	0.1479	0.1780	0.1462	0.1478	0.0961	0.1287
K	0,0022	0,0000	0,0016	0,0009	0,0030	0,0052
sum6	2,0000	2,0000	2,0000	2,0000	2,0000	2,0000
Na_start	0.1040	0.1204	0.1397	0.1033	0.0961	0.0944
components						
Diopside	0.4734	0.5315	0.4988	0.5618	0.5443	0.6216
Hedenbergite	0.1895	0.1618	0.2222	0.2010	0.870	0.1689
Jadeite	0.1052	0.1431	0.1181	0.1189	0.0087	0.1228
Opx	0.0630	0.1097	0.0637	0.0351	0.0092	0.0365

Üner, T. & Çakır, Ü., (2025), Journal of Scientific Reports-A, 062, 90-110

Tschermakite	0.1093	0.0110	0.0513	0.0523	0.1490	0.0245
Rest	0.0596	0.0430	0.0458	0.0308	0.1191	0.0258

11 amphiboles were chosen for this investigation based on mineral chemistry studies performed on amphibolites. Using the Al values acquired from hornblende EDS investigations, approximate pressure conditions under which the amphibolites formed were calculated. For this purpose, the Al-hornblende barometer calculation by [37] (1), along with similar methods proposed by [38] (2) and [39] (3), were utilized. The results derived from these formulas are summarized in Table 4.

$$P(\pm 3 \, kbar) = -3.92 + 5.03 \, Altot \tag{1}$$

$$P(\pm 1 \, kbar) = -4.76 + 5.64 \, Altot \tag{2}$$

$$P(\pm 0.6 \, kbar) = -3.01 + 4.76 \, Altot \tag{3}$$

The amphibole-plagioclase mineral pair was used to estimate the temperature conditions during metamorphism, employing the formulations by [40]. The following reactions were considered:

$$Edenite + 4 quartz = tremolite + albite$$
 (1)

$$Edenite + albite = richterite + anortit$$
 (2)

Thin-section examinations revealed the presence of both quartz and plagioclase minerals within the rocks, with the plagioclase minerals having undergone albitization. For this reason, formula (1) served as the foundation for temperature computations. Calculations were performed on three samples from section AKÇ-4A and seven samples from section AKÇ-5. The temperature range for AKÇ-4A samples was 562°C to 642°C, while AKÇ-5 samples ranged from 502°C to 683°C.

Table 4. Pressure and temperature values calculated based on amphibole and plagioclase minerals in amphibolites (formulation text provided).

Samp	ple No	Pressure-te	Pressure-temperature results					
		1*	2*					
	1_3	3.23	3.25	3.75				
AKÇ-4A	1_4	4.69	4.89	5.14				
	3_1	4.54	4.72	4.99				
	3_4	4.28	4.43	4.75				
	1_1	5.50	5.81	5.91				
	1_3	4.43	4.60	4.89				
_	1_4	8.97	9.69	9.19				
AKÇ-5	1_5	9.90	10.73	10.07				
?	1_7	9.56	10.36	9.75				
	4_3	9.87	10.70	10.04				
	4_5	4.88	5.10	5.31				

7. Geochemistry

Five amphibolite samples from the Eldivan and Ahlat ophiolites were analyzed to determine the origin of the metamorphic sole rocks (Table 5). Microscopic examinations of the amphibolites revealed that the samples had undergone varying degrees of alteration. Due to this alteration, mobility in major and certain trace elements, particularly large-ion lithophile elements (LILE), was observed [41], [42]. As a result, rare earth elements (REE) and high field strength elements (HFSE), which are resistant to modification, are preferred for determining the petrological features of rocks. [43], [44].

When plotted on a Zr/TiO2-Nb/Y diagram, all amphibolite samples from the Eldivan Ophiolite fall within the alkaline basalt field. In contrast, the Mi-42 sample from the Ahlat Ophiolite falls within the subalkaline basalt field (Fig. 13a). To determine the tectonic settings of the basalts representing the potential protoliths of the amphibolites, the Zr-Zr/Y (Fig. 13b) and Nb/Yb-Th/Yb (Fig. 13c) diagrams were utilized.

The chondrite- and primitive mantle-normalized rare earth element (REE) patterns of amphibolites from the Eldivan and Ahlat ophiolites are presented in Fig. 14a and Fig. 14b, respectively. For comparison, the REE values of normal mid-ocean ridge basalts (N-MORB), ocean island basalts (OIB), and enriched mid-ocean ridge basalts (E-MORB) are also included in the diagrams (values adopted from [45]; see Fig. 14a-b).

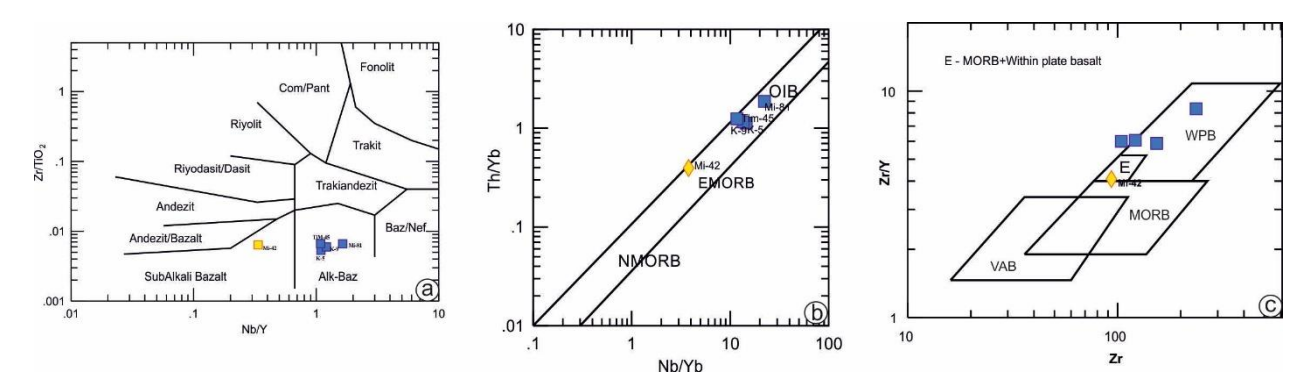


Fig. 13 a) Classification of amphibolites with Zr/TiO_2 -Nb/Y diagrams (after [47]), Discrimination of amphibolite samples in b) Nb/Y-Th/Yb and c) Zr/Y- Zr diagram (after, [48]).

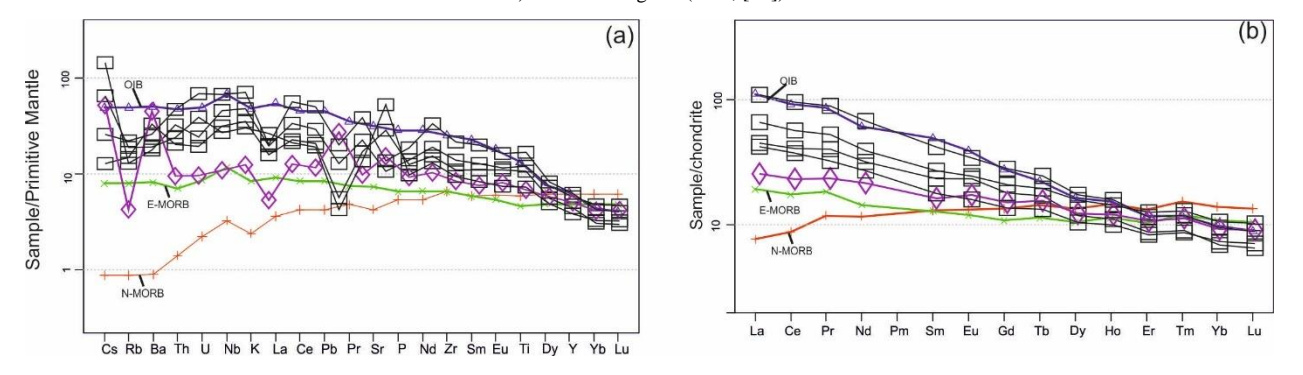


Fig. 14. Normalized spider diagrams for the amphibolites; a) primitive mantle (from, [49]) and b) chondrite (from, [50]). (OIB, N-MORB and MORB data taken from [45]).

8. Results and Discussion

This study examined the metamorphic sole rocks of the Eldivan and Ahlat ophiolites from geological, petrographical, and geochemical standpoints. These units are typically observed as tectonic slices between the volcanic-sedimentary series and tectonites and, occasionally, as lenses within the tectonites. Diabase dikes within the amphibolites indicate that the metamorphism occurred in an oceanic environment through intra-oceanic subduction rather than during the emplacement of the ophiolite. Therefore, it may be inferred that the metamorphic sole rocks have volcanic origins [46].

Table 5. Whole rock major oksite (%), trace elements (ppm) and REE (ppm) values of amphibolites.

	, ,	•			41 /
	K-5	K-9	Mİ-42	Mİ-81	TİM-45
SiO ₂	44.70	46.13	48.46	46.19	44.84
Al_2O_3	15.19	15.00	16.98	13.77	13.09
Fe_2O_3	3.88	4.15	3.05	5.15	3.12
FeO	7.75	8.86	10.24	8.27	6.66
MgO	7.44	8,04	6,24	10,61	7.41
CaO	15.66	10.65	8.83	8.60	21.28
Na_2O	2.20	3.51	4.22	2.61	0.84
K_2O	0,47	0,58	0,16	0,60	0.78
TiO_2	2.29	2.58	1.47	3.59	1.57
P_2O_5	0.27	0.30	0.20	0.40	0.21
MnO	0.17	0.19	0.15	0.21	0.22
LOI	3.60	3.00	3.90	2.80	2.40
Sum	99.70	99.73	99.75	99.65	99.68
Cr_2O_3	0.03	0.04	0.04	0.06	0.14
Zr	121.60	153.60	93.50	236.90	104.30
Ni	79.00	147.00	71.00	252.00	254.00
Sc	39.00	43.00	30.00	31.00	33.00
Ba	226.00	122.00	306.00	178.00	131.00
Ni	25.30	71.40	57.90	112.40	131.70
Be	1.00	1.00	1.00	1.00	1.00
Co	51.40	56.80	51.10	63.20	55.20
Cs	0.10	1.10	0.40	0.20	0.50
Ga	19.50	17.60	22.80	17.80	14.50
Hf	3.40	4.00	2.70	6.80	2.60
Nb	22.00	31.80	7.70	46.70	18.90
Rb	9.30	8.10	2.70	13.80	11.80
Sn	1,00	2,00	<1	2,00	<1

Üner, T. & Cakır, Ü., (2025), Journal of Scientific Reports-A, 062, 90-110

Sr	590.00	222.40	318.10	285.50	1081.00
Ta	1.40	1.90	0.50	2.80	1.20
Th	1.70	2,70	0,80	3,90	2,00
U	0.40	0.50	0.20	1.40	0.80
V	263.00	318.00	220.00	320.00	218.00
W	86.30	59.20	51.30	18.00	67.90
Y	20.10	26.20	22.90	28.40	17.40
La	15.30	22.60	8.60	37.80	14.30
Ce	36.20	50.70	20.40	86.40	33.20
Pr	4.63	6.10	2.68	10.41	3.71
Nd	20.50	25.30	13.80	44.20	17.40
Sm	4.83	5.61	3.34	8.73	3.66
Eu	1.83	1.92	1.35	2.70	1.24
Gd	5.02	5.86	4.20	7.92	3.79
Tb	0.81	0.93	0.74	1.18	0.63
Dy	4,08	5.46	4.25	6.03	3.59
Но	0.78	1.01	0.85	1.12	0.70
Er	1.96	2.85	2.42	2.61	1.87
Tm	0.27	0.39	0.34	0.36	0.26
Yb	1.51	2.34	2.03	2.09	1.61
Lu	0,22	0,35	0,31	0,30	0,24
Mo	0,10	< 0,1	1,10	<0,1	<0,1
Cu	64.10	63.50	57.80	76.10	6.90
Pb	0.40	0.90	1.90	1.40	0.30
Zn	29.00	53.00	101.00	44.00	27.00
Ni	25.30	71.40	57.90	112.40	131.70
As	< 0.5	< 0.5	< 0.5	0.80	0.60
Cd	< 0.1	<0.1	0.10	<0.1	<0.1

In amphiboles from the amphibolites, an increase in Fe content corresponds to an increase in Al_2O_3 values and a decrease in SiO_2 values. All amphiboles are classified within the calcic amphibole group based on Ca, Na, and Ca+Na values. Mineral chemistry indicates that the formation of edenite amphiboles, observed in the amphibolites, was influenced by high-temperature metamorphism. The pyroxenes in the amphibolites are interpreted as relict primary pyroxenes.

The formation conditions of the amphibolites, based on calculations, indicate a temperature range of approximately 501.58°C to 683.43°C and a pressure range of 3.25 to 10.73 kbar (calculated using the method of [38]. The presence of magmatic edenite and relict pyroxene within the amphibolites suggests that these rocks were derived from a mafic magmatic source, likely basaltic in composition. Geochemical studies also indicate that these units are alkaline in character and were derived from an intraplate basalt source similar to Ocean Island Basalts (OIB).

A review of the geochemical literature reveals that metamorphosed basaltic rocks, including amphibolites, display characteristics of Ocean Island Basalts (OIB), Mid-Ocean Ridge Basalts (MORB), and Island Arc Tholeitic Basalts (IAT) [15], [2], [52]. The amphibolite samples from the Eldivan and Ahlat ophiolites are situated within the intraplate basalt field. The amphibolite samples display greater enrichment than E-MORB and exhibit slight depletion relative to OIB. Nevertheless, the samples appear to have originated from an OIB-like mantle source, a conclusion supported by tectonic setting discrimination diagrams.

The chemical evaluations of the amphibolite samples indicate a trend between OIB and E-MORB characteristics. Geochemical studies suggest that the amphibolites were formed from melts produced by mixing two distinct types of magma. However, the tectonic setting diagrams suggest that the more dominant interpretation is derived from an OIB-like mantle source.

Acknowledgements

This article is derived from Tijen Üner's doctoral thesis titled "Petrology of Eldivan and Ahlat (Çankırı) Ophiolites" and was funded as part of the project numbered 2008-FBE-D006, supported by the Scientific Research Projects Directorate of Yüzüncü Yıl University.

References

- [1] R.A. Harris, 1998. Origin and tectonic evolution of the metamorphic sole beneath the Brooks Range ophiolite, Alaska. *Geological Society of America Special Paper*, 324, 293-312.
- [2] Ö.F. Çelik, M. Delaloye, 2006. Characteristics of ophiolite-related metamorphic rocks in the Beyşehir ophiolitic melange (Central Taurides, Turkey), deduced from whole rock and mineral chemistry. *Journal of Asian Earth Sciences*, 26,461-476.
- [3] O. Parlak, H. Yılmaz, Boztuğ, D., 2006. Origin and tectonic significance of metamorphic sole and isolated Dykes of the Divriği Ophiolite (Sivas, Turkey): Evidence for slab break-off prior to ophiolite emplacement. *Turkish Journal of Earth Sciences*, 15(1), 25-45.
- [4] Ö.F. Çelik, 2007. Metamorphic sole rocks and their mafic dykes in the eastern Tauride belt ophiolites (southern Turkey): implications for OIB type magma generation following slab break-off. *Geological Magazine*, 144, 849–866.
- [5] Ö. Elitok, K.Drüppel, 2008. Geochemistry and tectonic significance of metamorphic sole rocks beneath the Beyşehir–Hoyran ophiolite (SW-Turkey). *Lithos*, 322-353.
- [6]E. Gartzos, V.J. Dietrich, G. Migiros, K. Serelis, Th. Lymperopoulou, 2009. The Origin of Amphibolites from Metamorphic Soles Beneath the Ultramafic Ophiolites in Evia and Lesvos (Greece) and Their Geotectonic Implication. *Lithos*, 108, 224-242.
- [7] G. Torabi, N. Shirdashtzadeh, S. Arai, J. Koepke, 2011 Paleozoic and Mesozoic ophiolites of Central Iran: amphibolites from Jandaq, Posht-e-Badam, Nain and Ashin ophiolites. *Neues Jahrbuch für Geologie und Paläontologie*, 262, 2, 227-240.
- [8]C. Guilmette, R. Hebert, J. Dostal, A. Indares, T. Ullrich, E. Bedard, C. Wang, 2012. Discovery of a dismembered metamorphic sole in the Saga ophiolitic melange, South Tibet: Assesing an Early Cretaceous disruption of the Neotethyan supra-subduction zone and consequences on basin closing. *Gondwana Reserch*, 22, 398-414.
- [9] J. F. Parrot, 1980. The Baer-Bassit (Northwestern Syria) Ophiolitic Area. Ofioliti, Tethyan Ophiolite Special Issue, 9, 279-295.
- [10] H. Whitechurch, T. Juteau, 1984. Role of Eastern Mediterranean Ophiolites (Turkey, Syria, Cyprus) in the history of the Neo-Tethys. *Geological Society, London, Special Publications*, 17, 301-317.
- [11] K. Al-Riyami, A. Robertson, J. Dixon, C. Xenophontos, 2002. Origin and emplacement of the Late Cretaceous Baer-Bassit Ophiolite and its Metamorphic sole in NW Syria. *Lithos*, 65, 225-260.
- [12] H. Whitechurch, 1977. Les roches métamorphiques infra-péridotitiques du Baër-Bassit (NW Syrien) témoins de l'écaillage intra-océanique tethysien éetude pétrologiue et structurale. Doktora Tezi (3. cycle), Nancy Üniversitesi, 194s.
- [13] J.F. Parrot, H. Whitechurch, 1978. Subductions antèrieures au charriage Nord-Sud de la croûte téthysienne: facteur de metamorphisme de sèries sèdimantaires et volcaniques liees aux asseblages ophiolitiques syr-turcs, en schites verts et amphibolites. *Rev. Gèogr. Phys. Gèol. Dynam.*, 2, 20, 153-170.
- [14] Ü. Çakır, 1996. Toros-Umman Kuşağı Ofiyolit Tabanı Metamorfitlerinin Diğer Birimlerle Olan Jeokronolojik ve Yapısal İlişkileri. *Turkish Journal of Earth Science*, 5, 141-152.
- [15] P. Önen, R. Hall, 2002. Sub-ophiolite metamorphic rocks from NW Anatolia, Turkey. J. Metamorphic Geol., 18, 483-495.
- [16] J. Honnorez, C. Mével, R. Montigny, 1984. Geotectonic significance of gneissic amphibolites from the Vema fracture zone, equatorial mid-Atlantic ridge. Journal of Geophysical Research, 89 (B13), 11379–11400.

- [17] G.A. Challis, 1965. High-temperature contact metamorphism at the Red Hills ultramafic-Wairau valley-New Zealand. *Journal of Petrology*, 6.395-419.
- [18] J.J.Pamic, 1977. Variation in geothermometry and geobarometry of peridotite intrusions in the Dinaride Central Ophiolite Zone, Yugoslavia. *Am. Mineral.* 62, 874-886
- [19] R. A. Jamieson, 1979. The formation of metamorphic aureoles beneath ophiolites- Evidence from the St. Anthony Complex, Newfoundland, *Geology*.
- [20] M.P. Searle, J. Malpas, 1982. Petrochemistry and origin of sub-ophiolite metamorphic and related rocks in the Oman Mountains. *Journal of the Geological Society, London* 139, 235–48.
- [21] E. Sarıfakıoğlu, Y. Dilek, M. Sevin, 2017. New synthesis of the Izmir-Ankara-Erzincan suture zone and the Ankara mélange in northern Anatolia based on new geochemical and geochronological constraints, in R. Sorkhabi (ed), Tectonic Evolution, Collision, and Seismicity of Southwest Asia. *Geological Society of America Special Paper*, 525, 1
- [22] Ü. Çakır, T. Juteau, H. Whitechurch, 1978. Nouvelles preuves de l'ècaillage intra-ocèanique prècoce des ophiolites tèthysiennes: les roches mètamorphiques infra-pèridotitiques du massif de Pozanti-Karsanti (Turquie). *Bull. Soc. Gèol. France*, 7,20,1, 61-70.
- [23] R. Thuizat, R. Montigny, Ü. Çakır, T. Juteau, 1978. K—Ar investigations on two Turkish Ophiolites. In: Zartman, R.E. (Ed.), Short Papers of the 4th International Conference Geochronology, Cosmochronology, Isotope Geology. *Geological Surv. Am. Open-File Rep.* 78-701, 430–432.
- [24] O. Parlak, 2000. Geochemisrty and significance of mafic dyke swarm in Pozanti-Karsanti Ophiolite (Southern Turkey). *Turkish Journal Earth Science*, 9(1), 29-38.
- [25] E.M., Moores, 1981. Ancient suture zones within continents. Science, 213, 41–46.
- [26] A.I. Okay, O. Tüysüz, 1999. Tethyan sutures of northern Turkey. In B. Durand, L. Jolivet, F. Horváth, M. Séranne (Eds.), The Mediterranean basins: Tertiary extension within the Alpine orogeny. *Geological Society of London, Special Publication*, 156, 475–515.
- [27] B. Akyürek, E. Bilginer, E. Çatal, Z. Dağer, Y. Soysal, O. Sunu, O. 1980. Eldivan–Şabanözü (Çankırı), Hasayaz–Çandır (Kalecik–Ankara) dolayının jeolojisi. *MTA Rapor* No: 6741 (yayınlanmamış).
- [28] M.C. Göncüoglu, N. Turhan, K.Tekin, 2003. Evidence for the Triassic rifting and opening of the Neotethyan Izmir-Ankara Ocean, northern edge of the Tauride-Anatolide Platform, Turkey. In: Dekandia, FA, Cassinis, G. & Spina, A (Eds.) Late Paleozoic to Early Mesozoic events of Meditterranean Europe, and additional regional reports. *Bull. Geol. Soc. Italy, Special*, 2, 203-212.
- [29] E. Sarıfakıoğlu, Y., Dilek, M., Sevin, 2014. Jurassic-Paleogene intraoceanic magmatic evolution of the Ankara Mélange, north-central Anatolia, Turkey. *Solid Earth*, 5, 77–108.
- [30] M.A. Mueller, A. Licht, C. Campbell, F. Ocakoğlu, M.H., Taylor, L. Burch, T. Ugrai, M.Kaya, B. Kurtoğlu, P.M.C. Coster, G. Metais, K.C. Beard, 2019. Collision chronology along the İzmir-Ankara-Erzincan suture zone: Insights from the Sarıcakaya Basin, western Anatolia. *Tectonics*, 38, 3652-3674.
- [31] T. Üner, 2010. Eldivan ve Ahlat ofiyolitlerinin petrolojisi. Hacettepe Üniv., Fen Bilimleri Enstitüsü, Doktora Tezi, 2010D5836, 185s.
- [32] Ö.F. Çelik, A. Marzoli, R. Marschik, M. Chiaradia, F. Neubauer, İ. Öz, 2011. Early-Middle Jurassic intra oceanic subduction in the İzmir-Ankara-Erzincan Ocean, Northern Turkey. *Tectonophsics*, 509, 120-134.
- [33] A. Dangerfield, 2008. Geochemistry, structure and tectonic evolution of the Eldivan Ophiolite, Ankara Melange, Central Turkey. Department of Geological Sciences, Brigham Young University, Master of Science, 51 p.
- [34] B.E. Leake, 1968. A catalog of analyzed calciferous and subcalciferous amphiboles together with their nomenclature and associated minerals. *Geol. Soc. Am., Spec. Pap.* 98.
- [35] B.E. Leake, A.R. Wooley, C.E.S. Arps, W.D. Birch, M.C. Gilbert, J.D. Grice, F.C. Hawthorne, A. Kato, H.J. Kısch, G.V. Krivovichev, K. Linthout, J. Laird, J.A. Mandarino, V.W. Maresch, E.H. Nickel, N.M.SW. Rock, J.C. Schumacher, D.C. Smith, N.C.N. Stephenson, L.U. Ugraretti, E.J.W. Whittaker, G. Youzhi, 1997. Nomenclature of Amphiboles: Report of the Subcommittee on Amphiboles of the International Mineralogical Association, Commission on New Minerals and Mineral Names. *The Canadian Mineralogist*, Vol. 35, 219-246.
- [36] N.Morimoto, 1988. Nomenclature of pyroxenes. American Mineralogist, 73, 9-10, 1123-1133.
- [37] J.M. Hammarstrom, E. Zen, 1986. Aluminum in hornblende: An emprical igneous geobarometer. American Mineralogist, 71, 1297-1313.
- [38] L. S. Hollister, G.C. Grissom, E.K. Peters, H.H. Stowell, V.B. Sisson, 1987. Confirmation of the empirical correlation of Al in hornblend with pressure of solidification of calc-alkaline plutons. *American Mineralogist*, 72, 231-239.
- [39] M.W. Schmidt, 1992. Amphibole composition in tonalite as a function of pressure: an experimental calibration of the Al-in-hornblende barometer. *Contribution Mineral Petrol.*, 110, 304-310.
- [40] T. Holland, J. Blundy, 1994. Non-ideal interactions in calcic amphiboles and their bearing on amphibole plagioclase thermometry. *Contr. Mineral. and Petrol.* 116, 433–447 https://doi.org/10.1007/BF00310910
- [41] S.R. Hart, J.G. Schilling, J.R. Powell, 1973. Basalts from Iceland and along the Reykjanes Ridge: Sr isotope geochemistry. *Nature*, 246: 104-107
- [42] S.E. Humphris, G. Thompson, 1978. Trace element mobility during hydrothermal alteration of oceanic basalts. Geochimica et Cosmochimica Acta, 42, 127-136.
- [43] J.A. Pearce, J.R. Cann, 1973. Tectonic setting of basaltic volcanic rocks determined using trace element analysis. *Earth Planetary Science Letters*, 19, 290–300.

- [44] P.A. Floyd, J.A. Winchester, 1978. Identification and Discrimination of Altered and Metamorphosed Volcanic Rocks Using Immobile Elements. *Chemical Geology*, 21: 291-306.
- [45] S.S. Sun, W.F. McDough, 1989. Chemical and isotopic systematics of ocean basalts: Implications for mantle composition and processes. In A.D. Saunders, and M.J. Norry, (Eds.), Magmatism in the ocean basins. *Geological Society, London Special Publications*, 42, 313-346.
- [46] H. Williams, W.R. Smyth, 1973. Metamorphic auresoles beneath ophiolite suites and Alpine peridotites: tectonic implications with west Newfounland examples. *American Journal of Science*, 273, 594-621.
- [47] J.A. Winchester, P.A. Floyd, 1976. Geochemical magma type discrimination: Application to altered and metamorphosed basic igneous rocks. *Earth Planet. Science Letter*, 28, 459-469.
- [48] J.A. Pearce, M.J. Norry, 1979. Petrogenetic implications of Ti, Zr, Y and Nb variations in volcanic rocks. *Contributions to Mineralogy and Petrology*, 69, 33-47.
- [49] D.A. Wood, J. Joron, M. Treuil, 1979. A re-appraisal of the use of Trace Elements to classify and discriminate between magma series erupted in different tectonic settings. *Earth and Planet Science Letters*, 42, 2, 326-336.
- [50] N. Nakamura, 1974. Determination of REE, Ba, Fe, Mg, Na and K in carbonaceous and ordinary chondrites. *Geochimica et Cosmochimica Acta*, 38, 757-775.
- [51] P.A. Polat, J.F. Casey, R. Kerrich, 1996. Geochemical characteristics of accereted material beneath the Pozanti-Karsanti ophiolite. Turkey: Intra-oceanic detechment, assembly and obduction. *Tectonophysics*, 263, 249-276.
- [52] Ö. Vergili, O. Parlak, 2005. Geochemistry and tectonic setting of metamorphic sole rock and mafic dikes from the Pınarbaşı (Kayseri) Ophiolite, Central Anatolia. *Ophioliti* 30, 37-52.



Contents lists available at Dergipark

Journal of Scientific Reports-A

journal homepage: https://dergipark.org.tr/tr/pub/jsr-a



E-ISSN: 2687-6167 Number 62, September 2025

RESEARCH ARTICLE

Betaine induces apoptosis via ROS-independent mechanisms in U87 glioblastoma cells: a potential metabolic anticancer strategy

Neslihan Meriç ^{a*}, Ezgi Kar ^b, Fatih Kar ^c

^{a,*}Kütahya Health Sciences University, Faculty of Engineering and Natural Sciences, Department of Molecular Biology and Genetics, Kütahya, 43020, Türkive, ORCID:0000-0002-2878-5052

^bKütahya Health Sciences University, Faculty of Health Sciences, Department of Nutrition and Dietetics, Kütahya, 43020, Türkiye, ORCID: 0000-0003-2134-4067

^cKütahya Health Sciences University, Faculty of Medicine, Department of Biochemistry, Kütahya, 43100, Türkiye, ORCID: 0000-0001-8536-9806

Abstract

Betaine (trimethylglycine), a naturally occurring osmolyte and methyl donor, has attracted attention for its potential anticancer properties through its role in cellular stress responses and epigenetic regulation. Glioblastoma multiforme (GBM) represents one of the most aggressive forms of primary brain cancer characterized by rapid progression, poor prognosis, and resistance to conventional therapies. In this study, we aimed to investigate the dose- and time-dependent cytotoxic and pro-apoptotic effects of betaine on U87 glioblastoma cells, along with its influence on oxidative stress, gene expression, and protein-level markers. U87 cells were treated with increasing concentrations of betaine, and cell viability was assessed using the MTS assay. Apoptosis was evaluated via Annexin V/PI flow cytometry, while ROS levels were measured with DCFDA staining. Quantitative RT-PCR and ELISA tests were conducted to assess gene and protein expression patterns associated with apoptosis, oxidative stress, and inflammatory signaling. Our findings demonstrated that betaine reduced U87 cell viability in a concentration-dependent fashion, triggered late apoptosis and necrotic cell death, and markedly lowered intracellular reactive oxygen species (ROS) levels. Furthermore, betaine modulated the expression of key signaling molecules including PTEN, BCL-2, AKT1, and NF-κB, while increasing mitochondrial apoptotic markers such as CASP3 and cytochrome C. Interestingly, the anticancer effects of betaine appeared to occur through ROS-independent mechanisms. The results indicate that betaine may serve as a promising anticancer agent for glioblastoma, warranting further investigation in preclinical models.

© 2023 DPU All rights reserved.

Keywords: Betaine; Glioblastoma; Apoptosis; Oxidative Stress

Neslihan Meriç * Corresponding author. Tel.:+905302279700; fax: 0(274)2652191

E-mail address: neslihan.meric@ksbu.edu.tr

1. Introduction

Betaine (trimethylglycine) is a naturally occurring quaternary ammonium compound found in plants, animals, and microorganisms (Figure 1) [1]. It was first isolated from sugar beets in the 19th century and is now obtained through dietary sources such as wheat bran, spinach, seafood, and beets, or synthesized endogenously via choline metabolism [2]. By participating in methylation pathways, betaine contributes to epigenetic regulation through DNA methylation. Betaine functions via the enzyme betaine-homocysteine methyltransferase (BHMT) to convert homocysteine into methionine, supporting the maintenance of S-adenosylmethionine (SAM) levels. This process impacts various biological events including DNA, RNA, and histone methylation [3], thereby facilitating activation of tumor suppressor genes and repression of proto-oncogenes.

Fig. 1. Chemical structure of the betaine (trimethylglycine) molecule. The molecule contains a quaternary ammonium structure $(-N^+(CH_3)_3)$ with three methyl groups and a carboxylic acid group (-COOH) [1]

A wide range of experimental studies conducted both in vitro and in vivo has provided evidence of significant biological responses associated with the anticancer effects of betaine. In a study involving the DU-145 prostate cancer cell line, betaine was shown to inhibit cell proliferation in a dose-dependent manner, increase oxidative stress levels, induce apoptosis, and elevate proinflammatory cytokines such as TNF-\u03b1 and IL-6 [4]. Similarly, in HeLa cervical cancer cells, high doses of betaine inhibited cell growth and triggered apoptosis via caspase-3 activation, upregulation of p53, and downregulation of Bcl-2 expression [5]. A comprehensive study in oral squamous cell carcinoma (OSCC) cells showed that betaine suppresses invasion and migration by downregulating the expression of MMP1, MMP2, and MMP9 genes, as well as epithelial-mesenchymal transition (EMT) markers such as FN1 [6]. In animal models, betaine has also shown anticancer efficacy. In a colitis-associated colorectal cancer model (AOM/DSS-induced), betaine reduced tumor incidence, suppressed reactive oxygen species (ROS) production, and downregulated proinflammatory gene expression such as COX-2, TNF-\u03b1, and IL-6 [7]. The results imply that betaine has the potential to modulate the tumor microenvironment by reducing DNA damage and inflammation. Another study in the same model demonstrated that betaine improves glutathione metabolism, mitigates oxidative stress, and reduces inflammatory damage to the colonic mucosa [8]. Epidemiological evidence in humans also supports the protective role of betaine against cancer. According to the Long Island Breast Cancer Study Project, high dietary intake of betaine and choline was significantly associated with reduced breast cancer mortality. Furthermore, the rs3733890 polymorphism in the BHMT gene was reported to confer a protective effect on survival [9]. The anticancer potential of betaine is supported by its multifaceted biological activities including apoptosis induction, cell cycle regulation, epigenetic modification, inflammation suppression, and inhibition of cell invasion. However, the magnitude of these effects may vary depending on factors such as dose, duration, and cell type, indicating the need for further research into its underlying molecular mechanisms. Accordingly, this research set out to assess the doseand time-dependent cytotoxic, apoptotic, and oxidative stress-related effects of betaine on U87 glioblastoma cells, using molecular, biochemical, and flow cytometric approaches to better understand its underlying anticancer processes.

2. Materials and Methods

2.1. Propagation of glioblastoma cells and HEK-293

HEK-293 cells, immortalized human embryonic kidney epithelial cells, were used as a non-cancerous control group to compare the cytotoxic effects of betaine on tumor and non-tumor cells. These cells are frequently used as a reference in cancer studies due to their robust growth, human origin, and well-characterized molecular profile. Although not strictly "normal" cells, their lack of malignancy contrasted with the aggressive phenotype of glioblastoma, allowing us to better assess selective cytotoxicity.

2.2. Assessment of betaine-induced cytotoxicity in human glioblastoma cells

A stock solution of Betaine Hydrochloride was initially prepared by dissolving the compound in distilled water with continuous mixing at ambient temperature. This mixture was subsequently diluted with DMEM to obtain the required treatment levels. U87 glioblastoma cells were maintained in 96-well culture plates at a cell concentration of 5 × 10³ per well, each containing 200 μL of DMEM supplemented with 10% fetal bovine serum (FBS) and 1% PSA (10,000 U/mL penicillin, 10,000 μg/mL streptomycin, and 25 μg/mL amphotericin B). After cell attachment, they were exposed to increasing doses of betaine (high-dose: 0.5, 2.5, 5, 10, and 20 mg/mL; low-dose: 0.5 to 6 mg/mL, at 1 mg/mL intervals). Control wells received no treatment. Cell survival was analyzed after 24 and 48 h using the MTS-based CellTiter 96® AQueous One Solution Cell Proliferation Assay (Promega, Cat. No: G3580), according to the instructions supplied by the manufacturer. Absorbance was determined at 490 nm following a 3-h incubation at 37 °C in the dark. The half-maximal inhibitory concentration (IC₅₀) of betaine was calculated by comparing absorbance values with those from untreated controls.

2.3. Evaluating the effect of betaine on cancer cell proliferation and survival

2.3.1. Analysis of apoptosis

U87 cells were cultured into 6-well plates with a density of 500,000 cells per well. The cells received treatment with betaine at previously identified IC50 levels, conducted in triplicates for each tested condition. The cells were maintained in a humid environment at 37°C and 5% CO₂ for three days. After the incubation period, cells were harvested and pelleted by spinning at 1500 rpm for 5 minutes. Apoptotic activity was then assessed by suspending the obtained cell pellet in a 1X binding buffer, followed by labeling the cells with Annexin V conjugated to FITC and propidium iodide (PI) through a commercially available apoptosis assay kit (ABP, Cat. No: A026) according to the manufacturer's recommended protocol. Subsequently, the labeled cells underwent analysis using flow cytometry on a Cytoflex S analyzer (Beckman Coulter, USA; Cat. No: B47903). Data collection and gating methodologies followed standard practices and were consistent with previously published research [10, 11].

2.3.2. Assessment of oxidative stress via ROS detection

To evaluate ROS levels, cells were plated into wells at a concentration of 500×10^3 cells per well and subsequently exposed to effective concentrations of betaine. After a 48-hour incubation period, the cellular ROS levels were assessed utilizing a commercially provided DCFDA/H2DCFDA assay kit (Abcam; Catalog No: ab113851), performed according to the supplier's guidelines. Cells were incubated with the fluorescent dye DCFDA at a final concentration of 20 μ M for 30 minutes without any washing steps afterward. Fluorescent intensity was quantified via flow cytometry, utilizing excitation at 485 nm and emission detection at 535 nm. Tert-butyl hydrogen peroxide (TBHP) at a concentration of 50 μ M, prepared from a 55 mM initial stock, served as the positive experimental control [9,11].

2.3.3. Flow cytometric evaluation of sema 3A expression

After 48 h of treatment with effective dose of betaine, cells were collected and transferred to 1.5 ml tubes. Cells were labeled using SEMA3A Antibody (A-12) PE (Cat No: sc-74554 PE) by intracellular staining following the supplier's instructions and protocols outlined in previous studies. The specificity of SEMA3A staining was validated by using an unstained (UNS) control to assess background fluorescence and an isotype-matched PE-conjugated antibody as an isotype control in flow cytometry analyses. Labeled cells were then analyzed by Cytoflex S flow cytometry according to methods previously described in our experiments.

2.3.4 Gene expression analysis (RT-qPCR)

U87 cells were maintained in 6-well culture plates at a seeding density of 5 × 10⁵ cells per well and then treated with defined concentrations of betaine. After 24 h of incubation, cells were collected to extract total RNA. RNA purification was carried out with the PureLink RNA Mini Kit (Invitrogen, Thermo Fisher Scientific, Cat. No: 12183025), following the manufacturer's protocol. Complementary DNA (cDNA) was subsequently produced using the High Capacity cDNA Reverse Transcription Kit (Applied Biosystems, Cat. No: 4368814). Quantitative real-time PCR (qRT-PCR) experiments were conducted employing the Maxima SYBR Green/ROX qPCR Master Mix (Thermo Fisher Scientific, Cat. No: K0221), together with primers obtained from Oligomer (Turkey) (see Table 1). PCR amplifications were performed on the Bio-Rad CFX96 TouchTM Real-Time PCR platform. Gene expression analysis was carried out using the ΔΔCt approach, with GAPDH chosen as the internal control gene to ensure reliable and consistent quantification [10, 12].

Table 1. Oligonucleotide primers applied in qRT-PCR assays

Gene	Forward (5' to 3')	Reverse (5' to 3')	Function
GAPDH	TTTTGCGTCGCCAGCC	ATGGAATTTGCCATGGGTGGA	Serves as a control gene to standardize the measurement of expression levels
VEGF	TAAGTCCTGGAGCGTTCCCT	ACGCGAGTCTGTGTTTTTGC	Promotes the formation of new vasculature
p53	AAGTCTAGAGCCACCGTCCA	ACCATCGCTATCTGAGCAGC	Mutations in the p53 gene are associated with tumor advancement and reduced sensitivity to chemotherapy
PTEN	AGCTGGAAAGGGACGAACTG	ACACACAGGTAACGGCTGAG	Functions by blocking pathways that promote tumor cell growth and resistance to treatment.
BCL-2	AAAAATACAACATCACAGAGGAAGT	TCCCGGTTATCGTACCCTGT	Supports cancer cell survival by inhibiting programmed cell death.
AKT1	CCAGGATCCATGGGTAGGAAC	CTCCTCCTCCTCCTGCTTCT	Participates in signaling pathways that help cancer cells evade apoptosis and continue proliferating.
BAX	AGGGCCCTTTTGCTTCAG	TGTCCAGCCCATGATGGTTC	Plays a key role in initiating cell death processes.
BAK	GCAGGCTGATCCCGTCC	GGCTAAGGAGGTCCCAGAGA	Facilitates apoptosis by promoting mitochondrial membrane permeabilization.
NFKB	AACAGCAGATGGCCCATACC	AATAGGCAAGGTCAGGGTGC	Supports tumor development and dissemination, contributes to resistance against chemotherapy, heightens inflammatory signaling, and may also inhibit programmed cell death.

			Induces cell death in tumor cells
			through the activation of apoptosis
CAS-3	TGCTATTGTGAGGCGGTTGT	TCTGTTGCCACCTTTCGGTT	mechanisms.

2.3.5. Analysis of protein levels using ELISA

U87 cells were exposed to effective concentrations of betaine. After 48 hours, the expression levels of SEMA3A (E2078Hu), SEMA3E (E1562Hu), CASP3 (E4811Hu), Cytochrome C (E7110Hu), GPX-4 (E6887Hu), ACSL4 (E7227Hu), IL-6 (E0090Hu), TNF- α (E0099Hu), and IL-10 (E0102Hu) were quantified in the experimental groups using ELISA kits provided by BT LAB (China). Total antioxidant status (TAS) and total oxidant status (TOS) were determined using commercial kits from Rel Assay Diagnostics (Gaziantep, Turkey). TAS levels were expressed in mmol Trolox equivalents per liter, while TOS values were reported in μ mol H2O2 equivalents per liter. All kits used were specifically tailored for human (Hu) samples. Before performing ELISA, total protein concentrations in the samples were assessed using the Bradford assay to ensure precision. All procedures were performed following the manufacturer's guidelines, utilizing a Thermo Scientific Multiscan SkyHigh ELISA reader along with a Thermo Scientific Multiscan SkyHigh ELISA reader along with a Thermo Scientific Multiscan SkyHigh ELISA reader along with a Thermo Scientific Multiscan SkyHigh ELISA reader along with a Thermo Scientific Multiscan SkyHigh ELISA reader along with a Thermo Scientific Multiscan SkyHigh ELISA reader along with a Thermo Scientific Multiscan SkyHigh ELISA reader along with a Thermo Scientific Wellwash microplate washer.

2.4. Evaluation of statistical data

All analytical evaluations were performed using GraphPad Prism software (version 8.4.2; GraphPad Software, San Diego, CA, USA). Results were reported as the mean \pm standard deviation (SD) from a minimum of three separate biological experiments. For analyzing data involving more than two groups, one-way ANOVA followed by Tukey's post-hoc test was conducted. For comparisons involving only two groups, the unpaired two-tailed Student's t-test was applied. A p-value below 0.05 was interpreted as statistically meaningful. Significance levels were defined as follows: $*p \le 0.05$, $**p \le 0.01$, $***p \le 0.001$, and $****p \le 0.0001$.

3. Results

3.1. Evaluation of growth dynamics and survival rates in U87 and HEK-293 cells

Figure 2 shows the dose and time-dependent cytotoxic effects of betaine on U87 glioblastoma cells (Figure 2A and C) and non-tumorous HEK-293 embryonic kidney cells (Figure 2B and D) after 24 and 48 hours of application. In U87 cells, betaine was observed to significantly reduce cell viability at concentrations of 5 mg/ml and above. Especially at concentrations of 20, 10, 6 and 5 mg/ml, viability decreased well below the 50% threshold value at both time points. The calculated IC50 value at the end of 48 hours of application was determined as 4.1 mg/ml and IC25 value as 2.7 mg/ml. These findings demonstrate that betaine has a strong cytotoxic effect on glioblastoma cells. However, no significant decrease in viability was observed at doses of 2.5 mg/ml and lower; This shows that the dose-response relationship has a clear threshold (Figure 2A and C). In contrast, a dose-dependent decrease in viability was also observed in HEK-293 cells (Figure 2B and D), but this effect was milder compared to U87 cells. Although significant cytotoxicity was observed at high doses (20, 10, 6 and 5 mg/ml), cell viability remained above 50% at 2.5 and 0.5 mg/ml doses for 24 h. Even after 48 h, only a limited cytotoxic effect was observed at these low concentrations. This suggests that HEK-293 cells are more resistant to betaine.

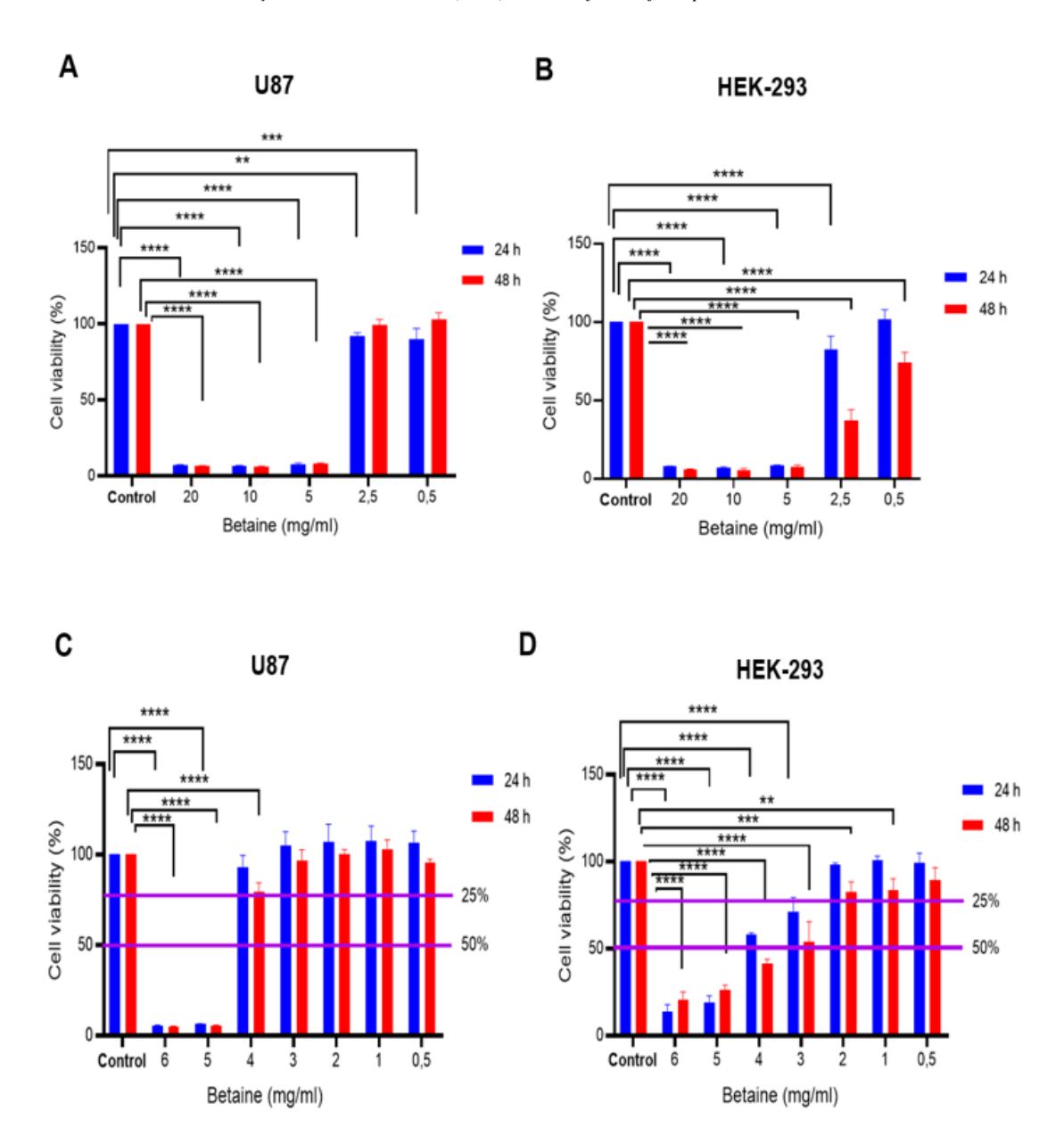


Fig. 2. Effect of betaine on the viability of U87 glioblastoma (A, C) and HEK-293 kidney epithelial cells (B, D) at 24 h and 48 h post-treatment. The bar graphs illustrate cell viability (%) after exposure to both high (A, B) and low (C, D) concentrations of betaine, assessed via MTS assay. Betaine treatment significantly reduced cell viability in both U87 glioblastoma (A, C) and HEK-293 normal kidney epithelial cells (B, D) in a dose- and time-related manner. In high-dose conditions (0.5–20 mg/mL), U87 cells (A) showed a pronounced loss of viability at \geq 5 mg/mL, while HEK-293 cells (B) were less sensitive at lower doses but exhibited significant reductions at 5 mg/mL and above. In the low-dose range (0.5–6 mg/mL), U87 cells (C) maintained high viability up to 4 mg/mL, but showed substantial cytotoxicity at 5 and 6 mg/mL, aligning with IC25 and IC50 levels (indicated by purple lines). HEK-293 cells (D) retained higher viability overall but showed significant decline starting from 3 mg/mL. Results are expressed as mean \pm SD of three independent replicates. Data-driven evaluation was performed using one-way ANOVA with Tukey's post hoc test (** p \equiv 0.01, ***p \equiv 0.001, ***p \equiv 0.0001).

3.2. Assessing the cytotoxic and anti-proliferative effects of betaine on U87 glioblastoma cells

3.2.1. Assessment of apoptosis in cancer cells

The effects of betaine on apoptosis in U87 glioblastoma cells showed significant changes depending on the dose and time (Figure 3). In Figure 3A, which shows the 48-hour application, the live cell ratio decreased significantly at IC25 (2.7 mg/ml) and especially at IC50 (4.1 mg/ml) doses; this decrease was found to be strongly significant based on statistical analysis at the high dose (****p < 0.0001). Under the same conditions, the late apoptosis ratio increased significantly and it was observed that the majority of the cells passed to the advanced stages of the apoptotic process (****p < 0.0001). In addition, a significant increase was observed in the necrotic cell ratio at the 48-hour high dose application, indicating that advanced cellular damage is not only limited to apoptosis but can also trigger the necrosis mechanism characterized by the disruption of cell membrane integrity. In contrast, in Figure 3B, which shows 24-hour betaine application, a limited but significant decrease in the rate of live cells was observed at lower doses (1 and 2 mg/ml) (**p < 0.01, *p < 0.05); and the rate of early apoptosis also showed a notable rise with statistical relevance (*p < 0.05). However, no significant change was detected in the rates of late apoptosis and necrosis during this period. The data obtained show that betaine creates a cytotoxic effect that progresses over time and increases depending on the dose in U87 cells, and that it activates more widespread cell death mechanisms, including early stages of apoptosis at low doses and short periods, and late apoptosis and necrosis at high doses and long periods.

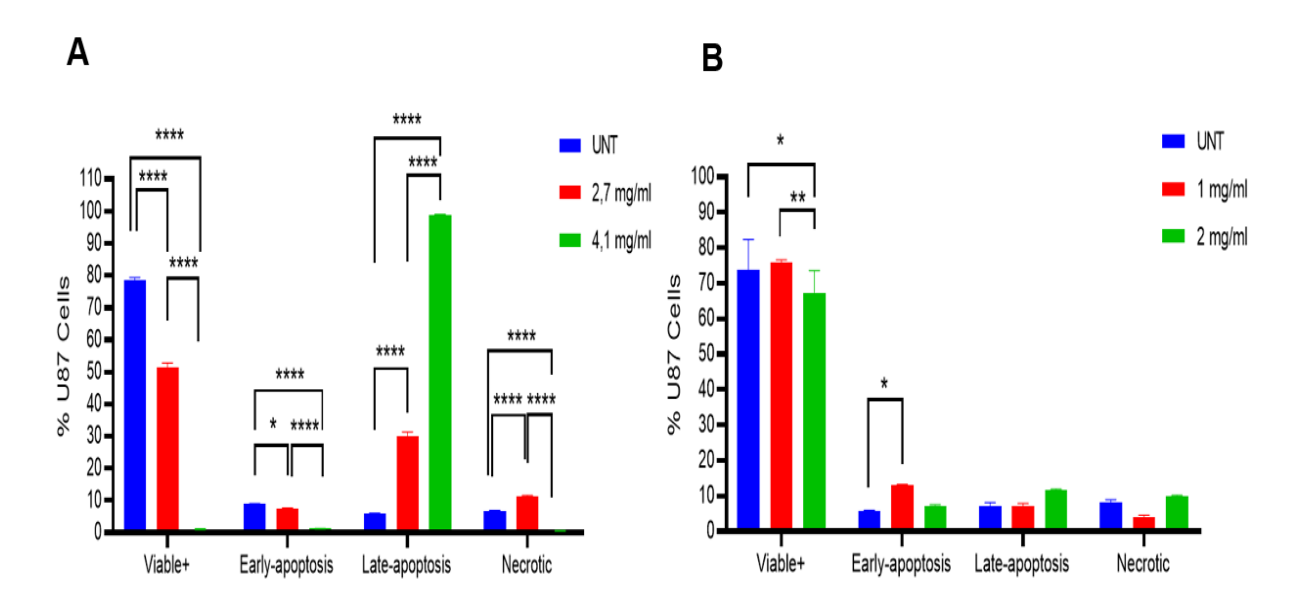


Fig.3. Flow cytometry analysis of betaine-treated U87 cells. (A) After 48 h, doses of 2.7 and 4.1 mg/mL significantly decreased viability and increased late apoptosis (****p < 0.0001). (B) At 24 h, doses of 1 and 2 mg/mL caused a slight but significant decrease in viability and increased early apoptosis (*p < 0.05, **p < 0.01). Values represent mean \pm SD (n = 3). Comparisons among groups were carried out through one-way ANOVA with Tukey's multiple comparison test.

Morphological changes caused by betaine in U87 glioblastoma cells showed significant differences depending on the dose and time (Figure 4). In the control group (UNT), cells maintained their regular monolayer structure, while cell morphology was uniform and their distribution was homogeneous. In the 24-hour betaine application, while a slight change in shape and cytoplasmic thickening were noted in the cells at a dose of 1 mg/ml, significant changes

indicating early and late apoptosis such as decrease in cell density, rounding and clustering were observed at a dose of 2 mg/ml. In the 48-hour applications, it was observed that the borders of the cells disappeared after the 2.7 mg/ml betaine treatment, intense cytoplasmic changes and cell shrinkage began. In the IC50 dose of 4.1 mg/ml application, it was observed that most of the cells became round, separated from the monolayer structure, and detachment and membrane disruptions suggesting advanced apoptosis and necrosis occurred.

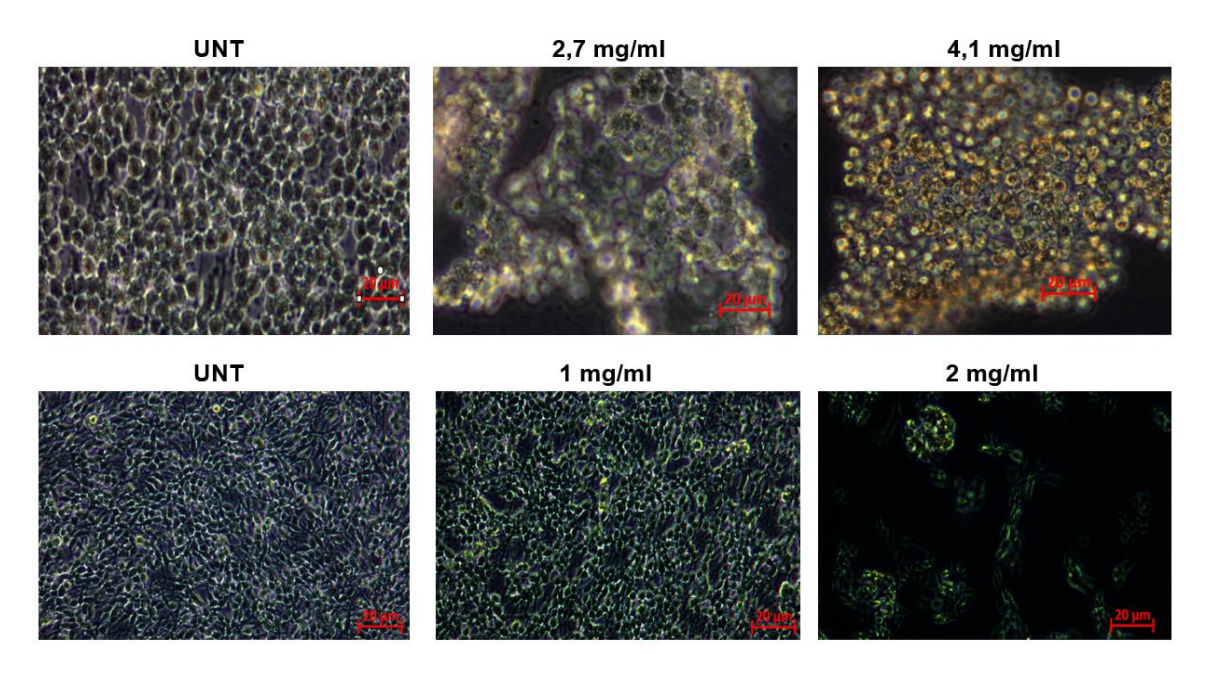


Fig.4. Representative microscopic images of U87 glioblastoma cells after 24 h (bottom) and 48 h (top) of betaine treatment at indicated concentrations. Control (UNT) cells show normal morphology and confluency, while betaine-treated cells exhibit dose-dependent morphological changes, including rounding, shrinkage, and detachment—indicative of apoptosis. Microscopic images were obtained using a ZEISS imaging system at $10 \times$ magnification. Scale bar = $20 \mu m$.

3.2.2. *Analysis of ROS activity*

DCFDA based ROS analyses presented in Figure 5 reveal that betaine significantly suppressed reactive oxygen species (ROS) levels in U87 glioblastoma cells in a dose- and time-dependent manner. While the DCFDA positive cell ratio was high in the control (UNT) and TBHP-treated positive control groups, this ratio was significantly decreased in the betaine-treated groups. Especially, the IC50 dose (4.1 mg/ml) at 48 h administration caused a notable reduction confirmed by statistical analysis in ROS levels (****p < 0.0001), and this decrease was supported by the simultaneous increase in the DCFDA negative cell ratio (Figure 5A). Similarly, significant ROS suppression was observed at 1 and 2 mg/ml doses at 24 h administration (****p < 0.0001) (Figure 5B). These findings indicate that the anticancer effect of betaine occurs by reducing intracellular oxidative stress, in contrast to the induction of prooxidative stress observed in most classical chemotherapeutics. Despite this decrease in ROS levels, the significant apoptosis and necrosis rates observed in previous analyses indicate that betaine can effectively trigger cell death through alternative mechanisms independent of ROS. Therefore, betaine is considered a unique anticancer agent that can not only have a strong antioxidant capacity but also can induce cytotoxic responses by targeting non-ROS signaling pathways.

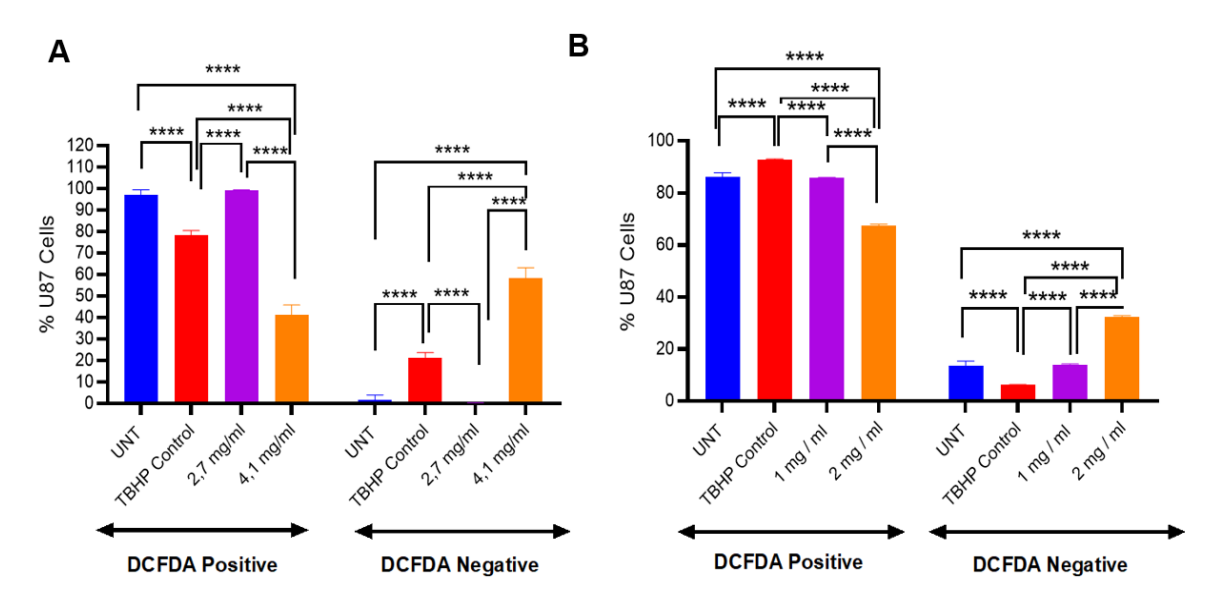


Fig. 5. Quantification of intracellular ROS levels in U87 cells after betaine treatment using DCFDA staining. (A) After 48 h of exposure, betaine significantly reduced the percentage of DCFDA positive (ROS+) cells in a manner proportional to the applied dose when evaluated against the untreated (UNT) and TBHP-induced oxidative stress control groups (****p < 0.0001). A concomitant increase in DCFDA negative (ROS-) cells was observed, especially at 4.1 mg/mL. (B) A similar but milder trend was detected after 24 h; 1 and 2 mg/mL betaine treatment led to a significant decrease in ROS+ cells and an increase in the ROS- population (****p < 0.0001). The findings are presented as mean ± SD (n = 3), and differences between groups were analyzed through one-way ANOVA with Tukey's post hoc comparison.

3.2.3. Quantification of sema 3A expression using flow cytometry

According to the flow cytometry data presented in the graph (Figure 6), approximately 100% of U87 glioblastoma cells were detected as Sema3A positive before betaine treatment. This high expression rate indicates that Sema3A is endogenously expressed intensively in U87 cells. Sema3A (Semaphorin 3A) is a signaling molecule that plays a role in processes such as cell invasion, migration and angiogenesis in cancer biology, apart from neural development. Therefore, such high expression of Sema3A in U87 cells suggests that this molecule may be associated with glioblastoma progression and aggressive phenotype. This finding indicates that changes in Sema3A expression following betaine treatment may be of biological and therapeutic importance.

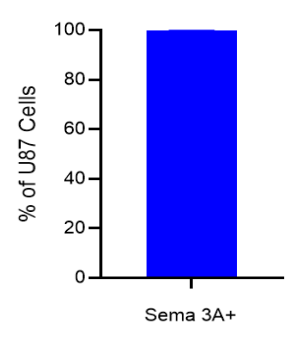


Fig.6. Flow cytometric analysis of Sema3A surface expression in U87 glioblastoma cells before betaine treatment. Almost 100% of the cell population was Sema3A positive (Sema3A⁺), indicating high basal expression of Sema3A in untreated cells before any experimental intervention.

3.2.4. Analysis of RT-PCR

The RT-qPCR results presented in Figure 7 show that betaine significantly modulated the gene expressions related to apoptosis and oxidative stress in U87 glioblastoma cells. Betaine treatment significantly increased the expression of the tumor suppressor gene PTEN, especially at the dose of 1 mg/ml (***p < 0.001), while it caused a meaningful decline with statistical validation in BCL-2, AKT-1 and NF-κB genes that promote cell survival and proliferation (*p < 0.05–***p < 0.001). These findings suggest that betaine promotes apoptosis by suppressing anti-apoptotic pathways such as PI3K/AKT and NF-κB. In addition, when evaluated together with ROS analyses, it was observed that betaine can induce apoptotic cell death despite reducing intracellular oxidative stress levels. This suggests that betaine may trigger apoptosis through ROS-independent pathways—particularly through the PTEN/AKT signaling axis and BCL-2 family members. The decrease observed in pro-apoptotic genes, particularly CASP3 and BAX, suggests that the classical effector phase of apoptosis may be regulated differently depending on cell type, timing, or decreased ROS levels. According to these findings, betaine both suppresses ROS through its antioxidant effects and induces apoptosis through a ROS-independent mechanism by targeting intracellular proliferative and survival signals.

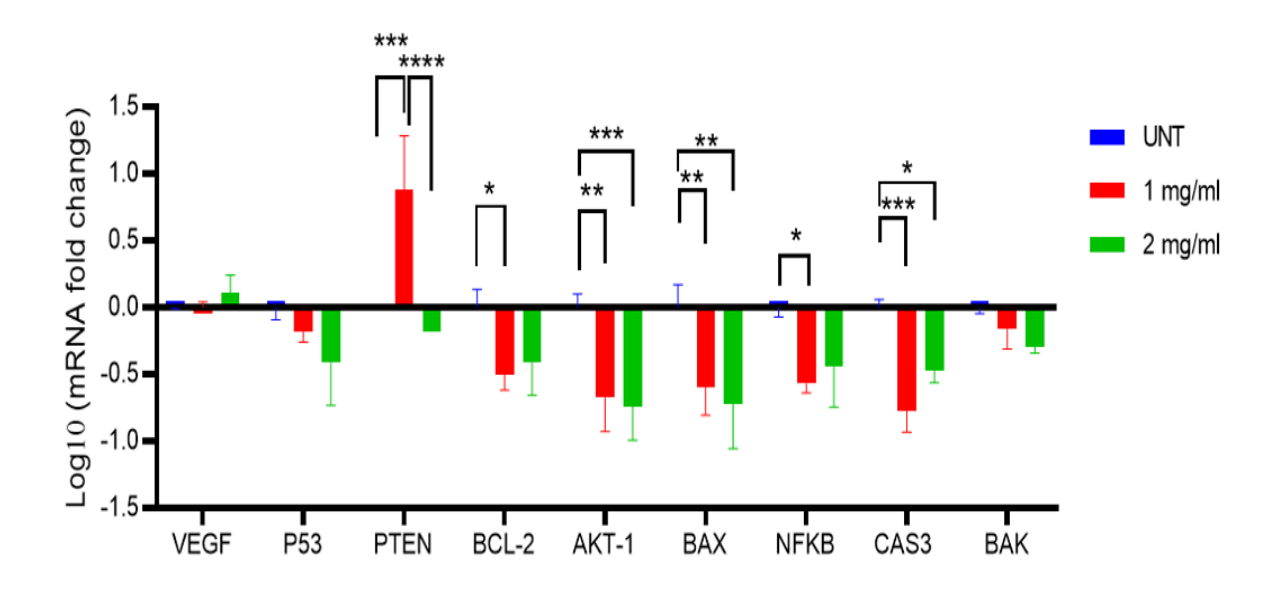


Fig 7. RT-qPCR analysis of gene expression levels in U87 glioblastoma cells treated with betaine (1 mg/ml and 2 mg/ml) for 24 h. Betaine treatment resulted in significant up-regulation of the tumor suppressor gene PTEN and down-regulation of important pro-apoptotic and anti-apoptotic genes including BCL-2, AKT-1, and NFKB. Pro-apoptotic markers such as BAX and CASP3 were also significantly down-regulated in a dose-dependent manner. Results are shown as \log_{10} fold changes compared to the untreated control (UNT); *p < 0.05, **p < 0.01, ***p < 0.001, ****p < 0.0001.

3.2.5. Analysis of protein levels using ELISA

Data obtained by ELISA show that betaine causes significant biochemical changes on apoptosis, oxidative stress and antioxidant defense systems in U87 glioblastoma cells. CASP3 (Figure 8F) and CYCS (Figure 8G) protein levels showed significant increases, especially at 1 mg/ml betaine dose (**p < 0.01), indicating that apoptosis is activated through the mitochondrial pathway. However, no significant change was observed in IL-6, IL-10 and TNF- α levels (Figure 8C, D, E), which represent the inflammatory response, indicating that betaine acts through intracellular signaling pathways rather than a direct inflammatory suppression effect on cytokine levels. There was no significant change in SEMA3A and SEMA3E levels (Figure 8A, B), indicating that betaine's anticancer effects may be independent of semaphorin-mediated signaling. In the evaluations made on antioxidant system, while a significant increase was observed in total antioxidant capacity (TAS) level at 1 mg/ml dose in 1 mg/ml betaine application (Figure 8I, **p < 0.01), this value decreased at 2 mg/ml dose. In contrast, total oxidant level (TOS) decreased significantly at 2 mg/ml dose (Figure 8İ, *p < 0.05). These results show that betaine at low dose strengthens intracellular antioxidant defense, while at high dose it directly suppresses ROS production and reduces net oxidative stress. In addition, the significant decrease observed in GPX4 level (Figure 8H, ****p < 0.0001) suggests that lipid peroxidation-sensitive cell death forms such as ferroptosis may also be involved in the process.

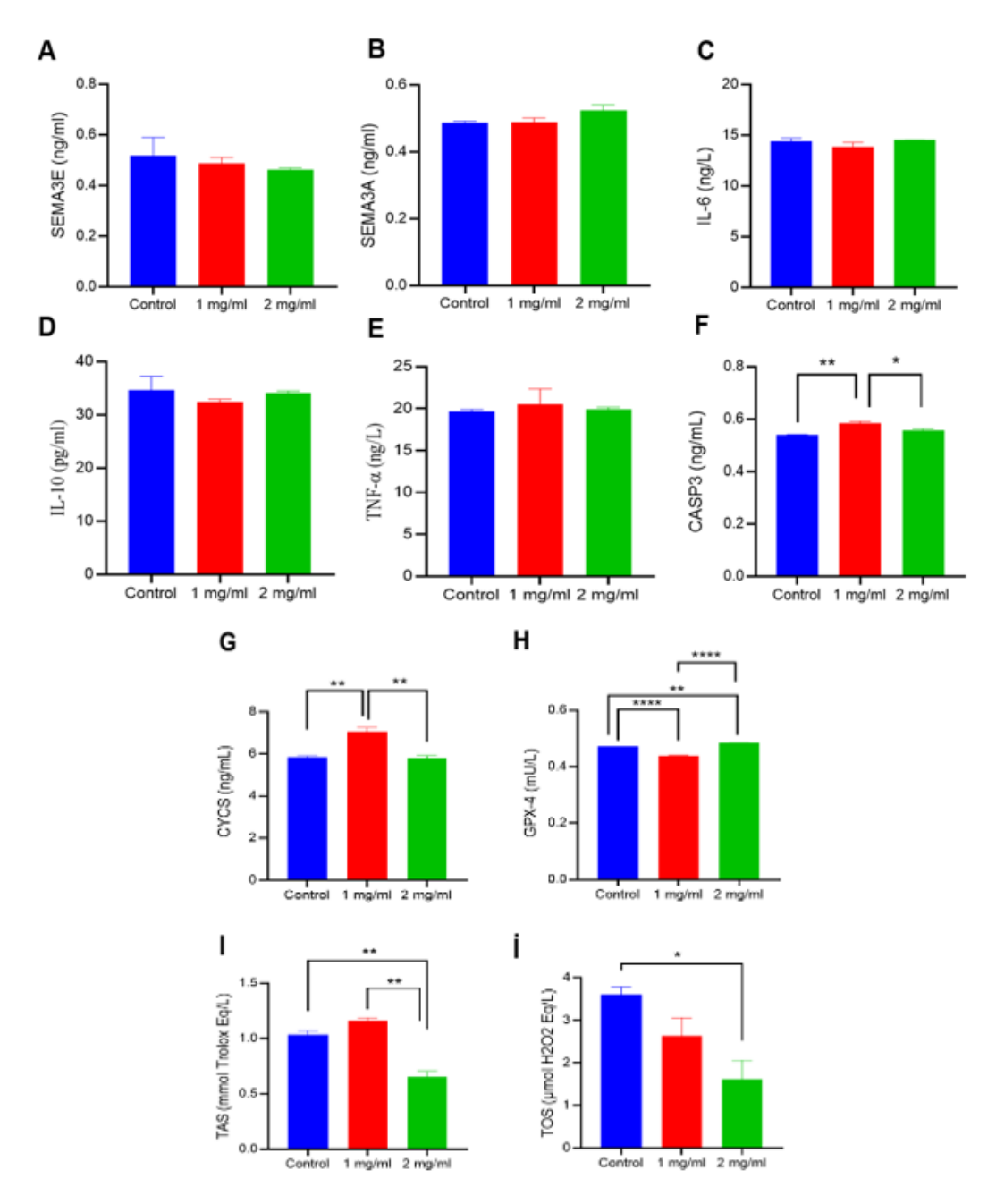


Fig.8. Quantification of multiple protein and oxidative stress markers in betaine-treated U87 cells. (A–B) ELISA analysis, no significant changes were observed in the levels of SEMA3E and SEMA3A after treatment among the groups. (C–E) The levels of proinflammatory cytokine IL-6, anti-inflammatory cytokine IL-10, and TNF- α also remained stable. (F) A significant increase in CASP3 levels was observed at both 1 mg/mL (**p < 0.01) and 2 mg/mL (**p < 0.05) betaine doses. (G) Cytochrome c (CYCS) was significantly elevated at 1 mg/mL (**p < 0.01), indicating mitochondrial pathway activation. (H) GPX4 levels were significantly decreased in both treatment groups (**p < 0.01, ****p < 0.0001), supporting ROS-independent apoptosis (I–İ) Total antioxidant capacity (TAC) was significantly decreased upon 2 mg/mL betaine administration (**p < 0.01), while total oxidant levels (TOS) decreased in a dose-dependent manner upon treatment (*p < 0.05).

4. Discussion

The outcomes of the present investigation provide compelling evidence that betaine exerts a significant cytotoxic effect on U87 glioblastoma cells, primarily through the induction of apoptosis via mitochondrial pathways. This is underscored by increased Annexin V/PI staining and decreased mitochondrial membrane potential following betaine treatment, consistent with the activation of the intrinsic apoptotic cascade. Notably, these changes were observed alongside a marked suppression of ROS levels, suggesting a redox-independent mechanism of apoptosis induction—an observation that contrasts with traditional views of oxidative stress as a pro-apoptotic trigger.

This paradoxical relationship between ROS suppression and increased apoptosis in glioblastoma cells offers an intriguing contrast to earlier reports in other cancer models. For instance, in studies involving colon cancer models, Kim et al. [7] observed that betaine reduced tumor formation by decreasing ROS and inflammatory cytokines such as TNF- α , IL-6, and COX-2. These effects were interpreted as protective, preventing DNA damage and tumor initiation. In our context, however, the suppression of ROS by betaine appears to disrupt redox signaling homeostasis in glioblastoma cells, potentially interfering with ROS-mediated survival signals and thereby facilitating apoptosis. This interpretation aligns with the growing recognition that cancer cell dependency on basal ROS levels for proliferation creates a therapeutic window that can be exploited by either increasing or depleting ROS.

Our gene expression results further support this mechanism, with significant upregulation of mitochondrial apoptotic markers such as CASP3 and CYCS, along with a reduction in anti-apoptotic BCL-2 levels. These findings are consistent with previous work by Guo et al. [5], who reported that betaine induced apoptosis in HeLa cells via increased caspase-3 and p53 expression while suppressing BCL-2. Additionally, we observed a downregulation of NF-κB gene expression, suggesting a broader suppression of survival and inflammatory signaling. Kar et al. [4] similarly demonstrated that betaine inhibited NF-κB and promoted apoptosis in prostate cancer cells.

The comparison between U87 glioblastoma cells and HEK-293 epithelial cells revealed that betaine exerts a more pronounced cytotoxic effect on cancer cells, as demonstrated by a sharper decline in viability at lower concentrations and earlier time points. While HEK-293 cells also exhibited reduced viability at higher doses, their overall resistance to betaine supports its preferential targeting of tumorigenic cells. These findings underscore the potential therapeutic window where cancer cells can be effectively targeted while minimizing toxicity to normal tissue analogs.

A unique aspect of our study is its focus on glioblastoma, a malignancy known for its high resistance to conventional therapies and limited responsiveness to immune modulation. The findings suggest that betaine's proapoptotic effects are not limited to gastrointestinal or epithelial-origin cancers but extend to neuroepithelial tumors such as glioblastoma. This opens the door for future investigations into whether betaine might enhance the efficacy of existing treatments like temozolomide or radiotherapy through mitochondrial sensitization.

Epidemiological data also lend support to the anticancer potential of betaine. Xu et al.[9] demonstrated that higher dietary intake of choline and betaine was associated with improved survival in breast cancer patients and highlighted the role of one-carbon metabolism and DNA methylation as potential mediators. Although our study did not explore epigenetic markers, it is plausible that betaine's function as a methyl donor may contribute to gene regulation in glioblastoma cells. Given the known epigenetic alterations in GBM, including DNA hypermethylation and histone modifications, further work is warranted to explore this dimension.

Furthermore, the inclusion of HEK-293 cells as a comparative control allowed for the evaluation of betaine's selectivity toward glioblastoma cells over non-tumorigenic counterparts, which is essential in assessing its therapeutic potential.

In conclusion, our study adds to the growing body of evidence that betaine possesses significant anticancer properties and may induce apoptosis in glioblastoma cells through mitochondrial and redox-independent mechanisms. This distinguishes its action in brain tumors from its well-documented anti-inflammatory and antioxidative roles in other cancer types. Future research should focus on in vivo models to validate these effects and on combinatorial studies integrating betaine with standard-of-care treatments to evaluate its translational potential in glioblastoma therapy.

Conflict of Interest

The authors declare that there are no conflicts of interest related to this study.

Acknowledgments

OpenAI and GoogleAI were utilized to enhance the wording used in the text.

Author Contributions

NM was responsible for designing the study, planning the experiments, collecting the data, and performing the data analysis. EK and FK contributed to the experimental work and aided in analyzing the data.

References

- [1] PubChem, "Betaine Hydrochloride." Accessed: Jun. 20, 2025. [Online]. Available: https://pubchem.ncbi.nlm.nih.gov/compound/11545
- [2] M. K. Arumugam, M. C. Paal, T. M. Donohue, M. Ganesan, N. A. Osna, and K. K. Kharbanda, "Beneficial Effects of Betaine: A Comprehensive Review," *Biology*, vol. 10, no. 6, Art. no.456, 6, Jun. 2021, doi: 10.3390/biology10060456.
- [3] S. A. Fahmy, F. Ponte, I. M. Fawzy, E. Sicilia, and H. M. E.-S. Azzazy, "Betaine host–guest complexation with a calixarene receptor: enhanced in vitro anticancer effect," *RSC Adv.*, vol. 11, no. 40, pp. 24673–24680, Jul. 2021, doi: 10.1039/D1RA04614D.
- [4] F. Kar, C. Hacioglu, S. Kacar, V. Sahinturk, and G. Kanbak, "Betaine suppresses cell proliferation by increasing oxidative stress-mediated apoptosis and inflammation in DU-145 human prostate cancer cell line," *Cell Stress Chaperones*, vol. 24, no. 5, pp. 871–881, Sep. 2019, doi: 10.1007/s12192-019-01022-x.
- [5] Y. Guo et al., "Betaine Effects on Morphology, Proliferation, and p53-induced Apoptosis of HeLa Cervical Carcinoma Cells in Vitro," Asian Pac. J. Cancer Prev., vol. 16, no. 8, pp. 3195–3201, 2015, doi: 10.7314/APJCP.2015.16.8.3195.
- [6] P. Kulthanaamondhita et al., "Betaine Induces Apoptosis and Inhibits Invasion in OSCC Cell Lines," Int. J. Mol. Sci., vol. 25, no. 19, Art. no. 10295, 19, Jan. 2024, doi: 10.3390/ijms251910295.
- [7] D. H. Kim *et al.*, "Anti-inflammatory effects of betaine on AOM/DSS-induced colon tumorigenesis in ICR male mice," *Int. J. Oncol.*, vol. 45, no. 3, pp. 1250–1256, Sep. 2014, doi: 10.3892/ijo.2014.2515.
- [8] D. H. Kim, B. Sung, H. Y. Chung, and N. D. Kim, "Modulation of Colitis-associated Colon Tumorigenesis by Baicalein and Betaine," *J. Cancer Prev.*, vol. 19, no. 3, pp. 153–160, Sep. 2014, doi: 10.15430/JCP.2014.19.3.153.
- [9] X. Xu et al., "High intakes of choline and betaine reduce breast cancer mortality in a population-based study," FASEB J., vol. 23, no. 11, pp. 4022–4028, 2009, doi: 10.1096/fj.09-136507.
- [10] N. Meriç, E. Albayrak, Z. Gülbaş, and F. Kocabaş, "MEIS inhibitors reduce the viability of primary leukemia cells and Stem cells by inducing apoptosis," *Leuk. Lymphoma*, vol. 65, no. 2, pp. 187–198, Feb. 2024, doi: 10.1080/10428194.2023.2275532.
- [11] N. Meriç, E. Kar, and F. Kar, "4-Methylthiazole triggers apoptosis and mitochondrial disruption in HL-60 cells," *Mol. Biol. Rep.*, vol. 51, no. 1, p. 997, Sep. 2024, doi: 10.1007/s11033-024-09939-y.
- [12] N. Meriç, E. Kar, and F. Kar, "Pro-Apoptotic and Mitochondria-Disrupting Effects of 4-methylthiazole in K562 Leukemia Cells: A Mechanistic Investigation," *Tissue Cell*, p. 102937, Apr. 2025, doi: 10.1016/j.tice.2025.102937.



Contents lists available at Dergipark

Journal of Scientific Reports-A

journal homepage: https://dergipark.org.tr/tr/pub/jsr-a



E-ISSN: 2687-6167 Number 62, September 2025

RESEARCH ARTICLE

Receive Date: 17.01.2025 Accepted Date: 20.03.2025

MCST-based finite element solution for short-fiber-reinforced microbeam vibration with the effects of rotary inertia and Pasternak medium

Büşra Uzun*

Bursa Uludag University, Engineering Faculty, Department of Civil Engineering, Gorukle Campus, 16059, Bursa/Türkiye, ORCID: 0000-0002-7636-7170

Abstract

A survey of the literature shows the absence of a microstructure-dependent finite element model that accounts for the vibration of short-fiber-reinforced microbeams with modified couple stress theory, rotary inertia, and Pasternak elastic medium. The present work is directed toward filling this gap in the literature. In the present study, the longitudinal and transverse Young's moduli of the short-fiber-reinforced material are modeled using the Halpin-Tsai equations. Additionally, the rule of mixture is considered for the calculation of the short-fiber-reinforced material mass density. Using Rayleigh beam theory, modified couple stress theory and finite element methodology, the research investigates the various effects such as the fiber Young's modulus, fiber mass density, fiber volume fraction, material length scale parameter and elastic medium stiffnesses. In this study, fibers are assumed to be randomly distributed in the matrix since fiber orientation in small-scale composite structures is difficult and even impossible in some cases. The results of the analysis presented in this study are expected to be helpful in the design of nano-electro-mechanical systems and micro-electro-mechanical systems.

© 2023 DPU All rights reserved.

Keywords: Short-fiber-reinforced microbeam; modified couple stress theory; rotary inertia; finite element method; Pasternak medium

^{*} Corresponding author. Tel.: +90-224-294-2636 fax: +90-224-294-1907. *E-mail address:* buzun@uludag.edu.tr

1. Introduction

In nature and mechanical systems, there are various environments with harsh conditions. Additionally, the same environment can also remain under the influence of contrasting conditions for short periods of time. Therefore, the production of materials that can withstand harsh conditions and the creation of structural elements from these materials are important issues. Composites are especially preferred to overcome rough conditions such as corrosion and sudden temperature changes. Composites are formed by combining materials with different characteristics from each other. They consist of at least two materials and can be produced in various forms. Some of these forms are layered, functionally graded, sandwich, fiber-reinforced, particle-reinforced, etc. These different forms have various advantages and disadvantages over each other and various studies [1–5] have been presented in the literature to understand their mechanical responses.

The usage of composite materials formed with fibers has revealed potential in a number of industries, including sports, automotive, construction, aerospace, biomedical engineering and marine [6-10]. In such composites, the fiberreinforced matrix can be ceramic, metal or polymer. Compared to other composites, polymer matrix composites offer a number of beneficial qualities, including high strength, high stiffness and low weight [11]. The fibers can be placed continuously or discontinuously in the matrix. Short-fiber-reinforced composite (SFRC), which is a discontinuous form, stands out with its easy processing and low production cost compared to continuous fiber-reinforced composites [12]. In the last fifty years, there have been noteworthy developments in the micromechanics of composites and one of the main objectives of the micromechanics of composite materials is to determine the general properties of heterogeneous materials that are effective in terms of the properties and microstructures of their components [13]. In addition, rapid developments in nanotechnology and microtechnology have enabled the discovery and production of small-scale materials with superior properties, making nanocomposites and microcomposites one of the most remarkable structures. In nano-reinforced composites, the reinforcement materials are usually in the form of short fibers, and these small-scale composite structures have been widely used in medicine, aerospace and defense industry, nano-electro-mechanical systems (NEMS), and micro-electro-mechanical systems (MEMS) devices [14]. Additionally, many situations where it is not possible to orient the reinforcement material in small-scale composites have been overcome by randomly oriented composite models.

Various mechanical responses of nano- and micro-scale beam elements have been extensively studied by researchers. It is seen that the studies to explore the response of the mentioned nano- and micro-scale beams have not been carried out with classical theories (CTs). Instead of classical theories, higher-order elasticity theories such as modified couple stress theory (MCST) [15], nonlocal elasticity theory [16] and modified strain gradient theory [17], which include various numbers of scale parameters in their formulations, are preferred. This is because experiments on nano/micro-mechanical systems and materials have shown that their responses are quite different from forecasts based on classical theories. It is possible to address these differences that classical theories cannot capture with the mentioned higher-order elasticity theories. Higher-order elasticity theories, which can achieve this with the scale parameters they contain, are critical for small-scale devices with an expensive application area. Because the applications of such devices require precise and expensive technology, research on their design and response should be done in accordance with reality. Of course, the properties of these devices can be realized through experiments and molecular dynamics simulations, but these methods have several disadvantages compared to theoretical approaches. These disadvantages include high costs for experiments, limited computer capacities and time for molecular dynamics simulations. Approaches based on higher-order elasticity theories overcome such disadvantages and help to provide more practical solutions.

Kong et al. [18] have presented analytical solutions for the free vibration of cantilever and simply-supported microbeams based on MCST. Civalek et al. [19] have investigated the effect of rotary inertia on the vibration frequencies of simply-supported (SS) carbon nanotubes based on MCST. In the study, the authors have obtained the frequencies of carbon nanotubes via Navier's solution. Akgöz and Civalek [20] have explored the free vibration of thick microbeams resting on a two-parameter elastic foundation using MCST and various beam theories. Thick

microbeams are considered in the study under thermal loads and SS boundary conditions. The authors have calculated the free vibration frequencies and critical temperature changes of microbeams modeled by four different beam theories using the Navier solution technique. Uzun et al. [21] have studied the free vibration of cantilever nanotube-based sensors with MCST and Rayleigh beam theory (RBT). Using a finite element (FE) solution, the authors have discussed the free vibration frequencies of single-walled carbon nanotube-based cantilever sensors. Tang et al. [22] have considered the MCST-based vibration of microbeams in flow and with clamped ends using the differential quadrature method. Hoai and Kien [23] have analyzed the nonlinear bending of cantilever microbeams with nonuniform crosssections by MCST and the nonlinear FE method. Alfred et al. [24] have investigated the nonlinear vibration of microbeams composed of functionally graded material in the context of MCST and with the effect of a three-parameter foundation model. The free vibration response of SS functionally graded composite Timoshenko microbeams based on MCST and moving mass effect has been demonstrated by a finite element method by Vu et al. [25]. Zhang and Liu [26] have used MCST to study the vibration of SS bi-directional functionally graded composite microbeams with pores in the cross-section. In the study, the authors have considered the dynamic response of porous bi-directional functionally graded composite microbeams using a novel third-order shear deformation theory and the finite element method. Rahi [27] has explored the vibrational frequencies of the multiple-layer microbeam in the context of MCST. Uzun and Yaylı [28] have presented the free vibration of silicon nanobeams with five different boundary conditions (simply-supported at both ends, clamped at both ends (CC), one end clamped and the other end simply-supported (CS), one simply-supported and the other end guided, one end clamped and the other end guided) and two different crosssection types based on modified stress couple theory and RBT using the FE method. The authors have mainly aimed to present how the guide boundary condition and the cross-section type affect the frequencies of silicon nanobeams in their studies and extra external effects have not been included. Ong et al. [29] have investigated the vibration of systems consisting of two microbeams based on MCST under different boundary conditions. The microbeams modeled by Euler-Bernoulli beam theory (EBBT) are connected to each other by springs and both analytical solutions and finite element simulations of microbeam systems are presented. Togun and Bağdatlı [30] have proposed the nonlinear vibration of Euler-Bernoulli nanobeams with different boundary conditions using MCST and the perturbation method. The stability of a cantilever laminated composite microbeam on a Winkler foundation has been investigated by Akbaş [31] using the MCST and the Ritz method. MCST is frequently used in the analysis of beam-type elements and has also been preferred by researchers for the analysis of small-sized rod [32], plate [33] and shell [34] elements. In addition to MCST, we also find studies [35-40] using other higher-order elasticity theories mentioned in the literature. As can be seen from the provided literature review, higher-order theories have been adopted in the analysis of various elements such as carbon nanotube, homogeneous nanobeam/microbeam, nanowire, functionally graded nanobeam/microbeam in porous and perfect forms, laminated composite microbeam, carbon nanotube-reinforced nanobeam/microbeam. Recently, short-fiber-reinforced nanobeams have been added to the list of small-scale elements whose mechanical response has been considered. However, since these are quite new in the literature, studies are limited. Gül [14] has indicated the transverse vibration of SFRC Euler-Bernoulli and Timoshenko nanobeams based on the nonlocal strain gradient theory and Ritz method. A semi-analytical solution for thermal vibration of embedded SFRC nanobeams constrained at both ends by deformable springs using nonlocal strain gradient theory and Stokes' transformation has been presented by Akpınar et al. [41]. The critical buckling loads of simply-supported short-fiberreinforced nanobeams have been discussed by Kafkas [42] using the nonlocal elasticity theory and three different beam theories. Gül [43] has explored the buckling loads of SFRC nanobeams at different boundary conditions using strain gradient theory and the Ritz method.

As can be understood, the analysis of short-fiber-reinforced small-sized beams based on higher-order elasticity theories is a relatively new subject. There is no study on the vibration analysis of short-fiber-reinforced microbeams embedded in an elastic medium based on MCST. This study aims to present an original contribution to the literature by addressing a previously unstudied issue of free vibration of embedded short-fiber-reinforced microbeams with a method based on MCST and finite element solution. In this work, the free vibration of randomly distributed short-fiber-reinforced microbeam (SFR-MB) is analyzed within the framework of MCST using Rayleigh beam theory. The

Winkler-Pasternak elastic medium effect is included in the analyses and the frequencies of the composite microbeam are calculated by the finite element method. The stiffness matrices and mass matrices of short-fiber-reinforced microbeams on the Winkler-Pasternak elastic medium are derived via a weighted residual method for the finite element analysis. It is shown that the finite element formulation considering a microbeam element with two nodes and a total of four degrees of freedom works properly by giving comparison studies with different publications in the literature. Then, the effects of Young's modulus ratio, mass density ratio, Winkler spring coefficient, Pasternak shear layer coefficient, short fiber volume fraction and material length scale parameter on the non-dimensional frequencies of short-fiber-reinforced microbeam are investigated for the case with simply-supported boundary condition. In addition to the detailed examination of the results of the simply-supported boundary condition, the frequency values of homogeneous microbeams presented in the literature under different boundary conditions are compared with those of short-fiber-reinforced microbeams. The results of the analyses are presented graphically and the variation of the non-dimensional frequencies is discussed to reflect the effects of different parameters.

2. Composite Materials Reinforced with Short Fibers

In this work, as mentioned before, the free vibration of composite microbeams reinforced with short fibers is investigated via the MCST-based finite element method and with the influences of rotary inertia, Pasternak elastic medium and size-dependency. The composite microbeam is considered with a matrix of rectangular cross-section and randomly oriented circular short fibers inside the section (Figure 1). The elastic properties of a composite are often predicted by micromechanical models based on the individual material and geometric properties of the composite. To determine the elastic properties of the SFRC microbeam, the Halpin-Tsai model [44] is used. This model, which is a semi-empirical method, takes into account the geometric properties and orientation of the filler, which is an important parameter for reinforcement efficiency [45]. Additionally, this study adopts the Halpin-Tsai model because this model contains simple and generalized equations to approximate the results of exact micromechanical analyses and can be easily used in the design process [10]. Based on the Halpin-Tsai equations, the following Young's modulus expressions for SFRC materials are written by [10]:

$$E_{1} = E_{m} \left(\frac{1 + V_{Sf} \left(\frac{2L_{Sf}}{d_{Sf}} \right) \frac{(E_{Sf}/E_{m}) - 1}{(E_{Sf}/E_{m}) + (2L_{Sf}/d_{Sf})}}{1 - V_{Sf} \frac{(E_{Sf}/E_{m}) - 1}{(E_{Sf}/E_{m}) + (2L_{Sf}/d_{Sf})}} \right)$$
(1)

$$E_{2} = E_{m} \left(\frac{1 + 2V_{sf} \left(\frac{\left(E_{sf}/E_{m}\right) - 1}{\left(E_{sf}/E_{m}\right) + 2}\right)}{1 - V_{sf} \left(\frac{\left(E_{sf}/E_{m}\right) - 1}{\left(E_{sf}/E_{m}\right) + 2}\right)} \right)$$
(2)

In the above expressions, E_1 and E_2 are the longitudinal and transverse Young's moduli of SFRC material, respectively. E_{sf} , V_{sf} , d_{sf} and L_{sf} specify the short fiber's Young's modulus, volume fraction, diameter and length, respectively. Lastly, E_m denotes the Young's modulus of the matrix material. Through the use of Eqs. (1) and (2), the Young's modulus of randomly oriented SFRC material (\bar{E}) is obtained as follows [10]:

$$\bar{E} = \frac{3E_1}{8} + \frac{5E_2}{8} \tag{3}$$

The mathematical procedure giving the Young's modulus of SFRC material is presented above. Based on E_1 and E_2 , the shear modulus of randomly oriented SFRC materials is written as follows [10]:

$$\bar{\mu} = \frac{E_1}{2} + \frac{E_2}{4}$$
 (4)

In Eq. (4), $\bar{\mu}$ is the shear modulus of randomly oriented SFRC material. In addition, mass density of the SFRC material ($\bar{\rho}$) is obtained via the rule of mixture presented by [10]:

$$\bar{\rho} = \rho_{sf} V_{sf} + \rho_m (1 - V_{sf}) \tag{5}$$

Where, ρ_m and ρ_{sf} are the mass densities of the matrix and short fibers, respectively.

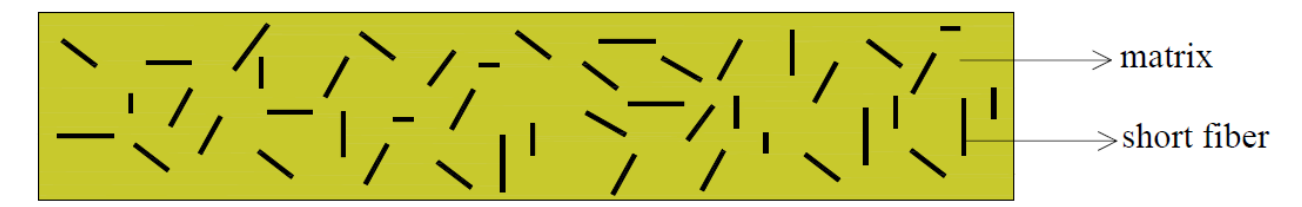


Fig. 1. Randomly oriented short-fiber-reinforced composite material.

3. Modified Couple Stress Theory for Vibration of SFR-MB

Yang et al. [15] have developed the MCST, a higher-order elasticity approach. This theory has been proposed by modifying the classical couple stress theory of Toupin [46], Mindlin and Tiersten [47] and Koiter [48]. To ensure that the couple stress tensor is symmetric, an additional balance condition is imposed on the moments of the couples, thus reducing the number of additional material length scale parameters from two to one in this theory. Therefore, the MCST has emerged as a more advantageous approach to capture the size effect in microstructures with only one material length scale parameter in addition to the Lamé constants [49, 50]. Since determining the material parameters is a challenging task, the single parameter of MCST becomes more advantageous and as can be understood from the literature review, MCST has been widely used by many scholars to develop the governing equations of microstructures and to study their mechanical behaviors. Therefore, this theory is preferred for the vibration of SFRC microbeams in this work. A microbeam's displacement fields based on EBBT can be written as [18]:

$$u_{r} = -z\partial_{r}w(x,t) \tag{6}$$

$$u_{\nu} = 0 \tag{7}$$

$$u_z = w(x, t) \tag{8}$$

Where, u_x , u_y and u_z are the x, y and z components of the displacement field, respectively. w(x,t) = w and t define the transverse displacements of any midline point and time, respectively. Also, $\partial_x w(x,t) = \partial w(x,t)/\partial x$. The frequencies of homogeneous and functionally graded microbeams based on MCST have been previously investigated by different studies in literature. However, the vibration of SFRC microbeams based on MCST has not been previously studied in the literature. The goal of this study is to fill this gap. In this study, the free vibration of SFRC microbeams under the effects of Winkler-Pasternak medium and rotary inertia will be investigated by MCST and the frequencies of the microbeam will be obtained by the FE method. Hamilton's principle can be applied to derive the equation of motion for the SFRC microbeam [51]:

$$\int_{t_{\star}}^{t_{2}} \left[\delta T - (\delta U - \delta W)\right] dt = 0 \tag{9}$$

In Eq. (9), δ specifies the variation operator, t_1 and t_2 denote the initial and finish times, respectively. T, U and W are the kinetic energy, strain energy and work done by elastic medium, respectively. MCST, which includes only one material length scale parameter, suggests that the strain energy density relies on both the strain tensor and the curvature tensor. The strain energy expression by neglecting Poisson's effect, derived by Kong et al. [18] for linear elastic isotropic materials takes the following form for short-fiber-reinforced materials:

$$U = \frac{1}{2} \int_0^{L_{MB}} \left[(\bar{E}I + \bar{\mu}Al_m^2) (\partial_{xx}w(x,t))^2 \right] dx$$

$$= \frac{1}{2} \int_0^{L_{MB}} \left[\left(\frac{3E_1}{2} + \frac{5E_2}{2} \right) I(\partial_{xx}w(x,t))^2 + \left(\frac{E_1}{2} + \frac{E_2}{4} \right) Al_m^2 (\partial_{xx}w(x,t))^2 \right] dx$$
(10)

It should be noted here that randomly oriented short-fiber-reinforced composites exhibit isotropic material properties [43]. In Eq. (10), L_{MB} , I and A are the length, moment of inertia and cross-sectional area of the short-fiber-reinforced microbeam, respectively. It should be noted that since the cross-section of the microbeam is rectangular, its height is h and its width is b. Also, l_m is the material length scale parameter. This parameter in the equation distinguishes MCST from classical theory and allows the size effect to be studied. Lastly, $\partial_{xx}w(x,t) = \partial^2 w(x,t)/\partial x^2$. The kinetic energy of the microbeam T can be defined as follows [19]:

$$T = \frac{1}{2} \int_0^{L_{MB}} \left[\bar{\rho} A(\partial_t w(x,t))^2 + \bar{\rho} I(\partial_{xt} w(x,t))^2 \right] dx \tag{11}$$

In which, $\partial_t w(x,t) = \partial w(x,t)/\partial t$ and $\partial_{xt} w(x,t) = \partial^2 w(x,t)/\partial x \partial t$. Lastly, the work done by the resultant forces due to the Winkler-Pasternak medium W can be written as below [20]:

$$W = \frac{1}{2} \int_0^{L_{MB}} [k_{sl}(\partial_x w(x,t))^2 - k_{ws} w(x,t)^2] dx$$
 (12)

In Eq. (12), k_{sl} and k_{ws} are the shear layer and subgrade springs' stiffnesses of the medium, respectively. The first variation of Eq. (9) can be given as follows:

$$\int_{t_{1}}^{t_{2}} \int_{0}^{L_{MB}} \left[\bar{\rho} A \partial_{t} w \delta \partial_{t} w + \bar{\rho} I \partial_{xt} w \delta \partial_{xt} w - \left(\frac{3E_{1}}{8} + \frac{5E_{2}}{8} \right) I \partial_{xx} w \delta \partial_{xx} w - \left(\frac{E_{1}}{8} + \frac{E_{2}}{4} \right) A l_{m}^{2} \partial_{xx} w \delta \partial_{xx} w + k_{sl} \partial_{x} w \delta \partial_{x} w - k_{sl} \partial_{x} w \delta \partial_{xx} w \right] dx dt = 0$$

$$(13)$$

By using partial integration and setting the δw to zero under the double integral, the free vibration equation of the SFRC microbeam based on the MCST, including rotary inertia and two-parameter elastic medium effects (see Figure 2), is obtained as follows [20]:

$$\left(\frac{3E_1}{8} + \frac{5E_2}{8}\right)I\partial_{xxxx}w + \left(\frac{E_1}{8} + \frac{E_2}{4}\right)Al_m^2\partial_{xxxx}w + \bar{\rho}A\partial_{tt}w - \bar{\rho}I\partial_{xxtt}w - k_{sl}\partial_{xx}w + k_{ws}w = 0$$
 (14)

Here, $\partial_{xxxx}w(x,t) = \partial^4w(x,t)/\partial x^4$ and $\partial_{xxtt}w(x,t) = \partial^4w(x,t)/\partial x^2\partial t^2$. Eq. (14) is the free vibration equation including the rotary inertia $(\bar{\rho}I)$ effect. This equation can be reduced to various sub-problems by neglecting some parameters. In this equation, the MCST-based vibration of embedded short-fiber-reinforced Euler-Bernoulli microbeams can be investigated by neglecting the rotary inertia effect, while the MCST-based vibration of short-fiber-reinforced Euler-Bernoulli microbeams in the non-embedded state can be investigated by neglecting both the rotary

inertia and elastic medium (k_{sl} and k_{ws}) effects. Neglecting only the shear layer (k_{sl}) effect in the equation, we obtain the equation governing the free vibration of SFRC Rayleigh microbeams in the Winkler elastic medium.

4. Finite Element Solution for Vibration of SFR-MB

In this section, a weighted residual-based FE approach is derived to analyze the free vibration frequencies of SFRC microbeams resting on the Winkler-Pasternak elastic medium, considering the effects of small-scale and rotary inertia. The short-fiber-reinforced microbeam is discretized into smaller microbeam elements for computational analysis. The number of these microbeam elements will be denoted as N^{MBE} in this study. Each microbeam element is modeled using two nodes, with two degrees of freedom per node, representing the transverse displacement and rotational angle. Therefore, each FE has four degrees of freedom in total. The node displacement vector, $\mathbf{w}^d = [w_i \quad \theta_i \quad w_j \quad \theta_j]^T$, represents the displacements and rotations at both ends (i and j points) of the microbeam element. The displacement field of the SFR-MB can be described using the shape function vector ζ derived from the physical behavior of the microbeam and the FE discretization. This shape function vector allows the approximation of both displacement and rotation of the SFR-MB at each nodal point, ensuring that boundary conditions and continuity between elements are satisfied. ζ can be given as:

$$\boldsymbol{\zeta} = \begin{bmatrix} \zeta_1 \\ \zeta_2 \\ \zeta_3 \\ \zeta_4 \end{bmatrix}^T \tag{15}$$

here, ζ_1 , ζ_2 , ζ_3 and ζ_4 are defined as follows [35, 52]:

$$\zeta_1 = 1 - \frac{3x^2}{L_{MBE}^2} + \frac{2x^3}{L_{MBE}^3} \tag{16}$$

$$\zeta_2 = x - \frac{2x^2}{L_{MBE}} + \frac{x^3}{L_{MBE}^2} \tag{17}$$

$$\zeta_3 = \frac{3x^2}{L_{MBE}^2} - \frac{2x^3}{L_{MBE}^3} \tag{18}$$

$$\zeta_4 = -\frac{x^2}{L_{MBE}} + \frac{x^3}{L_{MBE}^2} \tag{19}$$

In the shape functions given above, the length of each microbeam element is denoted by L_{MBE} . Using the shape functions, the vertical deflection of the microbeam can be represented as follows:

$$w = \zeta w^d = w_i \zeta_1 + \theta_i \zeta_2 + w_i \zeta_3 + \theta_i \zeta_4 \tag{20}$$

Based on the MCST, which incorporates the influences of Winkler-Pasternak elastic medium, small-scale and rotary inertia, the residual Γ required to acquire the weak form of the governing differential equation for free vibration is given by:

$$\Gamma = \left(\frac{3E_1}{8} + \frac{5E_2}{8}\right)I\partial_{xxxx}w + \left(\frac{E_1}{8} + \frac{E_2}{4}\right)Al_m^2\partial_{xxxx}w + \bar{\rho}A\partial_{tt}w - \bar{\rho}I\partial_{xxtt}w - k_{sl}\partial_{xx}w + k_{ws}w \tag{21}$$

By selecting the shape functions as weighting functions, we can formulate the differential equation in its weighted integral form. This involves multiplying the residual Γ by these weighting functions and integrating the result over the entire length of the microbeam.

$$\int_{0}^{L_{MBE}} \left(\boldsymbol{\zeta}^{T} \left(\frac{3E_{1}}{8} + \frac{5E_{2}}{8} \right) I \partial_{xxxx} w + \boldsymbol{\zeta}^{T} \left(\frac{E_{1}}{8} + \frac{E_{2}}{4} \right) A l_{m}^{2} \partial_{xxxx} w + \boldsymbol{\zeta}^{T} \bar{\rho} A \partial_{tt} w \right) dx = 0$$

$$- \boldsymbol{\zeta}^{T} \bar{\rho} I \partial_{xxtt} w - \boldsymbol{\zeta}^{T} k_{sl} \partial_{xx} w + \boldsymbol{\zeta}^{T} k_{ws} w$$

$$(22)$$

By applying integration by parts to Eq. (22) and utilizing the chain rule, we obtain the general form:

$$\int_{0}^{L_{MBE}} \left(\left(\frac{3E_{1}}{8} + \frac{5E_{2}}{8} \right) I d_{xx} \boldsymbol{\zeta}^{T} d_{xx} \boldsymbol{\zeta} \boldsymbol{w}^{d} + \left(\frac{E_{1}}{8} + \frac{E_{2}}{4} \right) A l_{m}^{2} d_{xx} \boldsymbol{\zeta}^{T} d_{xx} \boldsymbol{\zeta} \boldsymbol{w}^{d} + \bar{\rho} A \boldsymbol{\zeta}^{T} \boldsymbol{\zeta} \ddot{\boldsymbol{w}}^{d} \right) dx = 0$$

$$+ \bar{\rho} I d_{x} \boldsymbol{\zeta}^{T} d_{x} \boldsymbol{\zeta} \ddot{\boldsymbol{w}}^{d} + k_{sl} d_{x} \boldsymbol{\zeta}^{T} d_{x} \boldsymbol{\zeta} \boldsymbol{w}^{d} + k_{ws} \boldsymbol{\zeta}^{T} \boldsymbol{\zeta} \boldsymbol{w}^{d}$$

$$(23)$$

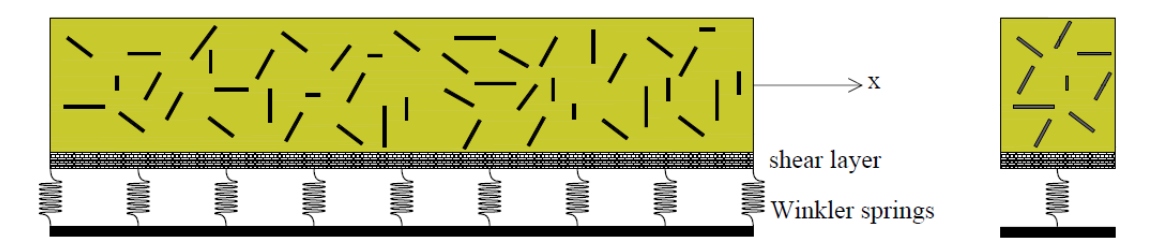


Fig. 2. Short-fiber-reinforced microbeam resting on Pasternak medium.

In which, $d_{xx}\zeta^T = d^2\zeta^T/dx^2$, $d_x\zeta^T = d\zeta^T/dx$, $d_{xx}\zeta = d^2\zeta/dx^2$, $d_x\zeta = d\zeta/dx$ and $\ddot{w^d} = d^2w^d/dt^2$. Matrix motion formulation of SFRC microbeam elements can be written as $(K^C + K^M + K^W + K^P)w^d + (M^A + M^I)\ddot{w^d} = 0$. To derive the mass and stiffness matrices of the short-fiber-reinforced microbeam, we substitute the shape functions from Eqs. (16)-(19) into Eq. (23) and perform the integrations term by term. The resulting matrices are defined as below:

$$K^{C} = \int_{0}^{L_{MBE}} \left(\frac{3E_{1}}{8} + \frac{5E_{2}}{8} \right) I d_{xx} \zeta^{T} d_{xx} \zeta dx = \frac{\left(\frac{3E_{1}}{8} + \frac{5E_{2}}{8} \right) I}{L_{MBE}^{3}} \begin{bmatrix} 12 & 6L_{MBE} & -12 & 6L_{MBE} \\ 6L_{MBE} & 4L_{MBE}^{2} & -6L_{MBE} & 2L_{MBE}^{2} \\ -12 & -6L_{MBE} & 12 & -6L_{MBE} \\ 6L_{MBE} & 2L_{MBE}^{2} & -6L_{MBE} & 4L_{MBE}^{2} \end{bmatrix}$$
(24)

$$K^{M} = \int_{0}^{L_{MBE}} \left(\frac{E_{1}}{8} + \frac{E_{2}}{4}\right) A l_{m}^{2} d_{xx} \zeta^{T} d_{xx} \zeta dx = \frac{\left(\frac{E_{1} + \frac{E_{2}}{8}\right) A l_{m}^{2}}{L_{MBE}^{3}}}{L_{MBE}^{3}} \begin{bmatrix} 12 & 6L_{MBE} & -12 & 6L_{MBE} \\ 6L_{MBE} & 4L_{MBE}^{2} & -6L_{MBE} & 2L_{MBE}^{2} \\ -12 & -6L_{MBE} & 12 & -6L_{MBE} \\ 6L_{MBE} & 2L_{MBE}^{2} & -6L_{MBE} & 4L_{MBE}^{2} \end{bmatrix}$$
(25)

$$K^{W} = \int_{0}^{L_{MBE}} k_{ws} \zeta^{T} \zeta dx = \frac{k_{ws}}{420} \begin{bmatrix} 156L_{MBE} & 22L_{MBE}^{2} & 54L_{MBE} & -13L_{MBE}^{2} \\ 22L_{MBE}^{2} & 4L_{MBE}^{3} & 13L_{MBE}^{2} & -3L_{MBE}^{3} \\ 54L_{MBE} & 13L_{MBE}^{2} & 156L_{MBE} & -22L_{MBE}^{2} \\ -13L_{MBE}^{2} & -3L_{MBE}^{3} & -22L_{MBE}^{2} & 4L_{MBE}^{3} \end{bmatrix}$$
 (26)

$$K^{P} = \int_{0}^{L_{MBE}} k_{sl} d_{x} \zeta^{T} d_{x} \zeta dx = \frac{k_{sl}}{30L_{MBE}} \begin{bmatrix} 36 & 3L_{MBE} & -36 & 3L_{MBE} \\ 3L_{MBE} & 4L_{MBE}^{2} & -3L_{MBE} & -L_{MBE}^{2} \\ -36 & -3L_{MBE} & 36 & -3L_{MBE} \\ 3L_{MBE} & -L_{MBE}^{2} & -3L_{MBE} & 4L_{MBE}^{2} \end{bmatrix}$$

$$(27)$$

$$M^{A} = \int_{0}^{L_{MBE}} \bar{\rho} A \zeta^{T} \zeta dx = \frac{\bar{\rho} A}{420} \begin{bmatrix} 156L_{MBE} & 22L_{MBE}^{2} & 54L_{MBE} & -13L_{MBE}^{2} \\ 22L_{MBE}^{2} & 4L_{MBE}^{3} & 13L_{MBE}^{2} & -3L_{MBE}^{3} \\ 54L_{MBE} & 13L_{MBE}^{2} & 156L_{MBE} & -22L_{MBE}^{2} \\ -13L_{MBE}^{2} & -3L_{MBE}^{3} & -22L_{MBE}^{2} & 4L_{MBE}^{3} \end{bmatrix}$$
 (28)

$$M^{I} = \int_{0}^{L_{MBE}} \bar{\rho} I d_{x} \zeta^{T} d_{x} \zeta dx = \frac{\bar{\rho}I}{30L_{MBE}} \begin{bmatrix} 36 & 3L_{MBE} & -36 & 3L_{MBE} \\ 3L_{MBE} & 4L_{MBE}^{2} & -3L_{MBE} & -L_{MBE}^{2} \\ -36 & -3L_{MBE} & 36 & -3L_{MBE} \\ 3L_{MBE} & -L_{MBE}^{2} & -3L_{MBE} & 4L_{MBE}^{2} \end{bmatrix}$$
 (29)

As can be seen from Eqs. (24)-(29), the short-fiber-reinforced microbeam has four stiffness and two mass matrices. In these equations, K^C and M^A are stiffness and mass matrices derived from classical (local) beam theory. The matrix K^M , associated with the MCST, incorporates the material length scale parameter. If K^M is neglected, the FE solution reduces to the RBT based on classical mechanics. The matrix K^W results from the Winkler medium, while K^P arises due to the Pasternak shear layer effect. Lastly, the matrix M^I represents the influence of rotary inertia on the free vibration of the SFRC microbeam.

In order to calculate the free vibration frequencies of a SFR-MB resting on the Winkler-Pasternak elastic medium using the FE method and to consider small-scale and rotary inertia effects, it is necessary to determine the total mass and stiffness matrices. The microbeam finite element stiffness matrix is given by $K^{MBE} = K^C + K^M + K^W + K^P$, and the microbeam finite element mass matrix is $M^{MBE} = M^A + M^I$. After calculating the microbeam finite element stiffness and mass matrices, the global stiffness and mass matrices of SFR-MB are established. Lastly, the boundary conditions for the short-fiber-reinforced microbeam are applied. The supports at the ends of the microbeam make the rotation and/or deflection zero. While the deflection is equalized to zero at the points where the simply-supported end, both the deflection and rotation are zero at the points where the clamped support is located. On the other hand, no restriction is made in the case that there is no support at the end of the microbeam. Then, the free vibration solution of the microbeam can be described as:

$$\left| \sum_{e=1}^{N^{MBE}} K^{MBE} - \omega_n^2 \sum_{e=1}^{N^{MBE}} M^{MBE} \right| = 0 \tag{30}$$

Here, N^{MBE} is the finite element number, ω is the circular frequency of the short-fiber-reinforced microbeam and n is the mode number.

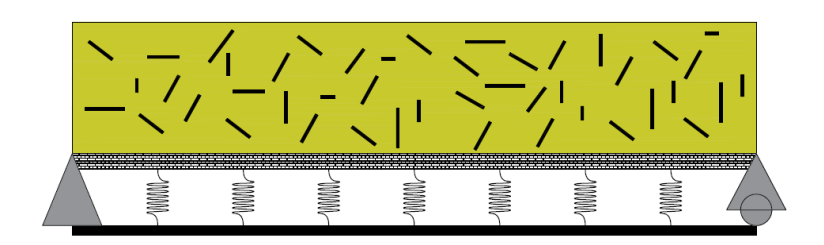


Fig. 3. Simply-supported short-fiber-reinforced microbeam resting on Pasternak medium.

5. Results and Discussion

In this section, the numerical findings on the free vibration frequencies of short-fiber-reinforced microbeams resting on Winkler-Pasternak elastic medium by incorporating rotary inertia effects and small-scale effects based on MCST are discussed. In this study, where the solution based on the FE method is given, comparative analyses are performed to validate the FE solutions at first. Then, the influences of different parameters on the vibration behavior of the microbeams are evaluated. As a result of the analyses, the following non-dimensional quantities are given for use in figures and tables:

$$\beta_n = \omega_n L_{MB}^2 \sqrt{\frac{\rho_{mA}}{E_{mI}}} \tag{31}$$

$$\lambda_{ws} = \frac{k_{ws}L_{MB}^4}{E_{mI}} \tag{32}$$

$$\lambda_{sl} = \frac{k_{sl}L_{MB}^2}{E_{ml}} \tag{33}$$

Here, β_n , λ_{ws} and λ_{sl} are the non-dimensional frequency, Winkler spring coefficient and Pasternak shear layer coefficient, respectively.

Firstly, various comparison and validation studies are presented. The geometric and material parameters used for the validation studies given in Tables 1 and 2 are as follows: E = 1.44 GPa, v = 0.38, h = b/2, $\rho = 1220$ kg/m³ and $l_m = 17.6$ μ m. Table 1 shows a comparison study for nanobeams based on MCST and rotary inertia effect, but without elastic foundation effects. For a simply-supported homogeneous nanobeam, the non-dimensional frequency $(\bar{\omega}_n)$ according to MCST, including the rotary inertia effect, is given by Civalek et al. [19]:

$$\overline{\omega}_{n} = \frac{n^{2}\pi^{2}}{L_{MB}^{2}} \sqrt{\frac{EI + \mu Al_{m}^{2}}{\rho_{A} + \rho_{I} \frac{n^{2}\pi^{2}}{L_{MB}^{2}}} L_{MB}^{2} \sqrt{\frac{\rho_{A}}{EI}}}$$
(34)

Table 1 presents the dimensionless frequencies obtained from Eq. (34) of Civalek et al. [19] and the finite element method using different element numbers (N^{MBE}) varying from 10 to 80. The microbeam parameters are set as $L_{MB} = 6h$ and $h = l_m$. To neglect elastic medium effects, λ_{ws} and λ_{sl} are taken as zero in the finite element method.

Table 1. Comparison of dimensionless frequencies for a SS homogeneous modified couple stress beam without elastic medium effects (RBT).

n	Ea. (34)	This study	Difference	This study	Difference (%)	This study	Difference (%)	This study	Difference (%)
""	Eq. (51)	Tins study	Difference	Tins study	Birrerence (70)	Tins stady	Difference (70)	Tins stady	Difference (70)

		$N^{MBE}=10$	(%)	$N^{MBE}=20$		$N^{MBE}=30$		$N^{MBE} = 40$		
1	22.5675	22.5676	0.0004	22.5675	0.0000	22.5675	0.0000	22.5675	0.0000	
2	87.3895	87.3989	0.0108	87.3901	0.0007	87.3896	0.0001	87.3896	0.0001	
3	187.0795	187.1792	0.0533	187.0859	0.0034	187.0808	0.0007	187.0795	0.0000	
4	312.5043	313.0175	0.1642	312.5377	0.0107	312.5109	0.0021	312.5064	0.0007	
5	455.2170	456.9823	0.3878	455.3346	0.0258	455.2406	0.0052	455.2245	0.0016	
	Eq. (24)	This study	Difference	This study	Difference	This study	Difference	This study	Difference	
n	Eq. (34)	$N^{MBE}=50$	(%)	$N^{MBE} = 60$	(%)	$N^{MBE} = 70$	(%)	$N^{MBE} = 80$	(%)	
1	22.5675	22.5675	0.0000	22.5675	0.0000	22.5675	0.0000	22.5675	0.0000	
2	87.3895	87.3895	0.0000	87.3895	0.0000	87.3895	0.0000	87.3895	0.0000	
3	187.0795	187.0795	0.0000	187.0795	0.0000	187.0795	0.0000	187.0795	0.0000	
4	312.5043	312.5052	0.0003	312.5047	0.0001	312.5045	0.0001	312.5044	0.0000	
5	455.2170	455.2201	0.0007	455.2185	0.0003	455.2178	0.0002	455.2175	0.0001	

The results in Table 1 show that the exact solutions provided by Civalek [19] and the solution given by the finite element method are closely matched. The first mode frequencies show a remarkable agreement for all other element numbers except $N^{MBE} = 10$, confirming the accuracy of the FE model for low vibration modes. For higher modes, small discrepancies are observed when fewer elements are used. However, these differences decrease significantly as the number of finite elements increases. At $N^{MBE} = 80$, the FE results are same to the results of Eq. (34) for the first four modes. Since this study will not address high vibration modes, it is deemed appropriate for the finite element number to be 50 ($N^{MBE} = 50$).

Akgöz and Civalek [20] have examined the thermo-elastic vibration behavior of microbeams resting on Winkler-Pasternak elastic medium using the MCST. They have based their analyses on various beam theories, such as EBBT, parabolic, Timoshenko, and sinusoidal beam theories. For comparison, the focus here is on the results obtained using the EBBT while neglecting temperature variations. In the present validation study, the mass matrix M^I associated with rotary inertia is neglected. The comparison of the non-dimensional natural frequencies is presented in Table 2. The parameters used in this analysis are $L_{MB}=30h$, $\lambda_{WS}=200$, and $\lambda_{SI}=20$.

Table 2. Comparison of dimensionless frequencies for a SS homogeneous microbeam resting on the Winkler-Pasternak medium ($L_{MB}=30h$, $\lambda_{ws}=200$, $\lambda_{sl}=20$, EBBT).

	L /1		This stud	dy, Eq. (30)			D-f [20]	Difference
n	h/l_m	$N^{MBE}=10$	$N^{MBE}=20$	$N^{MBE}=30$	$N^{MBE}=40$	$N^{MBE}=50$	Ref. [20]	(‰)
1		30.3039	30.3038	30.3038	30.3038	30.3038	30.3038	0
2	1	96.5722	96.5635	96.5630	96.5630	96.5629	96.5629	0
3		210.2778	210.1773	210.1718	210.1709	210.1706	210.1704	0.00095
1		23.2779	23.2779	23.2779	23.2779	23.2779	23.2779	0
2	3	57.4589	57.4549	57.4547	57.4546	57.4546	57.4546	0
3		117.0080	116.9578	116.9550	116.9546	116.9545	116.9544	0.00086
1		22.5070	22.5070	22.5070	22.5070	22.5070	22.5070	0
2	6	52.3137	52.3103	52.3101	52.3101	52.3101	52.3101	0
3		104.0628	104.0201	104.0178	104.0174	104.0173	104.0172	0.00096
1	10	22.3392	22.3391	22.3391	22.3391	22.3391	22.3391	0

2	51.1491	51.1459	51.1457	51.1457	51.1456	51.1456	0
3	101.0869	101.0459	101.0437	101.0433	101.0432	101.0431	0.00099

The results in Table 2 show a strong correlation between the FE solutions in this study and the findings of Akgöz and Civalek [20]. The dimensionless frequencies for various modes and h/l_m ratios show excellent agreement in the finite element solutions, especially at high element numbers. This consistency confirms the validity of the finite element model when elastic medium effects are included and rotary inertia is neglected. For the first mode, the frequencies are almost the same for all methods and element numbers, indicating that the lower modes are less sensitive to the discretization level in the finite element analysis. Small differences appear in higher modes when fewer elements ($N^{MBE} = 10$) are used, but these differences decrease as the number of finite elements increases. At $N^{MBE} = 50$, the FE results satisfactorily converge to the reference values provided by Ref. [20].

Figures 4 and 5 compare the dimensionless frequencies of SFRC microbeams with those of homogeneous microbeams (H-MBs) in the literature for different boundary conditions. The article presented by Togun and Bağdatlı [30] is taken as a reference for these two figures. In these figures, the dimensionless frequencies of homogeneous and SFRC beams with CC, SS and CS are shown according to the changing material length scale parameter. The properties of short-fiber-reinforced microbeams for these figures are as follows: $V_{sf} = 0.1$, $h = 17.6 \, \mu m$, $L_{sf}/d_{sf} = 3$, b = 2h, $L_{MB} = 25h$, $\lambda_{WS} = \lambda_{sl} = 0$. Additionally, the E_{sf}/E_m and ρ_{sf}/ρ_m values for Figure 4 and Figure 5 are as follows, respectively: $E_{sf}/E_m = 10 \, \& \rho_{sf}/\rho_m = 1$, $E_{sf}/E_m = 1 \, \& \rho_{sf}/\rho_m = 2$.

Figure 4 shows us that the frequencies of microbeams reinforced with short fibers having high Young's modulus are higher than those of homogeneous microbeams. This is because the stiffness of the microbeam increases with fiber reinforcement. On the other hand, the frequencies of matrices reinforced with short fibers having high mass density are lower than those of homogeneous microbeams. The increased mass density of the microbeam explains this. On the other hand, when the boundary conditions are compared, it is clearly seen that the highest frequencies are obtained for CC while the lowest are obtained for SS. Although the frequency ratios of homogeneous and reinforced microbeams are equal under all boundary conditions, it is understood that the ease of observing the difference between the frequency differences increases as the boundary condition becomes stiffer. It is also understood from the results given in these figures that short-fiber-reinforced microbeams are slightly more affected by the change of the material length scale parameter.

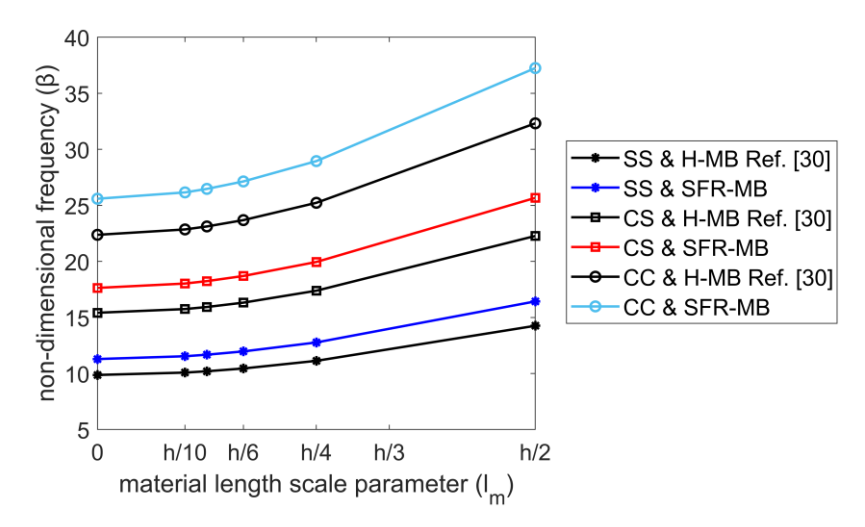


Fig. 4. Comparison of homogeneous and short-fiber-reinforced microbeams' frequencies for different boundary conditions with $\rho_{sf}/\rho_m=1$ & $E_{sf}/E_m=10$ (EBBT).

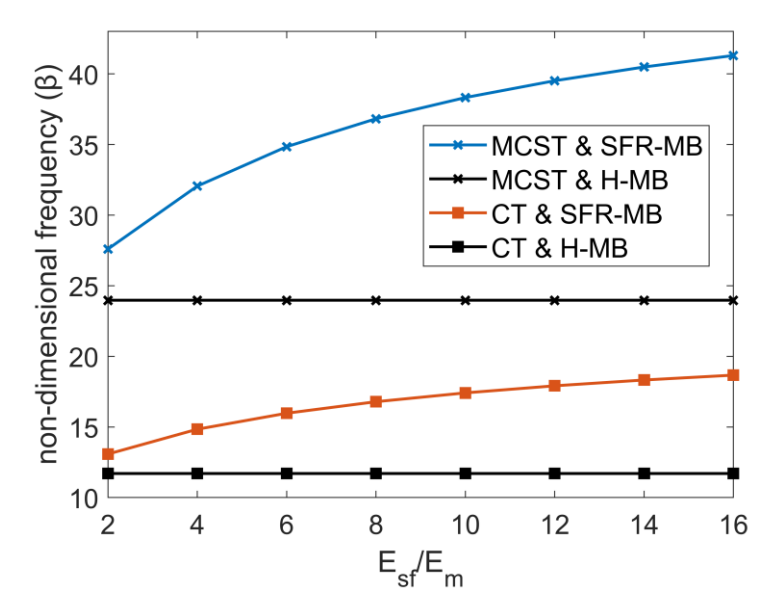


Fig. 5. Comparison of homogeneous and short-fiber-reinforced microbeams' frequencies for different boundary conditions with $\rho_{sf}/\rho_m=2$ & $E_{sf}/E_m=1$ (EBBT).

To validate the accuracy and reliability of the finite element model utilized in this study, foundational studies from the literature examining the vibration behavior of microbeams based on MCST are specifically chosen. Reference studies are broadly accepted within academic circles, demonstrating strong alignment with the present research in terms of theoretical frameworks, applied boundary conditions, and material/geometric configurations. Consequently, the outcomes of these studies are employed for validation analyses, robustly confirming the validity of the presented finite element model.

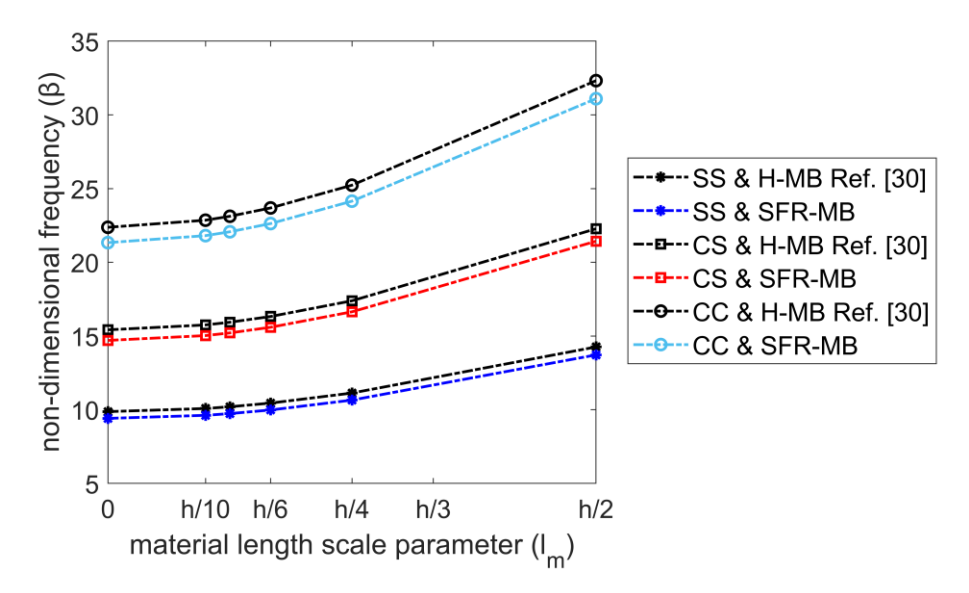


Fig. 6. Effect of E_{sf}/E_m for different theories $(\rho_{sf}/\rho_m = 1)$.

In the next stage of the study, the free vibration frequencies of simply-supported SFRC microbeams will be investigated in the light of various effects. These effects are fiber Young's modulus, fiber volume ratio, fiber mass density, material length scale parameter, shear layer, and subgrade springs' stiffnesses. The analyses based on the MCST are performed with $l_m = 17.6 \, \mu m$ and the analyses based on classical theory are realized with $l_m = 0$, unless otherwise stated. $V_{sf} = 0.4$, $h = 17.6 \, \mu m$, b = 2h, $L_{MB} = 25h$, $L_{sf}/d_{sf} = 5$, $\lambda_{ws} = 20$, $\lambda_{sl} = 2$ are considered in this study unless otherwise specified. In this study, the effect of short fiber reinforcements on the frequencies of microbeams is investigated by keeping the matrix properties constant and varying the fiber properties. For this purpose, the effect of different values of E_{sf}/E_m and ρ_{sf}/ρ_m are discussed throughout the study. But, for investigations the effects of other parameters are considered with $E_{sf}/E_m = 10$ and $\rho_{sf}/\rho_m = 2$.

Figure 6 demonstrates the effects of the ratio E_{sf}/E_m on the frequencies based on both CT and MCST. Furthermore, for the microbeam where both E_{sf}/E_m and ρ_{sf}/ρ_m are equal to 1, i.e., the homogeneous microbeam, the frequencies based on both CT and MCST are plotted for an effective comparison. E_{sf}/E_m is considered in eight different values from 2 to 16 in this figure. The point to be emphasized here is which theory is more affected by the variation of the E_{sf}/E_m ratio. Looking at the curves representing short-fiber-reinforced microbeams, it can be seen that the increase in MCST is higher. To express this situation in more detail and numerically, the following result can be stated: The ratio of the frequencies obtained for $E_{sf}/E_m = 16$ to the frequencies of the homogeneous microbeam is 1.72 for MCST and 1.6 for CT. In other words, the frequencies obtained for short-fiber-reinforced microbeam and $E_{sf}/E_m = 16$ are 72% higher than the frequencies of homogeneous microbeam in the size-effective case, while the frequencies obtained for short-fiber-reinforced microbeam and $E_{sf}/E_m = 16$ are 60% higher than the frequencies of homogeneous microbeam in the size-independent case. In addition, although the variation of E_{sf}/E_m is in equal ranges, the increases in frequencies are not linear. The curve tends to flatten as the E_{sf}/E_m value increases. In other words, changing E_{sf}/E_m at higher values affects the frequencies less.

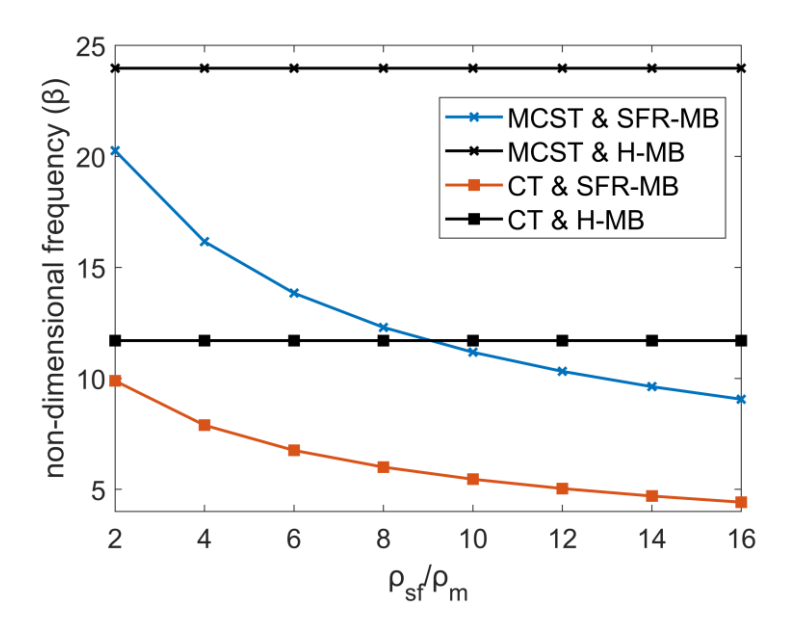


Fig. 7. Effect of ρ_{sf}/ρ_m for different theories $(E_{sf}/E_m = 1)$.

In Figure 7, the effects of ρ_{sf}/ρ_m ratio on the free vibration frequencies based on both CT and MCST are presented. ρ_{sf}/ρ_m is investigated in eight different values from 2 to 16 in this figure. As noticed earlier, the frequencies of homogeneous micro-sized beams are higher than the frequencies of short fiber reinforced microbeams due to the increased microbeam mass density due to the increase of ρ_{sf} . This decrease is also clearly noticeable in both the size-dependent and the size-independent cases. Again, similar to the effect of E_{sf}/E_m , the decrease in frequencies is not linear, although the variation of ρ_{sf}/ρ_m is in equal ranges.

Figures 8 and 9 show the dimensionless vibration frequencies for both CT and MCST in the first and second vibration modes, respectively. These figures investigate the effects of shear layer and subgrade springs' stiffnesses with parameters λ_{sl} and λ_{ws} varying from 20 to 160. In both graphs, the increase in the non-dimensional frequencies of the SFR-MB with increasing value of λ_{sl} is clearly visible. In fact, the increase in the value of λ_{ws} also leads to an inflation in the dimensionless frequencies of the SFR-MB. This increase is clearly visible in the graphs only for mode 1 and CT. The interpretations that can be clearly made from these two figures are as follows: λ_{sl} has a much larger effect on the dimensionless frequencies of the SFR-MB than λ_{ws} . When the frequency changes of the first and second modes are analyzed, the change of the medium parameters affects the frequencies in the first mode more. Finally, increasing the medium parameters causes the frequencies of the CT to increase more than the frequencies of the MCST. Figures 10-13 are drawn to illustrate these effects in more detail. These figures show the frequency ratios of the first mode of MCST, the first mode of CT, the second mode of MCST and the second mode of CT, respectively, and the frequency ratios are calculated as follows:

$$frequency\ ratio = \frac{\beta_n \ for\ \lambda_{WS} \ge 40}{\beta_n \ for\ \lambda_{WS} = 20}$$
(35)

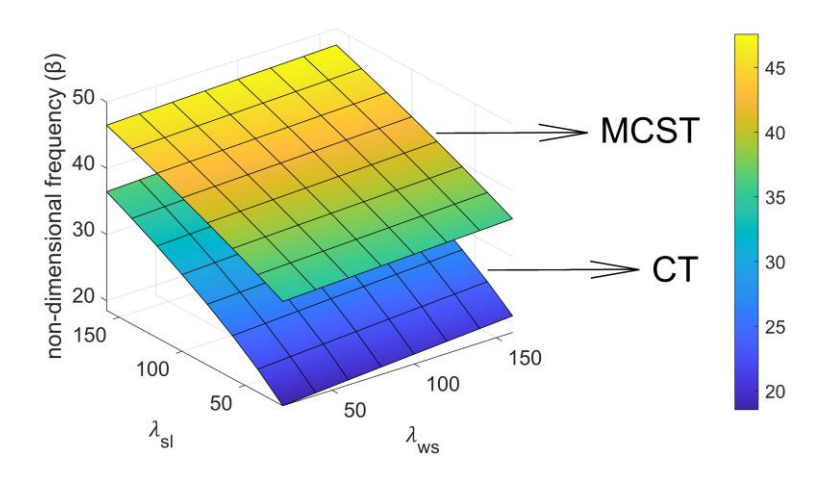


Fig.8. Effect of λ_{sl} and λ_{ws} for different theories (1st mode).

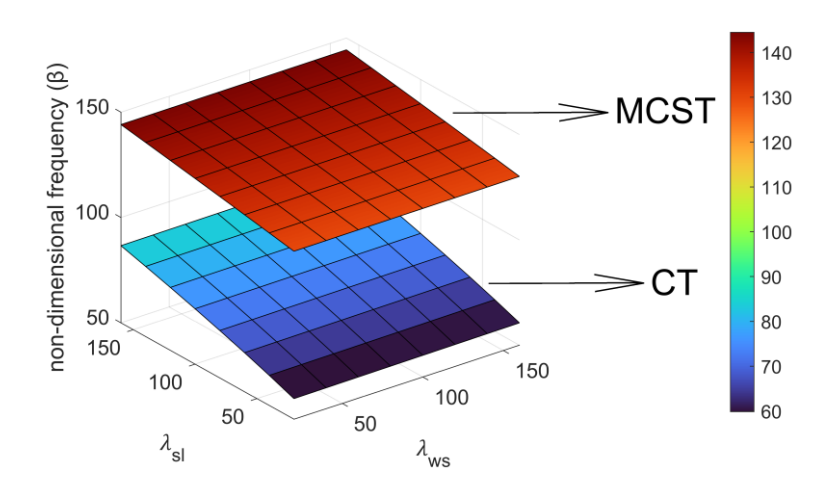


Fig. 9. Effect of λ_{sl} and λ_{ws} for different theories (2nd mode).

The focus of Figures 10-13 is to present the effect of subgrade springs' stiffnesses in a more understandable way for different shear layer stiffnesses and mode numbers. Figures 10 and 11 plot the first mode frequency ratios of the short-fiber-reinforced microbeam based on MCST and CT, respectively for different λ_{sl} versus λ_{ws} ranging from 40 to 160. The first thing to notice in these figures is that the frequency ratios decrease as λ_{sl} increases. This means that as λ_{sl} increases, the effect of λ_{ws} on the non-dimensional frequencies of the SFRC microbeam decreases.

Additionally, the frequency ratios of the CT are higher than the frequency ratios of the MCST. This is because, as mentioned before, the elastic medium has more influence on the analysis performed with the CT.

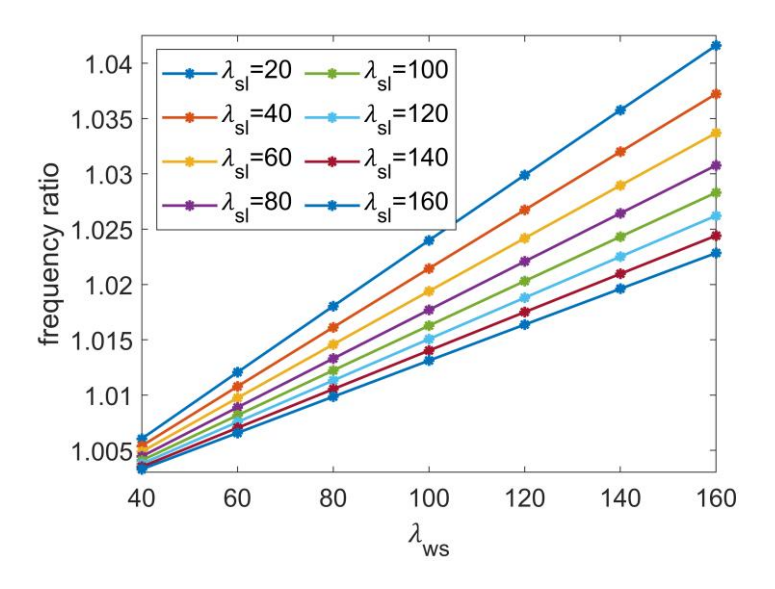


Fig. 10. Variation of frequency ratio for MCST (1st mode).

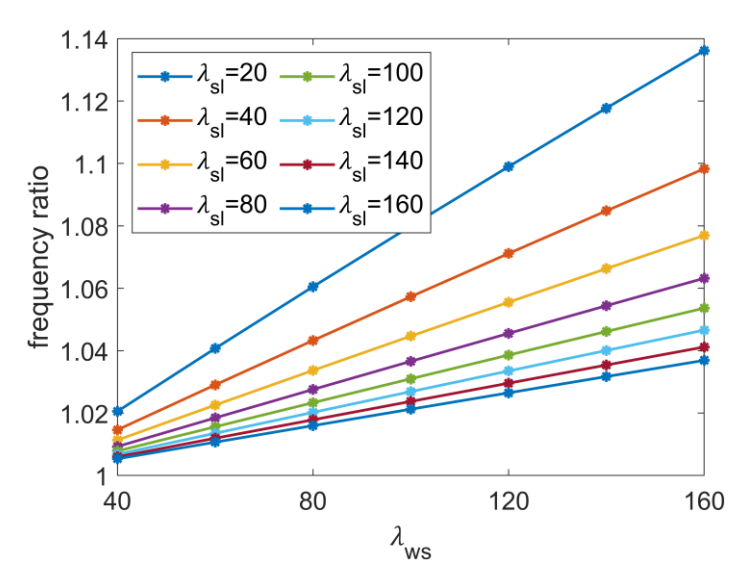


Fig. 11. Variation of frequency ratio for CT (1st mode).

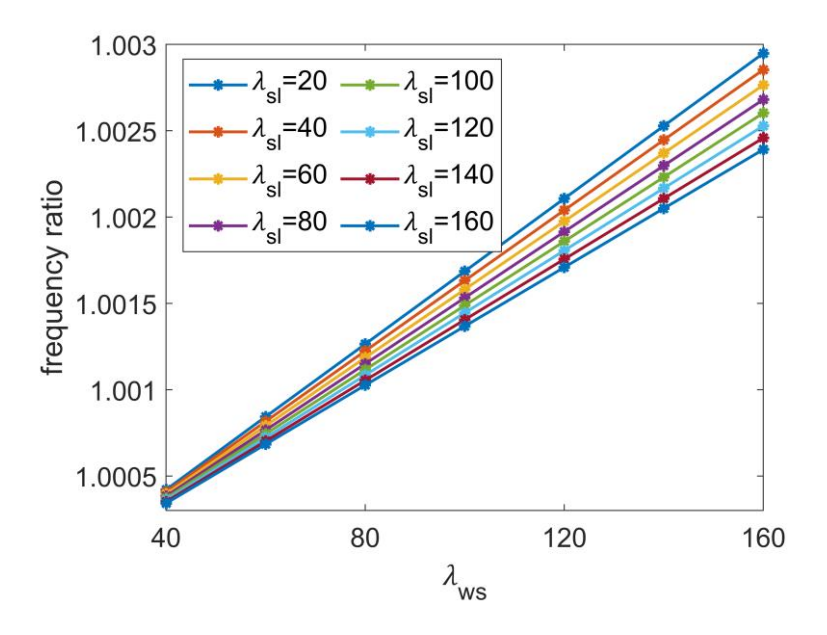


Fig. 12. Variation of frequency ratio for MCST (2nd mode).

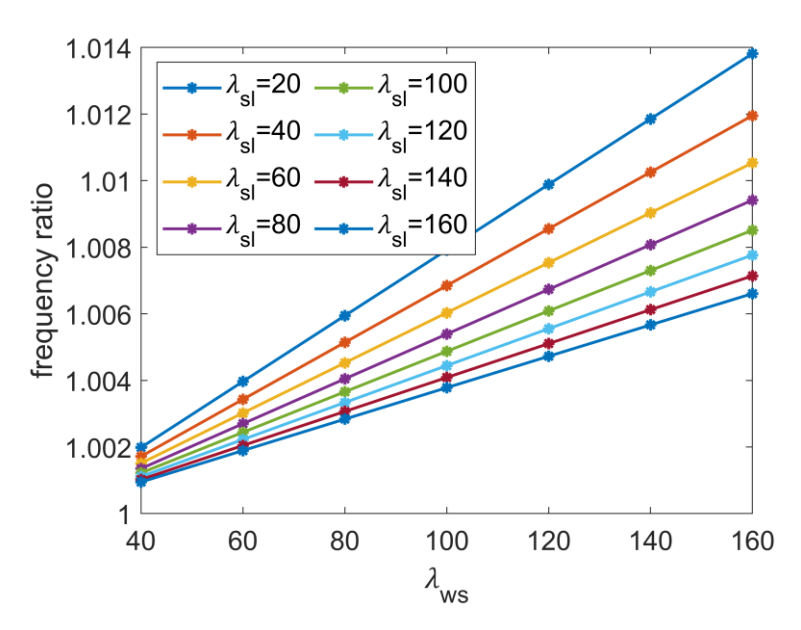


Fig. 13. Variation of frequency ratio for CT (2^{nd} mode).

In Figure 14, the effect of l_m is examined for the first three modes. Eight different material length scale parameters ranging from 0.25h μm to 2h μm are considered and the dimensionless frequencies of the classical theory are also plotted. As is well known, when $l_m=0$, the frequencies are reduced to the CT. It is clear from the figure that increasing l_m results in an increase in the dimensionless frequencies of the SFR-MB. This increase is lowest for the

first vibration mode and highest for the third vibration mode. So, it follows that the influence of l_m increases as the mode number increases.

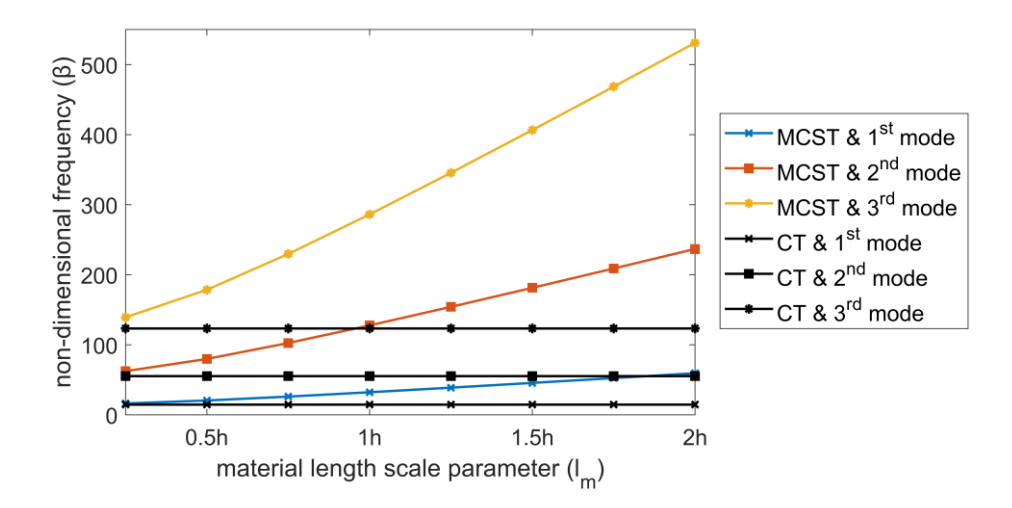


Fig. 14. Effect of l_m for different mode numbers.

In Figure 15, the effect of short fiber volume fraction is investigated for the first mode and for different medium types. For Winkler medium, $\lambda_{ws} = 20$ is considered while for Pasternak medium $\lambda_{ws} = 20$ & $\lambda_{sl} = 2$. As the stiffness of the microbeam increases with the increment in short fiber volume fraction, there is a significant increase in frequencies and this increase is valid for all cases. What is noteworthy here is the change in the frequency difference between different medium types with increasing fiber volume fraction. In the case where V_{sf} is 0.1, the difference between the frequencies for the three cases examined is significant, while it is understood that these differences decrease with increasing V_{sf} . As V_{sf} increases, all frequency values start to approach the frequencies obtained for Pasternak medium. It is clear from this that the increase in short fiber volume fraction is a more important parameter for microbeams without medium effect.

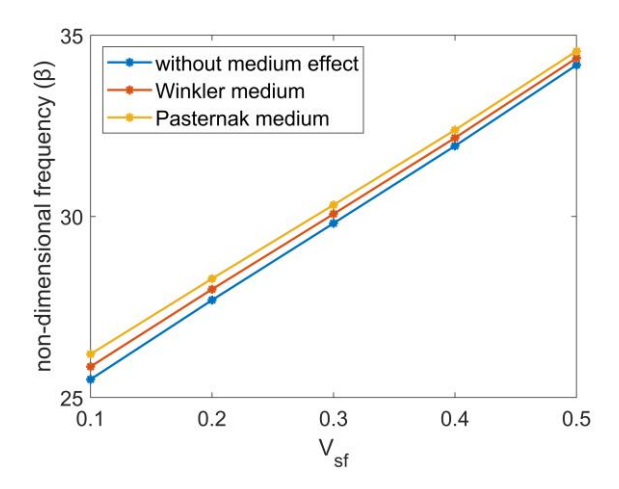


Fig. 15. Effect of V_{sf} for different medium types.

As it is known, the study also takes into account the rotary inertia effects. The frequencies given so far have been calculated together with the rotary inertia effect. In Figure 16, the frequency ratios of SFR-MBs are given for the first three modes and microbeam lengths ranging from $10h \ \mu m$ to $40h \ \mu m$ to show the rotary inertia effect. The frequency ratios are obtained as follows:

$$frequency\ ratio = \frac{\beta_n\ for\ EBBT}{\beta_n\ for\ RBT} \tag{36}$$

The frequency ratios being greater than one means that the frequencies obtained with EBBT are higher than those obtained with RBT. In other words, not considering the rotary inertia effect causes us to calculate the frequencies slightly higher. There are two remarkable situations in this analysis. These are the effects of rotary inertia on the vibration mode and the microbeam length. As can be seen, increasing the mode number also causes the frequency ratios to rise. This means that the difference between the frequencies of RBT and EBBT is higher in the high modes, meaning that rotary inertia is more effective in the high modes. However, increasing the microbeam length causes the frequency ratios to decrease, meaning that the frequency values of RBT and EBBT come closer to each other. This shows that the effect of rotary inertia decreases as the microbeam length increases.

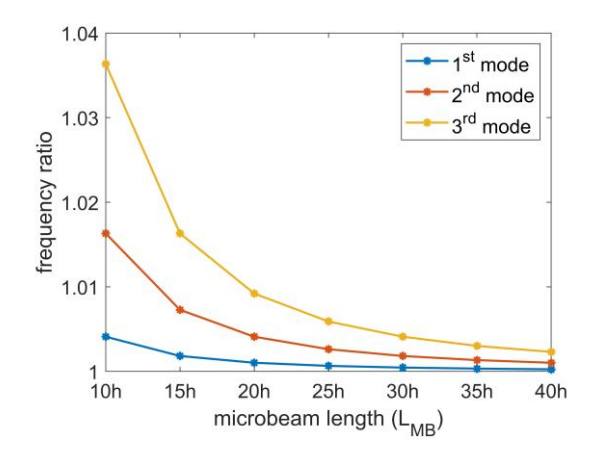


Fig. 16. Effect of rotary inertia versus microbeam length.

6. Conclusions

In this paper, the vibration behavior of short-fiber-reinforced microbeams with Pasternak medium and small-size effects is investigated. The size effect is treated by MCST and rotary inertia is also included in the analyses. The Young's modules of short-fiber-reinforced microbeam are calculated based on the Halpin-Tsai formulations and the mass density is calculated in the context of the mixture rule. The vibration frequencies of the short-fiber-reinforced microbeam on Pasternak medium are obtained by a finite element method. The finite element formulation of the shortfiber-reinforced microbeam based on the MCST is derived by the weighted residual method. In the finite element formulation, the effect of the material length scale parameter is combined with the shear stiffness, thus giving an additional stiffness matrix to the classical theory. The increase in the stiffness matrix shows that the size effect has an increasing effect on the frequencies of the short-fiber-reinforced microbeam. This result, which is quite different from the classical theory, suggests that the scale effect should be considered in micro-electro-mechanical system elements under transverse vibration. The analyses show that there is an increase in the frequencies of short-fiber-reinforced microbeams with the rise of the material length scale parameter. The size effect in microstructures increases the vibration frequencies by increasing stiffness. The Young's modulus ratio and mass density ratio also have a significant effect on the vibration frequencies of the composite microbeam. In the case of increasing E_{sf}/E_m , the vibration frequencies obtained are much higher than the homogeneous case, and it is observed that the stiffer short fibers increase the vibration frequencies of the microbeam significantly. On the other hand, the increase in mass density ratio has a decreasing effect on frequencies. The two-parameter elastic medium causes the short-fiber-reinforced microbeam to become more rigid, resulting in an increase in the microbeam frequencies. It can be easily seen from the analysis that the stiffness of the shear layer has a greater effect on the microbeam frequencies. In addition, when the effect of fiber volume fraction in the presence and absence of elastic medium is examined, it is understood that the fiber ratio in the composite microbeam is more effective at frequencies in the absence of elastic medium. As mentioned, in small-scale composite structures, the reinforcement material's orientation is either impossible or involves difficulties in most cases. In this study, the vibration frequencies presented for randomly oriented short-fiberreinforced microbeams are intended to be helpful for the design of nano-electro-mechanical systems, micro-electromechanical systems, nano/micro sensors and atomic force microscopes.

Acknowledge

This study received no specific funding or financial support.

Contribution statement

All processes of the study were carried out by the author Büsra Uzun.

References

- [1] M. Shokravi, "Vibration analysis of silica nanoparticles-reinforced concrete beams considering agglomeration effects.," *Computers and Concrete*. vol. 19, no. 3, pp. 333–338, 2017.
- [2] V. Kahya, "Buckling analysis of laminated composite and sandwich beams by the finite element method.," *Composites Part B: Engineering*. vol. 91, pp. 126–134, 2016.
- [3] Ş.D. Akbaş, "Post-buckling analysis of a fiber reinforced composite beam with crack.," *Engineering Fracture Mechanics*. vol. 212, pp. 70–80, 2019.
- [4] R. Ekici, V. Abaci, and J. Reddy, "3D Micro-Structural Modeling of Vibration Characteristics of Smart Particle-Reinforced Metal-Matrix Composite Beams.," *International Journal of Structural Stability and Dynamics*. vol. 19, p. 1950078, 2019.
- [5] Z. Wang, X. Wang, G. Xu, S. Cheng, and T. Zeng, "Free vibration of two-directional functionally graded beams.," *Composite structures*. vol. 135, pp. 191–198, 2016.
- [6] F. Rubino, A. Nisticò, F. Tucci, and P. Carlone, "Marine application of fiber reinforced composites: a review.," *Journal of Marine Science and Engineering*. vol. 8, no. 1, p. 26, 2020.
- [7] G. Marmol, D.P. Ferreira, and R. Fangueiro, "Automotive and construction applications of fiber reinforced composites.," In: Fiber Reinforced Composites. pp. 785–819. Elsevier (2021).
- [8] S. Rawat and J. Saxena, "Fiber-reinforced polymer: applications in biomedical engineering.," In: *Materials for Biomedical Engineering*. pp. 393–429. *Elsevier* (2019).
- [9] M. Sreejith and R.S. Rajeev, "Fiber reinforced composites for aerospace and sports applications.," In: *Fiber Reinforced Composites*. pp. 821–859. *Elsevier* (2021).
- [10] B.D. Agarwal, L.J. Broutman, B.D. and K. Chandrashekhara, Analysis and performance of fiber composites Third edition. John Wiley & Sons, 2015.
- [11] A. Raju and M. Shanmugaraja, "Recent researches in fiber reinforced composite materials: A review.," *Materials Today: Proceedings*. vol. 46, pp. 9291–9296, 2021.
- [12] A. Dorigato, G. Fredi, and A. Pegoretti, "Application of the thermal energy storage concept to novel epoxy–short carbon fiber composites.," *Journal of Applied Polymer Science*, vol. 136, no. 21, p. 47434, 2019.
- [13] S.I. Kundalwal, "Review on micromechanics of nano- and micro-fiber reinforced composites.," *Polymer Composites*. vol. 39, no. 12, pp. 4243–4274, 2018.
- [14] U. Gul, "Dynamic analysis of short-fiber reinforced composite nanobeams based on nonlocal strain gradient theory.," *Proceedings of the Institution of Mechanical Engineers, Part C: Journal of Mechanical Engineering Science*. vol. 238, no. 7, pp. 2641–2676, 2024.
- [15] F. Yang, A.C.M. Chong, D.C.C. Lam, and P. Tong, "Couple stress based strain gradient theory for elasticity.," *International journal of solids and structures*. vol. 39, no. 10, pp. 2731–2743, 2002.
- [16] A.C. Eringen, "Linear theory of nonlocal elasticity and dispersion of plane waves.," *International Journal of Engineering Science*. vol. 10, no. 5, pp. 425–435, 1972.
- [17] D.C. Lam, F. Yang, A.C.M. Chong, J. Wang, and P. Tong, "Experiments and theory in strain gradient elasticity.," *Journal of the Mechanics and Physics of Solids*. vol. 51, no. 8, pp. 1477–1508, 2003.
- [18] S. Kong, S. Zhou, Z. Nie, and K. Wang, "The size-dependent natural frequency of Bernoulli–Euler micro-beams.," *International Journal of Engineering Science*. vol. 46, no. 5, pp. 427–437, 2008.
- [19] Ö. Civalek, H. Ersoy, H.M. Numanoğlu, and B. Akgöz, "Small size and rotary inertia effects on the natural frequencies of carbon nanotubes.," *Curved and Layered Structures*. vol. 5, no. 1, pp. 273–279, 2018.
- [20] B. Akgöz and Ö. Civalek, "Vibrational characteristics of embedded microbeams lying on a two-parameter elastic foundation in thermal environment.," *Composites Part B: Engineering*. vol. 150, pp. 68–77, 2018.
- [21] B. Uzun, U. Kafkas, and M.Ö. Yaylı, "Free vibration analysis of nanotube based sensors including rotary inertia based on the Rayleigh beam and modified couple stress theories.," *Microsystem Technologies*. vol. 27, no. 5, pp. 1913–1923, 2021.
- [22] M. Tang, Q. Ni, L. Wang, Y. Luo, and Y. Wang, "Size-dependent vibration analysis of a microbeam in flow based on modified couple stress theory.," *International Journal of Engineering Science*. vol. 85, pp. 20–30, 2014.
- [23] B.T.T. Hoai and N.D. Kien, "Size-dependent nonlinear bending of tapered cantilever microbeam based on modified couple stress theory.," *Vietnam Journal of Science and Technology*. vol. 62, no. 6, pp. 1196–1209, 2024.
- [24] P.B. Alfred, C.V. Ossia, and A. Big-Alabo, "Free nonlinear vibration analysis of a functionally graded microbeam resting on a three-layer

- elastic foundation using the continuous piecewise linearization method.," Archive of Applied Mechanics. vol. 94, no. 1, pp. 57-80, 2024.
- [25] A.N.T. Vu, V.N. Pham, and D.K. Nguyen, "Vibration analysis of functionally graded microbeams with a moving mass based on Timoshenko beam theory.," In: *IOP Conference Series: Materials Science and Engineering*. pp. 012002. *IOP Publishing* (2023).
- [26] Q. Zhang and H. Liu, "On the dynamic response of porous functionally graded microbeam under moving load.," *International Journal of Engineering Science*. vol. 153, p. 103317, 2020.
- [27] A. Rahi, "Vibration analysis of multiple-layer microbeams based on the modified couple stress theory: analytical approach.," *Archive of Applied Mechanics*. vol. 91, no. 1, pp. 23–32, 2021.
- [28] B. Uzun and M.Ö. Yayli, "Size-dependent free vibration of silicon nanobeams with different boundary conditions and beam theories.," p. 2021.
- [29] O.Z.S. Ong, M.H. Ghayesh, and S. Hussain, "Size-dependent dynamics of double-microbeam systems with various boundary conditions via modified couple stress theory.," *Microsystem Technologies*. vol. 27, no. 8, pp. 3193–3210, 2021.
- [30] N. Togun and S.M. Bağdatli, "Application of Modified Couple-Stress Theory to Nonlinear Vibration Analysis of Nanobeam with Different Boundary Conditions.," *Journal of Vibration Engineering & Technologies*. vol. 12, no. 4, pp. 6979–7008, 2024.
- [31] Ş.D. Akbaş, "Stability Analysis of a Laminated Composite Micro scaled beam embedded in elastic medium using modified coupled stress theory.," *Journal of Computational Applied Mechanics*. vol. 55, no. 1, pp. 26–38, 2024.
- [32] R. Hassannejad, S.A. Hosseini, and B. Alizadeh-Hamidi, "Influence of non-circular cross section shapes on torsional vibration of a microrod based on modified couple stress theory.," *Acta Astronautica*. vol. 178, pp. 805–812, 2021.
- [33] F.Y. Genao, J. Kim, and K.K. Žur, "Nonlinear finite element analysis of temperature-dependent functionally graded porous micro-plates under thermal and mechanical loads.," *Composite Structures*, vol. 256, p. 112931, 2021.
- [34] A. Mohammadpour, S.J. Mehrabadi, P. Yousefi, and H. Mohseni-Monfared, "Free vibration analysis of functionally graded porous elliptical microshells using modified couple stress theory.," *Waves in Random and Complex Media*. vol. 35, no. 1, pp. 947–972, 2025.
- [35] C. Demir, K. Mercan, H.M. Numanoglu, and O. Civalek, "Bending response of nanobeams resting on elastic foundation.," *Journal of Applied and Computational Mechanics*. vol. 4, no. 2, pp. 105–114, 2018.
- [36] H.M. Numanoğlu, "Thermal vibration of zinc oxide nanowires by using nonlocal finite element method.," *International Journal of Engineering and Applied Sciences*. vol. 12, no. 3, pp. 99–110, 2020.
- [37] I. Ahmadi, "Vibration analysis of 2D-functionally graded nanobeams using the nonlocal theory and meshless method.," *Engineering Analysis with Boundary Elements*. vol. 124, pp. 142–154, 2021.
- [38] A. Karamanli and T.P. Vo, "A quasi-3D theory for functionally graded porous microbeams based on the modified strain gradient theory.," *Composite Structures*. vol. 257, p. 113066, 2021.
- [39] B. Gia Phi, D. Van Hieu, H.M. Sedighi, and A.H. Sofiyev, "Size-dependent nonlinear vibration of functionally graded composite microbeams reinforced by carbon nanotubes with piezoelectric layers in thermal environments.," *Acta Mechanica*. vol. 233, no. 6, pp. 2249–2270, 2022.
- [40] B. Uzun and M.O. Yayli, "Accurate and efficient analytical simulation of free vibration for embedded nonlocal CNTRC beams with general boundary conditions.," *Physica B: Condensed Matter.* vol. 695, p. 416556, 2024.
- [41] M. Akpinar, B. Uzun, and M.O. Yayli, "On the thermo-mechanical vibration of an embedded short-fiber-reinforced nanobeam.," *Advances in nano research*. vol. 17, no. 3, pp. 197–211, 2024.
- [42] U. Kafkas, "Farklı Kiriş Teorilerine Göre Kısa Fiber Takviyeli Nano Kirişlerin Kritik Burkulma Yüklerinin Değerlendirilmesi.," *Kafkas Üniversitesi Fen Bilimleri Enstitüsü Dergisi.* vol. 17, no. 1, pp. 1–14, 2024.
- [43] Ufuk Gül, "Kısa Elyaf Hizalanmasının Kompozit Nanokirişlerin Burkulmasına Etkisi.," In: Kisa Elyaf Hizalanmasının Kompozit Nanokirişlerin Burkulmasına Etkisi. pp. 696–710. İTÜ Yayınevi (2023).
- [44] J.C. Halpin and S.W. Tsai, "Effects of environmental factors on composite materials.," p. 1969.
- [45] S. Zhao, Z. Zhao, Z. Yang, L. Ke, S. Kitipornchai, and J. Yang, "Functionally graded graphene reinforced composite structures: A review.," *Engineering Structures*. vol. 210, p. 110339, 2020.
- [46] R. Toupin, "Elastic materials with couple-stresses.," Archive for rational mechanics and analysis. vol. 11, no. 1, pp. 385–414, 1962.
- [47] R.D. Mindlin and H.F. Tiersten, "Effects of couple-stresses in linear elasticity.," *Archive for Rational Mechanics and Analysis*. vol. 11, no. 1, pp. 415–448, 1962.
- [48] W.T. Koiter, "Couple stresses in the theory of elasticity. I and II Proc K Ned Akad Wet 1964.," B (67). pp. 17–44,.
- [49] A.M. Dehrouyeh-Semnani and M. Nikkhah-Bahrami, "A discussion on evaluation of material length scale parameter based on microcantilever test.," *Composite Structures*. vol. 122, pp. 425–429, 2015.
- [50] H.-T. Thai, T.P. Vo, T.-K. Nguyen, and S.-E. Kim, "A review of continuum mechanics models for size-dependent analysis of beams and plates,," *Composite Structures*. vol. 177, pp. 196–219, 2017.
- [51] J.N. Reddy, "Energy Principles and Variational Methods in Applied Mechanics, John Willy and Co.," *Inc. New Jersey, USA*, 542p. p. 59, 2002.
- [52] M.H. Omurtag, Cubuk sonlu elemanlar. Birsen Yayınevi, 2010.

TOURNAR UNIVERSITY OF THE PROPERTY OF THE PROP

Contents lists available at Dergipark

Journal of Scientific Reports-A

journal homepage: https://dergipark.org.tr/tr/pub/jsr-a



E-ISSN: 2687-6167 Number 62, September 2025

RESEARCH ARTICLE

Exploring matrix applications across interdisciplinary domains: insights from business, geology and robotics

Khadeejah James Audu^{a*}, Mahmud Adeiza Lawal^b, Oloruntobi Olalekan Balogun^c, Abraham Ajeolu Oluwasegun^d, Stephen Udugbai Egbe^e

Abstract

The paper focuses on exploring the use of matrices in Business, Geology, and Robotics, in order to determine how such combination can solve practical aspects of problems and promote multidisciplinary approach. In this regard, the paper reviews the principles and practices of matrices as a mathematical tool, to demonstrate their relevance within the context of scientific and engineering activities. This research deploys complex and advanced matrix techniques and explores the impacts of these techniques to problems in each of the fields and demonstrate their practicality through the application of real-world applications.

The methodology provides a comprehensive review of matrix application by using quantitative methods. The results show the importance of use of matrices in these fields. In the field of Robotics, it extends to motion control and spatial orientation through the use of matrices. In Geology, matrix methods are applied in analyzing seismic data so as to produce a more accurate explanation and summary of the earth's internal structure. In Business, matrices were utilized in establishing the profit margin on businesses and to help manage investment portfolios.

© 2023 DPU All rights reserved.

Keywords: Matrices; Geology; Matrix Application; Business

^{a,*}Federal University of Technology, Department of Mathematics, Minna, Nigeria, ORCID: 0000-0002-6986-3491

^bFederal University of Technology, Department of Mathematics, Minna, Nigeria, ORCID: 0009-0006-0637-2704

^cFederal University of Technology, Department of Mathematics, Minna, Nigeria, ORCID: 0009-0007-4931-6355

^dFederal University of Technology, Department of Mathematics, Minna, Nigeria, ORCID: 0009-0005-2295-968X

Federal University of Technology, Department of Mathematics, Minna, Nigeria, ORCID: 0009-0009-3917-7157

^{*} Corresponding author. Tel.: +234 902 733 6744 E-mail address: k.james@futminna.edu.ng

1. Introduction

Matrices are fundamental and essential mathematical structures that are widely used in a variety of fields due to the numerous favorable features they possess as shown in [1-2]. A matrix can be defined basically as a rectangular array of its members arranged into rows and columns; due to matrices containing deep and complex relationships of data that are needed in biology, physics, engineering, computer science and other fields. Likewise, in geology and earth sciences, matrices are applied for the processing of spatial data including seismic surveys, geological surveys, and Geographic Information Systems (GIS) in [3].

In the same vein, matrices are pervading in business, economics and finance where models of supply and demand, input – output analysis and portfolio extension employed in [4, 15]. Similarly, social science disciplines such as sociology and psychology apply the matrices for network analysis, factor analysis, and structural equation modelling in the study of complex systems and relationships between variable(s) [5].

Furthermore, in robotics and control systems, the kinematics, dynamics and control of robotic systems is enhanced through the use of matrices as pointed out by [6, 13, 18]. The needful requirement of matrix transformation and Jacobian matrix in [19, 20] for computing the trajectories of a robot, positions of manipulators and poses of end effectors, made motion planning highly effective.

Researchers have dedicated great amount of effort to study the matrix system and how it can be applied in various disciplines. Study in [7], [8] reveals how matrix can be applied in decision models in evaluating strategic alternatives, highlights the basic operations and properties of matrices. Studies in [9, 10, 14] shows how matrix can be applied in mathematical modeling based on matrix theory and the distinct characteristics of matrices and their applications in linear algebra, optimization, and signal processing respectively. Research on the application of matrix cannot be exhausted as it concerns our daily lives. The novelty of this work lies in further investigation into matrix application in areas that affect our existence and to explore the efficiency and computational implications in addressing problems encountered in businesses, geology and robotics.

The motivation is derived from the significance of enhancing linear algebra for solving problems widely applied in fields like engineering and physics. This study helps to bridge the gap between logical approach and the practical applications and also reveals new opportunities for problem solving across different fields.

This work considers three exploratory analyses one for each field that work carefully using the algorithm from each field. The exploratory analysis for the business application deals with finding the profit margin and investment for each business using the algorithm for the business application.

Likewise, in geology, the analysis shows the recorded amplitude at several different intervals and it shows that the cumulative amplitude of the sensors decreases across the sensors.

In robotics, the analysis exemplifies the positioning of matrices in robotics in kinematics and control systems where precise calculations of the position and orientation of the robot in space are performed.

In subsequent sections, matrix was used to solve detailed and illustrative problems involving the selected topics and discipline.

2. Methodology

2.1. Matrix operations

Matrices are grid of numbers or variables arranged in rows and columns and their numbers are called elements or entries of the matrix. A standard matrix can be mathematically express as

$$P = m \times n = \begin{bmatrix} a_{11} & \cdots & a_{1n} \\ \vdots & \ddots & \vdots \\ a_{m1} & \cdots & a_{mn} \end{bmatrix}$$
 (1)

which can be defined by diverse operations such as addition, subtraction and multiplication as demonstrated in [11], [12].

Transpose in Matrix: A matrix in linear algebra is said to be transposed when its rows and columns are switched, creating a new matrix. Below is an example of the main ideas regarding transpose: The transpose of matrix P in (1) is commonly denoted by P^T .

$$P^{T} = n \times m = \begin{bmatrix} a_{11} & \cdots & a_{m1} \\ \vdots & \ddots & \vdots \\ a_{1n} & \cdots & a_{mn} \end{bmatrix}$$
 (2)

The rows and columns are switched to determine the transpose.

i. Matrix Addition and Subtraction: Matrix addition and subtraction are fundamental operations in linear algebra that involves combining two matrices of the same dimensions.

For example, consider two matrices of the same size, denoted as

$$R = \begin{bmatrix} r_{11} & \cdots & r_{1n} \\ \vdots & \ddots & \vdots \\ r_{m1} & \cdots & r_{mn} \end{bmatrix} \text{ and } Q = \begin{bmatrix} q_{11} & \cdots & q_{1n} \\ \vdots & \ddots & \vdots \\ q_{m1} & \cdots & q_{mn} \end{bmatrix}$$
(3)

The addition and subtraction are performed element wise respectively as

$$R - Q = \begin{bmatrix} r_{11} - q_{11} & \cdots & r_{1n} - q_{1n} \\ \vdots & \ddots & \vdots \\ r_{m1} - q_{m1} & \cdots & r_{mn} - q_{mn} \end{bmatrix}$$
(4)

And similarly,

$$R + Q = \begin{bmatrix} r_{11} + q_{11} & \cdots & r_{1n} + q_{1n} \\ \vdots & \ddots & \vdots \\ r_{m1} + q_{m1} & \cdots & r_{mn} + q_{mn} \end{bmatrix}$$
 (5)

These operations are commutative and associative, meaning the order of addition or grouping does not affect the result.

ii. Matrix Multiplication: The multiplication of N matrices follows the rule of matrix multiplication, where for matrices $p_1, p_2, ..., p_N$ the product is:

$$P = P_1 \times P_2 \times P_3 \times \cdots \times P_N$$

For valid multiplication, the dimensions must be compatible. That is,

$$P_1 \in \mathbb{R}^{m_1 \times m_2}$$
, $P_2 \in \mathbb{R}^{m_2 \times m_3}$, ..., $P_N \in \mathbb{R}^{m_N \times m_{N+1}}$

Then the resulting product matrix *P* will have the dimensions:

$$P \in \mathbb{R}^{m_1 \times m_{N+1}}$$

Hence, matrix multiplication is distributive.

2.2. Application of matrix in business

If q_{mn} represents the purchased quantity in a business, then the matrix can be interpreted as a record of the quantities of different products purchased in different transactions or periods. The purchased matrix is then given as

$$Q = \begin{bmatrix} q_{11} & \cdots & q_{1n} \\ \vdots & \ddots & \vdots \\ q_{m1} & \cdots & q_{mn} \end{bmatrix}_{m \times n}$$
 (6)

Here, q_{ij} represents the quantity of product j in transaction i, with iii ranging from l to m and j ranging from l to m.

The price matrix P is an $n \times p$ column matrix representing the prices of n products in p different pricing scenarios (different stores, different times, or different customer groups):

$$P = \begin{bmatrix} p_{11} & \cdots & p_{1n} \\ \vdots & \ddots & \vdots \\ p_{m1} & \cdots & p_{mn} \end{bmatrix}_{n \times n}$$
 (7)

Here, p_{np} is the price of product n in pricing scenario p. P_{jk} is the price of product j in pricing scenario k, with j ranging from l to p and k from l to p.

To calculate the total profit (Π) , it is obtained by the multiplication of the matrices $Q \times P$ that calculates the total profit for each transaction based on the quantities of products sold and their corresponding prices.

$$\Pi = Q.P \tag{8}$$

$$\Pi = \begin{bmatrix} q_{11} & \cdots & q_{1n} \\ \vdots & \ddots & \vdots \\ q_{m1} & \cdots & q_{mn} \end{bmatrix}_{m \times n} \cdot \begin{bmatrix} p_{11} & \cdots & p_{1n} \\ \vdots & \ddots & \vdots \\ p_{m1} & \cdots & p_{mn} \end{bmatrix}_{n \times p}$$
(9)

$$\Pi = \begin{bmatrix} \pi_{11} & \cdots & \pi_{1p} \\ \vdots & \ddots & \vdots \\ \pi_{m1} & \cdots & \pi_{mp} \end{bmatrix}_{m \times n}$$
(10)

where each element π_{ik} is given by:

$$\pi_{ik} = \sum_{j=1}^{n} q_{ij} p_{jk} \tag{11}$$

Thus, π_{ik} represents the total profit from transaction i underpricing scenario k

2.2.1. Algorithm for business application

Step 1: Define the Matrices

Let Q and P be the matrix representing the quantities of products sold across each transaction and the prices of products respectively

Step 2: Validate the Matrix Dimensions

Ensure that the number of columns in matrix Q aligns with the number of rows in matrix P by confirming the dimensions of the matrices.

Step 3: Initialize the Result Matrix Π

Define matrix Π to store total profits, where each element π_{ik} represents the profit for transaction i under pricing scheme k.

Step 4: Compute the Total Profit

Counted the total profit for each transaction i in matrix G by multiplying the quantities in the transaction by their matching product prices in P and sums the results. Save the total profit in the suited row of matrix Π . Compute each entry π_{ik} in matrix Π as follows:

$$\pi_{ik} = \sum_{j=1}^{n} q_{ij} p_{jk}$$

Step 5: The produced matrix Π shows the total profit for each transaction across different pricing schemes.

2.3. Application of matrix in geology

Seismic surveys involve multiple sources and receivers that record seismic wave amplitudes over time. The recorded data can be structured as a matrix:

$$S = \begin{bmatrix} s_{11} & \cdots & s_{1n} \\ \vdots & \ddots & \vdots \\ s_{m1} & \cdots & s_{mn} \end{bmatrix}$$

$$(12)$$

 $S = GR \tag{12}$

where,

S is the seismic signal matrix $\mathbb{R}^{m \times p}$,

G is the wave propagation operator $\mathbb{R}^{m \times n}$,

R is the reflectivity matrix $\mathbb{R}^{n \times p}$,

 s_{ij} represents the seismic amplitude recorded at receiver i at time sample j

m is the number of receiver stations,

n is the number of time samples per recording.

Each column corresponds to a recorded seismic trace at a given receiver, and each row represents a snapshot of the wavefield at a particular time.

In practical seismic data analysis, there is need to estimate R given S and G. This involves solving the inverse problem:

$$R = G^{-1}S$$

If G is non-square,

$$R = (G^TG + \lambda I)^{-1}G^TS$$

where λ is a regularization parameter.

2.3.1. Algorithm for geology application

Step 1: Write down the seismic Data from different sources.

Step 2: Analyzing the seismic data for Seismic readings from multiple sensors and coordinates of sensors and time of signal reception.

Step 3: Matrix seismic data should be represented in rows, sensors and columns also represent time intervals; elements are seismic signal strengths.

Step 4: Compute Reflectivity Matrix R

Step 4: preprocessing and normalizing the data if necessary to Filter noise from seismic data

Step 5: Identify patterns or anomalies in the reconstructed seismic data matrix. To Compare with known geological formations.

2.4. Application of matrix in robotics

Using a quaternion q to represent rotations in 3D space. defined as:

$$q = w + xi + yj + zk \tag{13}$$

where

w is the scalar (real) component.

x, y, z are the vector (imaginary) components.

i, j, k are the fundamental quaternion units satisfying: $i^2 = j^2 = k^2 = ijk = -1$

Given a point in 3D space, represented as a pure quaternion:

$$p = 0 + x'i + y'i + z'i$$

its rotated version p' under quaternion q is obtained using the transformation:

$$p' = qpq^{-1}$$

Simplifying, we obtain the transformed coordinates, leading to the 3×3 rotation matrix ensuring proper rotation without gimbal lock:

$$R(q) = \begin{bmatrix} 1 - 2(y^2 + z^2) & 2(xy - wz) & 2(xz + wy) \\ 2(xy + wz) & 1 - 2(x^2 + z^2) & 2(yz - wx) \\ 2(xz - wy) & 2(yz + wx) & 1 - 2(x^2 + y^2) \end{bmatrix}$$
(14)

The matrix provides a compact way to rotate any vector using quaternion parameters.

2.4.1. Algorithm for robotic application

Input: A unit quaternion q = (w, x, y, z)

Output: The rotation matrix R(q)

Step 1: Extract Quaternion Components

q = (w, x, y, z), separate its scalar and vector components.

Step 2: Compute Square Terms

Step 3: Compute Cross Terms

Step 4: Construct Rotation Matrix

Step 5: Normalize q

Step 6: Apply Rotation

3. Exploratory Analysis

This section will explore the applications of matrices in Business, Geology and Robotics by conducting three experiments on the various domains. Exploration one will focus on applying matrix in a business problem, then exploration two will apply matrix techniques to solve a geological problem and finally exploration three aims at applying matrix operations in a robotic problem.

Exploration 1: Given the supermarket sales dataset [21] containing the quantity of products sold and their unit prices, construct matrices representing these values. Compute the total revenue for each transaction using matrix multiplication.

Quantity Matrix (Q)- The column vector representing the quantity of products sold per transaction:

$$\begin{bmatrix} 7\\5\\7\\8\\\vdots \end{bmatrix}$$
 (15)

Unit Price Matrix (P) - A row vector representing the unit price of products:

$$\begin{bmatrix} 74.69 \\ 15.28 \\ 46.33 \\ 58.22 \\ \vdots \end{bmatrix}^{T}$$
 (16)

Exploration 1 was thoroughly analyzed using the algorithms outlined in section 2.1.1. These algorithms provided a structured approach that allowed for proper evaluation of the data and provision of the total profit for each sale in (8).

$$\begin{bmatrix}
522.83 \\
76.40 \\
324.31 \\
465.76 \\
\vdots
\end{bmatrix}$$
(17)

Exploration 2: A geophysicist records seismic signals from 50 sources using 70 receivers. The goal is to estimate the reflectivity matrix R, which represents the subsurface structure, from observed seismic amplitudes using the relationship:

Seismic Data Matrix S, Wave Propagation Matrix G,

$$S = \begin{bmatrix} s_{11} & \cdots & s_{1,70} \\ \vdots & \ddots & \vdots \\ s_{50,1} & \cdots & s_{50,70} \end{bmatrix}_{50 \times 70} G = \begin{bmatrix} g_{11} & \cdots & g_{1,70} \\ \vdots & \ddots & \vdots \\ g_{50,1} & \cdots & g_{50,70} \end{bmatrix}_{50 \times 70}$$
(18)

Compute G^TG

$$G^{T}G = \begin{bmatrix} g'_{11} & \cdots & g'_{1,70} \\ \vdots & \ddots & \vdots \\ g'_{70,1} & \cdots & g'_{70,70} \end{bmatrix}_{70\times70}$$
(19)

Adding regularization to Inversion Matrix

$$G^{T}G + \lambda I = \begin{bmatrix} g'_{11} + \lambda & \cdots & g'_{1,70} \\ \vdots & \ddots & \vdots \\ g'_{70,1} & \cdots & g'_{70,70} + \lambda \end{bmatrix}_{70 \times 70}$$
(20)

Inverse of Regularized Matrix using LU decomposition or iterative solvers to reduce computational cost

$$(G^T G + \lambda I)^{-1} = \begin{bmatrix} r_{11} & \cdots & r_{1,70} \\ \vdots & \ddots & \vdots \\ r_{70,1} & \cdots & r_{70,70} \end{bmatrix}_{70 \times 70}$$
(21)

Product of G^TS

$$G^{T}S = \begin{bmatrix} h_{11} & \cdots & h_{1,70} \\ \vdots & \ddots & \vdots \\ h_{70,1} & \cdots & h_{70,70} \end{bmatrix}_{70 \times 70}$$
(22)

Final Reflectivity Matrix R

$$R = (G^TG + \lambda I)^{-1}G^TS$$

$$R = \begin{bmatrix} r'_{11} & \cdots & r'_{1,70} \\ \vdots & \ddots & \vdots \\ r'_{70,1} & \cdots & r'_{70,70} \end{bmatrix}_{70 \times 70}$$
 (23)

The application of matrices in geology was considered and fully explored in addressing this problem through stepby-step approach of the algorithms provided in section 2.3.1 and this approach allowed for a comprehensive understanding of geological data.

Table 3: Result for Exploration Three

	First Time Interval	Second Time Interval	 Seventieth Time Interval
Sensor 1	r' ₁₁	r'_{12}	 $r'_{1,70}$
Sensor 2	r'_{21}	r'_{22}	 $r'_{2,70}$
Sensor 3	r'_{31}	r'_{32}	 $r'_{3,70}$
Sensor 70	$r'_{70,1}$	$r'_{70,2}$	 $r'_{70,70}$

Outcome: Table 3 reveals that the cumulative amplitude of the sensors Exploration 3: Apply two rotations in the following planes for the vector V

$$V = \begin{bmatrix} 1\\2\\3\\4 \end{bmatrix} \tag{24}$$

- 1. 90° rotation in the xy-plane
- 2. 45° rotation in the zw-plane

$$R(q) = \begin{bmatrix} 1 - 2(y^2 + z^2) & 2(xy - wz) & 2(xz + wy) & 0\\ 2(xy + wz) & 1 - 2(x^2 + z^2) & 2(yz - wx) & 0\\ 2(xz - wy) & 2(yz + wx) & 1 - 2(x^2 + y^2) & 0\\ 0 & 0 & 0 & 1 \end{bmatrix}$$
(25)

Rotation 1: 90° in the xy-plane with axis (0,0,1)

$$q_1 = \sin(45) + (0i + 0j + 1k)\sin 45$$
$$= 0.707 + 0.707k$$

$$R_{q1} = \begin{bmatrix} \cos 90 & -\sin 90 & 0 & 0\\ \sin 90 & \cos 90 & 0 & 0\\ 0 & 0 & 1 & 0\\ 0 & 0 & 0 & 0 \end{bmatrix} = \begin{bmatrix} 0 & -1 & 0 & 0\\ 1 & 0 & 0 & 0\\ 0 & 0 & 1 & 0\\ 0 & 0 & 0 & 0 \end{bmatrix}$$
(26)

Rotation 2: 45° in the zw-plane with axis (0,0,1,1)

$$\begin{aligned} q_2 &= \cos(22.5^{\circ}) + (0i + 0j + 1k + 1w)\sin(22.5^{\circ}) \\ q_2 &= \cos(22.5) + (0i + 0j + 1k)\sin(22.5) \\ &= 0.93 + 0.382k + 0.382w \end{aligned}$$

$$R_{q2} = \begin{bmatrix} 1 & 0 & 0 & 0 \\ 0 & 1 & 0 & 0 \\ 0 & 0 & \cos 45 & -\sin 45 \\ 0 & 0 & \sin 45 & \cos 45 \end{bmatrix} = \begin{bmatrix} 1 & 0 & 0 & 0 \\ 0 & 1 & 0 & 0 \\ 0 & 0 & 0.707 & -0.707 \\ 0 & 0 & 0.707 & 0.707 \end{bmatrix}$$

$$(27)$$

Apply transformations to the point:

$$V = \begin{bmatrix} 1 \\ 2 \\ 3 \\ 4 \end{bmatrix}$$

Apply R_{q1}

$$V' = R_{q1} \times V = \begin{bmatrix} 0 & -1 & 0 & 0 \\ 1 & 0 & 0 & 0 \\ 0 & 0 & 1 & 0 \\ 0 & 0 & 0 & 0 \end{bmatrix} \begin{bmatrix} 1 \\ 2 \\ 3 \\ 4 \end{bmatrix} = \begin{bmatrix} -2 \\ 1 \\ 3 \\ 4 \end{bmatrix}$$

Apply R_{q2}

$$V'' = R_{q2} \times V' = \begin{bmatrix} 1 & 0 & 0 & 0 \\ 1 & 1 & 0 & 0 \\ 0 & 0 & 0.707 & -0.707 \\ 0 & 0 & 0.707 & 0.707 \end{bmatrix} \begin{bmatrix} -2 \\ 1 \\ 3 \\ 4 \end{bmatrix} = \begin{bmatrix} -2 \\ 1 \\ -0.707 \\ 4.95 \end{bmatrix}$$
(28)

After applying both quaternion-based transformations using matrix operations, the transformed point is:

$$V'' = (-2, 1, -0.707, 4.95)$$

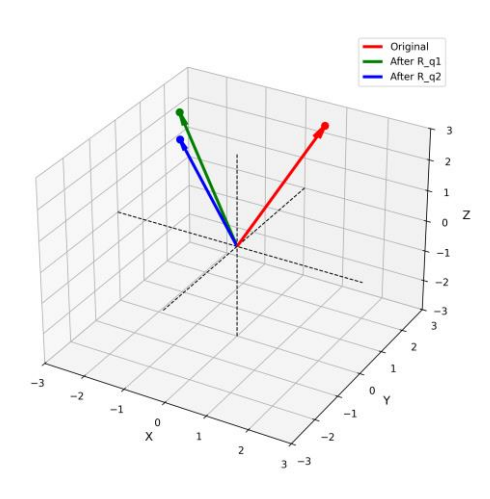


Fig. 1. Quaternion Rotation Visualization for the vector V

4. Discussion of Result

The results from the three experiments conducted provide a comprehensive demonstration of the applications of matrices in various fields including business, geology, data science and robotics. Each experiment showcases the versatility and effectiveness of matrix operations in solving real-world problems.

In the first experiment, the total profit matrix was computed by multiplying the quantity matrix (Q) with the unit price matrix (P), providing the total revenue for each transaction. Data preprocessing involved cleaning the dataset, extracting relevant columns, and ensuring dimensional consistency for valid matrix multiplication. The results offer insights into sales performance.

In the second experiment, the estimated reflectivity matrix R reveals key subsurface structures by capturing variations in seismic amplitudes recorded from 50 sources and 70 receivers. The accuracy of R depends on the source-receiver geometry, with denser coverage improving resolution, while noise and inversion instability may introduce artifacts that require regularization. While major reflectors are well-imaged, deeper or more complex structures requires advanced inversion techniques like machine learning-based inversion, to learn complex relationships between seismic data and reflectivity.

In the third experiment, the transformation results show how sequential quaternion-based rotations effectively reposition the vector in 3D space, demonstrating the impact of rotational matrices on spatial orientation. The first

rotation, R_{q1} , performs a 90-degree transformation about the z-axis, while the second rotation, R_{q1} , applies a 45-degree transformation in the w-k plane, further altering the vector's direction. The plotted visualization clearly captures these effects, highlighting the correctness of the transformation approach and its relevance to robotics and kinematics applications.

5. Conclusion

In conclusion, the use of matrices in various spheres including business, geology, and robotics showcases the usefulness of matrices in promoting better analytical and operational efficiency. In the case of business, matrices played a role in financial and inventory analysis which make it possible for firms to utilize resources most efficiently and thus, enhance their profitability. In geology, particularly in seismic data processing, matrices are essential for modelling subsurface structures, enhancing resource exploration, and improving environmental assessments. In robotics, they enable precise motion control, kinematics, and data processing, contributing to intelligent automation. The increasing complexity of real-world problems necessitates advanced matrix-based techniques, particularly in high-dimensional seismic inversion and large-scale robotic systems. As computational power grows, research should focus on leveraging parallel computing and optimized numerical methods to handle vast datasets efficiently, improving accuracy and performance in seismic imaging, resource exploration, and intelligent control systems.

Acknowledgement

The authors would like to appreciate the staff of Department of Mathematics, Federal University of Technology Minna, Nigeria for their support towards this research article.

Author Contribution

K. J. Audu was responsible for the conceptualization of the study and provided supervision. M. A. Lawal prepared the initial draft of the manuscript. O. O. Balogun carried out the computations and contributed to manuscript editing. A. A. Oluwashegun critically reviewed the manuscript. S.U. Egbe contributed to writing and further editing

References

- [1] G. Airlangga, "Advanced Seismic Data Analysis: Comparative study of Machine Learning and Deep Learning for Data Prediction and Understanding," *Brilliance: Research of Artificial Intelligence*, vol. 3, no. 2, pp. 456–465., 2024.
- [2] K. J. Audu, "Application of Singular Value Decomposition technique for compressing images," Gadau Journal of Pure and Allied Sciences, 2022, 1(2), 82–94.
- [3] S. Barnett, "Distinct Characteristics of Matrices and Their Applications in Linear Algebra, Optimization, and Signal Processing", Journal of Mathematical Applications in Engineering, 2023, 78(1), 45-58.
- [4] X. Guan, "Matrices: Essential Tools Across Disciplines," Journal of Mathematical Applications, 2022, 45(2), 123-135.
- [5] A. Gómez, B. Martinez, C. Lopez and D. Rodriguez, "Application of Matrix-Based Decision Models in Evaluating Strategic Alternatives," Strategic Management Journal, 2021, 38(3), 210-225.
- [6] X. Guan, "Basic Operations and Properties of Matrices," International Conference on Statistics, Applied Mathematics, and Computing Science (CSAMCS 2021),12163.
- [7] X. Song, "Research On Application of Mathematical Modeling Based On Matrix Theory," Frontiers in Computing and Intelligent Systems, 2022, 2(2), 19-21.
- [8] S. Barnett, "Distinct Characteristics of Matrices and Their Applications in Linear Algebra, Optimization, and Signal Processing," Journal of Mathematical Applications in Engineering, 2023, 78(1), 45-58.
- [9] P. Boito, "Matrix Structures and Matrix Functions," Proceedings of the 2023 International Symposium on Symbolic and Algebraic Computation.
- [10] k. J. Audu, O. O. Oluwole, Y. A. Yahaya, S. D. Egwu, "The Application of Linear Algebra in Machine Learning," School of physical sciences biennial international conference Futminna 2024.
- [11] M. Ceddia, L. Comuzzi, N. Di Pietro, T. Romasco, A. Specchiulli, A. Piattelli, and B. Trentadue, "Finite element analysis (FEA) for the evaluation of retention in a conometric connection for implant and prosthesis," Osteology, 2023, 3(4), 140–156.

- [12] X. Chen, Y. Zhang, Q. Wang, and Z. Liu, "Matrix-Based Optimization Techniques: Maximizing Resource Utilization and Minimizing Production Costs," Journal of Operations Management, 2021, 45(2), 67-82.
- [13] K. J. Audu, Y. C. Elisha, Y. A. Yahaya, S. A. Akande, "The Practical Integration of Linear Algebra in Genetics, Cubic Spline Interpolation, Electric Circuits and Traffic flow," Bitlis Eren University Journal of Science and Technology, 2024, 14(1), 23-42.
- [14] A. A. Hadi, "Matrix Application in Engineering Problems. In Intelligent Systems and Networks," Springer Singapore, 2021, 589-598.
- [15] J. Smith, R. Adams, S. Brown, and M. Davis, "Application of Linear Programming Models Formulated in Matrix Form," Operations Research, 2021, 65(4), 123-135.
- [16] Q. Song, and Q. Zhao, "Recent Advances in Robotics and Intelligent Robot's Applications," Applied Sciences, 2024, 14(10), 4279.
- [17] J. Vince, "Matrix algebra. In Mathematics for Computer Graphics," Springer London, 2022, (pp. 119–150).
- [18] Z. Wang, S. Li, W. Liu, and Q. Zhao, "Matrix-Based Control Techniques in Regulating Trajectory and Velocity," Automatica, 2021,67, 89-102.
- [19] A. Martinez, B. Lopez, C. Rodriguez, and D. Garcia, "Application of Matrix-Based Dynamic Models in Analyzing Robotic Manipulator Motion," IEEE Transactions on Robotics, 2022, 36(3), 456-469.
- [20] I. Tomozei, C. Sebu, and T. Axinte, "Simulations of A 2R Robotic Arm with MATLAB Program," Technium: Romanian Journal of Applied Sciences and Technology, 2023,10, 1–5.
- [21] S. Ghosh, Supermarket Sales Data Analysis Sheet1.csv. GitHub.2024. Available at: https://github.com/sushantag9/Supermarket-Sales-Data-Analysis/blob/master/supermarket_sales%20-%20Sheet1.csv (Accessed 25 Mar 2025).



Contents lists available at Dergipark

Journal of Scientific Reports-A

journal homepage: https://dergipark.org.tr/tr/pub/jsr-a



E-ISSN: 2687-6167 Number 62, September 2025

RESEARCH ARTICLE

Investigation of physicochemical and filtration performances of Agdoped PVDF-cellulose composites prepared by different precipitation methods

Huseyin Gumus^{a,*}

^{a,*}Bilecik Seyh Edebali University, Osmaneli Vocational School, 11500, Osmaneli, Bilecik/Türkiye, ORCID: 0000-0002-2029-7978

Abstract

In this study, the physical and filtration properties of PVDF-Cellulose polymeric composites containing silver particles were prepared with two different methods and their structure were investigated. In the first method, precipitation with NaBH $_4$ in solution medium (method I), and in the second method, composites were prepared according to phase separation by mixing previously precipitated powder. The molecular interactions of the prepared samples were analysed by FTIR spectroscopy, and the surface properties were imaged by SEM device. Changes in the thermal resistance of the composites were investigated by TG-DTA analysis. Filtration properties of flat-shaped composites were evaluated according to pure water flux and methyl orange model pollution removal performance. Thanks to the homogeneous pore distribution of the composites prepared by the solution precipitation method, the pure water flux of $53 \text{ Lm}^{-2}\text{h}^{-1}\text{bar}^{-1}$ and the MO rejection efficiency were calculated as 46.5% for AgP1. The formation of contamination on the membrane surfaces were analysed and the composite prepared by method I had been found as least rough surface. It was understood that the preparation methods of the composites are the effective variables in porosity, water retention and filtration efficiency.

© 2023 DPU All rights reserved

Keywords: Filtration; polymeric composites; silver particles; contamination accumulation

* Corresponding author. Tel.: +90 228 2142841 E-mail address: hsyngms2016@gmail.com

1. Introduction

Ceramic and polymeric structures are mainly used in the physical separation of pollutants in water. While the high physical and chemical resistance of ceramic structures is the reason for preference. The difficulties in adjusting the pore structure and the high cost have increased the use of polymeric structures. For this reason, synthetic and natural

polymers such as polyvinylidene fluoride (PVDF), polysulfone (PSF), polyether sulfone (PESU), cellulose, cellulose acetate (CA), chitosan and their mixtures are used in filtration applications [1]. The ability to adjust the desired thickness (150-300 μ m) and pore width of the polymer, having good physical and chemical resistance, easy processing and low cost have increased the preference of polymeric composites in filtration applications. This makes it easier to convert PVDF into membranes [2]. Solid or liquid additives added to PVDF in solution form are effective in regulating the pore size and membrane structure. TiO_2/Al_2O_3 doped ultrafiltration PVDF membranes have been used in oil/water separation [3].

Thanks to the increased hydrophilicity, oil separation was achieved and contamination accumulation on the membrane surface was prevented [4]. Polyvinylpyrrolidone was cross-linked to the PVDF surface by grafting method. The sulfobetaine monomers structure formed on the surface pores that acted as sieves [5]. LiCl, clay, and various metal oxides were used as additives to improve the desired properties of the polymer [6], [7]. Ortho phosphoric acid and glycerol added PVDF obtained by the NIPs method in triacetin solution exhibited good CO₂ flux performance thanks to its large pore structure in gas purification [8]. PVDF membrane with dopamine grafted to the surface was activated with silver nanoparticles. The contact angle of membrane gained a high hydrophobic property of 150°.

Cellulosic structures are biodegradable composite materials that can be obtained from various biological materials. Cellulose acetate, carboxymethyl cellulose, methyl cellulose and nano-micro cellulosic structures can be used as membranes directly or by various chemical processes [9]. In addition, cellulose and its derivatives can be prepared from many biomass by various physical and chemical methods and are clean, environmentally friendly alternatives to petroleum-derived composites [10]. Cellulose particles obtained by hydrolyzing textile wastes were dissolved in DMAc and mixed with 50% PVDF to prepare PVDF-Cellulose composites [11]. When the cellulose ratio of the composite reaches 75%, the physical strength decreases. The best composition was obtained at a 1:1 PVDF-Cellulose ratio. Cellulose mixed with PVDF increases the surface hydrophilicity of the structure. In addition, the Ag particles added to the structure provide antimicrobial properties to the composite in addition to the surface properties, and are effective in preventing the accumulation of dirt on the surface of filtration membranes. Due to the wide band gap (3.2 eV), TiO₂ with anatase structure was activated with Ag⁺ to ensure absorption in the visible light region, and the resulting hydrogel was coated on the glass surface by spin coating method. The composite with a surface area of 85-231 m²/g showed 98.86% performance in the catalytic removal of methylene blue and methyl orange from water with photocatalytic effect in the presence of UV [12]. Due to its high UV absorption capacity, TiO2 is frequently used in photocatalytic applications. The addition of silver cation to the structure reduced the energy level between the conduction bands of the molecule and allowed absorption in the visible region.

Silver nano/micro particles are usually made by adding a reductant to the silver salt solution. In addition, many microorganisms, plant extracts and enzymes were used as reductants to obtain Ag particles with the green method [13]. AgNNPs with a size of 32 nm reduced with R. aculeatus plant extract showed high antimicrobial activity against Bacillus subtilis and Enterobacter aerogenes ATCC 13048 [14]. Different reductants, temperatures, mixing rate and times, as well as the method of fixing Ag particles to the composite have the potential to make significant changes in the physical and chemical properties of the composite. In this study, Ag particles were incorporated to PVDF-Cellulose composite mixed with cellulose at a ratio of 1:1 in order to increase the hydrophilic property by two different methods. Ag precipitation with NaBH4 in solution medium (Method I) and PVDF-Cellulose composites with Ag particles added precipitated with NaBH₄ (Method II) were prepared by phase inversion. The physical and filtration performances of membranes incorporating Ag into the PVDF-cellulose polymeric mixture by two different method, precipitation and powder mixing will be examined in this study for the first time according to our literature research. SEM, FTIR and TG-DTA analyses, porosity, water retention and contact angle measurements of the composites were performed. The performance of the composites in removing methyl orange as a model pollutant from water was tested in a filtration cell. Methyl orange is anionic character at neutral pH. It interacts with the membrane surface with the organic groups it contains, making it easier to obtain information about the surface structure. In addition, organic dyes such as methyl orange, Methylene Blue, Congo Red, and Malachite Green are frequently used in industrial activities and cause serious water pollution. Filtration, an advanced version of the traditional adsorption method, is a fast and practical solution.

Due to the functional groups of MO that tend to bond as a result of interaction, their widespread use in industry, and their polluting properties, various methods are being developed to separate them from water. [15,16]. Contamination accumulation of surface experiments and flux performances were reported in this study for Ag incorporated PVDF-Cellulose composites by two different methods.

2. Materials

In our previous study, cellulose particles separated from textile waste were mixed as composite material [11]. Polyvinylidene fluoride (PVDF; Solef 6010, mw:530.000) and analytical grade polymer solvent N,N-Dimethylacetamide (DMAC, 87.12 g/mol, 99%) were purchased from Sigma-Aldrich. Silver nitrate, AgNO₃ (169.87 g/mol, 4.350 g/cm³, ≥99%) and sodium borohydride (37.83 g/mol) were purchased from Sigma-Aldrich as silver salt. Methyl orange (MO, or Orange III) aqueous solution was used as model dye pollutant and distilled water were used as solvent and phase inversion, respectively.

2.1. Preparation of Ag particle added polymeric composites

The synthesis of Ag-doped composites was carried out by two different methods. Method I: 1.6 g of 1:1 PVDF-Cellulose mixture was dissolved in 10 ml of DMAc at 80 °C. Then, AgNO₃ at the amount 10% of the polymer was added in accordance with our former study [13] by stirring in a very small amount of solvent. NaBH₄, equal to the molar ratio of Ag, was added by stirring at a constant temperature. The mixture first turned orange-yellow and then dark brown due to the formation of Ag particles. The solution was poured onto a 20x20 cm glass surface and distributed to a thickness of approximately 250 µm. The glass plate was quickly placed in the water bath and the composite was prepared by phase inversion. The composite containing 10% Ag in proportion to the polymer mass was named AgP1. In the preparation of AgP2 composite with the method II, a polymer solution preparation process similar to AgP1 was applied. For this, first a certain amount of AgNO₃ was dissolved in 100 ml of water. NaBH₄ in Ag molar ratio was added slowly and stirred at 250 rpm. First a yellow then a dark brown precipitate was obtained. The precipitate was filtered and washed with pure water, dried at 40 °C and ground. For the homogenization, ground Ag particles were sieved through a 17-micron sieve. Ag particle at amount 10% of the polymer was added to the solution of PVDF-Cellulose in DMAc and mixed. Then, the mixture spread on the glass was phase inverted in a water bath to obtain AgP2. Ag-free PVDF-cellulose (PC) composite was prepared as a control sample with the same method. Ag particle and composite preparation steps were presented in Fig. 1.

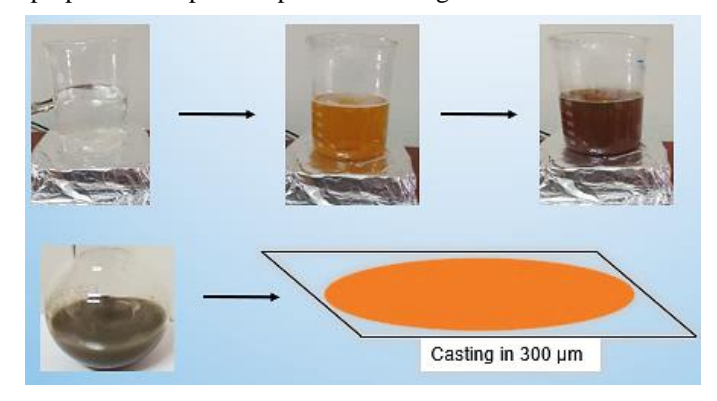


Fig. 1. Illustration of AgP and AgP-doped composite preparation.

2.2. Characterization

The properties of the composites were investigated by functional group, surface images and thermal analysis methods. FTIR analyses were performed with ATR method in the range of 650-4000 cm⁻¹ (Perkin Elmer). For SEM images, gold-coated composite surfaces were scanned at 10 kV power (Carl Size Ultra Plus). For cross-sectional surface images, composites were fractured and imaged in liquid nitrogen. For thermal analyses, 12-15 mg samples were heated at 10 °C/min heating rate in a 5 mL/min nitrogen atmosphere and were performed in the range of 25-700 °C (Seiko Exstar 7200 thermal analyzer). The mass change versus temperature graph was obtained. For the calculation of water retention capacity%, which is an important feature for membranes, the membranes were cut into 2x2 cm dimensions before being wet. They were weighed after being lightly wiped (Ww) by paper, composites were dried at 40 °C for two hours and weighed again (Wd). The same procedures were repeated with 3 repetitions. The WU% capacity of the membranes was calculated according to equation 1:

$$\mathbf{WU}(\%) = \frac{\mathbf{w_w} - \mathbf{w_d}}{\mathbf{w_w}} \mathbf{x100} \tag{1}$$

The porosity of the membranes was calculated in terms of %PO according to equation 2;

$$PO(\%) = \frac{W_W - W_d}{dA\delta} \times 100 \tag{2}$$

Here d is the density of pure water (1 g/ml), A is the membrane area (4 cm²) and δ is the thickness value of the wet membrane (cm) determined by the Insize thickness measuring device. Surface hydrophilicity is an indicator of the water permeability of the membranes and is determined by the contact angle measurement. The contact angle values of the membranes were measured with at least 3 repetitions according to the sessile drop method using the KSV Attention, Finland contact angle device.

2.3. Filtration and reusability tests

Pure water flux (PWF) tests of the membranes were performed in a constant flux cell. Flux values were calculated in Lm⁻²h⁻¹bar⁻¹. The flux pressure of the system was tested in the range of 0.5, 1 and 1.5 bar. Pure water was passed through the membranes and conditioned. Pure water flux calculation was made according to equation 3.

$$PWF = \frac{V}{At}$$
 (3)

In this equation, V represents the volume of pure water passing through the membrane (L), A represents the membrane area $(1.7x10^{-3} \text{ m}^2)$, and h represents the flux time. MO removal experiments were performed in the same membrane cell. Previously, the membrane was adjusted to constant flux with pure water. 3L, 40 mg/L MO solution was pumped into the filtration cell. The filtered MO concentration was analyzed in a UV-Vis spectrometer (Shimadzu, 2550) at 466 nm wavelength. MO removal performance was calculated according to equation 4:

$$\mathbf{E}_{\mathbf{AD}}(\%) = \left(\frac{c_0 - c_e}{c_0}\right) \mathbf{x} \mathbf{100} \tag{4}$$

Here C₀ is the initial concentration and C_e is the concentration of the filtered MO solution. The reuse efficiency of the membranes and their resistance to surface contamination were tested. For this purpose, the MO filtered membranes

were washed with 0.25 mol.L^{-1} hydrochloric acid and then the pure water flux values were measured. This process was repeated 3 times. The flux recoveries of the (FRR) membranes were calculated according to equation 5.

$$FRR(\%) = \left(\frac{PWF_3}{PWF_1}\right) \times 100 \tag{5}$$

PWF₁ represents the initial pure water flux of the membrane, PWF₃ represents the flux performance after the 3^{rd} iteration. Using the flux values, the reversible (R_r), irreversible (R_{ir}) and total fouling (R_t) rates resistances against the pollution accumulated on the membrane surface were calculated with equations 6-8 [17].

$$R_r(\%) = \left(1 - \frac{\text{PWF}_3 - \text{PWF}_2}{\text{PWF}_1}\right) \times 100$$
 (6)

$$R_{ir}(\%) = \left(1 - \frac{\text{PWF}_3}{\text{PWF}_1}\right) \times 100 \tag{7}$$

$$R_t(\%) = \left(1 - \frac{PWF_2}{PWF_1}\right) \times 100 \tag{8}$$

3. Results and discussion

3.1. Characterization

Infrared spectrums of pristine and composites presented in Fig.2 indicating the effect of Ag addition by two methods. Although it was mixed with cellulose, the characteristic peaks of PVDF were observed more clearly. This

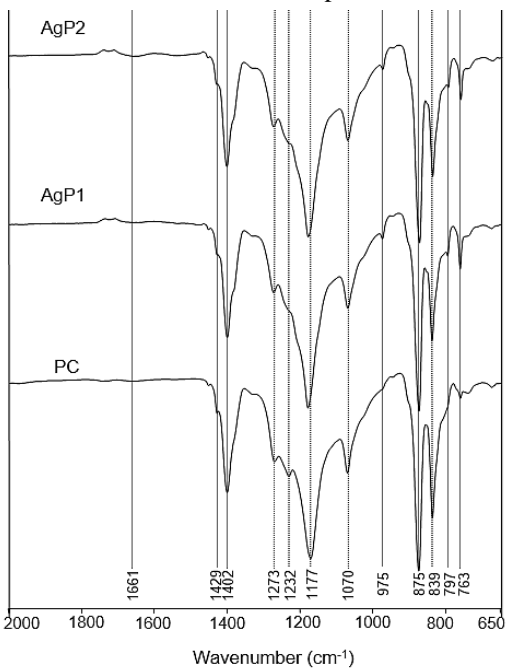


Fig. 2. FT-IR spectrum of PC and composites.

may be due to the differences in structural formation as a result of the PVDF-cellulose-powder interaction. CH and CF₂ bond stretching vibrations for PVDF were observed at 1403 and 877-1175 cm⁻¹ respectively [18]. CF stretching vibration corresponded to at around 1071-1072 cm⁻¹ and no exact change had been observed with Ag addition. α-phases of PVDF in PC could be seen by 763, and 975 cm⁻¹ bands [19]. The bands at around 838-840 cm⁻¹ with 1273 and 1431 cm⁻¹ confirmed the presence of α and β-phases. Intensity of 977 cm⁻¹ increased while a new clear band showing β-PVDF emerged at around 796 cm⁻¹ for all composites [20]. Intensity of characteristic 1232 cm⁻¹ band for PC decreased for modified samples. Reducing intensity of this band and emerging of new bands indicated that Ag addition resulted in noticeable readjustment for crystal phases of polymer and alpha/betha phases of PVDF increased. In addition to changes of crystallinity for PC, the bands emerged at around 1630-1661 cm⁻¹ for AgP1 and AgP2 represents carbonyl groups of amid bending vibrations from primary and secondary amines with the bands at around 1540 cm⁻¹ of N-H vibration [21].

At the SEM images of composites presented in Fig. 3 it was seen that cross section of PC consisted of sponge like (top) and finger-like structures (upper). Finger like channels shrink towards top surface of membrane and turned to pores which are main component for filtration. At the method I, Ag addition to polymer can be seen clearly from the SEM images. Thick skin layer on the top surface of AgP1 was best indicator for changes compared with pristine PC. A well dispersion and interaction of Ag with polymer matrix in dope solution effective due to application method (I). Another important change observed at the top surface of AgP1 was formation of noticeable pores on the surface of membranes. Pores with radius 205-327 nm width formed on the smooth surface of composite membranes. Although AgP2 has similar cross section structure as PC in terms of sponge and finger like structure distribution, tightly sequenced structure of AgP2 can be seen from the images. Agglomerated structures formed on the PC which reduce filtration performances of membrane became more compact. A lot of pores with 182-225 nm width were formed on the top surface of composites. Large quantity of pores indicated that slow phase inversion occurred in the phase inversion process due to high concentration of dope solution. The formation of porous structure on the AgP2 doped PC surface confirmed that phase inversion rate of AgP2 solution was faster than AgP1. It is understood from the results that the preparation method is very important, and that AgP1 creates a nearly uniform surface thanks to

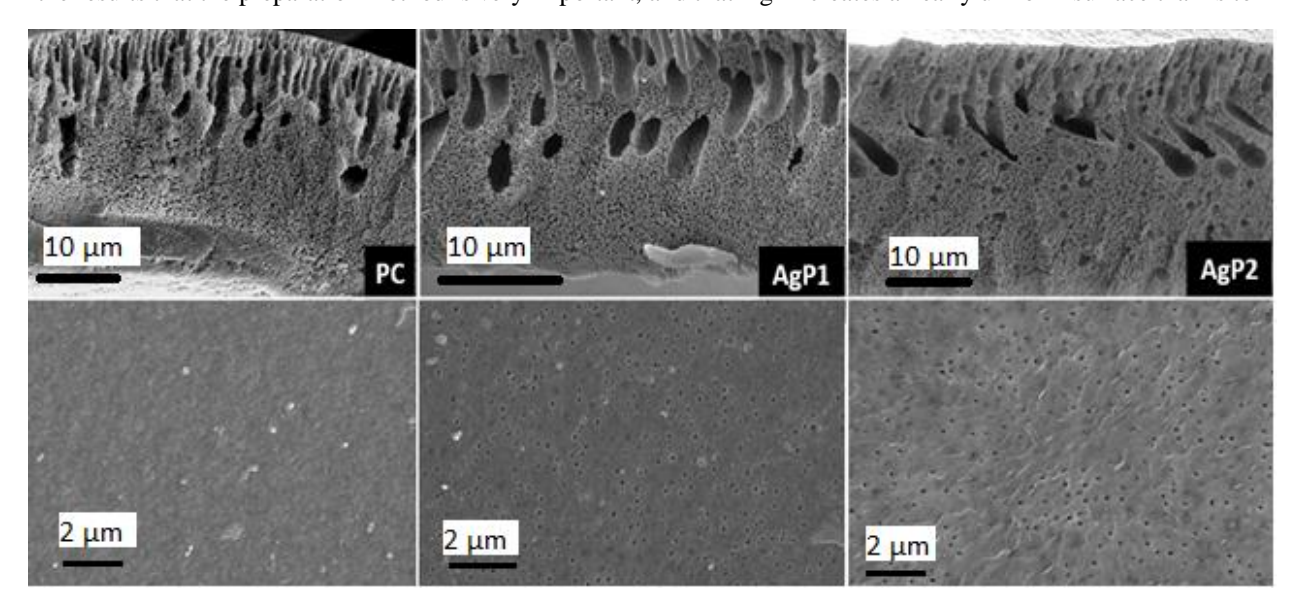


Fig. 3. SEM images of composites, cross section (top) and surface (bottom) respectively.

its homogeneous distribution and controlled nucleation. While precipitation in solution is difficult to control but provides a more homogeneous distribution, powder mixing is easy but results in heterogeneous formations. Thermal decomposition of PC and composites were investigated. Due to organic nature of polymer matrix, and very few amounts of Ag, a little number of residues had been observed after thermal analysis Fig. 4. Decomposition of PC and AgP1, AgP2 occurred at two stages at around 448-470 and 530-542 °C. Decomposition starts with breaking of CH and CF bonds of polymer and progresses by weight loss. Ag addition slightly decreased the decomposition temperature of PC. That may be core effect of Ag that absorb heat. Thus, the thermal degradation of the polymer accelerated. Polymer additives have the potential to alter the thermal behavior of the composite. This change depends on many factors, including the type and amount of additive, the polymer type, and the composite preparation method [22]. Also, dispersion of Ag among polymer chain can make cavities which are called as pores and channels effective in transportation and filtration. These additives weaken the structure rather than clay like additives strengthened effect. At the DTA curves of samples (Fig. 4), main exothermic peak emerged as a result of decomposition of organic structure was observed at decreasing temperatures for all samples. It was recorded at 558 °C for PC however it was 545 and 533 °C for AgP1 and AgP2 respectively. Water uptake and porosity of membranes were measured to observe

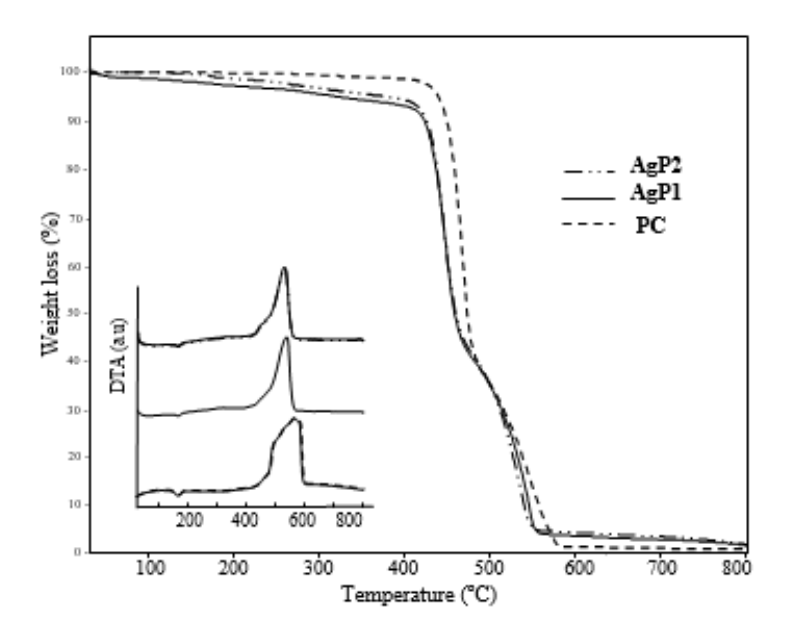


Fig. 3 Thermal analysis curves of PC and composites.

Ag addition effect with different methods. From the results presented at Table 1, water uptake values of AgP1 changed proportionally with its porosity values. Water uptake and porosity of composites were increased to 65.4 and 58.5% respectively. It can be concluded that increase in porosity promoted to increase of water absorbed inside the membrane which consequently measured as increasing at water uptake. Although there is a strong relationship between pore numbers (%) and water absorbed (%) inside the structure of a membrane, a different trend was observed with porosity and water uptake values of AgP2 compared with AgP1. Highest water uptake was obtained with AgP2 membrane. Presumably larger pores were formed inner site of the AgP2 composite due to enlarged molecular structure. The powders added to the polymeric structure is in the form of small particles. So, deviations from homogeneous distribution occurred. As a result, differences in attraction occur in nucleation, which changes the pore size during phase inversion. The surface hydrophilicity of the membranes was investigated. The Ag additive effective in terms of structural change as well as interaction with water molecules in changing the hydrophilicity of the surface. The contact

angle value of the PC composite was recorded as 64° due to the hydrophilic structure of cellulose [23]. The increase in the contact angle of AgP1 indicates that the structure has gained some hydrophobic properties. The reason for this is that the structure has become less rough with the addition of Ag. Thus, the penetration of water molecules into the membrane has slowed down. The reason for this is that the structure has become less rough with the addition of Ag. Thus, the penetration of water molecules into the membrane has slowed down. The main reason for the higher hydrophilicity of AgP2 is its rough surface. The more nonuniform distribution of Ag particles compared to AgP1 has increased the surface roughness. In parallel with this, the penetration of water droplets increased with the wide pores. The contact angle value is an effective parameter in adjusting the surface properties.

Table 1 Properties of composites.

Membrane	Water uptake (%)	Porosity (%)	Contact Angle (°)
PC	56.8±1.1	51.5±1.0	64±1.2
AgP1	65.4 ± 0.7	58.5 ± 0.8	75±1.3
AgP2	69.1 ± 0.8	55.8±1.5	73±1.1

3.2. Filtration results

The filtration tests of the membranes were carried out in a cylindrical flux cell at room temperature in the pressure range of 0.5-1.5 bar. After the permeability of the membrane was incorporated to the appropriate flux value with pure water, the MO solution was filtered. The pure water flux values and MO filtration performance of the membranes are presented in Fig. 5. While the flux values of the Ag-added composites prepared with both methods partially decreased compared to PC, the MO removal values of composites increased. AgP2 exhibited the highest pure water flux and good MO removal. Although the amount of Ag added to the polymer was the same, the change in the membrane structure was different and that affected the flux and removal performance. While the relatively more dispersed and varying-sized pore structure of AgP2 provided high flux performance, it caused a decrease in the MO removal efficiency. The highest MO removal performance of AgP1 was found to be 46.5% (those were 26.2 and 42.9% for PC and AgP2 respectively). The highest MO removal performance of AgP1 can be directly explained by the membrane structure. The solution precipitation method applied in the production of AgP1 provided a more uniform porous membrane thanks to the uniform distribution of Ag particles. The densely arranged and small porous pore structure compared to AgP2 and PC was effective in the removal of MO by AgP1. One of the many parameters affecting the filtration performance is the chemical properties of the filtered material. In this study, the MO solution was tested as a model pollutant at neutral pH value [24]. Heavy metals, medical wastes, organic-inorganic chemicals, dyes-oilspetroleum derivatives are the main substrates separated by filtration [25]. The interaction and bonding of the functional groups of the surface and the substrate or their repulsion is the most important feature that determines the filtration efficiency. Physical or chemical adsorption as a result of the repulsion of opposing groups provides a certain amount of pollution removal from the filtered solution. However, the accumulation of pollutant on the membrane surface usually causes a decrease in flux and therefore a decrease in filtration efficiency [26,27]. The resistance of the membranes to fouling accumulation was analyzed by measuring the pure water flux after MO filtration. After the membranes subjected to MO filtration, they were washed and rinsed in 0.25 mol/L acidic solution for 5 min, the pure water flux performances were measured. The experiments were repeated in 3 replicates and the FRR, reversible (R_r), irreversible (R_{ir}) and total fouling (R_t) values were calculated according to the equation [5-8] and the graphics are given in Fig. 5. When compared with PC, the FRR values of the composites increased, after MO filtration all FRR values decreased with different ratio. The best FRR was obtained with AgP2 with 89.2%. While the large pore structure resulted in decreased MO removal performance, the pores were less blocked. The mechanism of the decrease in the

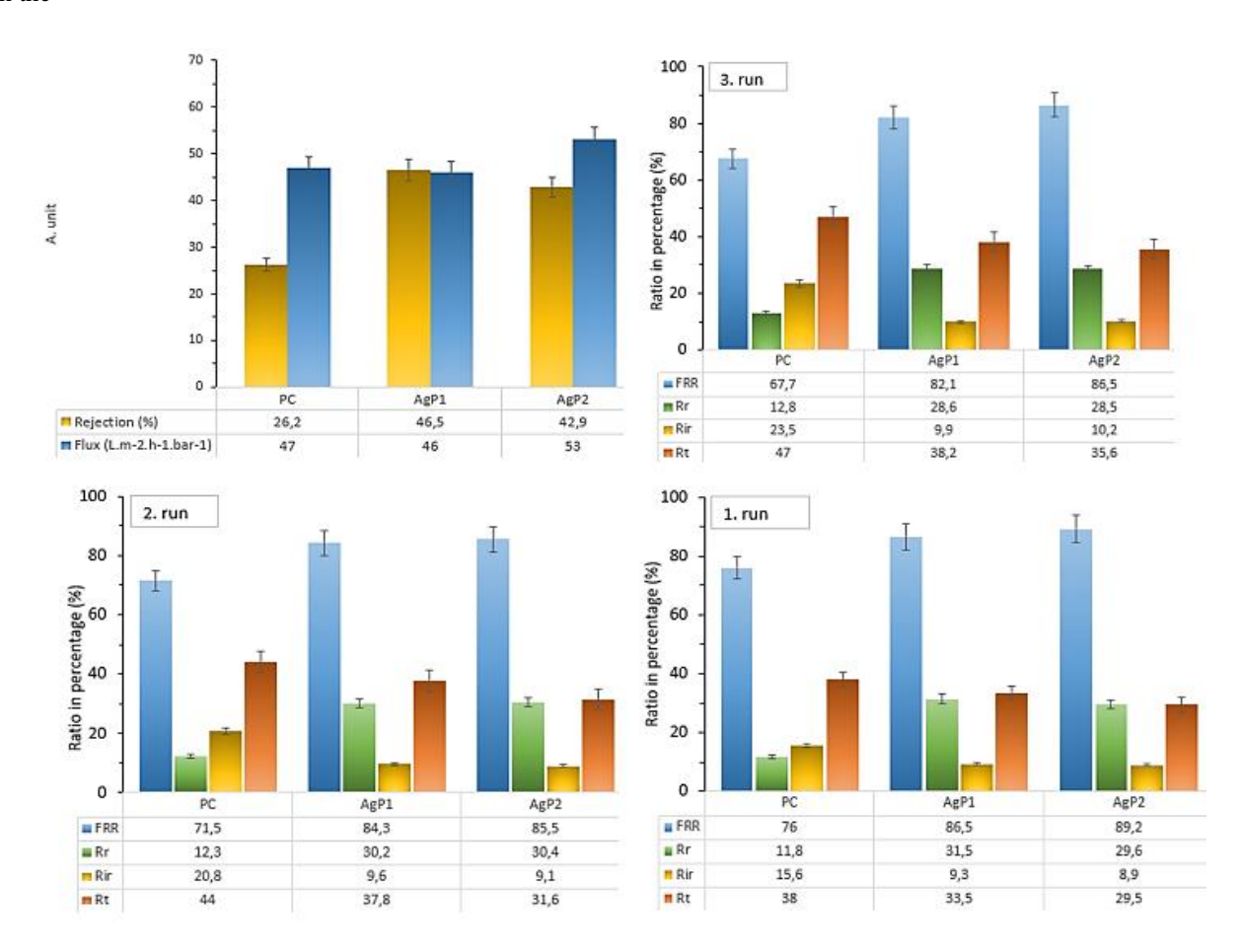


Fig. 5 MO removal and pure water flux, reversible (Rr), irreversible (Rir) and total fouling ratio (Rt) of MO filtrated P and composite membranes during 3-run recycling process. Area: 1.7x10⁻³ m², 1500 mL 40 mg/L MO solution, conditioning pressure = 1 bar, application pressure = 0.5 bar, three consecutive steps of MO filtration (1st step), filtration after water washing (2nd and 3rd step), time of washing = 5 min.

FRR value can be explained by the accumulation of fouling on the membrane surface and in the pores. The change in FRR in repeated uses provides information about the interaction of the fouling with the membrane. The R_r values of PC and composites increased very little rate close to the constant value, whereas R_{ir} reached the highest value only in PC. A little increase was observed in R_{ir} values of composites. These results mean that the MO accumulation on the composite surface occurs with weak interaction. Thus, the removal of contaminants from the surface becomes easier. High Rir indicates that the interaction between the surface and the contaminant molecules may be chemisorption and the clogging is more permanent [28]. R_t , which varies inversely with FRR values, indicates the total fouling value. The highest R_t was calculated with MO filtered PC flux values, while the lowest was obtained with AgP2. Considering the surface properties, AgP2 exhibited better filtration and pollution resistance despite containing roughness suitable for permanent settlement of pollutants. The main reason for this is the pore structure with different dimensions. This difference was effective in continuing its function as a result of clogging of small pores while clogging of large pores

less. There are 8-20% difference among the filtration performance of AgP1 and AgP2. However, the filtration performance of both composites is higher than PC. AgP1 exhibit better efficiency especially in the separation of oil-water mixtures thanks to its high hydrophobic feature. Additive anchoring is a method that has a great effect in regulating many properties of the polymeric structure. AgP1 and AgP2 composites offer different outputs worth applying with their different physical and filtration properties. Hydrophilicity and fouling have complex mechanisms that are shaped by many parameters such as membrane structure, pore volume and number, functional groups of the filtered molecule, and filtration conditions. Therefore, specific evaluation of each composite in terms of the filtered molecule and filtration conditions can yield more accurate results [29].

Conclusions

In this study, the physical and filtration properties of the composites prepared by fixing Ag particles to the PVDF-Cellulose mixture with different methods were investigated. The changes in the functional groups were investigated with FT-IR and the changes in the phase of the polymer were recorded. It was understood from the SEM images that the composites gained different properties as a result of the two methods. While AgP1 prepared with Method I had a more uniform and smoother structure, a rougher and more particle-like structure was formed in AgP2. The Ag additive caused both structures to decompose faster than PC by decreasing the decomposition temperature as a result of thermal heating. Flux, FRR and reusability of membranes were effective in the filtration efficiency. The hydrophobic structure of AgP1, understood from the high contact angle values, was more vulnerable in the accumulation of molecules on the surface. However, the small pores of AgP1 exhibited less resistance to clogging than AgP2. Despite its rough surface suitable for the adhesion of contaminants, AgP2 with heterogeneous pore sizes showed better filtration efficiency. AgP1 exhibited the highest MO removal as 46.5% compared to 26.2% for PC. The type of additive anchoring has the potential to directly affect the structure of the composite, and both Ag-doped composites provided better filtration efficiency than PC.

Acknowledgments

This work was financially supported by TUBİTAK (Scientific and Technological Research Council of Turkey) with grant number 222Z333.

Authors' contributions

Manuscript conception and design, experimental and interpretation, writing and supervision were conducted out by Huseyin Gumus.

References

- [1] Y. Zhang, X. Duan, B. Tan, Y. Jiang, Y. Wang, and T. Qi, "PVDF microfiltration membranes modified with AgNPs/tannic acid for efficient separation of oil and water emulsions," *Colloids and Surfaces A: Physicochemical and Engineering Aspects*, vol. 644, p. 128844, Jul. 2022, doi: 10.1016/j.colsurfa.2022.128844.
- [2] F. Liu, N. A. Hashim, Y. Liu, M. R. M. Abed, and K. Li, "Progress in the production and modification of PVDF membranes," *Journal of Membrane Science*, vol. 375, no. 1, pp. 1–27, Jun. 2011, doi: 10.1016/j.memsci.2011.03.014.
- [3] X. S. Yi *et al.*, "The influence of important factors on ultrafiltration of oil/water emulsion using PVDF membrane modified by nano-sized TiO₂/Al₂O₃," *Desalination*, vol. 281, pp. 179–184, Oct. 2011, doi: 10.1016/j.desal.2011.07.056.
- [4] A. İ. Yucak and F. U. Nigiz, "Emūlsifiye Edilmiş Yağın Polivinilflorür/PolivinilProlidin Membran İle Saflaştırılması," *ejosat*, no. 17, pp. 769–775, doi: 10.31590/ejosat. 643677.
- [5] Q. Li, Q. Bi, H.-H. Lin, L.-X. Bian, and X.-L. Wang, "A novel ultrafiltration (UF) membrane with controllable selectivity for protein separation," *Journal of Membrane Science*, vol. 427, pp. 155–167, Jan. 2013, doi: 10.1016/j.memsci.2012.09.010.
- [6] M. Tomaszewska, "Preparation and properties of flat-sheet membranes from poly(vinylidene fluoride) for membrane distillation," *Desalination*, vol. 104, no. 1, pp. 1–11, Apr. 1996, doi: 10.1016/0011-9164(96)00020-3.

- [7] A. S. Apaydın and P. Onsekizoğlu Bağcı, "Membran Ayırma Tekniklerinin Meyve Suyu İşlemedeki Uygulamaları," *Gıda*, vol. 50, no. 3, pp. 442–465, Jun. 2025, doi: 10.15237/gida.GD25027.
- [8] A. Mansourizadeh, A. F. Ismail, M. S. Abdullah, and B. C. Ng, "Preparation of polyvinylidene fluoride hollow fiber membranes for CO₂ absorption using phase-inversion promoter additives," *Journal of Membrane Science*, vol. 355, no. 1, pp. 200–207, Jun. 2010, doi: 10.1016/j.memsci.2010.03.031.
- [9] Q. Bi, Q. Li, Y. Tian, Y. Lin, and X. Wang, "Hydrophilic modification of poly(vinylidene fluoride) membrane with poly(vinyl pyrrolidone) via a cross-linking reaction," *Journal of Applied Polymer Science*, vol. 127, no. 1, pp. 394–401, 2013, doi: 10.1002/app.37629.
- [10] M. Z. Tufan and C. Özel, "Cellulose and its derivatives as biodegradable materials: A review," *Journal of Scientific Reports-A*, no. 059, pp. 87–104, Dec. 2024, doi: 10.59313/jsr-a.1498226.
- [11] H. Gumus and B. Buyukkidan, "Physicochemical properties and adsorption performances of textile waste based hydrolyzed cellulose-PVDF composites," *Rev. Roum. Chim.*, vol. 67, no. 3, pp. 197–205, 2022, doi: DOI: 10.33224/rrch.2022.67.3.08.
- [12] D. Komaraiah, E. Radha, J. Sivakumar, M. V. Ramana Reddy, and R. Sayanna, "Photoluminescence and photocatalytic activity of spin coated Ag+ doped anatase TiO₂ thin films," *Optical Materials*, vol. 108, p. 110401, Oct. 2020, doi: 10.1016/j.optmat.2020.110401.
- [13] H. Gumus, "Green synthesis of infrared controlled AgNP/graphite/polyvinylidene fluoride composite membranes for removal of organic pollutants," *Journal of Photochemistry and Photobiology A: Chemistry*, vol. 460, p. 116160, Mar. 2025, doi: 10.1016/j.jphotochem.2024.116160.
- [14] F. Karakaya, A. S. Bülbül, M. Bekmezci, and F. Şen, "Silver nanoparticle synthesis by biogenic reduction method and investigation of antimicrobial, antibiofilm, anticancer activities," *Journal of Scientific Reports-A*, no. 055, pp. 1–15, Dec. 2023, doi: 10.59313/jsr-a.1277894.
- [15] L. R. Buddiga, G. R. Gajula, and G. Jaishree, "Methyl Orange Dye degradation of dual doped TiO₂ nanoparticles under visible light Irradiation," *Journal of the Indian Chemical Society*, vol. 102, no. 9, p. 101938, Sep. 2025, doi: 10.1016/j.jics.2025.101938.
- [16] A. Ikhlaq et al., "Catalytic ozonation for the removal of methyl orange in water using iron-coated Moringa oleifera seeds husk," *Process Safety and Environmental Protection*, vol. 199, p. 107248, Jul. 2025, doi: 10.1016/j.psep.2025.107248.
- [17] Z. Chen et al., "Photocatalytic antifouling properties of novel PVDF membranes improved by incorporation of SnO₂-GO nanocomposite for water treatment," Separation and Purification Technology, vol. 259, p. 118184, Mar. 2021, doi: 10.1016/j.seppur.2020.118184.
- [18] Q. Wang, X. Wang, Z. Wang, J. Huang, and Y. Wang, "PVDF membranes with simultaneously enhanced permeability and selectivity by breaking the tradeoff effect via atomic layer deposition of TiO₂," *Journal of Membrane Science*, vol. 442, pp. 57–64, Sep. 2013, doi: 10.1016/j.memsci.2013.04.026.
- [19] F. Shi, Y. Ma, J. Ma, P. Wang, and W. Sun, "Preparation and characterization of PVDF/TiO₂ hybrid membranes with different dosage of nano-TiO₂," *Journal of Membrane Science*, vol. 389, pp. 522–531, Feb. 2012, doi: 10.1016/j.memsci.2011.11.022.
- [20] H. Dzinun, M. H. D. Othman, A. F. Ismail, M. H. Puteh, M. A. Rahman, and J. Jaafar, "Photocatalytic degradation of nonylphenol using co-extruded dual-layer hollow fibre membranes incorporated with a different ratio of TiO₂/PVDF," *Reactive and Functional Polymers*, vol. 99, pp. 80–87, Feb. 2016, doi: 10.1016/j.reactfunctpolym.2015.12.011.
- [21] Y. Mansourpanah and Z. Jafari, "Efficacy of different generations and concentrations of PAMAM–NH₂ on the performance and structure of TFC membranes," *Reactive and Functional Polymers*, vol. 93, pp. 178–189, Aug. 2015, doi: 10.1016/j.reactfunctpolym.2015.04.010.
- [22] A. A. Issa, M. A. Al-Maadeed, A. S. Luyt, D. Ponnamma, and M. K. Hassan, "Physico-Mechanical, Dielectric, and Piezoelectric Properties of PVDF Electrospun Mats Containing Silver Nanoparticles," C, vol. 3, no. 4, Art. no. 4, Dec. 2017, doi: 10.3390/c3040030.
- [23] Y. Ibrahim, E. Abdulkarem, V. Naddeo, F. Banat, and S. W. Hasan, "Synthesis of super hydrophilic cellulose-alpha zirconium phosphate ion exchange membrane via surface coating for the removal of heavy metals from wastewater," *Science of The Total Environment*, vol. 690, pp. 167–180, Nov. 2019, doi: 10.1016/j.scitotenv.2019.07.009.
- [24] H. Gumus and B. Buyukkidan, "Low-cost preparation of photocatalytic hydrolyzed cellulose composites, activated with one-step synthesized graphene oxide-metal oxide for dye degradation," *Cellulose*, vol. 32, no. 7, pp. 4573–4593, May 2025, doi: 10.1007/s10570-025-06521-y.
- [25] S. K. Ramachandran and P. Sathishkumar, "Membrane-based techniques for pollutants removal: An outlook on recent advancements," *Current Opinion in Environmental Science & Health*, vol. 36, p. 100513, Dec. 2023, doi: 10.1016/j.coesh.2023.100513.
- [26] A. Cemanovic, N. Manav, A. Kizilet, and O. Cinar, "Recent advances in membrane fouling control in wastewater treatment processes," vol. 3 no 2 2019
- [27] Y. A. Tayeh, M. Y. D. Alazaiza, T. M. Alzghoul, and M. J. Bashir, "A comprehensive review of RO membrane fouling: Mechanisms, categories, cleaning methods and pretreatment technologies," *Journal of Hazardous Materials Advances*, vol. 18, p. 100684, May 2025, doi: 10.1016/j.hazadv.2025.100684.
- [28] I. Ounifi et al., "Antifouling Membranes Based on Cellulose Acetate (CA) Blended with Poly(acrylic acid) for Heavy Metal Remediation," Applied Sciences, vol. 11, no. 10, p. 4354, May 2021, doi: 10.3390/app11104354.
- [29] R. Kumar and A. F. Ismail, "Fouling control on microfiltration/ultrafiltration membranes: Effects of morphology, hydrophilicity, and charge," *Journal of Applied Polymer Science*, vol. 132, no. 21, 2015, doi: 10.1002/app.42042.



Contents lists available at Dergipark

Journal of Scientific Reports-A

journal homepage: https://dergipark.org.tr/tr/pub/jsr-a



E-ISSN: 2687-6167 Number 62, September 2025

RESEARCH ARTICLE

Deep learning-based automated garbage image classification using light-weight models

Gozde Yolcu Oztela*

^aSakarya University, Software Engineering, Sakarya, TurkiyeORCID: 0000-0002-7841-2131

Abstract

Garbage classification is essential for various aspects like health, economy and environment. The awareness of the users' separation of garbage has not been gained yet. So, garbage classification is done manually in waste sorting facilities. This is timeconsuming and a difficult task; thus, automated systems are needed for this area. With this motivation, a deep learning-based system that provides automated classification of garbage has been developed in this study. In the study, five-types waste were used. These are glass, plastic, battery, paper and metal waste. Mobile Netv3, ShuffleNet, EfficientNetb2, SqueezeNet, GoogleNet and MobileViT models were retrained with the transfer learning approach to classify garbage images. According to the training and testing processes performed on the Garbage Dataset, EfficientNetb2 obtained the highest performance with 0.9768 accuracy, 0.9769 precision, 0.9768 recall, and 0.9768 F1-score values. To better demonstrate the benefits of transfer learning approach, EfficientNetb2 was also trained from scratch and almost 18% smaller accuracy score than transfer learning was obtained. Moreover, to evaluate system generalization ability, the trained EficientNetb2 model was tested on another dataset. 0.9700 accuracy, 0.9706 precision, 0.9700 recall, 0.9701 f1-score values were obtained in the second dataset. The high scores on the second dataset may be related to less complex data included in this dataset and high-system generalization capacity. The future target of the study may be to integrate the system into an embedded system. Therefore, light-weight models were specially selected. These models use fewer parameters, run in less time, and require less processing load, which are requirements of the embedded systems. This system can be used in smart city projects, waste management systems, and even the development of robotic waste collection technologies. In addition to helping reduce environmental pollution, it can also contribute to reducing human labor and contributing to recycling. © 2023 DPU All rights reserved.

* Corresponding author. Tel.: +90 (264) 295 32 39. *E-mail address*: gyolcu@sakarya.edu.tr

.

Keywords: Garbage image classification; transfer learning; deep learning; CNN; MobileViT.

1. Introduction

Garbage classification is a crucial task in terms of protecting the ecological environment and achieving resource reuse. Based on the World Bank, global waste volumes will be 2.59 billion tons by 2030 and 3.4 billion tons by 2050 [1]. Although, in many places, garbage classification is currently being done by the users who throw away the garbage, this awareness among people is still lacking [2]. Garbage classification is done by personnel at waste sorting facilities, which is a very time-consuming and difficult task. So, there is a critical need to develop automated computer vision-based systems to classify garbage.

On the other hand, garbage image classification is a challenging task for several reasons, such as complex image backgrounds, similar-shape categories, and low-quality images [3]. Owing to technological development, high-performance image analysis studies can be done in recent years [4,5,6]. For a high-performance image analysis, there are two critical needs. The first one is in sufficient quantity and quality training data. This requirement is ensured owing to next-generation camera systems and high-capacity storage devices. The second one is creating a well-designed model for the problem. In classical machine learning, there is feature extraction step. This process requires expert knowledge. Recently, owing to deep learning approaches, the feature extraction step is automatically applied. Thus, deep learning makes more effective image analysis possible.

Although there are some garbage classification studies in the literature, there are still some gaps in this field. In [7], Support Vector Machine (SVM) and Convolutional Neural Networks (CNN) approaches were compared to classify 3 types of waste, namely plastic, paper and metal. In their study, SVM was superior to CNN (94.8% vs. 83%). In [8], a dataset which includes two classes namely organic, and recyclable was used. This dataset was trained with the different deep learning architectures for waste classification tasks, and accuracy rates were compared. The authors' self-created CNN model showed the best accuracy as 91.84%. Different from these studies, the proposed study focused on 5-class garbage classification with high-performance rate. In [9], three Convolutional Blocks with different filter sizes and Mish activation function were used. The flattened output of the last MaxPool2D layer was used for three fully connected layers with Softmax activation for multi-class prediction. DenseNet169 obtained the best accuracy as 99.58%. In [10], YOLOv5 was used to detect waste, such as plastic, paper, glass, metal, cardboard, and biodegradables. [11] applied transfer learning based on the DenseNet169 pre-trained model for this task and classified five dataset types. 82% accuracy as obtained in their study. In [12], a garbage bin was designed, including the hardware structure and the mobile app. Then, a model based on ResNet-34 was created, and its structure was optimized. Finally, the superiority of the proposed system was evaluated with constructed garbage data.

Recently, deep learning approaches showed outstanding performance in computer vision problems, such as image classification, segmentation and detection [13,14]. Transfer learning provides high performance even with limited data by leveraging pre-trained models [15,16]. Inspired from this literature studies, this study presents a deep transfer learning-based automated system for five-class garbage image classification task. Some popular pre-trained networks such as MobileNet-v3_large, SqueezeNet, GoogleNet, MobileViT, EfficientNetb2, ShuffleNet were retrained for garbage image classification tasks, and their results were compared. The study has some contributions to the literature as follows:

- I. **High generalization capacity:** After training on a dataset, testing is applied on a second dataset, thus the system's generalization capacity is tested. It gives good results as reported in the Experimental Results section.
- II. **High-performance results with Light-weight models:** Light-weight models such as MobileNetv3, SqueezeNet, GoogleNet, and MobileVit were chosen for this task, because this study is planned as a first step for an embedded system that automatically separates the waste.

III. **Robust system owing to Transfer Learning:** In order to show benefits of the transfer learning, best-performing model has also been trained from scratch with the same training set. Approximately 18% lower results have been obtained in these experiments. This highlights the benefits of transfer learning.

2. Deep Transfer Learning for Garbage Image Classification

In the proposed system, different pre-trained models have been used for the garbage image classification task, and their results have been compared. For this purpose, firstly, the models that were trained initially with the ImageNet Dataset [17] have been used. The last layers of these models have been modified to classify 5-type waste images. Then, using the existing parameters, training has been applied. These operations are shown in Figure 1.

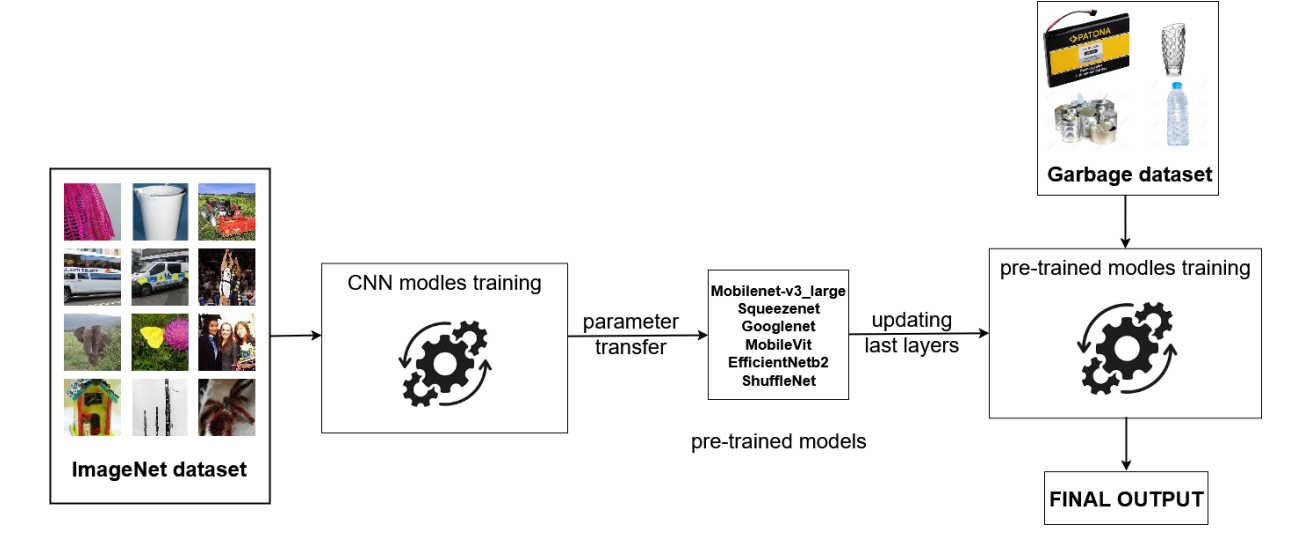


Fig. 1. Proposed system pipeline.

2.1. Convolutional neural network

Owing to deep learning, many problems have been solved with high efficiency and success rates recently. CNN, a subfield of deep learning, is used in image analysis problems. CNNs that take raw images as input can automatically perform feature extraction and classification stages.

CNNs are created by combining layers such as convolutional, pooling, dropout, fully-connected, and classification in different ways. In the convolutional layer, images are processed with filters, and feature maps are obtained using the convolution process as shown in Equation 1. In the equation, I is input image, K is kernel and S is the convolution result [18].

$$S(i,j) = (I * K)(i,j) = \sum_{m} \sum_{n} I(i+m,j+n) x K(m,n)$$
 (1)

In the pooling layer, the image size is reduced, this operation reduces processing load and prevents overfitting. Dropout is another approach to avoid overfitting. Owing to dropout, some neurons are ignored along with their

connections in some iterations.

In applications, CNNs can be structured and trained from scratch or transfer learning can be used. Transfer learning is using a pretrained successful model for a new task. This approach usually obtains high success rates in a shorter time [19]. Transfer learning shows successful results in different tasks, such as remote sensing [20,21], medical image analysis [22], face analysis [23], etc.

In this study, using transfer learning approach, some pre-trained networks were retrained for the garbage image classification task instead of designing a CNN from scratch. They showed successful performances, and their success rates were compared based on different metrics. Light-weight models were chosen because this system can be integrated with an embedded system. The used networks and some of their features are shown in Table 1. Floating Point Operations Per Second (FLOP) is a performance measure, expressing the number of floating-point operations that the system can perform per second. It is used in areas that require high computational power, such as deep learning. The FLOP values of the models used in this study are also shown in Table 1.

Network	#Parameter (M)	Size (MB)	FLOP	Depth	Input Size
MobileNet-v3_large [24]	5.48	21.1	231.32 MMac	62	224x224
SqueezeNet [25]	1.24	4.7	836.82 MMac	26	227x227
GoogleNet [26]	6.62	49.7	1.51 GMac	59	224x224
MobileViT [27]	5.6	19	N.A.	20	256x256
EfficientNetb2 [28]	9.1	35.2	410.2 MMac	115	260x260
ShuffleNet [29]	1.36	5.3	152.39 MMac	56	224x224

Table 1. Used Networks and their features.

2.2. Mobile vision transformer model

Although CNNs work with fewer parameters than transformers, CNNs are spatially local. Vision transformers can learn global representations. On the other hand these models are heavy-weight. To combine the strengths of CNN and Vision transformer Networks; the Mobile Vision Transformer (MobileViT) Network was developed.

MobileViT architecture is formed by combining classic convolution and MobileNet blocks [27]. While convolution performs local processing, MobileViT blocks transform this local processing into global processing using transformers. Compared to transformers, training is performed with fewer parameters in MobileViT. Figure 2 shows general architecture of MobileViT. Convolution layers learn general features such as edge, colors, texture, etc. Owing to MobileNet blocks, deeper features can be learned. MobileViT blocks divide the image into patches. Using transformer encoder, it learns long-range dependencies. Finally, owing to fully connected and softmax layer, the prediction is applied.

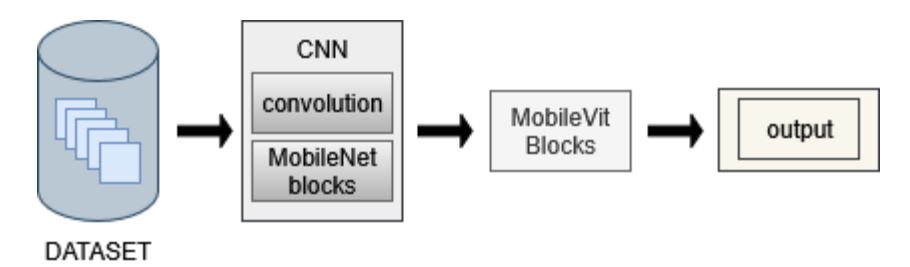


Fig. 2. MobileViT structure.

3. Experimental Results

In this study, experiments were performed using the Google Colab platform. Models were trained efficiently with GPU support. PyTorch and torchvision libraries were used in pretrained model loading and data preparation steps. Pre-trained MobilViT model was used in the study with timm library [30].

3.1. Dataset and data preparation

In the proposed study, training and testing have been applied using a publicly available dataset, namely Garbage Dataset [31,32]. The dataset includes 10 distinct classes of garbage with 19,762 images. It contains common household waste items for a wide range of applications. In the study, five recyclable garbage classes [33,34] are used.

In deep learning applications, a large amount of data is needed, and the amount of data affects the success rate. Different methods can be applied to increase data amounts, such as synthetic data generation and data augmentation. Based on [35], using high-quality data significantly improves the system performance. In this study, some data augmentation approaches are used to increase the amount of data. These are given in Table 2.

Table 2. Data augmentation processes which are applied to Garbage Dataset.

Flipping	Horizontal and vertical
Rotation btw	-15 and +15
Shearing	+/- 10 vertical and horizontal

The class' name and data distribution of the used dataset are given in Table 3.

Table 3. Dataset classes and number of images for each class.

Class	# Total sample
Plastic	1984
Metal	1020
Glass	3061
Paper	1680
Battery	944

Looking at the sample counts in the dataset, the class with the fewest samples is battery, with 944. A new dataset was created by randomly selected samples from all classes using balanced splitting, with 944 samples. Then, the subsets have been created with randomly selected samples as 80% training, 10% validation, and 10% testing (approximately). This results in a balanced distribution across classes in the new dataset, with 755 samples for training, 94 for validation, and 95 for testing per class. Figure 3 illustrates some samples from different classes of Garbage Dataset.

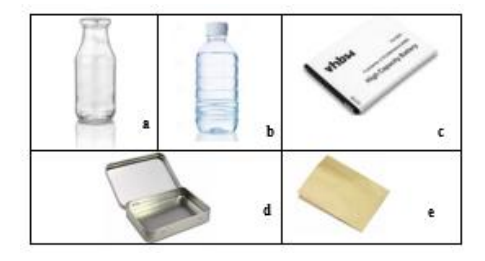


Fig. 3. Some samples from the dataset [31,32] (a) glass; (b) plastic; (c) battery; (d) metal; (e) paper.

In order to evaluate the system's generalization ability, another dataset has also been used for testing. This is also a publicly available dataset, which is included in Kaggle [36]. To provide clarity of the paper, this dataset name will be mentioned as Garbage Classification-2 dataset. This dataset contains 12 classes with 15150 image samples. In this study, the battery, glass, paper, plastic, and metal classes, which are common with the first Garbage Classification dataset, have been used for test purpose. In the Garbage Classification-2 dataset, there are 3 types of glass classes, namely, green glass, white glass, and brown glass. These are combined into a single glass class to match the classes with the first dataset. This dataset includes 945 battery, 2011 glass, 1050 paper, 865 plastic, 769 metal samples. All of these samples have been used for testing purpose, training has not been applied using this dataset.

3.2. Comparative results

3.2.1. Used parameters

This study performed experiments on different pre-trained models, and their results were compared. For a fair comparison, the same parameters were used for all models, which have been reported in Table 4.

Table 4. Training parameter.	
Optimizer	Adam
Learning rate	0.001
Image size	224x224
Loss function	Cross entropy loss
#Epochs	100

Table 4. Training parameter

3.2.2. Used evaluation metrics

In the literature, the classification systems are usually evaluated using the accuracy, precision, recall, and F1-score metrics. Thus, in this study, the evaluation has been applied using these metrics (eq. 2-5).

$$Accuracy = \frac{TP + TN}{TP + FP + TN + FN} \tag{2}$$

$$Precision = \frac{TP}{TP + FP} \tag{3}$$

$$Recall = \frac{TP}{TP + FN} \tag{4}$$

$$F1 - score = \frac{2xPrecisionxRecall}{Precision+Recall}$$
 (5)

where, TP is true positive, FP is false positive, FN is false negative, and TN is true negative.

3.2.3. Experiments

The comparative results of the models are given in Table 5. In this table, weighted precision, weighted recall, and weighted F1-score are shown. As seen, in terms of success rate metrics, EfficientNetb2 outperformed other models. Its parameter number is greater than others, as mentioned in Table 1. Thus, this is an expected result. The accuracy-epoch and loss-epoch graphs for EfficientNetb2 training are given in Figure 4.

Table 5. Model comparison table.

Model	ACC	Precision	Recall	F1-score	Inference time (ms)
MobileNet-v3-large	0.9684	0.9690	0.9684	0.9685	8.03
SqueezeNet	0.9284	0.9297	0.9284	0.9285	9.30
GoogleNet	0.9600	0.9609	0.9600	0.9601	11.04
MobileViT	0.9558	0.9559	0.9558	0.9557	11.60
EfficientNetb2	0.9768	0.9769	0.9768	0.9768	18.48
ShuffleNet	0.9495	0.9497	0.9495	0.9493	8.52

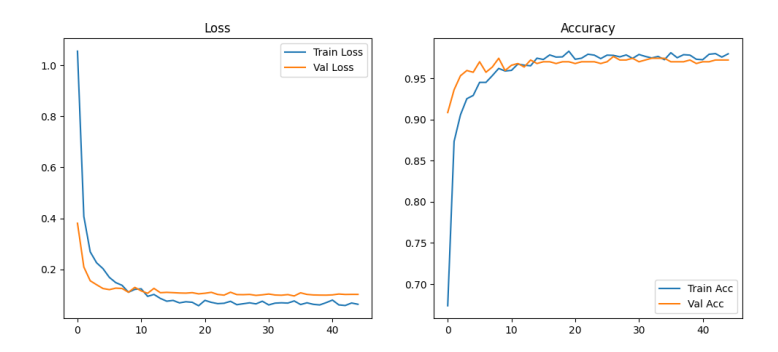


Fig. 4. The accuracy-epoch and loss-epoch graphs for efficientNetb2.

As seen from Figure 4, the training and validation losses were initially high, decreased rapidly, and reached a low and stable level starting around epoch 10. Similarly, the training and validation accuracy rates increased rapidly within the first few epochs and stabilized at 96%. The close performance between training and validation demonstrates that the model is not prone to overfitting and has good generalization ability. These results demonstrate that the proposed model performs with high accuracy and stability in the classification task.

Figure 5 shows some samples from false predictions. As seen in Figure 5, some images are complex to distinguish their classes. For example, Figure 5a can be considered as metal by human eyes. Similarly, in Figures 5b and 5c; plastic and glass can be very confusing to distinguish from images. In these classes, false predictions can be explained for this reason. Figure 5d includes many materials from different types. The confusion can be related to this situation.

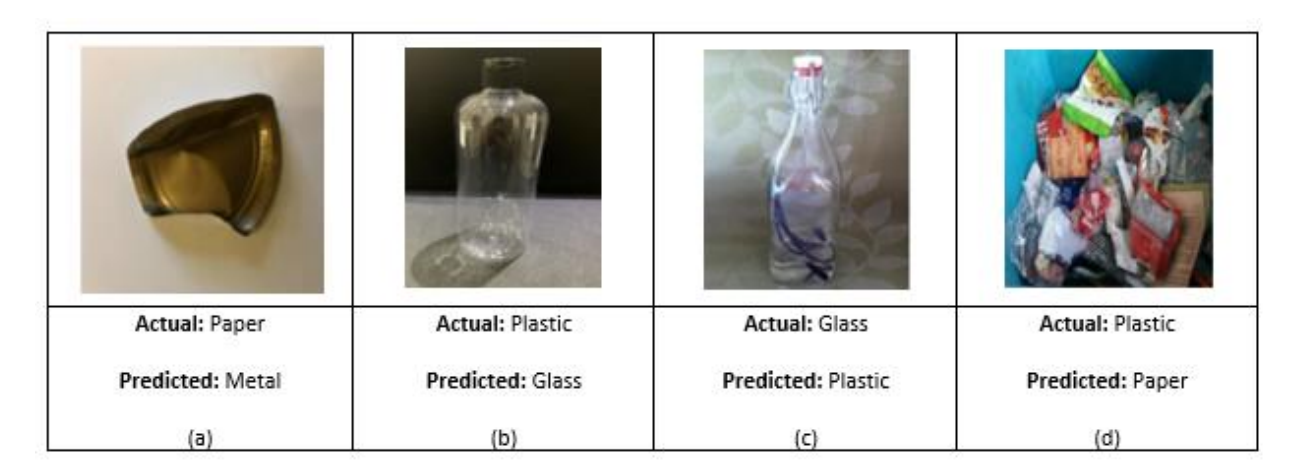


Fig. 5. Some visual results for efficientb2 on Garbage Dataset [31,32]. (a) actual: paper, predicted: metal, (b) actual: palastic, predicted: glass, (c) actual: glass, predicted: plastic, (d) actual: plastic, predicted: paper

In order to evaluate system generalization capacity, the trained efficientNetb2 model was also tested on another dataset. The test on this dataset showed successful results. The scores are as follows: accuracy: 0.9700, precision: 0.9706, recall: 0.9700, f1-score: 0.9701. It is observed that, the Garbage Classification-2 dataset includes more clear and less complex images compared to the first Garbage Classification dataset. The high scores may be explained by this state and high-capacity system generalization capacity.

To emphasize the benefits of transfer learning, other experiment has been applied. In this experiment, the EfficientNetb2 model, which shows the best performance as reported Table 5, has been retrained from scratch with randomly initialized filter values instead of transfer learning weights. In this experiment, 79.16% test accuracy, 79.71% precision, 79.16% recall, and 79.24% f1-score values have been obtained. Achieving 97.68 %, accuracy score, the transfer learning-based model clearly demonstrates the benefits of utilizing pre-trained weights. The confusion matrix for transfer learning of EfficientNetb2 is given in Figure 6(a), and training from scratch of EfficientNetb2 is given in Figure 6(b). As seen from this figure, compared to transfer learning, the correct predictions are slightly lower.

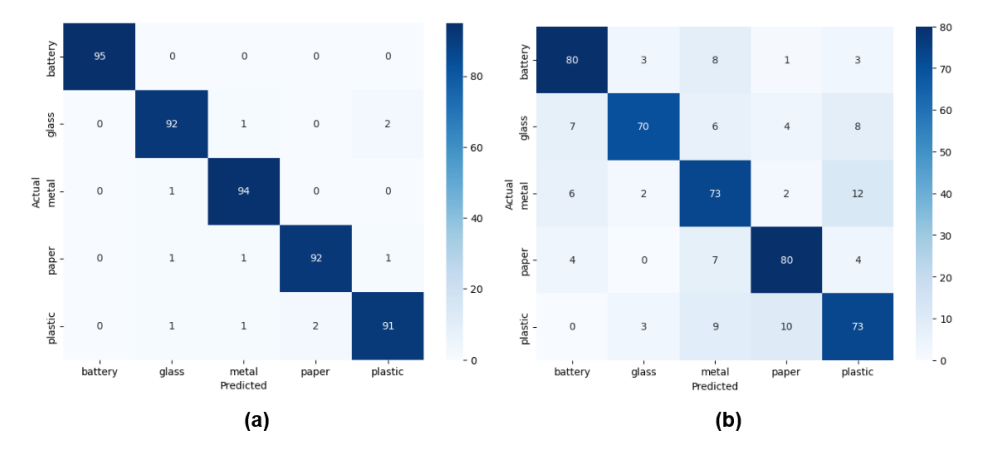


Fig. 6. Confusion matrix for (a) transfer learning, (b) training from scratch for efficientNetb2.

In another experiment, a random sample was selected in the test dataset, and noise, occlusion and dark light effects have been applied on the images using random different parameters. All original figures and modified figures have been used for best model, EfficientNetb2, and the model predicts its classes. The results can be seen Figure 7. As can be seen from the figure, the model's performance under various conditions is promising. The battery and metal images were correctly predicted by the model in all cases. For the glass class image, the model incorrectly classified the images under occlusion and dark light conditions. For the paper and plastic classes, the error occurred in the noise-added images.

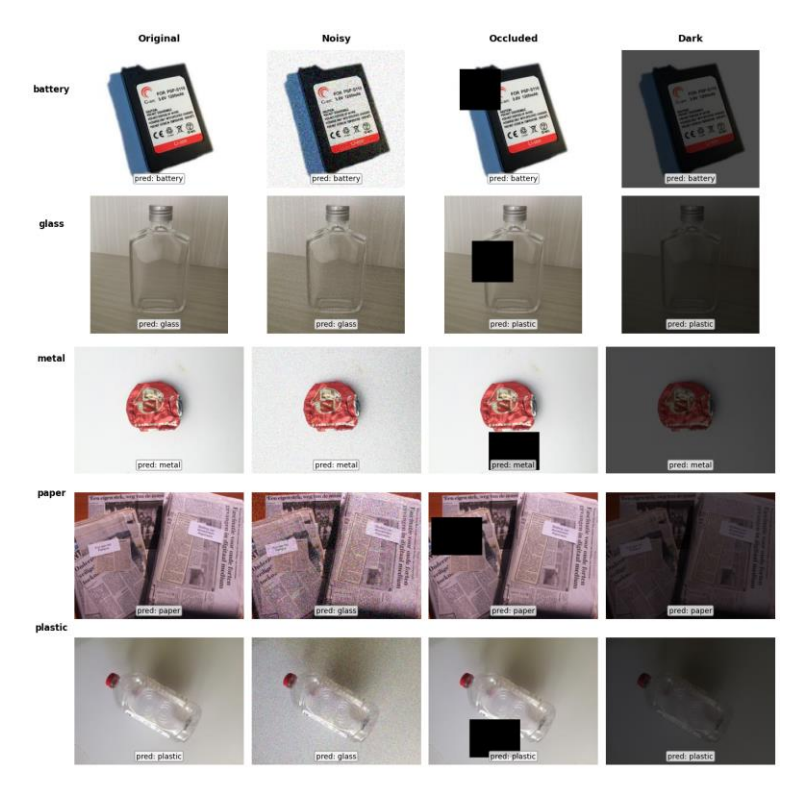


Fig. 7. System performance in different conditions.

3.3. Discussion

Experimental results indicate that while the system generally produces high-performance responses, some images were detected incorrectly. An examination of these false results revealed that this was due to visual similarity and background effects. Furthermore, the system's performance under occlusion, varying noise, and lighting conditions was analyzed. It was observed that it was less affected by these conditions and generally performed at high performance. The models used in the study are lightweight and suitable for use in embedded systems; they require little energy and resources. This system reduces the need for human labor, accelerates waste separation and improves accuracy, and contributes to environmental cleanliness.

4. Conclusion

This study presents an automated tool for garbage image classification task. In the study, different pre-trained

models were trained and tested for the garbage image classification task, and their results were compared. The EfficientNetb2 model performed best with 0.9768 accuracy, 0.9769 precision, 0.9768 recall, and 0.9768 F1-score values. As an ablation study, the EfficientNetb2 model, which shows the best performance, has been trained from scratch and almost 18% lower accuracy score was obtained. This approach emphasizes the impact of transfer learning in improving performance.

Another test was applied to a second dataset to better demonstrate the system generalization capacity. Based on the observations, the second dataset includes clearer images than the first dataset. Thus, high scores as 0.9700 accuracy, 0.9706 precision, 0.9700 recall, and 0.9701 f1-score values were obtained on this dataset.

This study contributes to the literature in terms of comparing the different deep-learning models for garbage image classification tasks. It can assist the personnel in classifying the garbage. Thus, it can help protect the ecological environment and achieve resource reuse. In the future, a real-time version of this study can be developed and integrated into garbage bins. Thus, automatic warning mechanisms can be designed to ensure that users throw their trash into the correct garbage bins.

Acknowledgements

This work did not benefit from external financial assistance from any public, commercial, or non-profit granting institutions.

Author contribution

Article was prepared by single author.

References

- [1] S. Kaza, R. Y. McDonald, and L. L. Zilberti, "What a Waste 2.0: A Global Snapshot of Solid Waste Management to 2050," *The World Bank*, Washington DC, 2018.
- [2] C. Zhihong, Z. Hebin, W. Yanbo, L. Binyan, and L. Yu, "A vision-based robotic grasping system using deep learning for garbage sorting," 2017 36th Chinese Control Conference (CCC), IEEE, 2017, pp. 1216–1221, doi: 10.23919/chicc.2017.8029147.
- [3] X. Li, T. Li, S. Li, B. Tian, J. Ju, T. Liu, and H. Liu, "Learning fusion feature representation for garbage image classification model in human-robot interaction," *Infrared Physics & Technology*, vol. 126, pp. 104457, 2023, doi: 10.1016/j.infrared.2022.104457.
- [4] N. S., V. R. K. Prabu, and K. R. Bhandari, "Computer Aided Based Performance Analysis of Glioblastoma Tumor Detection Methods using UNET-CNN," Int. J. Comput. Exp. Sci. Eng., vol. 10, no. 4, pp. 215–220, 2024, doi: 10.22399/ijcesen.515.
- [5] A. Toprak, "Determination of Colorectal Cancer and Lung Cancer Related LncRNAs based on Deep Autoencoder and Deep Neural Network," *Int. J. Comput. Exp. Sci. Eng.*, vol. 10, no. 4, pp. 201–210, 2024, doi: 10.22399/ijcesen.636.
- [6] K. B. Devananda Rao and M. Madhavi, "BCDNet: A Deep Learning Model with Improved Convolutional Neural Network for Efficient Detection of Bone Cancer Using Histology Images," *Int. J. Comput. Exp. Sci. Eng.*, vol. 10, no. 4, pp. 150–158, 2024, doi: 10.22399/ijcesen.430. [7] G. E. Skar, M. Mokbel, M. N. Darwich, A. Hadi, and A. Khneisser, "Comparing deep learning and support vector machines for autonomous waste sorting," 2016 IEEE Int. Multidisciplinary Conf. Eng. Technol. (IMCET), pp. 207–212, 2016.
- [8] A. Sevinç and F. Ozyurt, "Classification of recyclable waste using deep learning architectures," Firat University Journal of Experimental and Computational Engineering, vol. 1, no. 3, pp. 122–128, 2022, doi: 10.5505/fujece.2022.83997.
- [9] N. Haque, R. Toufiq, M. D. Z. Islam, and M. A. A. T. Shoukhin, "Garbage Classification Using a Transfer Learning with Parameter Tuning," 2024 6th Int. Conf. Electr. Eng. Inf. Commun. Technol. (ICEEICT), pp. 1252–1256, 2024, doi: 10.1109/iceeict62016.2024.10534450.
- [10] E. Z. Kuang, K. R. Bhandari, and J. Gao, "Optimizing Waste Management with Advanced Object Detection for Garbage Classification," arXiv, 2024, doi: 10.48550/ARXIV.2410.09975.
- [11] Q. Zhang, Q. Yang, X. Zhang, Q. Bao, J. Su, and X. Liu, "Waste image classification based on transfer learning and convolutional neural Network," *Waste Management*, vol. 135, pp. 150–157, 2021, doi: 10.1016/j.wasman.2021.08.038.
- [12] Z. Kang, J. Yang, G. Li, and Z. Zhang, "An Automatic Garbage Classification System Based on Deep Learning," *IEEE Access*, vol. 8, pp. 140019–140029, 2020, doi: 10.1109/access.2020.3010496.
- [13] A. Khan, A. Sohail, U. Zahoora and A. S. Qureshi, "Deep Learning for Image Classification: A Comprehensive Review," in *IEEE Access*, vol. 8, pp. 85225-85265, 2020, doi: 10.1109/ACCESS.2020.2992555.
- [14] N. Sindhwani, R. Anand, M. S., R. Shukla, M. P. Yadav ve V. Yadav, "Performance Analysis of Deep Neural Networks Using Computer Vision," *EAI Endorsed Transactions on Industrial Networks and Intelligent Systems (INIS)*, volume 8, issue 29, Oct 2021, doi: 10.4108/eai.13-10-2021.171318.

- [15] A. Brodzicki, M. Piekarski, D. Kucharski, J. Jaworek-Korjakowska ve M. Gorgoń, "Transfer Learning Methods as a New Approach in Computer Vision Tasks with Small Datasets," *Foundations of Computing and Decision Sciences*, cilt 45, sayı 3, ss. 179–193, Eyl 2020, doi: 10.2478/fcds-2020-0010.
- [16] R. Joshi, A. Maritammanavar, A. Singh and C. Kumar, "Transfer Learning in Computer Vision: Technique and Applications," *Journal of Propulsion Technology*, vol. 44, no. 1, pp. 81–83, Mar. 2023, doi: 10.52783/tjjpt.v44.i1.2210.
- [17] J. Deng, W. Dong, R. Socher, L.-J. Li, K. Li, and L. Fei-Fei, "ImageNet: A large-scale hierarchical image database," in Proc. 2009 IEEE Conf. Comput. Vis. Pattern Recognit. Workshops (CVPR Workshops), 2009, IEEE, doi: 10.1109/cvpr.2009.5206848.
- [18] I. Goodfellow, Y. Bengio, and A. Courville, Deep Learning, MIT Press, 2016.
- [19] I. Oztel, G. Yolcu, C. Oz, "Performance Comparison of Transfer Learning and Training from Scratch Approaches for Deep Facial Expression Recognition," in Proc. 2019 28th IEEE International Conference on Computer Science and Engineering (UBMK 2019), 11-15 September 2025, Samsun, Turkey.
- [20] J. Doe, & A. Smith, "Apple tree health recognition through the application of transfer learning for UAV imagery". *Journal of Precision Agriculture*, 2023.
- [21] L. Zhang and Y. Li, "Convolutional Neural Network for Remote-Sensing Scene Classification: Transfer Learning Analysis," *Remote Sensing Letters*, vol. 12, no. 3, pp. 245–258, 2021.
- [22] A. W. Salehi et al., "A study of CNN and transfer learning in medical imaging: Advantages, challenges, future scope," *Sustainability*, vol. 15, no. 7, Art. no. 5930, 2023, doi: 10.3390/su15075930
- [23] X. Cao, D. Wipf, F. Wen, G. Duan, and J. Sun, "A practical transfer learning algorithm for face verification," in *Proc. IEEE International Conference on Computer Vision (ICCV)*, 2013, pp. 3208–3215.
- [24] A. Howard, M. Sandler, G. Chu, L.-C. Chen, B. Chen, M. Tan, W. Wang, Y. Zhu, R. Pang, V. Vasudevan, Q. V. Le, and H. Adam, "Searching for MobileNetV3 (Version 5)," arXiv, 2019. [Online]. Available: https://doi.org/10.48550/ARXIV.1905.02244.
- [25] F. N. Iandola, S. Han, M. W. Moskewicz, K. Ashraf, W. J. Dally, and K. Keutzer, "SqueezeNet: AlexNet-level accuracy with 50x fewer parameters and <0.5MB model size (Version 4)," arXiv, 2016. [Online]. Available: https://doi.org/10.48550/ARXIV.1602.07360.
- [26] C. Szegedy, W. Liu, Y. Jia, P. SermaNet, S. Reed, D. Anguelov, D. Erhan, V. Vanhoucke, and A. Rabinovich, "Going deeper with convolutions (Version 1)," arXiv, 2014. [Online]. Available: https://doi.org/10.48550/ARXIV.1409.4842.
- [27] S. Mehta and M. Rastegari, "MobileViT: Light-weight, general-purpose, and mobile-friendly vision transformer (Version 2)," arXiv, 2021. [Online]. Available: https://doi.org/10.48550/ARXIV.2110.02178.
- [28] M. Tan and Q. V. Le, "EfficientNetV2: Smaller models and faster training," arXiv, 2021. [Online]. Available: https://doi.org/10.48550/ARXIV.2104.00298.
- [29] X. Zhang, X. Zhou, M. Lin, and J. Sun, "ShuffleNet: An extremely efficient convolutional neural Network for mobile devices (Version 2)," arXiv, 2017. [Online]. Available: https://doi.org/10.48550/ARXIV.1707.01083.
- [30] timm (PyTorch Image Models), "timm," 2024. [Online]. Available: https://huggingface.co/timm.
- [31] S. Kunwar, "Garbage dataset [Dataset]," Kaggle, 2024. [Online]. Available: https://doi.org/10.34740/KAGGLE/DSV/10182596.
- [32] S. Kunwar, "Managing household waste through transfer learning (Version 1)," arXiv, 2024. [Online]. Available: https://doi.org/10.48550/ARXIV.2402.09437.
- [33] Hillsborough County Recycling, "Hillsborough recycling guide," 2023. [Online]. Available: https://www.nieonline.com/tbtimes/downloads/supplements/2023HillsboroughRecycling_ENGLISHlo.pdf.
- [34] B. Huang, Z. Pan, X. Su, and L. An, "Recycling of lithium-ion batteries: Recent advances and perspectives," *J. Power Sources*, vol. 399, pp. 274–286, 2018, Elsevier BV.
- [35] S. Nesteruk, S. Illarionova, and A. Somov, "Image Dataset Augmentation A Survey and Taxonomy" Measurements and Instrumentation for Machine Vision, 2024, ISBN: 9781003343783
- [36] M. Mohamed, "Garbage classification (12 classes),", Kaggle, 2020.



Contents lists available at Dergipark

Journal of Scientific Reports-A

journal homepage: https://dergipark.org.tr/tr/pub/jsr-a



E-ISSN: 2687-6167 Number 62, September 2025

RESEARCH ARTICLE

Prioritization of renewable energy resources using intuitionistic fuzzy AHP and VIKOR methods: TR33 region example

Bahadır Yörür^a*, Emir Ay^b, Nutiye Şentürk^c, Hilem Orman^d, Simge Hilal İvacık^e

- ^{a,*}Kütahya Dumlupinar University, Enginnering Faculty, Industrial Enginnering Department, 43100, Kutahya, Türkiye, ORCID: 0000-0003-4370-4238
- ^bKütahya Dumlupinar University, Enginnering Faculty, Industrial Enginnering Department, 43100, Kutahya, Türkiye, ORCID: 0009-0000-1427-3737
- ^cKütahya Dumlupinar University, Enginnering Faculty, Industrial Enginnering Department, 43100, Kutahya, Türkiye, ORCID: 0009-0002-6690-542X
- ^dKütahya Dumlupinar University, Enginnering Faculty, Industrial Enginnering Department, 43100, Kutahya, Türkiye, ORCID: 0009-0002-8541-2276
- ^eKütahya Dumlupinar University, Enginnering Faculty, Industrial Enginnering Department, 43100, Kutahya, Türkiye, ORCID: 0009-0004-2936-2432

Abstract

Growing economies and the increasing world population increase electricity demand, one of the most important requirements of social and economic life. A large part of electricity generation is provided by fossil fuels, which brings environmental problems. Various initiatives are being taken around the world to overcome ecological problems. The last of these initiatives is the Paris Climate Agreement, in which Türkiye recently became a party. In accordance with this agreement, Türkiye is carrying out studies towards the net-zero carbon target in line with the 2030 interim target and the 2053 final target. Within the scope of studies carried out in the energy field, it aims to reduce carbon emission levels by increasing the installed capacity of renewable energy. The subject of this study is prioritizing renewable energy resources for the TR33 Region covering Manisa, Uşak, Kütahya and Afyonkarahisar provinces. An integrated methodology is used to prioritize energy resources. In this study, the Intuitionistic Fuzzy AHP method was applied to determine criteria weights, after which the Intuitionistic Fuzzy VIKOR method was used to rank the energy alternatives. In the study, five main criteria and 17 sub-criteria related to these main criteria were used, and five renewable energy alternatives were evaluated. The research outcomes reveal that geothermal energy represents the optimal renewable alternative for the region, followed sequentially by biomass, hydroelectric, wind, and solar sources.

^{*} Corresponding author. Tel.: 0 274 4434312; E-mail address: bahadir.yorur@dpu.edu.tr

1. Introduction

The growth of national economies around the world, as well as population growth, significantly increases energy consumption. By the 2050s, the world population is expected to approach 10 billion, and national economies are expected to grow by an average of 5% [1]. Moreover, Türkiye's annual population growth is expected to exceed 10% by 2050. Accordingly, Türkiye's final energy demand is projected to grow by around 40% over the next 20 years, and electricity demand is projected to grow twice as fast. With this increase, the share of electricity in final energy demand is expected to increase to 30% in 2040 [2]. The distribution of renewable energy (RE) resources in Türkiye's electricity production in 2020 is as follows; hydroelectric (67%), wind (16%), solar (12%), geothermal (3%) and biomass (2%) [3]. For 2021, approximately 33% of electricity production came from renewable energy, and this ratio varies from year to year. However, the rapid increase in demand over the years makes it difficult to reach the desired level of electricity production from renewable energy [1]. One of the most important reasons for this situation is that access to fossil fuels is cheap, and renewable energy is limited. It is estimated that coal, which is among the fossil resources, has a reserve life of 200 years, natural gas 65 years and oil 40 years [4]. Because fossil fuels are not an infinite source of energy and they cause damage to nature, the use of alternative energy sources is becoming more and more critical every day. Sources of renewable energy, such as geothermal, hydroelectric, biomass, wind, tidal, solar, and wave energy, are considered the best alternatives to fossil fuels in terms of their minimal damage to nature compared to fossil fuels, their derivation from natural resources and their sustainability.

The use of fossil fuels to generate electricity not only increases imports but also has environmental impacts. Despite the Kyoto Protocol and the Paris Agreement, the global temperature is rising, with CO2 emissions exceeding record levels, posing an increasing number of climate challenges and accelerating global warming at an alarming rate [5]. However, climate change and the effects of global warming have become urgent issues that need to be addressed in recent years. In this regard, Türkiye signed the latest International Paris Climate Agreement in 2021. Within the scope of this agreement, it announced its interim target for 2030 as 41% carbon reduction and its final target as net zero carbon by 2053. Using fossil fuels is one of the biggest obstacles to achieving net zero carbon. Although Türkiye is fossil fuel poor, it has rich renewable energy resources. However, despite its high renewable energy potential due to its geographical location, as of 2021, Türkiye ranks 18th among European Union (EU) countries in renewable energy use. Therefore, there is a need to focus on using renewable energy potential. Türkiye is a country with high potential, and studies on the correct use of this potential have recently gained momentum [1,4,6,7].

The application of MCDM approaches is common in evaluating, ranking, and selecting renewable energy alternatives. Recently, hybrid studies integrated with fuzzy logic have been included in the literature. During the use of MCDM methods, expert evaluations can sometimes be subjective. To eliminate this subjectivity and uncertainty at the decision point, fuzzy set approaches are integrated into the studies. Various fuzzy numbers have been developed so far, and intuitionistic fuzzy (IF) numbers, extensions of type 1 fuzzy numbers, provide more information than traditional ones because it includes values for non-membership in addition to the membership values. The intuitionistic fuzzy set proposed by Atanassov allows for a better transfer of the uncertainty contained in the problems [8].

In this study, the ranking of five different renewable energy types (solar, wind, geothermal, biomass, hydroelectric) will be realized for the region called TR33 development region, which is one of the 26 development regions of Türkiye. The TR33 region, which includes the provinces of Manisa, Kütahya, Uşak, and Afyonkarahisar, ranks sixth for population density and fifth for electricity consumption, disregarding large metropolitan regions such as Istanbul, Ankara, and Izmir. [9]. The transition to suitable clean energy sources for the region, which is at the forefront regarding population density and industry, is essential to achieve the net zero carbon target. For this purpose, renewable energy ranking for the TR33 region was carried out using five main criteria (technological, economic, environmental, social

and power quality) and 17 sub-criteria. The Intuitionistic Fuzzy AHP (IF-AHP) method was used to calculate criteria weights, which served as input for the Intuitionistic Fuzzy VIKOR (IF-VIKOR) approach to perform the ranking of energy alternatives.

2. Literature Review

MCDM methods have become more prevalent in the energy sector as different alternatives have emerged over time, and other evaluation criteria, especially environmental ones, have started to be considered. Various methods or hybrid studies are used for evaluation because each method has different advantages and disadvantages [2]. While the results obtained with these methods may differ for the region studied, different results can be produced even for the same area. Hybrid approaches are used to overcome such situations, and fuzzy numbers are included in the models.

Early research in the energy field reveals the use of MCDM methods applied individually. For instance, the ANP method has been used to identify suitable energy policies for Türkiye [10], while the Electre method has evaluated both fossil fuel and renewable energy plants [11]. Similarly, the Promothee method was employed for assessing various renewable energy scenarios at national and regional levels in Australia [12] and for sustainability assessment of renewable technologies in Scotland [13]. The AHP method determined priority rankings for RE investments in Türkiye [14], and the Electre method evaluated site selection for renewable energy sources in another Turkish study [15]. By evaluating different renewable and fossil fuels with the AHP method, an energy resource planning model for the microgrid is presented [16]. There is also literature integrating different MCDM methods. Terrados et al. proposed a methodology combining the Delphi method and SWOT analysis for regional renewable energy development [17]. The SWARA-ARAS hybrid method ranked four RE technologies using five sustainability criteria and fourteen subcategories [18]. Büyüközkan and Güleryüz (2016) developed an integrated framework for evaluating and selecting the RES for Türkiye, employing the DEMATEL method to analyse interrelations among criteria and the ANP method for ranking [19]. Another study utilized a methodology integrating SWARA and TOPSIS for selecting Türkiye 's most appropriate renewable energy sources [20].

Fuzzy numbers are often incorporated into MCDM methods to address subjectivity and uncertainty in expert opinions. The fuzzy AHP method was utilized to evaluate renewable energy resources in Taiwan [21]. In a study conducted in a Chinese province, a linguistic hesitant fuzzy set (LHFS) was proposed to better capture decision-makers' hesitation and inconsistencies [22]. Other approaches include TOPSIS based on triangular fuzzy numbers [23] and interval Type-2 fuzzy numbers [24]. In Türkiye, renewable energy investment alternatives have been assessed using the DEMATEL-weighted TOPSIS approach, considering standard interval fuzzy type-2 and hesitant fuzzy sets for comparative analysis [25]. Deveci et al. (2020) evaluated Türkiye's renewable energy options using the intuitionistic fuzzy CODAS method [26]. In the research carried out for Türkiye, intuitionistic fuzzy TOPSIS [2], distance to ideal solution using interval type 2 fuzzy sets [27] and a new hypervolume-based evaluation and ranking technique based on intuitionistic fuzzy sets [28] was performed. In another study using the intuitionistic fuzzy EDAS method, the most suitable renewable energy types for Türkiye were listed [29]. Fuzzy AHP based MCDM approach was used to determine microgrid component groups for rural area of Tanzania [30].

Table 1 summarizes renewable energy selection studies for Türkiye. For example, Kahraman et al. (2009) used fuzzy axiomatic design for ranking renewable energies, yielding similar results to fuzzy AHP [31]. A 2011 study combined fuzzy AHP and TOPSIS to evaluate renewable, fossil fuel, and nuclear energy options [32]. Ertay et al. (2013) compared the Macbeth and AHP methods under a fuzzy environment, finding wind and solar energy to be the most critical sources [33]. Another Turkish study ranked renewable energy systems with the fuzzy TOPSIS method while determining criteria weights using the Interval Shannon Entropy methodology [34]. Advanced methodologies have also been applied. For instance, hesitant fuzzy numbers were incorporated into the TOPSIS method to better model uncertainties in decision-making, with interval fuzzy type-2 AHP used for criteria weighting [35]. COPRAS and MULTIMOORA methods were applied separately, using AHP for criteria weighting, and yielded consistent results [36]. Eroğlu and Şahin (2020) introduced a neutrosophic number-based VIKOR framework for selecting

renewable energy sources in Türkiye, proposing a novel score and distance function [37]. Lastly, Deveci and Güler (2024) presented the HEART technique, a hypervolume-based evaluation and ranking method, for assessing Türkiye's energy alternatives. This study compared results from fossil fuels and renewable energy types using distance-based methods such as TOPSIS, VIKOR, and CODAS, finding consistent outcomes across methods [28].

Various ranking and weighting methods are employed both globally and in Türkiye. Of these methods, VIKOR, designed to obtain a consensus-oriented solution, is widely applied as a ranking tool in existing studies. For example, renewable energy selection for the Spanish energy system utilized the VIKOR method, with criteria weighting performed using the AHP method [38]. Similarly, in India, the VIKOR method was applied for selecting renewable energy for a university campus, with AHP used for criteria weighting; the results indicated wind energy as the optimal choice for the campus [39]. In this study, an integrated MCDM methodology was used to rank renewable energy alternatives in Istanbul, with fuzzy AHP assigning weights to the criteria and fuzzy VIKOR performing the alternative ranking, [40], Rani et al. (2019) proposed a VIKOR method based on Pythagorean fuzzy sets, incorporating novel measures of divergence and entropy [41]. In Pakistan, a methodology integrating AHP and fuzzy VIKOR was utilized to select suitable sites for solar installations [42]. For determining the renewable energy mix in tourist resorts, the VIKOR method was applied considering three main and nine sub-criteria [43]. In Egypt, hybrid renewable energy systems for a desalination plant were evaluated using an integrated approach combining fuzzy AHP and fuzzy VIKOR, with ten performance criteria considered [44]. In Kenya and sub-Saharan Africa, an integrated methodology combining BMW-TOPSIS-VIKOR methods was developed for evaluating and selecting hybrid renewable energy systems. The BMW method determined criteria weights, while TOPSIS and VIKOR ranked the alternatives [45]. In another study, a combined AHP-VIKOR approach was proposed to identify the most suitable renewable energy alternative for electricity generation. [46].

Table 1. Summary of studies on renewable energy selection in Türkiye using MCDM approaches.

Source	Method(s) Used	Aim of the Study	Result(s)
[31]	Fuzzy axiomatic design and fuzzy AHP	Selecting the optimal renewable energy alternative	Wind 2. Solar 3. Biomass 4. Geothermal Hydropower
[32]	Fuzzy TOPSIS	Selecting the best energy technology alternative	 Wind 2. Biomass 3. Solar 4. Combined heat and power Hydropower 6. Conventional Energy
[33]	Fuzzy Macbeth and Fuzzy AHP	Evaluating renewable energy alternatives under fuzziness	1.Wind 2. Solar 3. Biomass 4. Geothermal 5. Hydropowe (for AHP)
[12]	Fuzzy TOPSIS	Renewable energy supply systems ranking	1. Hydropower 2. Geothermal 3. Regulator 4. Wind
[19]	DEMATEL and AHP	Investment-oriented renewable energy selection	1.Wind 2. Solar 3. Biomass 4. Hydropower 5. Geotherma
[35]	Hesitant Fuzzy TOPSIS	Prioritization of renewable energy alternatives	1.Wind 2. Solar 3. Hydropower 4. Biomass 5. Geotherma 6. Wave Energy 7. Hydrogen Energy
[36]	COPRAS and MULTIMOORA	Selecting the optimal renewable energy alternative	1. Hydropower 2. Solar 3. Wind 4. Geothermal5. Biomass
[26]	Intuitionistic Fuzzy CODAS	Multi-criteria approach for evaluating renewable energy alternatives	1. Onshore wind 2. Solar 3. Biomass 4. Geothermal 5. Hydropower
[37]	Neutrosophic Fuzzy VIKOR	Selecting the renewable energy alternative and ranking of them	1 Solar 2. Wind 3. Biomass 4. Geothermal 5. Hydropowe
[28]	HEART	Presentation of a new MCDM methodology for ranking alternatives	1. Solar 2. Wind 3. Natural Gas 4. Geothermal 5. Biomas 6. Hydropower 7. Coal

The number of studies on energy choice, particularly renewable energy, has increased significantly recently. As summarized in Table 1, these studies are generally conducted throughout Türkiye, but Türkiye's diverse geographic characteristics also necessitate regional studies. Although there are studies conducted in different regions or at the provincial level in Türkiye, no renewable energy selection study has been conducted for our study area.

MCDM methods have been implemented using different criteria and hybrid approaches for energy selection. Various techniques, primarily the AHP method, have been used for criterion weighting under fuzziness, and rankings have been performed using different MCDM methods. Recent studies have incorporated fuzzy numbers into models to eliminate potentially subjective decision-makers' assessments and to cope with uncertain information. Intuitionistic fuzzy numbers provide a flexible model for accounting for uncertainty in real-world problems.

This study determined criteria weights using the intuitionistic fuzzy AHP method, while alternative rankings were actualized using the intuitionistic fuzzy VIKOR method. Extending the hybrid approach to intuitionistic numbers yields more accurate information for both methods. Furthermore, the regional study adds value to the ranking of alternatives due to the inclusion of regional characteristics.

3. Methodology

To prioritize renewable energy resources in the TR33 region, encompassing the provinces of Manisa, Afyonkarahisar, Kütahya, and Uşak, MCDM methods were employed. More precisely, the IF-AHP served to compute the criteria weights, and the IF-VIKOR method was adopted to establish the ranking of renewable energy alternatives. This integrated approach ensured a systematic evaluation and prioritization of the region's renewable energy options.

3.1. Preliminaries

The notion of intuitionistic fuzzy sets was introduced by Atanassov and is defined as follows [8]. Given a universe of discourse U, an intuitionistic fuzzy set A is expressed as:

$$A = \{\langle x, \mu_A(x), \vartheta_A(x) \rangle | x \in U\} \quad \mu_A : U \to [0,1], \vartheta_A : U \to [0,1]$$

$$\tag{1}$$

Here, where x is any element and A is a set, μ_A denotes the degree of membership and ϑ_A denotes the degree of non-membership.

$$0 \le \mu_{\mathsf{A}}(\mathsf{x}) + \vartheta_{\mathsf{A}}(\mathsf{x}) \le 1 \tag{2}$$

 π is the degree of hesitation for the intuitionistic fuzzy set, and π can be defined as a heuristic index of x in A as follows [47].

$$\pi_{\mathsf{A}}(\mathsf{x}) = 1 - \mu_{\mathsf{A}}(\mathsf{x}) - \vartheta_{\mathsf{A}}(\mathsf{x}) \tag{3}$$

Arithmetic operations for intuitionistic fuzzy numbers $\widetilde{A} = (\mu_{\widetilde{A}}, \vartheta_{\widetilde{A}})$ and $\widetilde{B} = (\mu_{\widetilde{B}}, \vartheta_{\widetilde{B}})$ can be defined as follows [48].

$$\tilde{A} \oplus \tilde{B} = (\mu_{\tilde{A}} + \mu_{\tilde{B}} - \mu_{\tilde{A}}\mu_{\tilde{B}}, \vartheta_{\tilde{A}}\vartheta_{\tilde{B}}) \tag{4}$$

$$\tilde{A} \otimes \tilde{B} = (\mu_{\tilde{A}}\mu_{\tilde{B}}, \vartheta_{\tilde{A}} + \vartheta_{\tilde{B}} - \vartheta_{\tilde{A}}\vartheta_{\tilde{B}}) \tag{5}$$

$$\lambda \tilde{A} = \left(1 - (1 - \mu_{\tilde{A}})^{\lambda}, \vartheta_{\tilde{A}}^{\lambda}\right) \tag{6}$$

$$\tilde{A}^{\lambda} = \left(\mu_{\tilde{A}}^{\lambda}, 1 - (1 - \vartheta_{\tilde{A}})^{\lambda}\right) \tag{7}$$

For equations (3) and (4), λ is a positive integer.

3.2. IF-AHP

The Intuitionistic Fuzzy AHP method is employed to determine the criteria weights. This approach is an adaptation of the methodology proposed by Büyüközkan and Güleryüz (2016b) [49]. Similar to the classical AHP method, decision-makers express their preferences using intuitionistic fuzzy sets and construct pairwise comparison matrices within the intuitionistic fuzzy AHP framework. The weighted intuitionistic fuzzy matrix is derived using the IFWA operator. Following the assessment of pairwise matrix consistency, the IF-AHP weights are determined. The method's steps are outlined below.

Step 1: In the first stage, the purpose of the problem, its criteria and sub-criteria, if any, are determined. In addition, alternatives are added to the model to create the hierarchy of the problem.

Step 2: The scale of evaluation is utilized to determine and compare the significance of the criteria. Table 2 shows the definitions and equivalent linguistic term forms in the intuitionistic fuzzy set for the nine-scale AHP evaluation.

•		,	
Definition of linguistic preference	AHP Equivalent	Intuitionistic fuzzy set (IFS)	Reciprocal IFS
Equally significant (ES)	1	(0.02,0.18,0.80)	(0.02, 0.18, 0.80)
Midpoint value (MV1)	2	(0.06, 0.23, 0.70)	(0.23, 0.06, 0.70)
Moderately more significant (MS)	3	(0.13, 0.27, 0.60)	(0.27, 0.13, 0.60)
Midpoint value (MV2)	4	(0.22, 0.28, 0.50)	(0.28, 0.22, 0.50)
Strongly more significant (SS)	5	(0.33, 0.27, 0.40)	(0.27, 0.33, 0.40)
Midpoint value (MV3)	6	(0.47, 0.23, 0.30)	(0.23, 0.47, 0.30)
Very strongly more significant (VSS)	7	(0.62, 0.18, 0.20)	(0.18, 0.62, 0.20)
Midpoint value (MV4)	8	(0.80, 0.10, 0.10)	(0.10, 0.80, 0.10)
Extremely more significant (EMS)	9	(1,0,0)	(0,1,0)

Table 2. The conversion of AHP preferences into intuitionistic fuzzy sets and their reciprocal forms.

Step 3: At this stage, the weights of the decision-makers are determined. As seen in Table 2, the importance levels of the decision makers are realized using the intuitionistic fuzzy set linguistic terms. This approach may change the importance levels of the decision-makers according to their experiences and knowledge on the subject. Equation (8) can be used to calculate the weight of the relevant decision maker if the kth decision maker is expressed as the intuitionistic fuzzy number $D_k = [\mu_k, \vartheta_k, \pi_k]$.

$$\lambda_k = \frac{\left(\mu_k + \pi_k \left(\frac{\mu_k}{\mu_k + \vartheta_k}\right)\right)}{\sum_{k=1}^l \left(\mu_k + \pi_k \left(\frac{\mu_k}{\mu_k + \vartheta_k}\right)\right)} \text{ ve } \sum_{k=1}^l \lambda_k = 1$$
(8)

Step 4: Decision makers' intuitionistic preference relationships are determined. Here, to establish intuitionistic preference relationships, each pairwise comparison matrix must be obtained. The importance levels of each criterion can be denoted by "W" and $\lambda = (\lambda_1, \lambda_2, ..., \lambda_l)$ is the weight of each decision maker and is also $\sum_{k=1}^{l} \lambda_k = 1$, $\lambda_k \in [0,1]$. The opinions of all decision-makers need to be brought together. Therefore, the IFWA operator aggregates decision-makers' evaluations to rank the importance levels of criteria and alternatives. Let's assume that $W_j^{(k)} = [\mu_j^{(k)}, \theta_j^{(k)}, \pi_j^{(k)}]$ is an intuitionistic fuzzy set given to criterion x_j by the kth decision maker. For the aggregation process, the IFWA operator given in equation (9) is used and the criteria weights are calculated in this way.

$$W_{j} = IFWA_{\lambda}(W_{j}^{(1)}, W_{j}^{(2)}, ..., W_{j}^{(l)}) = \lambda_{1}W_{j}^{(1)} \oplus \lambda_{2}W_{j}^{(2)} \oplus ... \oplus \lambda_{l}W_{j}^{(l)}$$

$$= \left[1 - \prod_{k=1}^{l} \left(1 - \mu_{j}^{(k)}\right)^{\lambda_{k}}, \prod_{k=1}^{l} \left(\vartheta_{j}^{(k)}\right)^{\lambda_{k}}, \prod_{k=1}^{l} \left(1 - \mu_{j}^{(k)}\right)^{\lambda_{k}} - \prod_{k=1}^{l} \left(\vartheta_{j}^{(k)}\right)^{\lambda_{k}}\right]$$

$$W = \left[W_{1}, W_{2}, \dots, W_{j}\right]$$

$$W_{i} = \left[\mu_{i}, \vartheta_{i}, \pi\right] (j = 1, 2, \dots, n)$$

$$(9)$$

Step 5: Construction of the total weighted IF decision matrix is required. It is obtained by combining the criterion weights (W) with the total intuitionistic decision matrix, as follows.

$$R \otimes W = \left\{ x, \mu_{A_i}(x), \mu_w(x), \vartheta_{A_i}(x) + \vartheta_w(x) - \vartheta_{A_i}(x), \vartheta_w(x) | x \in X \right\}$$

$$\tag{10}$$

$$\pi_{A_i}w(x) = 1 - \vartheta_{A_i}(x) - \vartheta_w(x) - \mu_{A_i}(x) \cdot \mu_w(x) + \vartheta_{A_i}(x) \cdot \vartheta_w(x)$$
(11)

In the final step, the total weighted intuitionistic fuzzy decision matrix is established as follows:

$$R^* = \begin{bmatrix} \mu_{A_1} w(x_1), \theta_{A_1} w(x_1), \pi_{A_1} w(x_1) & \mu_{A_1} w(x_2), \theta_{A_1} w(x_2), \pi_{A_1} w(x_2) & \dots & \mu_{A_1} w(x_n), \theta_{A_1} w(x_n), \pi_{A_1} w(x_n) \\ \mu_{A_2} w(x_1), \theta_{A_2} w(x_1), \pi_{A_2} w(x_1) & \mu_{A_2} w(x_2), \theta_{A_2} w(x_2), \pi_{A_2} w(x_2) & \dots & \mu_{A_2} w(x_n), \theta_{A_2} w(x_n), \pi_{A_2} w(x_n) \\ \vdots & \vdots & \ddots & \vdots \\ \mu_{A_m} w(x_1), \theta_{A_m} w(x_1), \pi_{A_m} w(x_1) & \mu_{A_m} w(x_2), \theta_{A_m} w(x_2), \pi_{A_m} w(x_2) & \dots & \mu_{A_m} w(x_n), \theta_{m} w(x_n), \pi_{A_m} w(x_n) \end{bmatrix}$$

$$(12)$$

$$R' = \begin{bmatrix} r'_{11} & r'_{12} & r'_{13} \dots r'_{1m} \\ r'_{21} & r'_{22} & r'_{23} \dots r'_{2m} \\ r'_{31} & r'_{32} & r'_{33} \dots r'_{3m} \\ & & & \\ & & & \\ & & & \\ r'_{n1} & r'_{n2} & r'_{n3} \dots r'_{nm} \end{bmatrix}$$

$$(13)$$

 $r'_{ij} = (\mu^*_{ij}, \vartheta^*_{ij}, \pi^*_{ij}) = (\mu_{A_i} x(x_j), \vartheta_{A_i} x(x_j), \pi_{A_i} x(x_j))$ constitutes an element within the complete weighted intuitionistic decision matrix.

Step 6: At this stage, the consistency of the pairwise comparison matrices of preference relations needs to be checked. For this purpose, the consistency ratio (CR) is computed, and the ratio is expected to be less than 0.10. The calculation for CR is given in equation (14). Table 3 can be used for the random index.

$$CR = \frac{(\lambda_{max} - n)/(n-1)}{RI} \tag{14}$$

Table 3. Random index (RI) values depending on matrix size.

	Random Index (RI)														
n	1	2	3	4	5	6	7	8	9	10	11	12	13	14	15
RI	0.00	0.00	0.58	0.90	1.12	1.24	1.32	1.41	1.45	1.49	1.51	1.53	1.56	1.57	1.59

Step 7: Intuitionistic fuzzy entropy weights and final entropy weights are calculated using equations (15) and

(16).

$$\overline{\overline{w}}_{i} = -\frac{1}{n \ln 2} \left[\mu_{i} \ln \mu_{i} + \vartheta_{i} \ln \vartheta_{i} - (1 - \pi_{i}) \ln(1 - \pi_{i}) - \pi_{i} \ln 2 \right]$$
(15)

$$w_i = \frac{1 - \overline{w}_i}{n - \sum_{i=1}^n \overline{w}_i} \text{ where } \sum_{j=1}^n \overline{\overline{w}}_i = 1$$
 (16)

3.3. IF-VIKOR

The application steps of the IF-VIKOR method are given below [50].

Step 1: The values of the alternatives should be given as intuitionistic fuzzy numbers on a criterion basis. Therefore, the values of the quantitative criteria should be converted into intuitive fuzzy numbers. Equation (17) converts quantitative data into intuitive fuzzy numbers.

$$\mu_{ij}(x_{ij}) = w_j \frac{1}{1+e^{-z_{ij}}} \text{ ve } \vartheta_{ij}(x_{ij}) = w_j^* \frac{1}{1+e^{z_{ij}}}$$
 (17)

Where

$$w_j = w_j^* = \frac{|1-s_j|}{|1+s_j|}$$
 ve $z_{ij} = \frac{x_{ij} - \bar{x}_j}{s_j}$; \bar{x}_j and s_j are the mean and standard deviation of the criterion C_j .

Following the completion of the transformation process, the intuitionistic fuzzy decision matrix is generated as follows:

$$D = \begin{bmatrix} (\mu_{11}, \vartheta_{11}) & (\mu_{12}, \vartheta_{12}) & \dots & (\mu_{1m}, \vartheta_{1m}) \\ (\mu_{21}, \vartheta_{21}) & (\mu_{22}, \vartheta_{22}) & \dots & (\mu_{2m}, \vartheta_{2m}) \\ \vdots & \vdots & \ddots & \vdots \\ (\mu_{n1}, \vartheta_{n1}) & (\mu_{n2}, \vartheta_{n2}) & \dots & (\mu_{nm}, \vartheta_{nm}) \end{bmatrix}$$

$$(18)$$

Step 2: For the benefit criterion (J_1) and cost criterion (J_2) , the intuitionistic fuzzy negative ideal solution $f^- = (\mu_j^-, \vartheta_j^-)$ and the intuitionistic fuzzy positive ideal solution $f^* = (\mu_j^*, \vartheta_j^*)$ are defined. The definitions are given in equations (19) and (20).

$$\mu_{j}^{-} = \left\{ \left(\min_{i} (\mu_{ij}) \mid j \in J_{1} \right), \left(\max_{i} (\mu_{ij}) \mid j \in J_{2} \right) \right\}; \vartheta_{j}^{-} = \left\{ \left(\max_{i} (\vartheta_{ij}) \mid j \in J_{1} \right), \left(\min_{i} (\vartheta_{ij}) \mid j \in J_{2} \right) \right\} \tag{19}$$

$$\mu_{j}^{*} = \left\{ \left(m_{i} x(\mu_{ij}) | j \in J_{1} \right), \left(m_{i} n(\mu_{ij}) | j \in J_{2} \right) \right\}; \vartheta_{j}^{*} = \left\{ \left(m_{i} n(\vartheta_{ij}) | j \in J_{1} \right), \left(m_{i} x(\vartheta_{ij}) | j \in J_{2} \right) \right\}$$

$$(20)$$

Step 3: Normalized intuitionistic fuzzy difference \bar{d}_{ij} is calculated with the help of equation (21).

$$\bar{d}_{ij} = \frac{\sqrt{\frac{1}{2} \left[\left(\mu_{ij} - \mu_{j}^{*} \right)^{2} + \left(\vartheta_{ij} - \vartheta_{j}^{*} \right)^{2} + \left(\pi_{ij} - \pi_{j}^{*} \right)^{2} \right]}}{\sqrt{\frac{1}{2} \left[\left(\mu_{j}^{*} - \mu_{j}^{-} \right)^{2} + \left(\vartheta_{j}^{*} - \vartheta_{j}^{-} \right)^{2} + \left(\pi_{j}^{*} - \pi_{j}^{-} \right)^{2} \right]}}$$
(21)

Step 4: Calculate the values of S_i, R_i and Q_i by equations (22) and (23).

$$S_i = \sum_{j=1}^m w_j * \bar{d}_{ij} \text{ and } R_i = m_{\bar{q}} x (w_j * \bar{d}_{ij})$$
 (22)

$$Q_i = \vartheta \frac{S_i - S^*}{S^- - S^*} + (1 - \vartheta) \frac{R_i - R^*}{R^- - R^*}$$
 (23)

Here; $S^* = \min_i(S_i)$, $S^- = \max_i(S_i)$, $R^* = \min_i(R_i)$, $R^- = \max_i(R_i)$ and the weight of the jth criterion is expressed by w_i . θ represents the weight of the maximum group benefit strategy, while $(1-\theta)$ represents the weight of the minimum individual regret.

Step 5: The alternative (A_1) ranked best according to the Q measure (minimum) is recommended as a compromise solution if the following two conditions are met.

- (1) Acceptable advantage: $Q(A_2)$ - $Q(A_1) \ge DQ$, where (A_2) is the second-ranked alternative in the ranking list according to Q. DQ = 1/(m-1), where "m" is the number of alternatives.
- (2) Acceptable stability in decision making: Alternative (A1) must also be the best ranked alternative in terms of S and/or R. The best ranked alternative in terms of Q is the alternative with the lowest Q value.

3.4. Assessment criteria of renewable energy sources

Selecting renewable energy options is a complex process that needs to take multiple viewpoints into account. Depending on the evaluation objectives, it can be examined from various perspectives, and different criteria can be used for evaluation. While technical and economic criteria were initially considered for evaluation, over time, environmental and social criteria were included in the evaluation models. The fluctuating output of renewable energy sources, notably solar and wind, necessitates incorporating power quality into the set of evaluation criteria.

Following the literature review and consultations with three decision-makers, five primary criteria and seventeen sub-criteria were established for the assessment of renewable energy options. Table 4 presents explanations of these main criteria and their sub-criteria. The hierarchical structure of the model is given in Figure 1. The energy sources evaluated are five: solar (A_1) , hydroelectric (A_2) , wind (A_3) , biomass (A_4) and geothermal (A_5) .

Table 4. Criteria	o for evaluatio	n and correspo	anding ext	lanations

Main Criteria	Sub-Criteria	Explanations	Type of sub-criteria	References
Technological (C ₁)	Technological maturity (C_{11})	Analysis of technological development expresses how widely technology has spread at national levels.	Qualitative	[2, 4, 22]
	Delivery time (C ₁₂)	Measures how long it takes to complete a process from start to finish.	Quantitative	[2, 4, 7]
	Productivity (C ₁₃)	It refers to how often we can get enough power from a potential source.	Qualitative	[7, 10, 19]
	Risk (C ₁₄)	Addresses the risk of disruption/failure of the power policies and technologies used.	Qualitative	[4, 28, 31]
Economic (C ₂)	Investment cost (C ₂₁)	These are the costs incurred during the feasibility and installation stages of renewable energy plants.	Quantitative	[2, 7, 28]
	Operation and maintenance cost (C ₂₂)	It refers to all operating and maintenance expenses incurred after the installation of the power plants.	Quantitative	[2, 7, 28]
	Service life (C ₂₃)	It is the concept that expresses the maximum period in which a renewable energy power plant can be operated.	Quantitative	[4, 20, 23]
	Payback period (C ₂₄)	iod It refers to the time when renewable energy sources reach the break- even point.		[24, 26]
Environmental (C ₃)	Land Requirement (C ₃₁)	It refers to the total area use in terms of land size when making power plant investment decisions.	Quantitative	[28, 34]

Yörür, et al., (2025)/ Journal of Scientific Reports-A, 062, 182-199

	Greenhouse Emissions (C ₃₂)	It covers CO ₂ emissions resulting from the use of renewable energy sources.	Quantitative	[34, 35]
	Environmental damage (C ₃₃)	It expresses the impact of the power plant on the areas in terms of both visual and biodiversity.	Qualitative	[19, 26]
	Necessity of waste disposal (C ₃₄)	It refers to the level of waste that may occur after energy production.	Qualitative	[10, 19]
Social (C ₄)	Social acceptance (C ₄₁)	It expresses the level of acceptance of all kinds of facilities built in the local community.	Qualitative	[26, 28]
	Job creation (C ₄₂)	These are the economic benefits that the power plant offers to society during the installation and production phase.	Quantitative	[4, 7, 26]
Power Quality (C ₅)	Sustainability (C ₅₁)	It is the measure of uninterrupted supply of electricity obtained from energy sources.	Qualitative	[7, 20]
	Resource potential (C ₅₂)	It includes the evaluation of the possible potential of energy types for the region within the scope of the project.	Qualitative	[34, 41]
	Durability (C ₅₃)	This criterion refers to the use of energy resources against various situations, especially natural events.	Qualitative	[26, 28]

The TR33 region has high potential for renewable energy resources, particularly geothermal. Accurately analysing this potential and developing appropriate investment plans are crucial for the region's development. All five energy types under consideration are located in the area. Furthermore, the criteria were evaluated by decision-makers familiar with the region. This allowed for an assessment based on the region's characteristics.

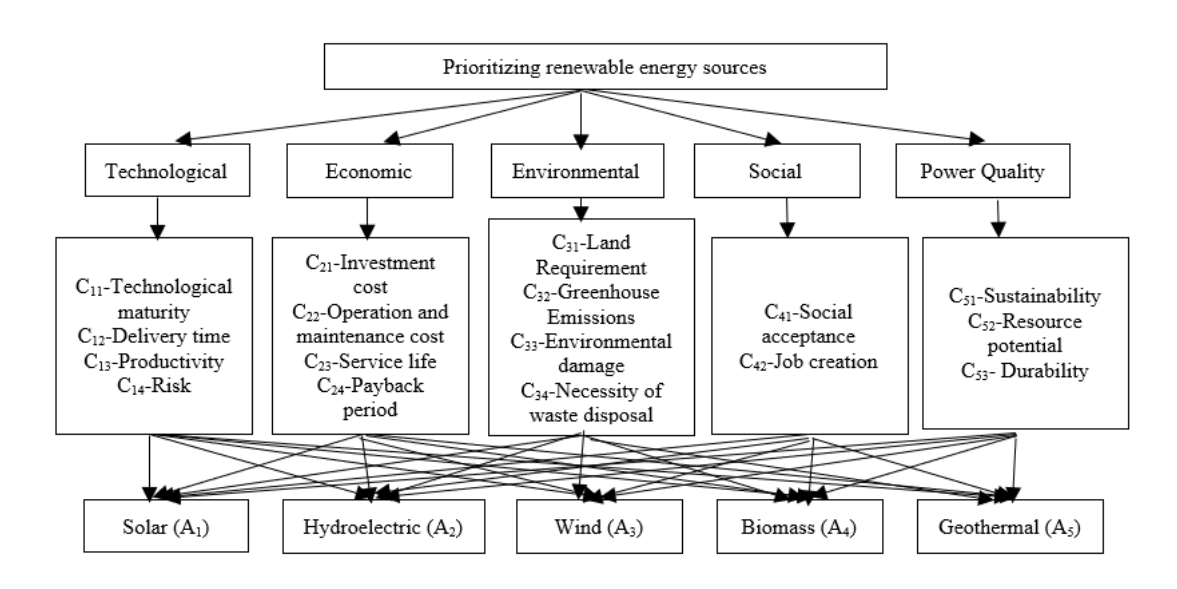


Fig. 1. Hierarchical structure for renewable energy source selection in TR33 region.

4. Case Study

An integrated IF-AHP-VIKOR methodology will be utilized to determine the optimal renewable energy alternatives for the TR33 region. In the previous sections, the main and sub-criteria that emerged as a result of the study's literature review were explained. In addition, the details of the methods were provided in the methodology section. To perform the analyses, the evaluation of three different decision-makers was taken. The first of these three decision-makers is an expert who has worked in the field of renewable energy at Kütahya Dumlupınar University, the other is an expert who works in the field of energy and works in the project development and implementation unit within the Zafer Development Agency, and the final evaluator is an expert who works as a mechanical engineer in the field of renewable energy production in the private sector. It was presumed that the decision-makers had identical importance levels, and as a result, a uniform weight of 0.33 was applied to all.

The relevant calculations will be shown on the technology sub-criteria. Expert evaluations on the technology sub-criteria are given in Table 5. The relevant assessments were converted into intuitionistic preferences, and intuitionistic preference relationship evaluations are shown in Table 6. Missing data in the table are completed with the "Reciprocal IFS" values in Table 2.

							2,						
_		DM1				DM2				DM3			
		C ₁₁	C_{12}	C_{13}	C_{14}	C_{11}	C_{12}	C_{13}	C_{14}	C_{11}	C_{12}	C_{13}	C_{14}
	C_{11}	ES	SS		MS	ES	MV3		MS	ES			MV1
	C_{12}		ES				ES			MV2	ES	MV2	MV3
	C_{13}	MV1	MV3	ES	MV2	MS	SS	ES	MV3	MV2		ES	MV3
	C_{14}		MS		ES		MV1		ES				ES
		CR = 0	0296			CR = 0	00.0617			CR = 0	0973		

Table 5. Linguistic evaluation matrices of technology sub-criteria.

Table 6. IFS equivalents of technology sub-criteria.

	C ₁₁	C_{12}	C_{13}	C_{14}
DM1	(0.02, 0.18, 0.80)	(0.33, 0.27, 0.40)	(0.23, 0.06, 0.70)	(0.13, 0.27, 0.60)
	(0.27, 0.33, 0.40)	(0.02, 0.18, 0.80)	(0.23, 0.47, 0.30)	(0.27, 0.13, 0.60)
	(0.06, 0.23, 0.70)	(0.47, 0.23, 0.30)	(0.02, 0.18, 0.80)	(0.22, 0.28, 0.50)
	(0.27, 0.13, 0.60)	(0.13, 0.27, 0.60)	(0.28, 0.22, 0.50)	(0.02, 0.18, 0.80)
DM2	(0.02, 0.18, 0.80)	(0.47, 0.23, 0.30)	(0.27, 0.13, 0.60)	(0.13, 0.27, 0.60)
	(0.23, 0.47, 0.30)	(0.02, 0.18, 0.80)	(0.27, 0.33, 0.40)	(0.23, 0.06, 0.70)
	(0.13, 0.27, 0.60)	(0.33, 0.27, 0.40)	(0.02, 0.18, 0.80)	(0.47, 0.23, 0.30)
	(0.27, 0.13, 0.60)	(0.06, 0.23, 0.70)	(0.23, 0.47, 0.30)	(0.02, 0.18, 0.80)
DM3	(0.02, 0.18, 0.80)	(0.28, 0.22, 0.50)	(0.28, 0.22, 0.50)	(0.06, 0.23, 0.70)
	(0.22, 0.28, 0.50)	(0.02, 0.18, 0.80)	(0.22, 0.28, 0.50)	(0.47, 0.23, 0.30)
	(0.22, 0.28, 0.50)	(0.28, 0.22, 0.50)	(0.02, 0.18, 0.80)	(0.47, 0.23, 0.30)
	(0.23, 0.06, 0.70)	(0.23, 0.06, 0.70)	(0.23, 0.47, 0.30)	(0.02, 0.18, 0.80)

The opinions of the kth decision maker are calculated collectively using the IFWA operator and Equations (9)-(11). For example, the calculations of μ_1 , ν_1 and π_1 of the first decision-maker are given below:

•
$$\mu_1 = 1 - ((1 - 0.02)^{0.33} * (1 - 0.33)^{0.33} * (1 - 0.23)^{0.33} * (1 - 0.13)^{0.33}) = 0.24$$
 (24)

•
$$\theta_1 = (0.18)^{0.33} * (0.27)^{0.33} * (0.06)^{0.33} * (0.27)^{0.33} = 0.09$$
 (25)

•
$$\pi_1 = 1 - (0.24 + 0.09) = 0.67$$
 (26)

Similarly, μ , ϑ and π values are calculated for other decision makers. The calculations of the technology sub-criteria for each decision maker are given in Table 7.

Table 7. Intuitionistic fuzzy judgment matrices of decision-makers regarding technology sub-criteria.

	DM_1			DM_2			DM_3		
	μ	θ	π	μ	θ	π	μ	θ	π
C ₁₁	0.24	0.09	0.67	0.31	0.12	0.57	0.22	0.13	0.65
C_{12}	0.26	0.16	0.58	0.25	0.12	0.63	0.32	0.15	0.53
C_{13}	0.27	0.14	0.59	0.33	0.15	0.52	0.33	0.14	0.53
C_{14}	0.24	0.11	0.65	0.20	0.14	0.66	0.23	0.07	0.70

As there is no distinction in weight among the decision makers, the aggregated values were calculated using the arithmetic mean and are shown in Table 8.

Table 8. Aggregate intuitionistic fuzzy judgment matrix of technology sub-criteria.

	μ	θ	π
C_{11}	0.26	0.11	0.63
C_{12}	0.28	0.14	0.58
C_{13}	0.31	0.14	0.55
C_{14}	0.22	0.11	0.67

The intuitionistic fuzzy entropy weights for decision-maker 1 are calculated via equation (15).

$$\overline{\overline{w}}_1 = -\frac{1}{4ln^2} [0.24 * (ln0.24) + 0.09 * (ln0.09) - (1 - 0.63) * ln(1 - 0.63) - (0.63 * ln2)] = 0.23$$
 (27)

The values of \overline{w}_2 , \overline{w}_3 and \overline{w}_4 were calculated in the same way and were found to be 0.25, 0.24 and 0.24, respectively. The final entropy weight of decision maker 1 is calculated using equation (16):

$$w_1 = \frac{1 - 0.23}{4 - (0.23 + 0.25 + 0.24 + 0.24)} = 0.25 \tag{28}$$

Table 9 summarizes the entropy weights of the three decision makers' evaluations of the technology sub-criteria and the total final entropy weights.

Table 9. Aggregate intuitionistic fuzzy judgment matrix of technology sub-criteria.

	DM1	DM2	DM3	Final Weight
C_{11}	0.25	0.23	0.26	0.25
C_{12}	0.25	0.18	0.20	0.21
C_{13}	0.25	0.32	0.30	0.29
C_{14}	0.25	0.27	0.24	0.25

To derive the final entropy weights of all criteria, each matrix is calculated individually. Table 10 summarizes these final entropy weights, and the normalized matrices yield the final evaluation criteria weights, also shown in Table 10.

Table 10. Technology sub-criteria weights and final entropy weight.

Main Criteria	Weighs	Sub-Criteria	Final entropy weights	Final evaluation criteria weights
Technological (C ₁)	0.22	C ₁₁	0.25	0.055
		C_{12}	0.21	0.046
		C_{13}	0.29	0.064
		C_{14}	0.25	0.055
Economic (C ₂)	0.25	C_{21}	0.44	0.110
		C_{22}	0.15	0.038
		C_{23}	0.18	0.045
		C_{24}	0.23	0.058
Environmental (C ₃)	0.20	C_{31}	0.14	0.028
		C_{32}	0.48	0.096
		C_{33}	0.20	0.040
		C_{34}	0.18	0.036
Social (C ₄)	0.15	C_{41}	0.29	0.043
		C_{42}	0.71	0.107
Power Quality (C ₅)	0.18	C_{51}	0.40	0.072
• • •		C_{52}	0.43	0.077
		C_{53}	0.17	0.030

Following the calculation of criteria weights through the intuitionistic fuzzy AHP method, the steps of the intuitionistic fuzzy VIKOR method are executed. Expert opinions regarding the qualitative criteria are given in Table 11, with linguistic variables used as shown in Table 12.

Table 11. Qualitative sub-criteria evaluations of decision makers.

Alternatives	Decision Makers	C ₁₁	C ₁₃	C ₁₄	C ₃₃	C ₃₄	C ₄₁	C ₅₁	C ₅₂	C ₅₃
Solar (A ₁)	DM1	EG	F	EP	EP	P	G	G	EG	EG
	DM2	F	F	F	F	P	F	F	G	F
	DM3	P	EG	EP	EP	EP	G	EG	G	EG
Hydroelectric (A ₂)	DM1	F	P	F	G	EP	EG	EG	P	P
	DM2	EP	G	F	F	F	EP	F	P	F
	DM3	G	F	P	F	EP	P	F	P	P
Wind (A ₃)	DM1	EP	P	P	F	P	F	P	P	F
/	DM2	G	F	F	F	P	P	F	G	F

	DM3	G	F	EP	F	EP	F	EG	EG	EG
Biomass (A ₄)	DM1	G	EP	EG	EP	G	F	EP	F	P
, ,	DM2	F	G	P	P	F	F	G	F	G
	DM3	F	P	EP	P	EG	G	F	F	F
Geothermal (A ₅)	DM1	G	P	G	P	G	F	G	G	P
	DM2	G	EG	EP	P	F	P	EG	G	G
	DM3	G	G	P	F	F	F	P	EP	P

Table 12. Evaluation scale for qualitative criteria.

Linguistik Variable	Extrelmely Poor (EP)	Poor (P)	Fair (F)	Good (G)	Extrelmely Good (EG)
Assigned Value	1	2	3	4	5

The data on quantitative criteria are presented in Table 13. The obtained data is based on literature review study. The units of quantitative criteria are as follows: Delivery time, service life, payback period; year, investment cost; \$/kw, operation and maintenance cost; \$/mw-year, land requirement; km²/mw, greenhouse emissions; gCO₂/kw-hour, job creation; person/mw. Based on this evaluation and data, an intuitionistic fuzzy decision matrix needs to be created.

Table 13. Evaluation scale for qualitative criteria.

Energy Resources	Delivery time	Investment Cost	Operation and Maintenance Cost	Service Life	Payback Period	Land Requirement	Greenhouse Emission	Job Creation
A ₁	2	3838	56780	25	1,850	0,040	41	0,530
A_2	1	1887	4120	25	0,900	8,100	24	0,400
A_3	4	3753	24050	30	11,800	0,050	11	0,330
A_4	2	2112	8660	20	1,920	20,000	230	1,000
A ₅	2	3681	164640	25	5,700	0,007	38	2,130

For all criteria except the qualitative criteria, the transformation process in equation (17) was used, and after completing the transformation, the decision matrix was obtained as shown in Table 14.

Table 14. Intuitionistic fuzzy decision matrix.

	C ₁₁	C ₁₂	C ₁₃	C ₁₄	C ₂₁	C ₂₂	C ₂₃	C ₂₄
A_1	[0.6,0.3]	[0.565, 0.386]	[0.7,0.2]	[0.5,0.5]	[0.456,0.415]	[0.512,0.418]	[0.521,0.286]	[0.705,0.156]
A_2	[0.5, 0.5]	[0.456,0.315]	[0.5, 0.5]	[0.6, 0.3]	[0.523, 0.382]	[0.706,0.173]	[0.471,0.423]	[0.621, 0.205]
A_3	[0.6,0.3]	[0.654, 0.310]	[0.6,0.3]	[0.5, 0.5]	[0.614,0.216]	[0.605, 0.256]	[0.652,0.215]	[0.523, 0.356]
A_4	[0.7, 0.2]	[0.521,0.388]	[0.6,0.3]	[0.6, 0.3]	[0.557,0.389]	[0.546, 0.247]	[0.356,0.348]	[0.612, 0.247]
A_5	[0.6,0.3]	[0.725, 0.186]	[0.5, 0.5]	[0.6, 0.3]	[0.415,0.487]	[0.386,0.596]	[0.622,0.279]	[0.425, 0.268]

Table 14. Intuitionistic fuzzy decision matrix (Continue).

	C ₃₁	C_{32}	C ₃₃	C ₃₄	C_{41}	C_{42}	C ₅₁	C ₅₂	C ₅₃
A_1	[0.569,0.268]	[0.416,0.287]	[0.6,0.3]	[0.5,0.5]	[0.6,0.3]	[0,548,0.312]	[0.705,0.125]	[0.548,0.321]	[0.5,0.5]
A_2	[0.705,0.200]	[0.561,0.349]	[0.7,0.2]	[0.6,0.3]	[0.5, 0.5]	[0.388,0.356]	[0.269,0.598]	[0.402,0.345]	[0.6,0.3]
A_3	[0.564,0.312]	[0.515, 0.109]	[0.5, 0.5]	[0.5, 0.5]	[0.5, 0.5]	[0.412,0.456]	[0.804, 0.107]	[0.625, 0.274]	[0.6,0.3]
A_4	[0.515,0.213]	[0.614, 0.205]	[0.6, 0.3]	[0.6, 0.3]	[0.6, 0.3]	[0.658, 0.298]	[0.564,0.321]	[0.515, 0.320]	[0.7, 0.2]
A_5	[0.385,0.396]	[0.489,0.345]	[0.6,0.3]	[0.5, 0.5]	[0.6, 0.3]	[0.705,0.123]	[0.608, 0.204]	[0.632,0196]	[0.5, 0.5]

After the creation of the decision matrix, it is necessary to define the intuitionistic fuzzy negative ideal solutions $f^- = (\mu_j^-, \theta_j^-)$ and the intuitionistic fuzzy positive ideal solutions $f^* = (\mu_j^*, \theta_j^*)$ for the benefit and cost criteria. Technological maturity (C₁₁), productivity (C₁₃), service life (C₂₃), social acceptance (C₄₁), job creation (C₄₂), sustainability (C₅₁), resource potential (C₅₂) and durability (C₅₃) are the benefit criteria. Remaining delivery time (C₁₂),

risk (C_{14}), investment cost (C_{21}), operation and maintenance cost (C_{22}), payback period (C_{24}), land Requirement (C_{31}), greenhouse emissions (C_{32}), environmental damage (C_{33}) and necessity of waste disposal (C_{34}) are the cost criteria.

Intuitionistic fuzzy negative ideal solutions and intuitionistic fuzzy positive ideal solutions are defined below, respectively.

$$f^- = \begin{cases} (0.5,0.5), (0.456,0.315), (0.5,0.5), (0.5,0.5), (0.456,0.415), (0.386,0.596), (0.356,0.348) \\ (0.425,0.268), (0.385,0.396), (0.416,0.287), (0.5,0.5), (0.5,0.5), (0.5,0.5), (0.388,0.356) \\ (0.269,0.598), (0.402,0.345), (0.5,0.5) \end{cases}$$

$$f^* = \begin{cases} (0.7,0.2), (0.725,0.186), (0.7,0.2), (0.6,0.3), (0.614,0.216), (0.706,0.173), (0.622,0.279) \\ (0.705,0.156), (0.705,0.200), (0.614,0.205), (0.7,0.2), (0.6,0.3), (0.6,0.3), (0.705,0.123) \\ (0.804,0.107), (0.632,0196), (0.7,0.2) \end{cases}$$

After obtaining the best and worst values, normalized intuitive fuzzy difference \bar{d}_{ij} values need to be calculated. Normalized intuitive fuzzy \bar{d}_{ij} difference values for all alternatives according to the criteria are presented in Table 15.

Table 15. Normalized intuitionistic fuzzy difference values.

	Criteria								
Alternatives	C ₁₁	C ₁₂	C ₁₃	C ₁₄	C ₂₁	C ₂₂	C ₂₃	C ₂₄	C ₃₁
A_1	0.455	0.985	0.000	0.656	0.480	0.480	0.756	0.515	0.385
A_2	0.000	0.550	0.000	0.998	0.480	0.655	0.385	0.880	0.880
A_3	1.000	0.000	0.480	0.550	0.650	0.385	0.550	0.600	0.550
A_4	0.000	0.998	0.850	0.656	0.480	0.660	0.550	0.600	0.550
A_5	1.000	0.0000	0.920	0.310	0.000	0.500	0.880	0.455	0.010

Table 15. Normalized intuitionistic fuzzy difference values (Continue).

	Criteria							
Alternatives	C_{32}	C ₃₃	C ₃₄	C ₄₁	C ₄₂	C ₅₁	C ₅₂	C ₅₃
A_1	0.300	0.385	0.885	0.500	0.888	0.550	0.860	0.550
A_2	0.550	1.000	0.885	0.385	0.554	0.500	0.550	0.550
A_3	0.000	0.385	0.550	0.500	0.900	0.500	1.000	0.720
A_4	0.300	0.500	0.630	0.650	0.995	0.550	0.995	0.800
A_5	0.000	0.000	0.385	0.650	1.000	0.500	1.000	0.800

 S_i , R_i and Q_i values are calculated for each alternative according to equations (22) and (23). The calculated values are presented in Table 37.

Table 16. S_i , R_i and Q_i values.

	Si	R_{i}	Qi
Solar (A ₁)	0.720	0.250	1.000
Hydroelectric (A ₂)	0.568	0.155	0.350
Wind (A ₃)	0.612	0.200	0.500
Biomass (A ₄)	0.422	0.100	0.095
Geothermal (A ₅)	0.315	0.085	0.000

According to Table 37, when the alternatives are ranked in the increasing order of Q_i , the best alternative is geothermal energy. The order of the alternatives is geothermal, biomass, hydroelectric, wind and solar, respectively.

5. Conclusion

One of the primary methods of transition to clean energy is accelerating the transition to renewable energy. During this transition, it is essential to prefer regionally appropriate resources. Many factors affect the decision to invest in renewable energy with high investment financing. Within the scope of this study, the aim is to evaluate renewable energy resources for the TR33 region, which includes Uşak, Kütahya, Afyonkarahisar, and Manisa provinces. For this purpose, it is aimed to use the intuitionistic fuzzy AHP-VIKOR integrated method. Solar, hydroelectric, wind, biomass and geothermal energy resources were evaluated during the evaluation process. Depending on these criteria, analyses were carried out using five main criteria (technological, economic, environmental, social, and power quality) and seventeen sub-criteria. Criteria weights were obtained with the intuitionistic fuzzy AHP method. Then, the obtained criteria weights were used as the input of the intuitionistic fuzzy VIKOR method.

According to the results of the analysis, geothermal energy has emerged as the most suitable energy type. The order of results obtained using intuitionistic fuzzy numbers was geothermal, biomass, hydroelectric, wind and solar. Especially according to the acceptable advantage criterion, which is the first condition of the VIKOR method, hydroelectric and biomass energy have emerged as preferable options. Table 1 presents the results of major studies conducted for Turkey. Generally, wind and solar energy are ranked first in these studies. Geothermal energy, on the other hand, is usually ranked last. Geothermal energy has a higher capacity utilization factor than other renewable energy types. Due to geographical features, the installed capacity is located in the Aegean region. While it ranks last for Turkey overall, it ranks first for the TR33 region covered by the study. The high installed capacity and potential of geothermal energy in this region, along with the high biomass potential due to agriculture and animal husbandry, provide a glimmer of hope regarding the feasibility of this ranking.

In this direction, priority should be given to biomass and hydroelectric energy types, respectively, starting with geothermal energy, for the TR33 region. Future studies could compare the results using different MCDM methods or fuzzy number extensions. Furthermore, criteria that prioritize public interest, such as social acceptance, could be incorporated into the model.

Acknowledgements

This study was supported by the project numbered 1919B012219210 within the scope of the 2209-A University Students Research Projects Support Program carried out by TUBITAK Directorate of Scientist Support Programs (BIDEB).

Author contribution

BY: Conceptualization, Investigation, Methodology, Project administration, Supervision, Validation, Review & Editing. **EA:** Conceptualization, Data curation, Investigation, Methodology, Validation, Visualization, Writing-original draft, Writing. **NŞ:** Conceptualization, Data curation, Investigation, Validation, Visualization, Data curation, Investigation, Validation, Visualization, Data curation, Investigation, Validation, Visualization

References

[1] A. Karaaslan and M. Gezen, "The evaluation of renewable energy resources in Turkey by integer multi-objective selection problem with interval coefficient," *Renewable Energy*, vol. 182, pp. 842-854, 2022, doi: 10.1016/j.energy.2018.09.165

[2] F. Bilgili, F. Zarali, M.F. Ilgün, C. Dumrul and Y. Dumrul, "The evaluation of renewable energy alternatives for sustainable development in Turkey using intuitionistic fuzzy-TOPSIS method," *Renewable Energy*, vol. 189, pp. 1443-1458, 2022, doi: 10.1016/j.renene.2022.03.058
[3] S. Mukhtarov, S. Yüksel and H. Dinçer, "The impact of financial development on renewable energy consumption: Evidence from Turkey," *Renewable Energy*, vol. 187, pp. 169-176, 2022, doi: 10.1016/j.renene.2022.01.061

- [4] Ö. Alkan and Ö.K. Albayrak, "Ranking of renewable energy sources for regions in Turkey by fuzzy entropy based fuzzy COPRAS and fuzzy MULTIMOORA," *Renewable Energy*, vol. 162, pp. 712-726, 2020, doi: 10.1016/j.renene.2020.08.062
- [5] Z. Khan, S. Ali, M. Umar, D. Kırıkkaleli and Z. Jiao, "Consumption-based carbon emissions and international trade in G7 countries: The role of Environmental innovation and Renewable energy," *Science of The Total Environment*, vol. 730, 138945, 2020, doi: 10.1016/j.scitotenv.2020.138945
- [6] G. Yilan, M.A.N. Kadirgan and G.A. Çiftçioğlu, "Analysis of electricity generation options for sustainable energy decision making: The case of Turkey," *Renewable Energy*, vol. 146, pp. 519-529, 2020, doi: 10.1016/j.renene.2019.06.164
- [7] İ. Topçu, F. Ülengin, Ö. Kabak, M. Işık, B. Unver and S.Ö. Ekici, "The evaluation of electricity generation resources: The case of Turkey," *Energy*, vol. 167, pp. 417-427, 2019, doi: 10.1016/j.energy.2018.10.126
- [8] K. Atanassov, "Intuitionistic fuzzy sets," Fuzzy Sets and Systems, vol. 20, pp. 87-96, 1986.
- [9] Turkish Statistical Institute, www.tuik.gov.tr. (accessed Feb. 1, 2024)
- [10] B.H. Ulutaş, "Determination of the appropriate energy policy for Turkey," *Energy*, vol. 30(7), pp. 1146-1161, 2005, doi: 10.1016/j.energy.2004.08.009
- [11] J.J. Wang, Y.Y. Jing and J.H. Zhoa, "Multi criteria evaluation model of renewable energy power plants based on ELECTRE method," In Energy Sustainability, vol. 48890, pp. 467-473, 2009, doi: 10.1115/ES2009-90104
- [12] K. Kowalski, S. Stagl, R. Madlener and I. Omann, "Sustainable energy futures: Methodological challenges in combining scenarios and participatory multi-criteria analysis," *European Journal of Operational Research*, vol. 197(3), pp. 1063-1074, 2009, doi: 10.1016/j.ejor.2007.12.049
- [13] M. Troldborg, S. Heslop and R.L. Hough, "Assessing the sustainability of renewable energy technologies using-criteria analysis: Suitability of approach for national-scale assessments and associated uncertainties," *Renewable and Sustainable Energy Reviews*, vol. 39, pp. 1173-1184, 2014, doi: 10.1016/j.rser.2014.07.160
- [14] T.Y. Ayan and H. Pabuçcu, "Evaluation of the renewable energy investment project with analytic hierarchy process method," *Suleyman Demirel University The Journal of Faculty of Economics and Administrative Sciences*, vol. 18(3), pp. 89-110. 2013.
- [15] C. Erdin and G. Özkaya, "Turkey's 2023 energy strategies and investment opportunities for renewable energy sources: Site selection on ELECTRE," Sustainability, vol. 11(7), 2136, 2019, doi: 10.3390/su11072136
- [16] S.S. Bohra, A. Anvari-Moghaddam and B. Mohammadi-Ivatloo, "AHP-Assisted multicriteria decision-making model for planning of microgrids," in 45th International Conference on Industrial Electronics Society (IES), 14-17th October, Lisbon, Portugal 2019, pp. 4557-4562 doi: 10.1109/IECON.2019.8926887
- [17] J. Terrados, G. Almonacid and P. Perez-Higueras, "Proposal for a combined methodology for renewable energy planning. Application to a Spanish region," *Renewable and Sustainable Energy Reviews*, vol. 13(8), pp 2022-2030, 2009, doi: 10.1016/j.rser.2009.01.025
- [18] C. Ghenai, M. Albawab and M. Battayeb, "Sustainability indicators for renewable energy systems using multi-criteria decision-making model and extended SWARA/ARAS hybrid method," *Renewable Energy*, vol. 146, pp. 580-597, 2020, doi: 10.1016/j.renene.2019.06.157
- [19] G. Büyüközkan and S. Güleryüz, "An integrated DEMATEL-ANP approach for renewable energy resources selection in Turkey," *International Journal of Production Economics*, vol. 182, pp. 435-448, 2016, doi: 10.1016/j.ijpe.2016.09.015
- [20] O. Derse and E. Yontar, "Determination of the most appropriate renewable energy source SWARA-TOPSIS method," *Journal of Industrial Engineering*, vol. 31(3), pp. 389-410, 2020, doi: 10.46465/endustrimuhendisligi.798063
- [21] Y-C. Shen, G.T.R. Lin, K-P. Li and B.J.C. Yuan, "An assessment of exploiting renewable energy sources with concerns of policy and technology," *Energy Policy*, vol. 38, pp. 4604-4616, 2010, doi: 10.1016/j.enpol.2010.04.016
- [22] H. Yuan, C. Li, W. Li, D. Liu and X. Li, "Linguistic hesitant fuzzy multi-criterion decision-making for renewable energy: A case study in Jilin," *Journal of Cleaner Production*, vol. 172, pp. 3201-3214, 2018, doi: 10.1016/j.jclepro.2017.11.038
- [23] P. Rani, A.R. Mishra, A. Mardani, F. Cavallaro, M. Alrashedi and A. Alrashidi, "A novel approach to extended fuzzy TOPSIS based on new divergence measures for renewable energy sources selection," *Journal of Cleaner Production*, vol. 257, 120352, 2020, doi: 10.1016/j.jclepro.2020.120352
- [24] A. Balın and H. Baraçlı, "A fuzzy multi-criteria decision making methodology based upon the interval type-2 fuzzy sets for evaluating renewable energy alternatives in Turkey," *Technological and Economic Development of Economy*, vol. 23(5), pp. 742-763, 2017, doi: 10.3846/20294913.2015.1056276
- [25] H. Dincer and S. Yuksel, "Balanced scored-based analysis of investment decisions for the renewable energy alternatives: A comparative analysis based on the hybrid fuzzy decision-making approach," *Energy*, vol. 175, pp. 1259-1270, 2019, doi: 10.1016/j.energy.2019.03.143
- [26] K. Deveci, R. Cin and A. Kağızman, "A modified interval valued intuitionistic fuzzy CODAS method and its application to multi-criteria selection among renewable energy alternatives in Turkey," *Applied Soft Computing Journal*, vol. 96, 10660, 2020, doi: 10.1016/j.asoc.2020.106660 [27] S. Hendiani and G. Walther, "Sustainability performance evaluation of renewable energy systems using a new multi-expert multi-criteria interval type-2 fuzzy distance to ideal solution approach," *Applied Energy*, vol. 347, 121436, 2023, doi: 10.1016/j.apenergy.2023.121436
- [28] K. Deveci and Ö. Güler, "Ranking intuitionistic fuzzy sets with hypervolume-based approach: An application for multi-criteria assessment of energy alternatives," *Applied Soft Computing*, vol. 150, 111038, 2024, doi: 10.1016/j.asoc.2023.111038
- [29] C. Dumrul, F. Bilgili, F. Zarali, Y. Dumrul and Z. Kiliçarslan, "The evaluation of renewable energy alternatives in Turkey using intuitionistic-fuzzy EDAS methodology," *Environmental Science and Pollution Research*, vol. 31, pp. 15503-15524, 2024, doi: 10.1016/J.ENERGY.2015.07.124
- [30] SS. Bohra, A. Anvari-Moghaddam, F. Blaabjerg and B. Mohammadi-Ivatloo, "Multi-criteria planning of microgrids for rural electrification," *Journal of Smart Environments and Green Computing*, vol. 1, pp. 120-134, 2021, doi: 10.20517/jsegc.2021.06
- [31] C. Kahraman, İ. Kaya and S. Cebi, "A comparative analysis for multiattribute selection among renewable energy alternatives using fuzzy axiomatic design and fuzzy analytic hierarchy process", *Energy*, vol. 34, pp. 1603-1616, 2009, doi: 10.1016/j.energy.2009.07.008

- [32] T. Kaya and C. Kahraman, "Multicriteria decision making in energy planning using a modified fuzzy TOPSIS methodology," *Expert Systems with Applications*, vol. 38, pp. 6577-6585, 2011, doi: 10.1016/j.eswa.2010.11.081
- [33] T. Ertay, C. Kahraman and İ. Kaya, "Evaluation of renewable energy alternatives using macbeth and fuzzy AHP multicriteria methods: The case of Turkey," *Technological and Economic Development of Economy*, vol.19(1), pp.38-62, 2013, doi: 10.3846/20294913.2012.762950
- [34] Ü. Şengül, M. Eren, S.E. Dhiraz, V. Gezder and A.B. Şengül, "Fuzzy TOPSIS method for ranking renewable energy supply systems in Turkey," Renewable Energy, vol. 75, pp. 617-625, 2015, doi: 10.1016/j.renene.2014.10.045
- [35] M. Çolak and İ. Kaya, "Prioritization of renewable energy alternatives by using an integrated fuzzy MCDM model: A real case application for Turkey," *Renewable and Sustainable Energy Reviews*, vol. 80, pp. 840-853, 2017, doi: 10.1016/j.rser.2017.05.194
- [36] A. Karaaslan and S. Aydın, "Evaluation of Renewable Energy Resources with Multi Criteria Decision Making Techniques: Evidence from Turkey," Atatürk University Journal of Economics and Administrative Sciences, vol. 34(4), pp. 1351-1375, 2020, doi: 10.16951/atauniiibd.749466 [37] H. Eroğlu and R. Şahin, "A neutrosophic VIKOR method-based decision-making with an improved distance measure and score function: Case study of selection for renewable energy alternatives," *Cognitive Computation*, vol. 12, pp. 1338-1355, 2020, doi: 10.1007/s12559-020-09765-x
- [38] J.R. San Cristabol, "Multi-criteria decision-making in the selection of a renewable energy Project in Spain: The Vikor method," *Renewable Energy*, vol. 36, pp. 498-502, 2011, doi: 10.1016/j.renene.2010.07.031
- [39] M. Kumar and C. Samuel, "Selection of best renewable energy source by using VIKOR method," *Technology and Economics of Smart Grids and Sustainable Energy*, vol. 2, pp. 1-10, 2017, doi: 10.1007/s40866-017-0024-7
- [40] T. Kaya and C. Kahraman, "Multicriteria renewable energy planning using an integrated fuzzy VIKOR&AHP methodology: The case of Istanbul," *Energy*, vol. 35, pp. 2517-2527, 2010, doi: 10.1016/j.energy.2010.02.051
- [41] P. Rani, A.R. Mishra, K.R. Pardasani, A. Mardani, H. Liao and D. Streimikiene, "A novel VIKOR approach based on entropy and divergence measures of Pythagorean fuzzy sets to evaluate renewable energy technologies in India," *Journal of Cleaner Production*, vol. 238, 117936, 2019, doi: 10.1016/j.jclepro.2019.11793
- [42] Y.A. Solangi, S.A.A. Shah, H. Zameer, M. Ikram and B.O. Saracoglu, "Assessing the solar PV power project site selection in Pakistan: based on AHP-fuzzy VIKOR approach," *Environmental Science and Pollution Research*, vol. 26, pp. 30286-30302, 2019, doi: 10.1016/j.rser.2015.07.014 [43] G. Zheng and X. Wang, "The comprehensive evaluation of renewable energy system schemes in tourist resorts based on VIKOR method," *Energy*, vol. 193, 116676, 2020, doi: 10.1016/j.energy.2019.116676
- [44] K.M. Kotb, M.R. Elkadeem, A. Khalil, S.M. Imam, M.A. Hamada, S.W. Sharshir and A. Dan, "A fuzzy decision-making model for optimal design of solar, wind, diesel-based RO desalination integrating flow-battery and pumped-hydro storage: Case study in Baltim, Egypt," *Energy Conversion and Management*, vol. 235, 113962, 2021, doi: 10.1016/j.enconman.2021.113962
- [45] M.R. Elkadeem, A. Younes, S.W. Sharshir, P.E. Campana and S. Wang "Sustainable siting and design optimization of hybrid renewable energy system: A geospatial multi-criteria analysis," *Applied Energy*, vol. 295, 117071, 2021, doi: 10.1016/j.apenergy.2021.117071
- [46] D. Abdul, J. Wengi and A.Tanveer, "Prioritization of renewable energy source for electricity generation through AHP-VIKOR integrated methodology," *Renewable Energy*, vol. 184, pp. 1018-1032, 2022, doi: 10.1016/j.renene.2021.10.082
- [47] B. Buran and M. Erçek, "Public transportation business model evaluation with Spherical and Intuitionistic Fuzzy AHP and sensitivity analysis," Expert Systems with Applications, vol. 204, 117519, 2022, doi: 10.1016/j.eswa.2022.117519
- [48] E. İlkbahar, C. Kahraman and S. Cebi, "Risk assessment of renewable energy investment: A modified failure mode and effect analysis based on prospect theory and intuitionistic fuzzy AHP," *Energy*, vol. 239, 121907, 2022, doi: 10.1016/j.energy.2021.121907
- [49] G. Büyüközkan and S. Güleryüz, "A new integrated intuitionistic fuzzy group decision making approach for product development partner selection," *Computers & Industrial Engineering*, vol. 102, pp 383-395, 2016b, doi: 10.1016/j.cie.2016.05.038
- [50] F.E. Boran, "A new approach for evaluation of renewable energy resources: A case of Turkey," *Energy Sources, Part B: Economics, Planning, and Policy*, vol. 13(3) pp. 196-204, 2018, doi: 10.1080/15567249.2017.1423414



Contents lists available at Dergipark

Journal of Scientific Reports-A

journal homepage: https://dergipark.org.tr/tr/pub/jsr-a



E-ISSN: 2687-6167

Number 62, September 2025

REVIEW ARTICLE

Receive Date: 18.02.2025 Accepted Date: 24.04.2025

A-to-I editing technologies: unlocking new avenues in cancer therapy

Hasret Turkmen^{a*}, Nefise Demir^b, Mustafa Şen^c, Mustafa Can^d

^aIzmir Katip Celebi University, Department of Nanoscience and Nanotechnology, Izmir, Türkiye, ORCID:0000-0001-8419-7207
^bIzmir Katip Celebi University, Department of Nanoscience and Nanotechnology, Izmir, Türkiye, ORCID:0000-0001-6311-4337
^cIzmir Katip Celebi University, Department of Engineering Sciences, Izmir, Türkiye, ORCID:0000-0002-2421-9184
^dIzmir Katip Celebi University, Graphene Application and Research Center, Izmir, Türkiye, ORCID:0000-0002-1749-8293

Abstract

This review examines the critical role of adenosine-to-inosine (A-to-I) RNA editing in oncology, focusing on its molecular mechanisms, clinical relevance, and therapeutic applications. The ADAR family of enzymes mediates A-to-I editing, influencing RNA stability, translation efficiency, and immune modulation. Dysregulated ADAR activity has shown a relationship with multiple cancers, including glioma, hepatocellular carcinoma, and breast cancer. This review is structured into three main sections. First, we provide an overview of the mechanisms of RNA editing and its regulatory functions in cancer biology. Next, we highlight its clinical relevance, particularly how altered RNA editing contributes to oncogenesis and immune evasion. Finally, we explore therapeutic strategies, including ADAR inhibitors, antisense oligonucleotides (ASOs), and inosine-mediated RNA modifications to restore gene expression balance. Restoring ADAR function involves correcting RNA editing imbalances, particularly tumor cells' disrupted equilibrium between ADAR1 and ADAR2. This modulation can counteract oncogenic RNA changes and enhance immunotherapy efficacy. We also elaborate on the clinical applications of RNA editing in precision medicine, highlighting its potential to revolutionize cancer therapy. Unlike permanent genomic modifications, RNA editing provides a reversible and dynamic approach, making it an attractive strategy for targeted cancer interventions. Integrating RNA editing strategies into oncology and biomedical research could pave the way for new therapeutic advances.

© 2023 DPU All rights reserved.

Keywords: RNA; inosine; cancer; modification; ADAR

* Corresponding author. Tel.: 543 576 85 63 E-mail address: hasret.turkmen98@gmail.com

1. Introduction

RNA (ribonucleic acid) transmits genetic information from DNA (deoxyribonucleic acid) to protein. DNA is copied (replicated) during cell division and transferred to new cells, while RNA uses this information to produce proteins. RNA, which is responsible for regulating basic cellular processes and many aspects of gene expression, undergoes a life cycle from transcription to translation and degradation, especially in eukaryotic cells. This process involves posttranscriptional modifications such as editing, methylation, polyadenylation, and other cellular mechanisms that determine RNA stability, localization, and function. RNA profiles play a critical role in regulating cellular functions, including cellular differentiation, development, stress responses, and pathological conditions. In the early 20th century, chemical modifications in nucleic acids became a focus of interest in clinical diagnosis and disease treatment. Although the basic components of nucleic acids began with the discovery of the ribose sugar in 1909 [1], naturally occurring chemical modifications of RNA were discovered in the 1960s [2]. The discovery of transfer RNA (tRNA), known for its critical role in transporting amino acids to ribosomes, and the elucidation of the double-helical structure of DNA by Watson and Crick [3] and the characterization of introns and exons in eukaryotic genes and a modified nucleotide known as inosine led to intense interest in this field [4]. Research on RNA editing, focusing on RNA methylation[5][6] and adenosine-inosine (A-I) conversion, has revealed the biological functions of posttranscriptional modifications. One of the most common mechanisms is the modification targeting double-stranded RNA regions by converting adenosine bases to inosine by adenosine deaminase (ADAR) enzymes[7]. This modification has affected various cellular processes carried out by mRNA (messenger RNA). In recent years, RNA editing technologies have rapidly developed thanks to CRISPR-Cas9, which can regulate gene expression, make precise changes in the genome, and also allow temporary and reversible genetic changes without changing the DNA sequence. The discovery of the CRISPR-Cas13 enzyme has made it possible to directly target RNA molecules. Cas9 causes permanent changes in the genome. Cas13, on the other hand, can cut or modify RNA sequences in a highly specific way. The modified variants of Adar enzymes have made programmable A-I RNA regulation processes more effective by combining with molecules guiding certain RNA sequences [8]. This method has expanded the usage areas of RNA -based therapies, and increased the accuracy of RNA regulation, making it possible to control target gene expression, correct pathogenic mutations, and precisely regulation of RNA functions. Thus, it allows the development of innovative treatment strategies for genetic diseases, neurodegenerative disorders, and some types of cancer that require control of gene expression without causing permanent genome changes. Fig. 1 summarizes the historical development of nucleic acid discovery, showing the major milestones from the discovery of the ribose sugar to modern RNA editing and gene modification techniques. A study on frog eggs and embryos led to the discovery of the first RNA modification and revealed the existence of an enzyme activity that can unwind RNA duplexes. As a result of these studies, nearly 180 different chemical changes were detected in mRNA[9]. Genetic information can be dynamically modified through RNA editing and directs many biological functions such as nervous system development, immune response, and disease processes [10]. RNA editing serves a vital function in post-transcriptional gene regulation and has a direct effect on RNA stability, translation efficiency, and protein diversity. These include A-to-I editing, Cytosine-Uracil (C-U) editing, Pseudouridylation, 5-Methylcytosine (m5C) modification, and N6-Methyladenosine (m6A) methylation.

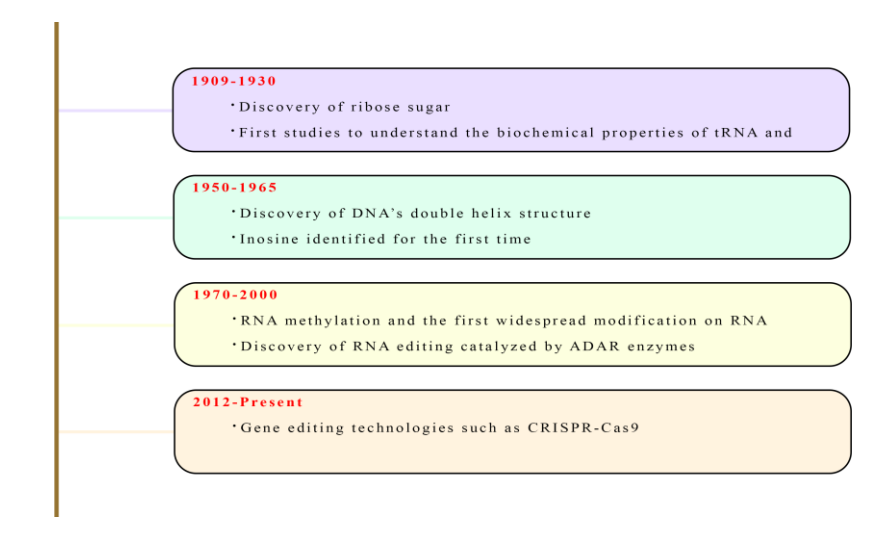


Fig. 1. From past to present: Development of chemical modifications in nucleic acids.

The A-I regulation, mediated by the ADAR enzyme family, enables the transformation of A into I. This mechanism facilitates the dynamic regulation of gene expression and protein activity by modifying the genetic information stored in RNA. ADAR enzymes edit regions of double-stranded RNA (dsRNA) and specifically target adenosine-uridine (AU) pairs. They remove an amino group from adenine and convert it to inosine. This RNA editing mechanism has allowed mRNAs to code for alternative amino acids, affecting the structure and function of the resulting proteins. Three types of ADAR enzymes that act on RNA have been identified in humans. These are briefly described below: ADAR1 has a crucial function in the interferon (IFN) response. Responsible for regulating various mRNAs and maintaining cellular homeostasis during immune activation.

ADAR1p110: Localized in the nucleus, this isoform of ADAR1 plays a vital role in regulating RNAs.

ADAR1p150: This isoform of ADAR1, induced by IFNs, is found predominantly in the cytoplasm, where it interacts with RNAs during immune responses and cellular stress. It contains an additional Z-DNA/RNA ($Z\alpha$) binding domain that enhances the ability to recognize and edit Z-RNA structures, thus contributing to substrate specificity [11].

ADAR2: ADAR2 is an integral part of the nervous system, particularly in the regulation of glutamate receptor mRNA. Its editing activity is vital for maintaining neuronal excitability and synaptic plasticity.

ADAR3: Expressed exclusively in the central nervous system, the functional role of ADAR3 is less well understood, as it is enzymatically inactive under normal conditions.

ADAR1 and ADAR2 share a modular organization with conserved catalytic domains; however, they exhibit different substrate specificities due to differences in RNA binding domains and catalytic domain structures. ADAR1 contains two Z-DNA/Z-RNA binding domains (ZBDs), three double-stranded RNA binding domains (dsRBDs), and a conserved deaminase domain. These features allow ADAR1 to preferentially target long double-stranded RNA structures, including noncoding RNAs and self-RNA species involved in immune regulation. Its ability to bind Z-conformation nucleic acids also links it to immune response modulation and antiviral defense mechanisms. ADAR2, on the other hand, lacks ZBDs but retains two dsRBDs and a catalytic deaminase domain, making it highly selective for specific coding regions, particularly in neuronal transcripts. ADAR2 is responsible for precisely regulating transcripts such as GluA2 (GRIA2), which regulates AMPA receptor function and synaptic plasticity. At the same time, ADAR2 is primarily involved in regulating neuronal gene expression and synaptic function. ADAR1 contains a structural zinc-binding domain that is not present in ADAR2 and that affects its interaction with specific RNA substrates. ADAR2 has cycle structures near the catalytic area that can affect the ability to target substrates that are

critical for neuronal function[12]. Endogenous ADAR enzymes in the cell can reduce immune responses compared to exogenous enzyme transmission, minimize toxicity, and promote ADAR enzymes, significantly increasing the desired RNA regulation efficiency for therapeutic applications. However, in this approach, it is necessary to carefully manage to prevent unwanted situations such as non-target arrangement and unwanted immune activation and to ensure specificity and safety. Recent developments aim to address these challenges, including the development of guidance RNA systems to overcome these difficulties. For example, the selective module of adar1 isoforms, which specifically targets the $Z\alpha$ area of the P150 isoform, has the potential to modulate immune reactions and reduce pathological RNA regulation [13].

2. RNA Modifications and ADAR Activity

One of the basic mechanisms is RNA modifications that regulate gene expression and provide precise control of intracellular processes by regulating RNA stability, translation, and functionality [9][14]. The A-to-I deamination modification found in tRNAs plays an active role in tRNA secretion decoding [15]. In addition, A-to-I RNA modifications found in mRNAs are catalyzed by ADARs acting on RNA. ADARs, which catalyze A-to-I conversion, an important RNA modification, play a role in RNA editing [16]. These modifications can extend the life of RNA or accelerate its degradation by acting on RNA. Among the three ADAR enzyme families found in mammals, ADAR1 and ADAR2 are the active ADAR enzymes, while ADAR3 is enzymatically inactive. ADAR1 and ADAR2 exhibit a modular arrangement in humans. ADAR1 and ADAR2 enzymes have a well-conserved C-terminal catalytic domain that catalyzes deamination from A to I. In addition, several double-stranded RNA (dsRNA) binding domains in the N-terminal region facilitate their specific interactions with double-stranded RNA substrates. This structural arrangement supports the roles of these enzymes in RNA editing and gene expression regulation [17]. The structural and functional differences between ADAR1 and ADAR2 contribute to their specific roles in cellular and immunological processes and facilitate their unique roles in RNA editing [18]. Inosine (I) is a modified nucleotide found in RNA, usually resulting from enzymatic modification of the adenosine (A) base, affecting the structure and function of RNA. Inosine, recognized by cellular mechanisms as guanosine (G), pairs with cytosine (C) during base pairing. Inosines exhibit properties very similar to those of guanosines. Thanks to this unique feature, this modification affects the mRNA sequence and translation process without altering the genetic code. In addition, it is critical for increasing genetic diversity, regulating neurotransmission, and controlling the immune system. A-to-I conversions, especially in coding regions, can increase protein diversity by altering codon recognition processes [19]. For example, inosine in mRNA can affect gene expression and alternative splicing. It allows tRNAs to pair with multiple codons that code for the same amino acid and increases codon-anticodon flexibility in tRNA. ADAR1 is highly active in innate immunity and cellular processes, and its overregulation may allow tumor cells to evade the immune system. ADAR1 and ADAR2 are active in embryonic cell types and have become a focus of interest in cancer studies. However, ADAR3 is enzymatically inactive and has no deaminase activity, and may play a non-enzymatic regulatory role in RNA editing activity. A variety of technologies and methodologies, including high-throughput RNA sequencing (RNA-Seq), Sanger sequencing, and CRISPR-based RNA targeting, have been used to assess ADAR activity. These techniques provide valuable information about the function of ADAR activity in biological processes and its importance in diseases, particularly cancer biology, functional consequences of RNA editing, neurodegenerative diseases, and immune regulation. It can also cause non-coding events by causing changes in RNA secondary structure. Lamer et al. [20] introduced AGS-associated mutations in the p110 and p150 isoforms to investigate the effects of these mutations on editing activity on model RNA substrates. Similarly, Karki et al. [17] performed analyses using two different RNA substrates to determine the deamination rates of mutants in the p110 isoform of ADAR1. Both studies examined the effects of different mutations of ADAR1 on RNA editing activity and showed that certain mutations severely impaired ADAR1 catalytic function, while others had more limited effects. The evidence supports the idea that RNA editing mechanisms have a crucial function in the pathogenesis of AGS and that certain mutations in ADAR1 may directly contribute to disease progression. Roth et al.[21] developed a computational tool called Alu Editing Index (AEI) to assess ADAR activity. Established a network-based interactive server to analyze the relationships between A-to-I editing events and cancer [22]. Along with all these studies, various techniques such as AEI, EndoVIPER-seq, and fluorescence-based systems have been used to assess ADAR activity and study the biological effects of this editing [13]. Accurate measurement of ADAR activity could deepen our knowledge of gene regulation mechanisms and contribute to the development of new therapeutic strategies in cancer research.

As a result, ADAR1 regulates mRNA and miRNAs involved in cancer promotion, supporting cell survival and sometimes acting in tumor suppression. ADAR2 regulation inhibits tumor growth. One of the critical processes of Ato-I RNA editing is C6-hydrolytic deamination catalyzed by ADAR enzymes. This modification is found in a variety of RNA types, including tRNAs, mRNAs, miRNAs, and certain viral RNAs [23]. ADAR enzymes catalyze the hydrolytic deamination of adenosine residues in dsRNA regions, converting them to inosine. In viral RNAs, this modification can affect viral replication and immune recognition. Detection of inosine has traditionally been used to identify these editing events by reverse transcription polymerase chain reaction (RT-PCR) [24] and cyanine ethylation at inosine modification sites, which is important in terminating cDNA synthesis [25][26][27]. In addition, Tao et al. [28] reported a derivatization strategy combined with liquid chromatography-tandem mass spectrometry (LC-MS/MS) analysis to further increase detection sensitivity and examine possible disease associations. The decoding behavior of inosine during reverse transcription has been systematically investigated using various reverse transcriptases, including avian myeloblastosis virus (AMV), Moloney murine leukemia virus (MMLv), and human immunodeficiency virus 1 (HIV-1) [29]. YUXI [30] reported the inosine chemical labeling and affinity molecular purification (ICLAMP) method using maleimide derivatives for the specific labeling and enrichment of inosine in nucleic acids. The ADAR enzyme removes the amino group (NH₂) from the adenosine molecule, which is usually found in dsRNA regions, and adds an oxygen atom. This is a hydrolytic deamination reaction that converts A-to-I. Inosine can change the protein-coding sequence by replacing adenosine in mRNA. This event gives rise to various protein isoforms. Inosine can alter the coding potential of mRNA, resulting in the production of different amino acids, as shown in Fig. 2. [29]. Through this process, RNA stability, translation, and gene expression are regulated.

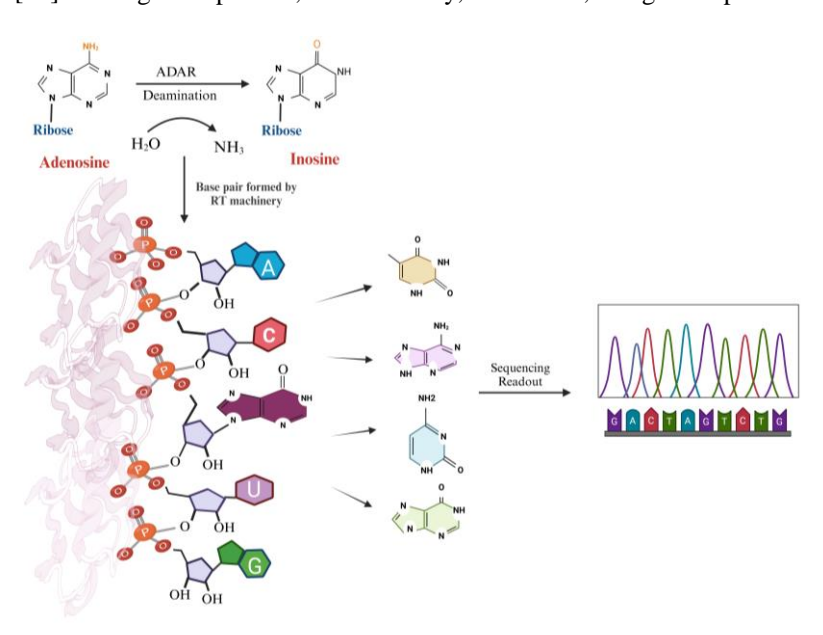


Fig. 2. Diagram illustrating the hydrolytic deamination process that converts adenosine (A) residues into inosine (I) through enzymatic catalysis.

Inosine in tRNAs is generated through the catalytic activity of adenosine deaminases (ADAT2/ADAT3) acting on tRNA, particularly in the anticodon loop. This modification increases the flexibility of codon recognition and allows inosine to base-pair with multiple codons [31]. As a result, it facilitates translational adaptability in both prokaryotic and eukaryotic systems and improves decoding of U and A terminator codons. First identified in tRNA in 1965 [4], inosine has greater importance in the anticodon stem-loop and contributes to the adaptability of the genetic code. However, aberrant inosine changes in tRNA or mutations in ADAT enzymes have been observed in relation to metabolic disorders, neurodegenerative diseases, mitochondrial dysfunction, and various cancers [32][33]. Additionally, post-transcriptional sulfur modifications in tRNA, such as 2-thiouridine (s²U), 4-thiouridine (s⁴U), 2-thiocytidine (s²C), and 2-methylthioadenosine (ms²A), play essential roles in multiple biological processes by contributing to RNA stability and function [34]. Moreover, phosphorothioate (PS) bonds in DNA, where one oxygen atom in the phosphate-sugar backbone is replaced by sulfur, offer protective benefits in genetic material stability by providing increased resistance to nuclease degradation. A structural representation of a 4-mer DNA (ATCG) and RNA (AUCG) containing a normal phosphodiester (PO) bond, a PS (Rp) bond, and a PS (Sp) bond is shown in Fig. 3. [35].

Fig. 3. Illustrative schematic of the 4-mer structures: (A) ATCG in DNA and (B) AUCG in RNA [35].

PS linkage makes nucleic acids more resistant to degradation by exonucleases and endonucleases. PS modifications involve the replacement of a non-bridging oxygen atom in the phosphate backbone of nucleic acids with a sulfur atom. In the context of RNA editing, phosphorothioate modifications have been utilized to improve the stability of antisense oligonucleotides (ASOs) that target ADAR-mediated A-to-I editing sites, ensuring prolonged effects in therapeutic applications. Additionally, PS modifications have been employed in synthetic tRNA molecules to improve their stability and efficiency in translational regulation, which may have implications for ADAT-mediated inosine modifications. This modification can occur in both DNA and RNA. The presence of this modification increases the stability and efficacy of nucleic acid-based drugs. PS modifications play an important role in stabilizing synthetic nucleic acids, making them indispensable for drug development, gene therapy, and molecular biology applications. Their ability to increase nuclease resistance and alter nucleic acid-protein interactions continues to attract interest in cancer treatment, improving the stability, specificity, and efficacy of RNA-based therapies.

Inosine is essential for tRNA maturation and may cause amino acid sequence miscoding due to its capacity to imitate guanosine, stemming from A-to-I editing in mRNA [36][37]. Dysregulated A-to-I regulation is involved in

human diseases, notably neurological abnormalities, signaling pathway problems, and malignancies [38][39]. There are studies describing that exposure to A-to-I regulation can lead to mRNA degradation [24]. Alterations of ADAR1 at the mRNA or protein level can affect its expression, location, and functionality. On glioblastoma revealed that RNA methyltransferase-like 3 (METTL3) modulates ADAR1 protein expression by targeting the m6A alteration adjacent to the termination codon of the ADAR1 transcript. This control influences glioma cell proliferation by altering ADAR1 levels [40]. Furthermore, research conducted by Alberto Bavelloni and associates demonstrated that ADAR1 p110 functions as a substrate for Akt kinase, with phosphorylation at T738 markedly diminishing ADAR1's RNA editing capability. This post-translational change may influence the course of disorders linked to RNA editing, underscoring the complex control of ADAR1 and its significance for disease biology [41]. As shown in Fig. 4S, highly recurrent chemical modifications in eukaryotic mRNA transcripts are located in the mRNA cap structure, 5' or 3' untranslated regions (UTRs), or in the transcript-specific coding region. These modifications are pivotal in regulating transcript stability, translation efficiency, and cellular localization, allowing precise control of gene expression in various biological processes. Coding region-specific modifications (shown in bold) have great importance in shaping the functional output of the mRNA by affecting the fidelity and efficiency of protein synthesis [42].

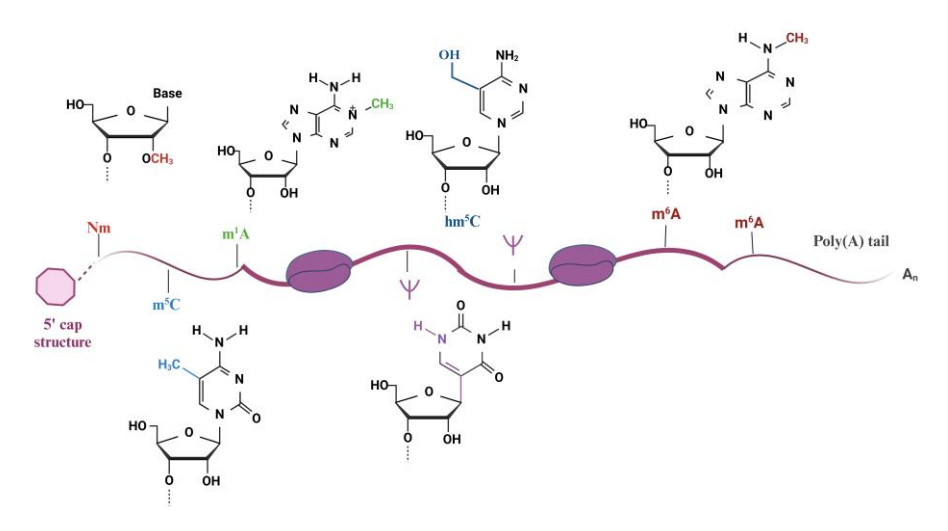


Fig. 4. Diagram illustrating chemical modifications in eukaryotic mRNA

ADAR enables extensive research in RNA editing technologies, emerging as a pivotal tool in recent years for applications ranging from genetic disorder correction to therapeutic RNA modifications. Important studies and technological innovations in the area of ADAR-based RNA editing[43] can be grouped under several headings:

- 1. RESTORE: RESTORE is designed for endogenous ADARs to edit specific RNA sequences with chemically modified antisense oligonucleotides (ASO). ASO consists of two main regions; the first region, the ADAR Recruitment Region, attracts ADAR to the target RNA, while the second region, the Target Specific Region, binds complementarily to the RNA sequence and performs editing from A-to-I. This system provides high specificity and has a broad RNA editing capacity. However, editing efficiency is low unless supported by IFN- α [44].
- 2. LEAPER and LEAPER 2.0: LEAPER allows endogenous ADAR enzymes to bind to RNA and perform editing using long antisense RNA sequences (arRNA); arRNA attracts ADAR to the target RNA by creating double-stranded RNA regions. In the LEAPER 2.0 system, the circular form of arRNAs was improved, editing efficiency was increased, and bystander effects were reduced. Editing efficiency reached 10% in mouse models developed for Hurler syndrome [45][46].
- 3. Clustered ADAR-Recruiting Guide RNAs for Efficient RNA Editing: This approach is a method in which the

RNA that directs ADAR to the target contains more than one binding sequence. Side effects (bystander edits) were minimized, and editing efficiency was increased with repeated binding sequences. RNA editing rate reached 10% in B16 mouse models [43].

- 4. AIMer Technology: It is a method that activates endogenous ADARs using short oligonucleotides. The stability of oligonucleotides has been increased by chemical modifications. High editing efficiency has been achieved in certain tissues, such as liver cells. Successful RNA editing has been achieved in the liver of human and animal models [43].
- 5. RESTARTv1 and RESTARTv2: RESTARTv1 is a system that performs RNA editing by combining the dCas13b protein with the catalytic domain of ADAR2. RESTARTv2 is an improved version that reduces off-target effects. Large protein sizes and off-target editing are the main limitations of the system. It has been applied to correct genetic mutations in cellular models such as neurons [47].
- 6. CRISPR-Based ADAR Systems: RNA editing is performed by combining CRISPR-Cas13 proteins with ADAR enzymes. It provides improved target specificity. It is easily applied in cellular models due to its low protein size. However, in CRISPR-based systems, there is a risk that bacterial proteins may trigger an immune system response [48].

7.CellREADR functions as a customizable RNA sensor-actuator technology that couples the detection of cell-specific RNA to the translation of an effector protein via the endogenous ADAR-mediated RNA sensing mechanism, enabling cell targeting, monitoring, and manipulation. The RNA-based device consists of a 5' sensor region complementary to the target cellular RNA and a 3' cargo region encoding a protein of interest. In metazoan cells, cargo translation is blocked via an ADAR-mediated A-to-I editing mechanism that removes a stop codon in the sensor region upon base pairing with the target cellular RNA. This system provides precise control over gene expression and cellular manipulation, expanding the potential applications of RNA editing in biomedical research and therapeutics [49].

miRNAs are single-stranded, non-coding RNAs that regulate gene expression through RNA interference (RNAi) mechanisms [27][28]. Their primary functions include targeting the 3' untranslated region (3'UTR) of mRNAs, leading to mRNA decay and/or translational repression [50]. A-to-I RNA editing can disrupt the interaction between miRNAs and their target mRNAs when editing occurs either on the miRNA itself or in the 3'UTR of the target mRNA. ADAR1 is essential to this process by directly binding to microRNA (miRNA) transcripts, which are crucial noncoding RNAs that regulate gene expression by binding to target genes [51]. ADAR is linked to miRNA preprocessing in cytoplasmic composition, miRNA loading into the RNA-induced silencing complex, miRNA gene silencing, and RNA interference pathways by regulating A-to-I editing of miRNA precursors or miRNA retargeting. These regulatory functions highlight the complex interplay between RNA editing, miRNA biogenesis, and posttranscriptional gene regulation. The deamination of viral RNAs by host deaminase enzymes has been specifically associated with measles virus (MV) infection [52]. This modification has been reported to be associated with the ability of the virus to manipulate the immune system and was first identified in human brain samples of MV [53]. Viral RNAs can cause ADAR1 overregulation, leading to excessive A-to-I RNA editing [54]. This enzyme facilitates the synthesis of complementary DNA (cDNA) from RNA templates and is widely used in genetic engineering and molecular cloning. Retroviral reverse transcriptase enzymes are essential for DNA synthesis from RNA and exhibit RNA/DNA-dependent DNA polymerase activity and ribonuclease H (RNase H) activity. These enzymes cleave the RNA template to produce RNA/DNA hybrids while simultaneously promoting DNA synthesis [55]. Regulatory structures that can both inhibit and activate mRNA translation through various mechanisms in eukaryotes are called G-quadruplexes (G4s), and G4s are secondary structures composed of repeated guanine sequences (TTAGGG-) that ensure the maintenance of genomic integrity and stability [56][57]. G4 structures are stabilized by metal ions, especially cations such as Na+, K+, and Li+. This stabilization occurs through the interaction of metal ions with the carbonyl oxygens of guanines [58]. These structures are mostly found in genomic areas such as human telomeric DNA and are crucial for the maintenance of telomeres. Telomeric structures are associated with cell aging and cancer phenotypes. Therapeutic agents directed against G4 structures may have potential use in cancer treatment.

N6-methyladenosine (m6A) is a predominant RNA modification, mostly found in mRNA, and is of great importance in regulating various aspects of RNA biology, including RNA stability, splicing, translation, and degradation [59]. Specifically, adding m6A to RNA may influence the binding of ADAR enzymes to RNA, thereby affecting A-to-I editing levels. The levels of adenosine methylation in mRNA are tightly controlled by a group of enzymes known as 'writers,' particularly METTL3 and METTL14, which work together to catalyze the addition of the methyl group to adenosine. Among the most notable readers are the YT521-B homology family proteins, such as YTHDF1, YTHDF2, and YTHDF3, which modulate critical processes like mRNA stability, translation efficiency, and decay. Importantly, METTL3 is the only enzyme within the m6A writer complex that possesses catalytic activity, making it central to regulating m6A modification and its subsequent effects on RNA metabolism and cellular functions [60]. Jesus et al. showed that METTL3 levels increase at the onset of T1D and then rapidly decrease. Additionally, they reported that m6A hypermethylation of oligoadenylate synthetase (OAS) genes and downregulation of METTL3 in both human pseudo-islet cells and EndoC-βH1 cells led to the upregulation of OAS proteins [60]. A-to-I regulation can significantly affect the immune response around the tumor microenvironment, causing inosin modifications to escape from immune surveillance of malignant tumors. Therefore, it can reduce the effectiveness of immunotherapies and the immunogenicity of RNA sequences. Understanding the interplay between m6A and A-to-I editing could provide novel insights into tumor biology and immune evasion mechanisms.

3. ADAR and Cancer

Cancer is the uncontrolled division of cells resulting from a combination of epigenetic, genetic, and environmental factors. Cancer cells exhibit high mutation rates and leverage mechanisms responsible for maintaining host immune system balance and homeostasis to evade immune responses. Environmental influences, such as exposure to carcinogens (e.g., tobacco smoke, radiation, pollutants), viral infections, chronic inflammation, and lifestyle factors, also contribute to tumor initiation and progression. In-depth understanding and study of the interactions between these factors by the scientific community is indispensable in the design of evidence-based prevention and treatment practices. RNA serves a critical function in cancer biology and is active in processes such as tumorigenesis, metastasis, and immune evasion. ADAR1 regulates the activation of innate immune responses when pathogenic or endogenous RNAs exhibit similar properties to viral RNAs. Cancer cell death can occur through the Type I IFN and protein kinase R (PKR) pathways with ADAR1 loss. Evaluations have shown that inhibiting ADAR1 as a single target may represent a new approach for treating a subset of cancer cells [61]. Chung et al. showed that RNA editing mediated by different ADAR1 mutants can completely suppress PKR activation in HEK293T cells [62].

RNA modifications are a different category of epigenetic modifications from classical modifications, which usually involve DNA and histones. Epitranscriptomic studies aim to understand RNA modifications, biogenesis mechanisms, and regulatory roles. Additionally, the evolutionary conservation of modified RNAs, their interactions, and connections with novel reader proteins are investigated [63]. The A-to-I transition results from deamination of the amino group at the C6 position of adenosine, altering the information content and potentially the secondary structure of RN [64]. A-to-I RNA editing leads to epitranscriptome and proteome diversity in various cancers [65]. ADAR1 reduces the immunogenicity of Alu sequences by performing A-to-I RNA editing on these sequences. This mechanism, which facilitates tumor cell evasion of immune surveillance, may reduce the efficacy of immunotherapies [66]. During metabolic reprogramming of tumor cells, tumor cells preferentially use glycolysis even under aerobic conditions due to the Warburg effect. The Warburg effect, which is frequently observed in cancerous tissues, leads to the accumulation of lactic acid, which leads to acidification of the tumor microenvironment [67]. Lactic acid accumulation increases the levels of A-to-I RNA editing and ADAR1 activity in the medium [68]. Therefore, lactic acid serves a critical function in disrupting tumor immune surveillance by reducing the immunogenicity of Alu sequences[69]. These results underscore ADAR1's role in immunotherapy resistance mechanisms and its importance as a potential therapeutic target.

Chemotherapy, which continues to be one of the cornerstones of cancer treatment, is frequently encountered with

resistance, which leads to poor clinical outcomes. Chemotherapy resistance occurs due to the complex interaction of multiple mechanisms. In particular, it is necessary to understand and address these mechanisms, such as drug excretion, DNA damage repair, apoptosis escape, epigenetic changes, intracellular drug metabolism, and tumor stem cells. Combination therapies that combine targeted therapies, immunotherapies, and conventional chemotherapy may be promising for cancer treatment. A deeper understanding of ADAR1-mediated RNA editing and its impact on chemotherapy resistance and immunotherapy success will contribute to the identification of new therapeutic targets. Nakano et al. [69] reported that DHFR, which is targeted by antifolate drugs such as methotrexate, is regulated by ADAR1 through A-to-I regulation and alters the binding sites of miR-25-3p and miR-125a-3p in the 3'-UTR region. In addition, they reported that ADAR1 serves a critical function in controlling the expression of the Dihydrofolate reductase (DHFR) gene. Hariharan et al.[70] reported that it enhances the resistance to antifolates by intensifying the A-to-I regulation of BAP1 in wild-type mesothelioma cells, strengthening the role of RNA editing in cancer treatment challenges. In addition, they reported that the knockdown of ADAR2 can increase the efficacy of cancer treatment by increasing the sensitivity to primary chemotherapeutic agents such as pemetrexed. ADAR1 and ADAR2, which regulate A-to-I RNA editing in cancer cells, affect chemotherapy resistance pathways. SCD1 is sustained through ADAR1-mediated A-to-I modulation in gastric cancer cells. This alteration improves the stability of SCD1 mRNA, hence facilitating the survival of cancer cells. Elevated SCD1 facilitates lipid droplet formation to mitigate endoplasmic reticulum (ER) stress and augment cancer stem cell proliferation. This mechanism increases treatment resistance in gastric cancer cells [71].

Increased expression and activation of ADAR1p150, a highly active A-to-I isoform, is a potential target for inhibiting ADAR1 activity in cancer. Rebecsinib is the first inhibitor reported [52] and has been shown to disrupt ADAR1p150 activation by binding to the spliceosome core complex. Since the N-terminus of ADAR1p150 contains a nuclear export signal, therapies targeting the nuclear export of ADAR1p150, such as selective nuclear export inhibitors (NEIs), it is effective in cancer treatment [72]. In preclinical models, NEIs such as Leptomycin B, Selinexor (KPT-330), and Eltanexor (KPT-8602) have been shown to have antitumor activity. KPT-330 has recently received US FDA approval for relapsed/refractory multiple myeloma[73]. Inhibition of the ADAR1 enzyme is an important strategy for pharmacologically targeting aberrant modifications in this editing. In diseases such as cancer, dysregulation of this editing can enhance oncogene activity or inactivate tumor suppressor genes. Inhibition of ADAR1 offers a therapeutic approach by blocking these processes [74]. Inosine-terminated molecules can bind to RNAs (e.g., mRNA, miRNA, and lncRNA) that regulate genes in cancer cells. This can inhibit or alter the activity of cancer-related genes. Increased inosine bases can be seen in cancer cells. This may contribute to tumorigenesis by affecting gene regulation and protein production. Molecules containing inosine can disrupt the normal functions of RNA, leading to cellular stress and apoptosis. Cancer cells are more sensitive to such changes in RNA.

Gliomas are malignant brain tumors in adults [75]. A-to-I editing is an important RNA modification in gliomas. ADAR2 leads to decreased RNA editing of the GluA2 subunit in gliomas in the Q/R region (glutamine-to-arginine site)[76]. The expression of ADAR3, a brain-specific adenosine deaminase, is associated with glioma progression[77] [78] [79]. A-to-I RNA editing has been extensively studied in liver cancer, particularly with antizyme inhibitor 1 (AZIN1) protein, and has been proven to contribute to liver cancer progression. Edited AZIN1 gains higher protein stability and promotes cell proliferation by forming a stronger affinity with antizyme. It also translocates from the cytoplasm to the nucleus, which promotes cancer progression [80]. Ghalali et al.[80] showed that the binding of regulated AZIN1 with the actin/myosin9 complex triggers the nuclear translocation of AZIN1 and is linked to prostate cancer. RNA and DNA analyses show that the Bladder cancer-associated protein (BLCAP) is overregulated in liver cancer. Overregulated BLCAP exhibits a proliferation-promoting phenotype in vitro and in vivo [81]. However, overregulated BLCAP loses its ability to block STAT3 activation and promotes cancer progression [82]. This mechanism suggests that the GABA A receptor may play a protective role in RNA editing [83]. Understanding the effects of regulatory enzymes such as ADAR2 and ADAR3 in gliomas and their effects in specific cancer types may lead to new therapeutic approaches in RNA editing. Furthermore, the functions of proteins such as AZIN1, BLCAP, and Gabra3 highlight the pivotal role of A-to-I RNA editing in different cancer types. These proteins can contribute

to cancer progression by undergoing changes in functional properties, stability, and cellular localization due to the A-to-I RNA regulation mediated by ADAR enzymes. For example, while ADAR1-mediated A-to-I regulation increases the oncogenic potential in hepatocellular carcinoma (HCC), while the excessive regulation of BLCAP disrupts the tumor suppressive function in multiple cancer types[84]. ADAR inhibitors will revolutionize future cancer treatment studies as more research is conducted on RNA regulatory mechanisms and therapeutic inosine-based molecules.

4. RNA Editing in Genetic and oOncological Therapies

The array context of adenosines plays a critical role in functional RNA areas such as translation starting zones (TIS), addition acceptance and donor zones, microRNA interaction points, and polyadenylation signals (PAS). Targeting these regions through RNA regulation can provide significant opportunities for therapeutic approaches, making precise control of protein expression and additional control processes. This ability may increase the efficacy of current strategies that include using antisense oligonucleotides (ASOs) that inhibit the function of TISs, splice sites, or PAS. In humans, ADAR1 and ADAR2 are the major regulatory enzymes that catalyze A-to-I conversion in mRNA. However, the correlation between mRNA expression levels and A-to-I editing activity across tissues is generally low (generally $R^2 = 0.2-0.25$), but this relationship is stronger in the brain, reaching up to $R^2 = 0.55$. This observation indicates that supplementary factors, including RNA splicing, RNA quantity, and the RNA-binding protein milieu, substantially affect editing efficiency. Although most tissues display comparable levels of RNA editing, significant deviations are observed in the cerebellum and arteries, which demonstrate the highest editing activity attributable to the strong co-expression of ADAR1 and ADAR2. Skeletal muscle has low editing levels, possibly associated with diminished ADAR1 expression and the role of the multifunctional protein AIMP2, which adversely affects the stability of both ADAR1 and ADAR2[85]. ADAR-mediated RNA editing has emerged as a revolutionary tool for designing RNA molecules, correcting certain mutations, and regulating protein activities. This method allows RNA modifications without causing permanent changes to the genome. ADAR-based RNA arrangement has made significant progress in a wide variety of applications from the treatment of genetic diseases to the correction of diseaserelated mutations and the treatment of genetic diseases. A schematic representation of the ADAR-based RNA editing mechanism is presented in Fig. 5. [86].

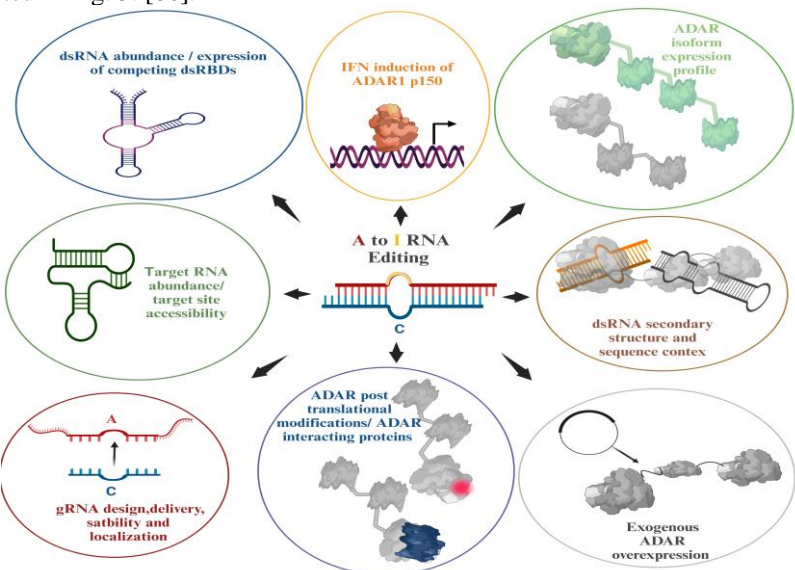


Fig. 5. Visual depiction of ADAR-based RNA Editing Engineering[87].

DNA regulation causes permanent genomic changes, but RNA regulation does not cause permanent changes and offers a dynamic approach. Therefore, RNA regulation stands out as a safer and more preferred method for the treatment of acute conditions such as viral infections or inflammation. For example, it allows the temporary correction of mutations related to neurological disorders (eg, RETT syndrome) and metabolic diseases (eg, transcarbamylase deficiency) without permanent changes in the genome[88]. In addition, RNA regulation offers cell-type-specific and time-controlled interventions. Thus, it is a promising alternative to traditional gene therapy approaches. New molecules and strategies for treating genetic diseases will improve both the safety and efficacy of RNA-based therapies and enable more widespread clinical applications in the future. Relevant clinical data support the broad applicability of these technologies.

Research on Rett syndrome, Duchenne muscular dystrophy, and ornithine transcarbamylase deficiency reveals the importance of RNA editing in genetic disorders. Rett Syndrome was studied in two mouse models; exogenous ADAR successfully corrected nonsense (MECP2 W104X) and nonsense (MECP2 R106Q) mutations, demonstrating the applicability of RNA editing to a variety of mutation types[87]. Similarly, Duchenne Muscular Dystrophy was studied in the mdx mouse model; RNA editing corrected a nonsense mutation, highlighting the potential to treat genetic muscle disorders[89]. RNA editing of the 5' splice site mutation in the splash mouse model for ornithine transcarbamylase deficiency restored proper splicing, demonstrating the ability of RNA editing to function effectively at the pre-mRNA level[90].

Alpha-1 Antitrypsin Deficiency (AATD) presents a promising target for RNA editing applications in human cells. ASOs targeting the SERPINA1 E342K mutation achieved greater than 40% RNA editing of mutant mRNA, demonstrating therapeutic applicability[44]. Although primarily associated with lung and liver diseases, AATD has also been linked to an increased risk of hepatocellular carcinoma (HCC) due to the accumulation of misfolded α1-antitrypsin in hepatocytes[91]. Regulation of mRNA and Protein Levels Targeting adenosine-containing motifs (e.g., splice acceptor sites, TISs, PAS) can therapeutically regulate mRNA and protein levels, demonstrating significant effects of RNA editing on genetic regulation[86]. Editing the β-site amyloid precursor protein cleaving enzyme cleavage site offers a therapeutic approach for Alzheimer's disease[92]. Selinexor, developed by Karyopharm Therapeutics, is a pioneering work that bridges the gap between ADAR inhibition and oncology therapies [93]. ADAR2's natural role in regulating ion channel permeability could be expanded to therapeutically modulate specific ion channels, particularly Nav1.7, which is important for pain management [85]. Wang et al. revealed that A-to-I RNA editing on COPA affects the reaction of colorectal cancer cells to immune checkpoint inhibitor treatment [94]. Shen et al.[95] found that CircNEIL3 levels were associated with the clinical stage of pancreatic ductal adenocarcinoma and the overall survival of patients. CircNEIL3 upregulates ADAR1, while ADAR1 regulates the biogenesis of circNEIL3 through a negative feedback loop.

5. Conclusion, Discussion, and Future Directions

A-to-I RNA editing is of vital importance as it enables modification of genetic material at the RNA level, thereby regulating RNA stability, gene expression, and protein functions. ADAR1 is a prominent member of the ADAR enzyme family and serves a critical function in cancer progression by allowing tumor cells to evade immune detection and develop resistance to chemotherapy. Research has shown that ADAR1 activity is associated with various malignancies, such as hepatocellular carcinoma, mesothelioma, and gastric cancer. In recent years, inhibition of ADAR enzymes has become an important area of research due to its potential to reduce chemotherapy resistance and re-recognize tumor cells by the immune system. Targeting ADAR1 and ADAR2 may serve a critical function thanks to the development of innovative approaches that are becoming increasingly used in cancer treatment. ADAR1p150 regulates immunity while ADAR1p110 plays a role in the cellular stress response. ADAR1 is a critical regulator in the context of innate immunity and has bridged the gap between the detection of endogenous and exogenous RNA molecules and the prevention of autoimmune responses. The Zα domain or ADAR1 p150 isoform stands out as potential therapeutic target to control A-to-I RNA editing and disrupt the oncogenic RNA balance in cancer cells.

Developments in RNA editing technologies have very important potential for precision therapeutic applications in oncology. Inosine can increase RNA stability due to its structural similarity to guanosine; however, irregular inosine regulation can lead to the disruption of cellular homeostasis and tumor formation. Inosine-based pharmacological approaches have the potential to normalize gene expression and activate tumor suppressor pathways, offering new therapeutic opportunities in cancer treatment. In addition, further investigation of the effects of inosine modifications on functional RNAs such as miRNA and tRNA may contribute to the identification of new therapeutic targets on gene regulation, protein synthesis, and cellular mechanisms. Molecules and aptamers containing inosine are promising in cancer treatment by targeting cancer-specific RNA sequences. AZIN1, which leads to changes in the expression level activity of ADARs during cancer progression, is one of the most studied ADAR1 targets. Thanks to its structure that allows programming of CRISPR-Cas13 enzymes, an RNA-guided RNA targeting system, it is a clinically promising platform that can effectively reduce target gene expression as it provides RNA binding and degradation in eukaryotic cells. Inosine-containing aptamers bind specifically to RNA segments and regulate gene expression or translation mechanisms, thus being used to treat viral infections and genetic diseases. The development of next-generation RNA editing technologies such as RESTORE, LEAPER, and AIMer may provide significant advances in RNA editing strategies by increasing editing specificity and minimizing off-target effects. Inhibition of ADAR1 may be effective in cancer treatment by increasing the sensitivity of immunotherapy. However, CRISPR-based gene editing provides permanent changes, while RNA editing often produces transient effects. This may render RNA editing inadequate for certain genetic diseases. In addition, the combined use of CRISPR and ADAR-based RNA editing approaches may lead to some undesirable immune responses due to system interactions. These challenges are summarized below:

- Off-target RNA editing may complicate therapeutic applications.
- Difficulties may be experienced in tissue-specific and efficient delivery of ADAR enzymes or RNA guide molecules.
 - Some supportive interventions may be required due to low editing efficiency in some systems.
 - Clinical use of exogenous ADAR enzymes may trigger immune responses, hindering their applicability.

To overcome these challenges, integrating RNA editing technologies into clinical use is critical. Specifically, targeting the ADAR1 P150 isoform can increase the effectiveness of immunotherapies by preventing tumor cells from escaping from the immune system. With the expansion of clinical applications, ADAR-based RNA regulation may become an important tool in the treatment of genetic diseases such as AATD, RETT syndrome, and Duchenne muscle dystrophy. This technology can correct genetic mutations in RNA instead of DNA levels, minimizing risks caused by permanent genetic changes. More precise guide RNA designs can minimize non-target effects and increase therapeutic security by connecting to target RNA sequences. The development of biomolecular systems that control real-time ADAR enzyme activity and amount may increase treatment effectiveness. Patient-specific RNA editing therapies could improve treatment success for genetic diseases, setting a new standard in individualized medicine. Additionally, facilitating the large-scale production of RNA editing technologies will make these technologies available to a wider audience. The applicability of ADAR-based regulation in a broader range of genetic and epigenetic diseases should be examined in detail in further studies.

Conflict Declaration

As the authors of this study, we declare that we have no declaration of conflict.

Acknowledgments

Hasret Türkmen was supported by TUBİTAK (Scientific and Technological Research Council of TÜRKİYE) [No: 123C441].

Author Contribution

H.T. designed the study, organized, and wrote the manuscript. N.D. drew all the figures. M.Ş. and M.C. reviewed and gave final approval of the manuscript.

References

- [1] P. A. Levene and W. A. Jacobs, "On the structure of thymus nucleic acid," J. Biol. Chem., vol. 12, pp. 411-420, 1912.
- [2] S. Delaunay, M. Helm, and M. Frye, "RNA modifications in physiology and disease: Towards clinical applications," *Nat. Rev. Genet.*, Feb. 2024. doi: 10.1038/s41576-023-00645-2.
- [3] J. D. Watson and F. H. C. Crick, "A structure for deoxyribose nucleic acid." *Exploratorium Origins Project*. [Online]. Available: https://annex.exploratorium.edu/origins/coldspring/printit.html (accessed Sep. 25, 2025).
- [4] R. W. Holley *et al.*, "Structure of a ribonucleic acid," *Science*, vol. 147, no. 3664, pp. 1462–1465, Mar. 1965, doi: 10.1126/science.147.3664.1462.
- [5] R. Desrosiers, K. Friderici, and F. Rottman, "Identification of methylated nucleosides in messenger RNA from Novikoff hepatoma cells," *Proc. Natl. Acad. Sci. U.S.A.*, vol. 71, no. 10, pp. 3971–3975, Oct. 1974, doi: 10.1073/pnas.71.10.3971.
- [6] K. D. Meyer and S. R. Jaffrey, "The dynamic epitranscriptome: N6-methyladenosine and gene expression control," *Nat. Rev. Mol. Cell Biol.*, vol. 15, no. 5, pp. 313–326, May 2014, doi: 10.1038/nrm3785.
- [7] B. L. Bass and H. Weintraub, "An unwinding activity that covalently modifies its double-stranded RNA substrate," *Cell*, vol. 55, no. 6, pp. 1089–1098, Dec. 1988, doi: 10.1016/0092-8674(88)90253-X.
- [8] D. B. T. Cox *et al.*, "RNA editing with CRISPR-Cas13," *Science*, vol. 358, no. 6366, pp. 1019–1027, Nov. 2017, doi: 10.1126/science.aaq0180. [9] I. A. Roundtree, M. E. Evans, T. Pan, and C. He, "Dynamic RNA modifications in gene expression regulation," *Cell*, vol. 169, no. 7, pp. 1187–1200, Jun. 2017, doi: 10.1016/j.cell.2017.05.045.
- [10] N. Jonkhout *et al.*, "The RNA modification landscape in human disease," *RNA*, vol. 23, no. 12, pp. 1754–1769, Dec. 2017, doi: 10.1261/rna.063503.117.
- [11] Y. Li *et al.*, "RNA-editing enzyme ADAR1 p150 isoform is critical for germinal center B cell response," *J. Immunol.*, vol. 209, no. 6, pp. 1071–1082, Sep. 2022, doi: 10.4049/jimmunol.2200149.
- [12] P. Mukherjee, "Molecular significance of the ADAR3 R-domain in mediating ADAR3-RNA interactions in vivo," Ph.D. dissertation, Indiana University, Bloomington, IN, USA, 2024.
- [13] Y. Jiao et al., "The role of ADAR1 through and beyond its editing activity in cancer," Cell Commun. Signal., Jan. 2024, doi: 10.1186/s12964-023-01465-x.
- [14] C. Liu, J. Cao, H. Zhang, and J. Yin, "Evolutionary history of RNA modifications at N6-adenosine originating from the R-M system in eukaryotes and prokaryotes," *Biology (Basel)*, vol. 11, no. 2, Feb. 2022, doi: 10.3390/biology11020214.
- [15] X.-L. Mao, G. Eriani, and X.-L. Zhou, "ADATs: Roles in tRNA editing and relevance to disease," *Acta Biochim. Biophys. Sin. (Shanghai)*, vol. 57, no. 1, pp. 73–83, Jul. 2024, doi: 10.3724/abbs.2024125
- [16] I. Barbieri and T. Kouzarides, "Role of RNA modifications in cancer," Nat. Rev. Cancer, Jun. 2020, doi: 10.1038/s41568-020-0253-2.
- [17] A. Karki, K. B. Campbell, S. Mozumder, A. J. Fisher, and P. A. Beal, "Impact of disease-associated mutations on the deaminase activity of ADAR1," *Biochemistry*, vol. 63, no. 3, pp. 282–293, Feb. 2024, doi: 10.1021/acs.biochem.3c00405.
- [18] E. Eisenberg and E. Y. Levanon, "A-to-I RNA editing—Immune protector and transcriptome diversifier," *Nat. Rev. Genet.*, Aug. 2018, doi: 10.1038/s41576-018-0006-1.
- [19] B. Zinshteyn and K. Nishikura, "Adenosine-to-inosine RNA editing," Wiley Interdiscip. Rev. Syst. Biol. Med., vol. 1, no. 2, pp. 202–209, Sep. 2009, doi: 10.1002/wsbm.10.
- [20] M. M. Lamers, B. G. van den Hoogen, and B. L. Haagmans, "ADAR1: 'Editor-in-Chief' of cytoplasmic innate immunity," Front. Immunol., vol. 10, p. 1763, 2019, doi: 10.3389/fimmu.2019.01763.
- [21] S. H. Roth, E. Y. Levanon, and E. Eisenberg, "Genome-wide quantification of ADAR adenosine-to-inosine RNA editing activity," Nat. Methods, vol. 16, no. 11, pp. 1131–1138, Nov. 2019, doi: 10.1038/s41592-019-0610-9. [22] K. Fritzell, L. Di Xu, M. Otrocka, C. Andréasson, and M. Öhman, "Sensitive ADAR editing reporter in cancer cells enables high-throughput screening of small molecule libraries," Nucleic Acids Res., vol. 47, no. 4, p. e22, Feb. 2019, doi: 10.1093/nar/gky1228.
- [23] H. Grosjean et al., "Enzymatic conversion of adenosine to inosine and to N1-methylinosine in transfer RNAs: A review," Biochimie, vol. 78, no. 6, pp. 488–501, 1996, doi: 10.1016/0300-9084(96)88148-5.
- [24] Y. Kawahara, "Quantification of adenosine-to-inosine editing of microRNAs using a conventional method," Nat. Protoc., vol. 7, no. 7, pp. 1426–1437, 2012, doi: 10.1038/nprot.2012.073.
- [25] M. Sakurai, T. Yano, H. Kawabata, H. Ueda, and T. Suzuki, "Inosine cyanoethylation identifies A-to-I RNA editing sites in the human transcriptome," Nat. Chem. Biol., vol. 6, no. 10, pp. 733–740, Oct. 2010, doi: 10.1038/nchembio.434. [26] T. A. Nguyen et al., "Direct identification of A-to-I editing sites with nanopore native RNA sequencing," Nat. Methods, vol. 19, no. 7, pp. 833–844, Jul. 2022, doi: 10.1038/s41592-022-01513-3.
- [27] J.-J. Chen et al., "Single-Base Resolution Detection of Adenosine-to-Inosine RNA Editing by Endonuclease-Mediated Sequencing," Anal.

- Chem., vol. 94, no. 24, pp. 8740–8747, Jun. 2022, doi: 10.1021/acs.analchem.2c01226. [28] W.-B. Tao, N.-B. Xie, Q.-Y. Cheng, Y.-Q. Feng, and B.-F. Yuan, "Sensitive determination of inosine RNA modification in single cell by chemical derivatization coupled with mass spectrometry analysis," Chin. Chem. Lett., vol. 34, no. 10, Art. no. 108243, Oct. 2023, doi: 10.1016/j.cclet.2023.108243.
- [29] Y.-Y. Zheng, K. Reddy, S. Vangaveti, and J. Sheng, "Inosine-Induced Base Pairing Diversity during Reverse Transcription," ACS Chem. Biol., vol. 19, no. 2, pp. 348–356, Feb. 2024, doi: 10.1021/acschembio.3c00555.
- [30] Y. Yuxi, Dissertation "Inosine chemical labeling and molecular purification of edited RNA & DNA using maleimide (マレイミドによる塩基編集を持つ核酸におけるイノシンの化学標識と分子精製技術の開発)," 2024. [Online]. Available: institutional repository (URL not provided). [Accessed: Sep. 25, 2025].
- [31] Y. Wang, Y. Zheng, and P. A. Beal, "Adenosine Deaminases That Act on RNA (ADARs)," in *Enzymes*, vol. 41, Academic Press, 2017, pp. 215–268, doi: 10.1016/bs.enz.2017.03.006.
- [32] A. G. Torres, E. Batlle, and L. Ribas de Pouplana, "Role of tRNA modifications in human diseases," Trends Mol. Med., vol. 20, no. 6, pp. 306–314, Jun. 2014, doi: 10.1016/j.molmed.2014.01.008.
- [33] M. Pereira, S. Francisco, A. S. Varanda, M. Santos, M. A. S. Santos, and A. R. Soares, "Impact of tRNA modifications and tRNA-modifying enzymes on proteostasis and human disease," Int. J. Mol. Sci., vol. 19, no. 12, p. 3738, Dec. 2018, doi: 10.3390/ijms19123738.
- [34] Y.-Y. Zheng, Y. Wu, T. J. Begley, and J. Sheng, "Sulfur modification in natural RNA and therapeutic oligonucleotides," RSC Chem. Biol., vol. 2, no. 8, pp. 990–1003, Aug. 2021, doi: 10.1039/D1CB00038A.
- [35] R. Saran, Z. Huang, and J. Liu, "Phosphorothioate nucleic acids for probing metal binding, biosensing and nanotechnology," Coord. Chem. Rev., vol. 428, p. 213624, Feb. 2021, doi: 10.1016/j.ccr.2020.213624.
- [36] "Gene organization and evolutionary history," *Genome Biol.* (web feature), 2012. [Online]. Available http://genomebiology.com/2012/13/12/252. [Accessed: Sep. 25, 2025].
- [37] I. Alseth, B. Dalhus, and M. Bjørås, "Inosine in DNA and RNA," Curr. Opin. Genet. Dev., vol. 26, pp. 116–123, Jun. 2014, doi: 10.1016/j.gde.2014.07.008.
- [38] X. Peng et al., "A-to-I RNA Editing Contributes to Proteomic Diversity in Cancer," Cancer Cell, vol. 33, no. 5, pp. 817–828.e7, May 2018, doi: 10.1016/j.ccell.2018.03.026.
- [39] R. Brusa et al., "Early-onset epilepsy and postnatal lethality associated with an editing-deficient GluR-B allele in mice," Science, vol. 270, no. 5242, pp. 1677–1680, Dec. 1995, doi: 10.1126/science.270.5242.1677.
- [40] V. Tassinari et al., "ADAR1 is a new target of METTL3 and plays a pro-oncogenic role in glioblastoma by an editing-independent mechanism," Genome Biol., vol. 22, no. 1, p. 51, Jan. 2021, doi: 10.1186/s13059-021-02271-9.
- [41] A. Bavelloni *et al.*, "AKT-dependent phosphorylation of the adenosine deaminases ADAR-1 and -2 inhibits deaminase activity," *FASEB J.*, vol. 33, no. 8, pp. 9044–9061, Aug. 2019, doi: 10.1096/fj.201800490RR.
- [42] H. Song et al., "Biological roles of RNA m5C modification and its implications in cancer immunotherapy," Biomark. Res., vol. 10, art. 15, Dec. 2022. doi: 10.1186/s40364-022-00362-8.
- [43] J. Song, Y. Zhuang, and C. Yi, "Programmable RNA base editing via targeted modifications," *Nat. Chem. Biol.*, vol. 20, no. 3, pp. 277–290, Mar. 2024, doi: 10.1038/s41589-023-01531-y.
- [44] T. Merkle *et al.*, "Precise RNA editing by recruiting endogenous ADARs with antisense oligonucleotides," *Nat. Biotechnol.*, vol. 37, no. 2, pp. 133–138, Feb. 2019, doi: 10.1038/s41587-019-0013-6.
- [45] L. Qu et al., "Programmable RNA editing by recruiting endogenous ADAR using engineered RNAs," Nat. Biotechnol., vol. 37, no. 9, pp. 1059–1069, Sep. 2019, doi: 10.1038/s41587-019-0178-z.
- [46] Z. Yi et al., "Engineered circular ADAR-recruiting RNAs increase the efficiency and fidelity of RNA editing in vitro and in vivo," Nat. Biotechnol., vol. 40, no. 6, pp. 946–955, Jun. 2022, doi: 10.1038/s41587-021-01180-3.
- [47] J. Song et al., "CRISPR-free, programmable RNA pseudouridylation to suppress premature termination codons," Mol. Cell, vol. 83, no. 1, pp. 139–155.e9, Jan. 2023, doi: 10.1016/j.molcel.2022.11.011.
- [48] M. R. O'Connell et al., "Programmable RNA recognition and cleavage by CRISPR/Cas9," Nature, vol. 516, no. 7530, pp. 263–266, Dec. 2014, doi: 10.1038/nature13769.
- [49] X. Yang et al., "CellREADR: An ADAR-based RNA sensor-actuator device," in Methods in Enzymology: ADARs, vol. 710, pp. 207–227, 2025, doi: 10.1016/bs.mie.2024.11.027.
- [50] K. Saliminejad, H. R. Khorram Khorshid, S. Soleymani Fard, and S. H. Ghaffari, "An overview of microRNAs: Biology, functions, therapeutics, and analysis methods," *J. Cell. Physiol.*, vol. 234, no. 5, pp. 5451–5465, May 2019, doi: 10.1002/jcp.27486.
- [51] T. Chen et al., "ADAR1 is required for differentiation and neural induction by regulating microRNA processing in a catalytically independent manner," Cell Res., vol. 25, no. 4, pp. 459–476, Apr. 2015, doi: 10.1038/cr.2015.24.
- [52] R. Cattaneo, A. Schmid, D. Eschle, K. Baczko, V. ter Meulen, and M. A. Billeter, "Biased hypermutation and other genetic changes in defective measles viruses in human brain infections," *Cell*, vol. 55, no. 2, pp. 255–265, Oct. 1988, doi: 10.1016/0092-8674(88)90048-7.
- [53] M. A. Billeter and R. Cattaneo, "Molecular biology of defective measles viruses persisting in the human central nervous system," in *The Paramyxoviruses*, D. W. Kingsbury, Ed. New York, NY, USA: Plenum Press, 1991, pp. 323–345.
- [54] R. C. Zahn, I. Schelp, O. Utermöhlen, and D. von Laer, "A-to-G hypermutation in the genome of lymphocytic choriomeningitis virus," *J. Virol.*, vol. 81, no. 2, pp. 457–464, Jan. 2007, doi: 10.1128/JVI.00067-06.
- [55] S. Werner and B. M. Wöhrl, "Homodimeric reverse transcriptases from Rous sarcoma virus mutated within the polymerase or RNase H active

- site of one subunit are active," Eur. J. Biochem., vol. 267, no. 15, pp. 4740-4744, Aug. 2000, doi: 10.1046/j.1432-1327.2000.01530.x.
- [56] J. D. Roberts, K. Bebenek, and T. A. Kunkel, "The accuracy of reverse transcriptase from HIV-1," *Science*, vol. 242, no. 4882, pp. 1171–1173, Nov. 1988, doi: 10.1126/science.2460925.
- [57] Y. Teng, M. Zhu, Y. Chi, L. Li, and Y. Jin, "Can G-quadruplex become a promising target in HBV therapy?," Front. Immunol., vol. 13, art. 1091873, Dec. 2022, doi: 10.3389/fimmu.2022.1091873.
- [58] C. Saintomé, S. Amrane, J.-L. Mergny, and P. Alberti, "The exception that confirms the rule: A higher-order telomeric G-quadruplex structure more stable in sodium than in potassium," *Nucleic Acids Res.*, vol. 44, no. 6, pp. 2926–2935, Apr. 2016, doi: 10.1093/nar/gkw003.
- [59] M. Frye, B. T. Harada, M. Behm, and C. He, "RNA modifications modulate gene expression during development," *Science*, vol. 361, no. 6409, pp. 1346–1349, Sep. 2018, doi: 10.1126/science.aau1646.
- [60] D. F. De Jesus *et al.*, "Redox regulation of m6A methyltransferase METTL3 in β-cells controls the innate immune response in type 1 diabetes," *Nat. Cell Biol.*, vol. 26, no. 3, pp. 421–437, Mar. 2024, doi: 10.1038/s41556-024-01368-0.
- [61] J. Rehwinkel and P. Mehdipour, "ADAR1: From basic mechanisms to inhibitors," *Trends Cell Biol.*, vol. 35, no. 1, pp. 59–73, Jan. 2025, doi: 10.1016/j.tcb.2024.06.006. (Epub Jul. 18, 2024.).
- [62] H. Chung et al., "Human ADAR1 prevents endogenous RNA from triggering translational shutdown," Cell, vol. 172, no. 4, pp. 811–824.e14, Feb. 2018, doi: 10.1016/j.cell.2017.12.038.
- [63] A. Kobayashi, Y. Kitagawa, A. Nasser, H. Wakimoto, K. Yamada, and S. Tanaka, "Emerging roles and mechanisms of RNA modifications in neurodegenerative diseases and glioma," *Cells*, vol. 13, no. 5, p. 457, Mar. 2024, doi: 10.3390/cells13050457.
- [64] O. Solomon *et al.*, "RNA editing by ADAR1 leads to context-dependent transcriptome-wide changes in RNA secondary structure," *Nat. Commun.*, vol. 8, no. 1, p. 1440, Dec. 2017, doi: 10.1038/s41467-017-01458-8.
- [65] F. J. Gassner *et al.*, "RNA editing contributes to epitranscriptome diversity in chronic lymphocytic leukemia," *Leukemia*, vol. 35, no. 4, pp. 1053–1063, Apr. 2021, doi: 10.1038/s41375-020-0995-6.
- [66] P. Mehdipour et al., "Epigenetic therapy induces transcription of inverted SINEs and ADAR1 dependency," Nature, vol. 588, no. 7836, pp. 169–173, Dec. 2020, doi: 10.1038/s41586-020-2844-1.
- [67] N. Y. Spencer and R. C. Stanton, "The Warburg effect, lactate, and nearly a century of trying to cure cancer," *Semin. Nephrol.*, vol. 39, no. 4, pp. 380–393, Jul. 2019, doi: 10.1016/j.semnephrol.2019.04.007.
- [68] M. Certo, C.-H. Tsai, V. Pucino, P. C. Ho, and C. Mauro, "Lactate modulation of immune responses in inflammatory versus tumour microenvironments," *Nat. Rev. Immunol.*, vol. 21, no. 3, pp. 151–161, Mar. 2021, doi: 10.1038/s41577-020-0406-2. [69] M. Nakano, T. Fukami, S. Gotoh, and M. Nakajima, "A-to-I RNA editing up-regulates human dihydrofolate reductase in breast cancer," *J. Biol. Chem.*, vol. 292, no. 12, pp. 4873–4884, Mar. 2017, doi: 10.1074/jbc.M117.775684.
- [70] A. Hariharan *et al.*, "Heterogeneous RNA editing and influence of ADAR2 on mesothelioma chemoresistance and the tumor microenvironment," *Mol. Oncol.*, vol. 16, no. 22, pp. 3949–3974, Dec. 2022, doi: 10.1002/1878-0261.13322. [71] T. L. Wong *et al.*, "ADAR1-mediated RNA editing of SCD1 drives drug resistance and self-renewal in gastric cancer," *Nat. Commun.*, vol. 14, no. 1, p. 7990, Dec. 2023, doi: 10.1038/s41467-023-38581-8.
- [72] H. Cheng, J. Yu, and C. C. Wong, "Adenosine-to-inosine RNA editing in cancer: Molecular mechanisms and downstream targets," *Protein Cell*, vol. 16, no. 6, pp. 391–417, Jun. 2025, doi: 10.1093/procel/pwae039.
- [73] J. Richter, D. Madduri, S. Richard, and A. Chari, "Selinexor in relapsed/refractory multiple myeloma," *Ther. Adv. Hematol.*, vol. 11, p. 204062072093062, Jan. 2020, doi: 10.1177/2040620720930629.
- [74] Y. A. Bernal, E. Durán, I. Solar, E. A. Sagredo, and R. Armisén, "ADAR-mediated A>I(G) RNA editing in the genotoxic drug response of vol. 25, 7424, 2024, doi: Int. Mol.Sci., no. 13, Jul. p. [75] Q. T. Ostrom, G. Cioffi, K. Waite, C. Kruchko, and J. S. Barnholtz-Sloan, "CBTRUS Statistical Report: Primary brain and other central nervous system tumors diagnosed in the United States in 2014-2018," Neuro-Oncol., vol. 23, suppl. 3, pp. iii1-iii105, Oct. 2021, doi: 10.1093/neuonc/noab200.
- [76] Z. Li *et al.*, "Aberrant alternative splicing pattern of ADAR2 downregulates adenosine-to-inosine editing in glioma," *Oncol. Rep.*, vol. 33, no. 6, pp. 2845–2852, Jun. 2015, doi: 10.3892/or.2015.3907.
- [77] V. Cesarini *et al.*, "ADAR2/miR-589-3p axis controls glioblastoma cell migration/invasion," *Nucleic Acids Res.*, vol. 46, no. 4, pp. 2045–2059, Feb. 2018, doi: 10.1093/nar/gkx1257.
- [78] V. Patil, J. Pal, K. Mahalingam, and K. Somasundaram, "Global RNA editome landscape discovers reduced RNA editing in glioma: Loss of editing of gamma-amino butyric acid receptor alpha subunit 3 (GABRA3) favors glioma migration and invasion," *PeerJ*, vol. 8, e9755, Sep. 2020, doi: 10.7717/peeri.9755.
- [79] Y. Zhang et al., "ADAR3 expression is an independent prognostic factor in lower-grade diffuse gliomas and positively correlated with the editing level of GRIA2Q607R," Cancer Cell Int., vol. 18, no. 1, p. 254, Dec. 2018, doi: 10.1186/s12935-018-0695-8.
- [80] A. Ghalali et al., "AZIN1 RNA editing alters protein interactions, leading to nuclear translocation and worse outcomes in prostate cancer," Exp. Mol. Med., vol. 54, no. 10, pp. 1713–1726, Oct. 2022, doi: 10.1038/s12276-022-00845-6.
- Exp.Mol.vol. no. pp. 10.1038/s12276-022-00845-6. [81] X. Hu et al., "RNA over-editing of BLCAP contributes to hepatocarcinogenesis identified by whole-genome and transcriptome sequencing," Cancer Lett., vol. 357, no. 2, pp. 510-519, Feb. 2015, doi: 10.1016/j.canlet.2014.12.006.
- [82] W. Chen et al., "A-to-I RNA editing of BLCAP lost the inhibition to STAT3 activation in cervical cancer," Oncotarget, vol. 8, no. 26, pp. 43201–43212, 2017, doi: 10.18632/oncotarget.17034. [Online]. Available: www.impactjournals.com/oncotarget.
- [83] K. Gumireddy *et al.*, "The mRNA-edited form of GABRA3 suppresses GABRA3-mediated Akt activation and breast cancer metastasis," *Nat. Commun.*, vol. 7, p. 10715, Feb. 2016, doi: 10.1038/ncomms10715.
- [84] J. Liu, F. Wang, Y. Zhang, J. Liu, and B. Zhao, "ADAR1-mediated RNA editing and its role in cancer," Front. Cell Dev. Biol., vol. 10, p.

- 956649, Jul. 2022, doi: 10.3389/fcell.2022.956649.
- [85] B. Z. Tan, H. Huang, R. Lam, and T. W. Soong, "Dynamic regulation of RNA editing of ion channels and receptors in the mammalian nervous system," *Mol. Brain*, vol. 2, p. 13, 2009, doi: 10.1186/1756-6606-2-13.
- [86] B. J. Booth *et al.*, "RNA editing: Expanding the potential of RNA therapeutics," *Mol. Ther.*, vol. 31, no. 6, pp. 1536–1557, Jun. 2023, doi: 10.1016/j.ymthe.2023.01.005.
- [87] D. Katrekar *et al.*, "Efficient *in vitro* and *in vivo* RNA editing via recruitment of endogenous ADARs using circular guide RNAs," *Nat. Biotechnol.*, vol. 40, no. 6, pp. 938–945, Jun. 2022, doi: 10.1038/s41587-021-01171-4. [88] K. H. Tamizkar and M. F. Jantsch, "RNA editing in disease: Mechanisms and therapeutic potential," *RNA*, vol. 31, no. 3, pp. 359–368, Feb. 2025, doi: 10.1261/rna.080331.124.
- [89] J. R. Sinnamon et al., "Targeted RNA editing in brainstem alleviates respiratory dysfunction in a mouse model of Rett syndrome," Proc. Natl. vol. e2206053119, Aug. doi: 10.1073/pnas.2206053119. Acad. U. S. A., 119, no. 33, 2022, [90] D. Katrekar et al., "In vivo RNA editing of point mutations via RNA-guided adenosine deaminases," Nat. Methods, vol. 16, no. 3, pp. 239-242, Mar. 2019, doi: 10.1038/s41592-019-0323-0.
- [91] H. A. Tanash and E. Piitulainen, "Liver disease in adults with severe alpha-1-antitrypsin deficiency," *J. Gastroenterol.*, vol. 54, no. 6, pp. 541–548,

 Jun. 2019, doi: 10.1007/s00535-019-01548-y.
- [92] X. Zhang and W. Song, "The role of APP and BACE1 trafficking in APP processing and amyloid-β generation," *Alzheimers Res. Ther.*, vol. 5, no. 5, p. 46, 2013. [Online]. Available: http://alzres.com/content/5/5/46
- [93] Y. Y. Syed, "Selinexor: First global approval," *Drugs*, vol. 79, no. 13, pp. 1485–1494, Sep. 2019, doi: 10.1007/s40265-019-01188-9. [94] S. Wang *et al.*, "COPA A-to-I RNA editing hijacks endoplasmic reticulum stress to promote metastasis in colorectal cancer," *Cancer Lett.*, vol. 553, 216995, Jan. 2023, doi: 10.1016/j.canlet.2022.216995.
- [95] P. Shen et al., "CircNEIL3 regulatory loop promotes pancreatic ductal adenocarcinoma progression via miRNA sponging and A-to-I RNA-editing," Mol. Cancer, vol. 20, no. 1, p. 51, Dec. 2021, doi: 10.1186/s12943-021-01333-7.